An integrated assessment framework for quantifying and forecasting water-related multi-hazard risk

Xiaodong Ming

School of Engineering

Newcastle University

A thesis submitted for the degree of Doctor of Philosophy

June 2019

Abstract

Disaster risks induced by different kinds of hazard may emerge in any place where human activities or properties exist. Most human settlements are exposed to more than one hazard. The multi-hazard risk analysis that assesses the potential loss caused by multiple natural hazards can provide a valuable reference for regional land-use planning, disaster prevention and emergency management. Although an increasing number of risk assessment methods related to multi-hazard have been developed recently, three main challenges remain in the current practices: (1) the disparate characteristics of hazards increase the difficulty of their combination and comparison, (2) the dependence and interactions between different hazards are often neglected, and (3) the results of multi-hazard risk assessment are not quantitative to show the probability of disaster loss.

This thesis aims to construct an integrated framework to quantify and forecast the risk of multiple water-related hazards including heavy rainfall, extreme river flow, and storm surge. The framework consists of the three typical components of disaster risk assessment containing hazard, vulnerability, and risk analysis and is applied in the Greater London and the Eden Catchment, UK. For hazard analysis, the joint probability and return period distributions are fitted for the three water-related hazards on the basis of dependence analysis and copula theory. A newly developed 2D hydrodynamic model is enhanced with auto Input-Output control and processing in a multi-GPU platform to drive numerous flood simulations. The frequency-inundation curves due to the combination of the three hazards are generated by connecting the joint return period functions and the results of flood simulations. The distribution of human life and properties in the research area are analysed and classified with different vulnerability curves that quantify the potential damage due to the severity of inundation. The component of risk analysis evaluates the probability of loss for human life or different types of properties according to the results from the hazard and vulnerability analysis.

The risk assessment framework considers the interaction and dependence between the multiple hazards by using hydrodynamic modelling and joint probability analysis,

respectively. It can produce fully quantitative results such as risk curves quantifying the probability of different damage states, and risk maps illustrating the expected loss in the research region. With the efficient 2D hydrodynamic model and the autoprocessing package, the framework is further applied to give flood and risk forecasting to the Eden Catchment by integrating with a numerical weather prediction model.

The framework shows a quantitative approach of multi-hazard risk assessment. It also provides an integrated procedure of flood risk analysis and forecast in consideration of the dependence and interactions between different water sources. The methodology and the findings are of interest to insurance companies, regional planners, economists, disaster-prevention authorities, and residents under the threat of flooding. The main source of uncertainties of the framework and the limitations are identified. Future work and further applications in other regions are recommended.

Acknowledgement

I own my deepest gratitude to my supervisor Qiuhua Liang for his patient guidance, continuous encouragement, and insightful advice throughout my PhD study. I also express my warmest gratitude to my supervisor Richard Dawson who gave me invaluable suggestions with his immense knowledge and inspiring support especially during the absence of other supervisors. I am profoundly grateful to Hiro Yamazaki who supervised me in the first two years of my PhD with great enthusiasm.

Heartfelt thanks also go to Chris Kilsby, Caspar Hewett, Greg O'Donnell, Francesco Serinaldi, Stephen Blenkinsop, Hayley Fowler, Stuart Barr, and Zhenhong Li for their indispensable advice, information, and support on different aspects of my research.

I am incredibly fortunate to have benefited from my colleagues and friends in water group, including Xilin Xia, Jingchun Wang, Jingming Hou, Reza Amouzgar, Luke Smith, Sam Mahaffey, Francesco Castellani, Golnaz Jahanshahi, Maria Pregnolato, Doug Richardson, Qian Li, Canqi Liu, Luis Felipe Duque, Jinghua Jiang, and Xiaoli Su. I would extend my gratitude to all the friends I met in Newcastle although the list of names is too long to write here. I appreciate all the happy time they brought to me in the past four years.

My sincere thanks to David Walker, Mhari Barnes, Fergus McClean, Laura McGinty, Michael Pollock, Kishor Acharya, and Daniel Leicester, who are not only my friends but also the proof-readers of this thesis. I would also like to thank the administrative staff and computing technicians in School of Engineering including Melissa Ware, Hannah Lynn, Lynn Patterson, and Graham Patterson for their professional and enthusiastic support.

I would like to thank my PhD sponsors: Newcastle University, Sir James Knott Studentship from Institute for Sustainability, and Henry Lester Trust.

This work would not be possible without the unreserved love and unconditional support from my dear wife, my parents, my brother, my sister, and my entire family. I would express my greatest thanks to them.

List of publications

Ming, X., Liang, Q., Yamazaki, H., Dawson, R., 2016. An integrated assessment framework for quantifying multi-hazard risk in large cities. *EGU General Assembly Conference 2016*, Vienna, Austria, 17th-22nd April 2016.

Ming, X., Liang, Q., Dawson, R., Yamazaki, H., Xia, X., 2016. Multi-source flood risk assessment based on joint probability analysis on costal areas. *The Geological Society Conference: Rain, Rivers, and Reservoirs*, Edinburgh, UK, 27th-29th September 2016.

Ming, X., Liang, Q., Xia, X., Dawson, R., 2018. Multi-source flood modelling with defence failure scenarios adaptive to various hydraulic conditions. *13th International Conference on Hydroinformatics*, Palermo, Italy, 1st-6th July 2018.

Contents

List of figures

List of tables

Chapter 1. Introduction

1.1 Background

Natural disasters have always been a big threat to the sustainable development of human societies (El-Masri and Tipple, 2002), and can be caused by various types of physical hazards, including flood, storm, drought, earthquake, landslide and so on. Most areas in the world have experienced and are under the threat of more than one type of hazard (Shi and Kasperson, 2015). Many catastrophes that lead to significant damage to properties and loss of human lives in history are attributed to the joint impact of multiple hazards (Munich Re, 2003). For example, the 1928 London Flood was caused by the concurrence of extreme river flow from the upstream River Thames and storm surge from the North Sea (Carlsson-Hyslop, 2010); and the 2009 Taiwan Debris flows are believed to have been directly triggered by the Typhoon Morakot and also influenced by the Chi-Chi earthquake that happened 10 years previously (Hsu et al., 2014; SHIEH et al., 2009).

Disaster risk assessment evaluates the likelihood and magnitude of potential disaster losses and plays a critical role in disaster reduction and mitigation (United Nations, 1999). Compared with single-hazard risk assessment, multi-hazard risk analysis can acquire a more comprehensive perception of the regional risk level and help better understand the mechanisms of various causes and the impact of the losses. It would provide integrated information to decision-makers in disaster risk management, urban planning, and future investment.

The awareness of the necessity to study multi-hazard risk has continued to grow since the concept of multi-hazard was proposed in the 1990s (Kappes et al., 2012). A number of large-scale studies have been attempted to appraise the general pattern of multi-hazard disaster risk in China (Shi, 2011), Europe (ESPON, 2006; Lung et al., 2013), the USA (FEMA, 2011), and the whole earth (Shi and Kasperson, 2015) with consideration of all the main types of disasters appearing in those areas. The assessing unit is typically the secondary administrative district (country, state, province, etc.) of the research region, and the results are shown as

qualitative rank or semi-quantitative risk index that can be used for comparison between the assessing units. To produce a more elaborate assessment, some multi-hazard risk assessments are performed for small regions with higher analysis resolutions. Examples include a GIS-based study in the city of Costa Rica using statistical approach to evaluate the risk of flood, earthquake and landslide (Westen et al., 2002), an assessment of coastal hazards in a beach located in Spain (Lozoya et al., 2011), and a high resolution raster-based ($20m \times 20m$) risk assessment of debris flow and rock fall in a settlement of Iceland (Bell and Glade, 2004). The small-scale evaluation of multi-hazard risk can focus on the most significant hazards to the local region and provide more quantitative results (Li et al., 2009). However, some common challenges or limitations exist in the current practice of multi-hazard risk assessment.

Firstly, the potential dependence of the occurrence of hazards is usually ignored in multi-hazard risk assessment but may significantly affect the prediction of multi-hazard joint frequency (Selva, 2013). The probabilistic relationship between hazards is usually simplified to be independent (Liu et al., 2016). Some joint probability studies have attempted to use statistical methods to estimate the dependence between two hazards (Horsburgh and Wilson, 2007; Petroliagkis et al., 2016; Zheng et al., 2014); but have not been extended to disaster risk assessment.

Another limitation is about the hazard interactions (Gill and Malamud, 2014) that are not properly investigated in most of the existing studies. The interactions refer to the impact of one hazard on the other hazard(s) and are very difficult to be simulated or quantified because of the complex process among the various physical forces (Kameshwar and Padgett, 2014). However, those interactions can significantly influence the degree of danger of the combined hazards. Currently, instead of physically-based models, the dominant approach to investigate the hazard interactions is either weight coefficients (Greiving et al., 2006) or statistical methods (Selva, 2013) that are empirical and may be problematic when facing unprecedented events or in new research areas and environments.

Moreover, it is a big challenge to produce fully quantitative results in multi-hazard risk assessment because of its high complexity. The qualitative measures like risk ranks or semi-quantitative measures like risk indexes are the typical illustrating method of multi-hazard risk (Kappes et al., 2012). However, those methods are only applicable to the comparison of risk level between the assessing units but cannot predict the possibility of disaster loss. The full quantitative results shown as probability-loss curves are very rare, especially for the assessment considering the dependence and interactions of multiple hazards but can provide

more detailed information of disaster risk and are valuable for both residents and decision-makers.

Therefore, to construct a quantitative multi-hazard risk assessment framework considering the dependence of occurrence and the physical interactions between the hazards is of great significance to both research and practice.

1.2 Terminology of disaster risk

It is always a challenge to find universal definitions for terminologies in an emerging and interdisciplinary subject. Concepts related to disaster risk have been proposed and defined by different researchers with various understandings based on their own academic background. To prevent confusion, it is necessary to summarise the glossary that will be used in this thesis.

1.2.1 Disaster risk

According to Oxford Dictionary, 'risk' can be defined as 'the possibility of something bad happening at some time in the future or a situation that could be dangerous or have a bad result'. While in the context of academic research, *risk* is generally recognized as the combination or interaction of several factors including hazard, vulnerability, exposure, resilience, coping capacity, etc. Some works have been done to compare and review the glossary of these concepts (Thywissen, 2006). The version of international standard terminology proposed by the United Nations (UNISDR, 2009) will be employed in this thesis as shown in Table 1-1.

Disaster can be caused by natural phenomenon, man-made accident, or the combination of the two. In this thesis, we only focus on the damage due to natural forces. So, the disaster means explicitly the natural disaster and the hazard refers to the natural hazard hereinafter unless otherwise specified. ***Hazard*** can be categorised as the indirect hazard and the direct hazard according to whether the hazard can directly trigger damage on the elements at risk. For example, rainfall is typically not a direct hazard to buildings. Instead, the inundation accumulated from rainfall is the direct hazard.

The definition of ***Vulnerability*** can derive many relevant concepts, such as resilience (Cutter et al., 2008), coping capacity (O'Brien et al., 2006), adaptivity (Smit and Wandel, 2006) etc. The generalised analysis of vulnerability would regard all these factors as the parameters of vulnerability function and sometimes even treats the exposure as the susceptibility attribute of

vulnerability (Capobianco et al., 1999; Klein and Nicholls, 1999). ***Exposure*** is defined as people and human property present in hazard zones that are thereby subject to potential losses. In this thesis, *exposure* is analysed separately from vulnerability as the extent of elements exposed to natural hazards.

In some research, risk may indicate the chance of harmful events happening, like a flood (Zheng et al., 2015), an earthquake (McCloskey et al., 2005), or a heat wave (Stott et al., 2004), but not necessarily refer to the loss caused by the events. In this thesis, ***Risk*** is strictly pointed to the potential consequence of events and used to quantify the probability of loss in the natural disaster. Hazard, vulnerability, and exposure are the three sides in "The risk triangle" that is a schematic representation of disaster risk described by Crichton (1999). To quantitatively evaluate disaster risk, an equation of Risk = Hazard x Vulnerability x Exposure is generally referenced in many literatures (Kron, 2002), which is utilised as the basis of calculating risk in this thesis.

Table 1-1 Terminology of disaster risk.

Concept	UNISDR Definition (UNISDR, 2009)	Note
Disaster	A serious disruption of the functioning of a community or a society involving widespread human, material, economic or environmental losses and impacts, which exceeds the ability of the affected community or society to cope using its own resources.	When a disaster is trigged by natural phenomenon, it is called a natural disaster
Risk	The potential disaster losses, in lives, health status, livelihoods, assets and services, which can occur to a particular community or a society over some specified future time period.	"Risk" in this thesis specifically refers to disaster risk
Hazard	A dangerous phenomenon, substance, human activity or condition that may cause loss of life, injury or other health impacts, property damage, loss of livelihoods and services, social and economic disruption, or environmental damage.	Refers to natural hazards in this thesis unless otherwise specified
Vulnerability	The characteristics and circumstances of a community, system or asset that make it susceptible to the damaging effects of a hazard.	Reflects both internal attributes and external environment
Exposure	People, property, systems, or other elements present in hazard zones that are thereby subject to potential losses.	The object of risk assessment

1.2.2 Multi-hazard risk

Multi-hazard is the natural stretch of the hazard definition and can be understood straightaway as *more-than-one-hazard* from its literal meaning without any ambiguity. However, the context of the multi-hazard issue is various in the views of different scholars and research groups. It has been regarded as the direct spatial overlap (Dilley et al., 2005) or comparison of single-hazard layers (Grünthal et al., 2006). Some researchers emphasise the statistical dependence between hazards (Klerk et al., 2015) while some focus on the triggering effect of hazards also known as hazard chains (Shi et al., 2010; Xu et al., 2014). In this thesis, the multi-hazard refers to the temporal concurrence, the spatial overlay, and the physical interactions of multiple hazards happening in the same area.

Multi-hazard risk is the potential disaster losses due to multiple hazards. It is also called "multi-risk" (Carpignano et al., 2009; Di Mauro et al., 2006; Fleming et al., 2014) or "integrated risk" (Greiving et al., 2006) in some papers. Multi-hazard risk analysis considers the impact of not only the multiple hazards but also the integrated vulnerability and the compound exposure in the multi-hazard situation. It is worth noting that the prediction of the probability of occurrence for multiple hazards without loss assessment (Wahl et al., 2015) is not complete enough to be regarded as multi-hazard risk analysis in this thesis.

1.3 Aims and objectives

This thesis aims to build a framework of multi-hazard risk assessment quantifying the potential flood loss at coastal areas due to the concurrence of heavy rainfall, extreme flow, and storm surge. The risk assessment framework is further combined with a numeric weather prediction model to give real-time risk forecasting for multi-hazard events. To achieve the overall aim of the PhD project, the following objectives will be explored and completed: :

- **To analyse the dependence and joint probability of multiple hazards**

Quantify the dependence of multiple hazards using statistical methods and estimate their joint probability and joint return period distributions, using the joint probability distributions to generate stochastic multi-hazard events with given non-exceedance probabilities or return periods, eventually better understanding the likelihood of occurrence of hazards at the different magnitude and with different combinations.

- **To simulate multi-hazard flood events with a 2D hydrodynamic model**

Explore the feasibility of applying fully hydrodynamic model in large-scale and high-resolution flood simulation with multiple water sources, validating the model for all the three water inputs and calibrating the model with appropriate parameters, using the random multi-hazard events of rainfall, river flow and total seawater level as inputs to drive the hydrodynamic model to simulate multi-hazard flooding.

- **To quantify multi-hazard disaster risks**

Estimate the frequency of flood inundation by combining the multi-hazard probability distributions with the simulated flood inundation maps from the hydrodynamic model, selecting the concerned elements of human properties and quantifying their amounts and values exposed to flood inundation, finding appropriate vulnerability curves of different human properties to estimate the disaster risks of damage or economic loss.

- **To apply the risk assessment framework in real-time risk forecasting**

Expand the risk assessment framework to provide real-time risk forecasting by using numerical weather forecasting products as inputs in the hydrodynamic model, producing forecasts of flood inundation in the multi-hazard environments and predictions of potential loss associated with the forecasted inundation maps, exposure data, and vulnerability curves.

1.4 Study regions

Two study regions are selected to achieve the four aforementioned research objectives: The Greater London catchment and the Eden catchment. The Greater London catchment includes Greater London and its downstream areas as shown in Figure 1-1. It has experienced many fluvial, pluvial, and coastal floods in history, such as the 1928 Thames Flood, the 1947 Upper Lee Flood, and the 1953 East Coast Flood (Environment Agency, 2012). Although fewer flood events can be found in recent decades due to the substantial improvement of flood defence systems, as a metropolitan region with a big population and high density of properties, Greater London can still be at risk when facing low frequent but high destructive water-related hazards, especially when the hazards are interrelated with each other. Instead of using the administrative boundary, this study region is defined based on the watershed of the Thames catchment from Kingston to the river mouth between Southend and Sheerness with a total area of 2,718 km^2. As a typical multi-hazard influenced area, the Greater London catchment is chosen to explore the first three objectives.

For risk forecasting that requires more recent events to evaluate its performance, the Eden catchment is selected as the study region instead of London that has no serious flooding in recent decades. The Eden catchment locates in the northwest of England with an approximate area of 2,500 km^2 (Figure 1-2). The main watercourse River Eden flows from southeast to northwest with three main tributaries: the Caldew, the Petteril, and the Eamont on its left and the Irthing on its right. The catchment is a wet region with an average annual rainfall over 2,800 mm which is three times of the annual average value in England. The largest settlement inside the catchment is City Carlisle located at the junction where River Caldew meets River Eden. The Eden catchment is fast responding to fluvial floods due to its steep topography in the upper region. In history, the lower area including Carlisle city centre has experienced many serious floods that are induced by either local intense rainfall or extreme upstream flows. The Eden estuary is identified as a high risky area that may suffer from compound flooding (Paprotny et al., 2018). Therefore, it is necessary to take into account the physical impact of estuarine sea level on upstream flow in hydrodynamic modelling, especially when a sea level rise is expected in the near future due to global warming (IPCC, 2014a).

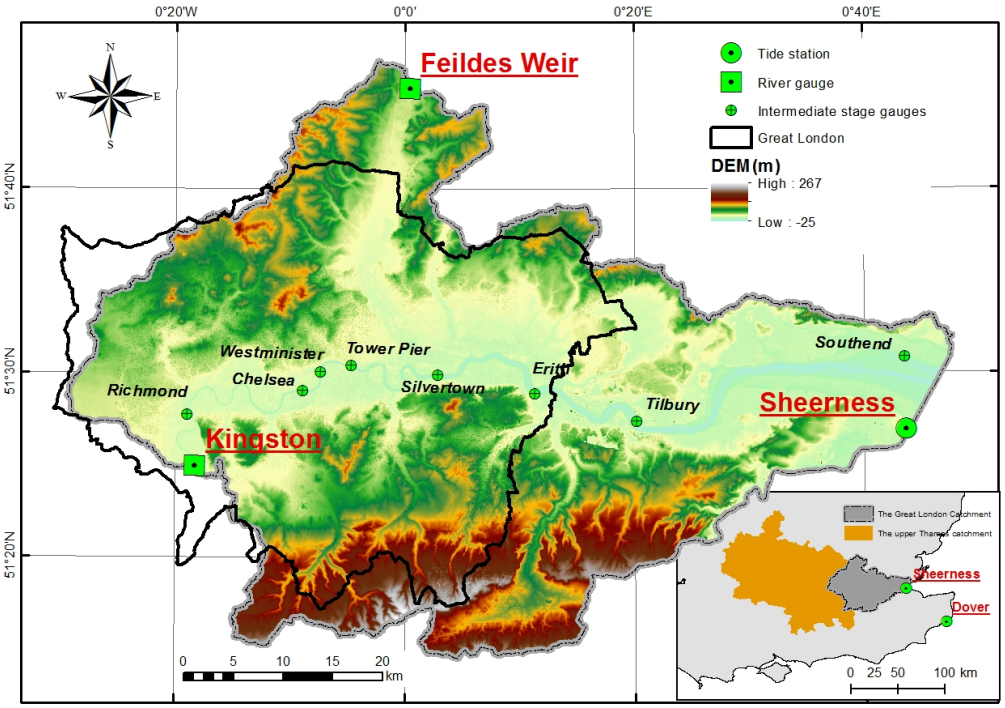

Figure 1-1. The Greater London catchment. DEM data provided by Digimap © Crown Copyright Ordnance Survey

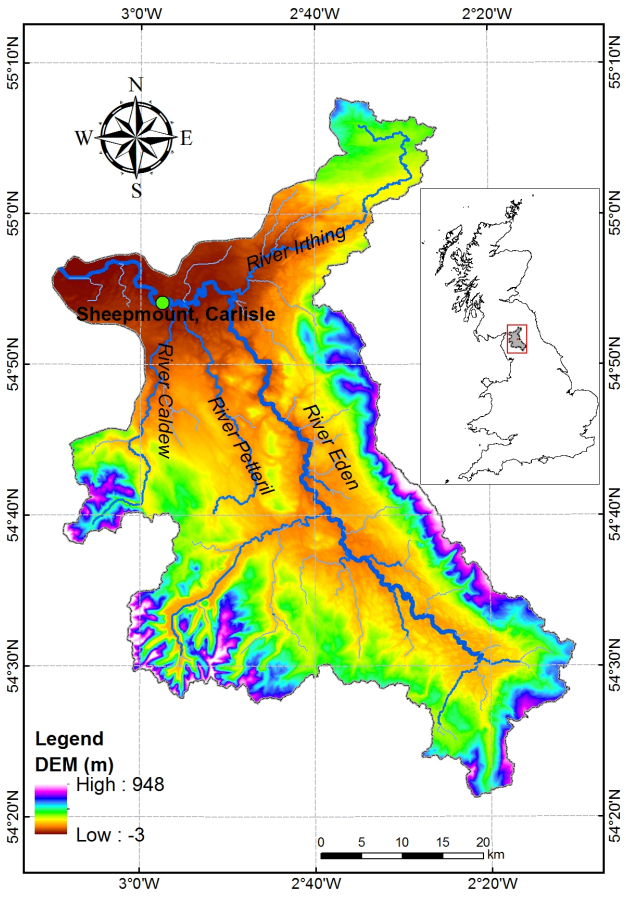

Figure 1-2. The Eden catchment and its location in Britain. The length of the Eden River is 145 km. The average and max discharges are 51.82 m^3/s and 1700 m^3/s at the Sheepmount river gauge.

1.5 Outline of thesis

Excluding the current chapter for Introduction, the rest of the thesis is organised as follows:

Chapter 2 gives a comprehensive literature review of the relevant fields including multi-hazard risk assessment, multivariate dependence analysis, hydrodynamic modelling, vulnerability analysis in multi-hazard context, and hazard and risk forecasting.

Chapter 3 introduces all the methods and tools applied in this thesis including asymptotical dependence analysis, copula function, a 2D hydrodynamic model, and the techniques for vulnerability and risk assessment.

Chapter 4 applies dependence measures and copula function to evaluate the different types of dependence among the hazards and estimate the joint probability distribution and return period of the three hazards.

Chapter 5 uses the 2D hydrodynamic model to simulate floods for various hazard combination scenarios and produce inundation maps and hazard curves by connecting multi-hazard inputs with their estimated frequency.

Chapter 6 demonstrates the entire procedure of multi-hazard risk assessment for buildings and road networks by combining the result of hazard, vulnerability and exposure analysis and show the quantitative results in the form of risk curves and risk maps.

Chapter 7 demonstrates real-time capability of the hydrodynamic model by integrating with a numeric weather prediction model to provide flood and risk forecasting in the catchment with multi-hazard impacts.

Chapter 8 draws the conclusions of the study and recommends future research in the research topic.

Chapter 2. Literature review

This chapter firstly gives a broad summary of multi-hazard risk research, followed by a review of dependence analysis in multi-hazard issues. Then, the review is focused on the simulating methods for compound flooding and the flood vulnerability analysis. At last, the current studies of hazard and risk forecasting for flooding is reviewed, and a summary is given to address the research gaps with objectives of this thesis.

2.1 An overview of multi-hazard risk analysis

The number of reported natural disasters experienced a sharp increase in the last decades, causing more and more mortality and economic loss (Winsemius et al., 2016). Disaster risk has become a prevailing research topic since the launch of the programme International Decades of Natural Disaster Reduction (IDNDR) (Housener, 1989) and the International Strategy for Disaster Reduction (ISDR) (IDNDR, 1994). As a large number of population and land area may be threatened by two or more hazards simultaneously (i.e. multiple hazards) (Dilley et al., 2005), it is essential to investigate the disaster risk under the effect of multiple hazards. Multi-hazard risk assessment aims to evaluate the integrated disaster risk caused by various hazards and has been gaining interest from numerous researchers in the recent decade (Gallina et al., 2016).

Multi-hazard is also expressed as compound events (Leonard et al., 2014) and increasingly being used in many literatures (Petroliagkis, 2018; Sadegh et al., 2018; Wahl et al., 2018; Ward et al., 2018). Multi-hazard can be categorised as three broad classifications according to the relationship between hazards: (1) concurrent hazards – the concurrence of two (or more) hazard events in time and/or space (Chen et al., 2012); (2) successive hazards – the recurrence of the same hazard within a significant time (SHIEH et al., 2009); (3) cascading hazards – primary hazards trigger other secondary/tertiary hazards or increasing the probability of other hazards, also known as hazard chains (Xu et al., 2014). In this thesis, only the concurrent hazards are considered for risk assessment.

The understanding of multi-hazard risk is divergent as an interdisciplinary topic (Kappes et al., 2012). However, its fundamental characteristics of interest can include:

1. **Dependence: the statistically dependent occurrence of multiple hazards**

   Some hazards may be relevant in terms of the causes, that the appearance of one hazard indicates the increase or decrease of the probability of the other hazard(s) happening. For example, an earthquake may raise the possibility of landslide (Miles et al., 2007), and heavy rainfall is usually accompanied with strong winds in monsoon regions (Shukla et al., 1977). The multi-hazard dependence analysis generally focuses on the statistical behaviour of the occurrence and magnitude of the hazards (Petroliagkis, 2018) and will be specifically reviewed in section 2.2.

2. **Hazard interaction: the physical mutual effect between hazards**

   One hazard can affect the physical process, magnitude, or the degree of danger of the other hazard(s). For example, strong wind can enlarge total water level (Escobar et al., 2004), and rainstorms may augment pluvial flooding area (Apel et al., 2015). As one of the focuses of multi-hazard study, Gill and Malamud (2014, 2016) have identified the interactions between 21 natural hazards from five hazard groups, which is a qualitative and comprehensive review for the various mutual relations between multiple hazards. Liu et al (2016) categorised the hazard interactions into four types including independent, mutually-exclusive, parallel, and cascading relations, according to the geophysical hazard-forming environment. Identifying and quantifying the hazard interactions are important issues in multi-hazard analysis.

3. **Integrated vulnerability: the likelihood of damage under the impact of multiple hazards**

   The elements at risk can experience different degrees of damage when acted by the coincident multiple hazards compared with the damage due to the individual hazard (Li and van de Lindt, 2012). It is essential to evaluate the integrated effect of all the considered hazards in multi-hazard risk assessment. The objective and subjective weight methods are commonly employed in the qualitative analysis that measures the integrated vulnerability in rank or index (ARMONIA, 2006). Statistical techniques are utilized in some papers to quantitatively investigate the integrated vulnerability of crops exposed to wind and rain (Ming et al., 2015), and turbines exposed to wind and

earthquakes (Mardfekri and Gardoni, 2015). Lee and Rosowsky (2006) employed some experimental data to analyse the integrated fragility of woodframe buildings due to the joint snow and earthquake loading.

As a summary of the three characteristics, "integration" is the common and critical word in the integrating process from the single-hazard risk to multi-hazard risk as an interrelated system (Kappes et al., 2010). According to the procedure of integration, the multi-hazard risk assessment can be divided into two types. The first type only integrates into the final step of risk assessment using the results from each individual hazard, which is actually the assessment of "multi-layer single-hazard risk" (Gill and Malamud, 2014). The integration in Type II methods are performed at the risk components, including the multi-hazard (Ehlen and Vargas, 2013), the integrated vulnerability (Rød et al., 2012), and the compound exposure (Novelo-Casanova and Suárez, 2012).

If we define the risk (R) as a function of the hazard (H), the vulnerability (V), and the exposure (E), the two types of multi-hazard risk assessment can be illustrated by formulas in Table 2-1. The symbol $\sum$ denotes the process of integration, which does not necessarily mean summation. The integration in the Type I assessment linearly combines the results of the single-hazard risk with proportions representing their contributions to the total risk. But the interrelations of the risk components from different hazards are generally ignored. In the Type II approaches, the integration of each risk component can better represent their interactions and interrelations but is usually problematic because of the complicated physical processes and the various hazard quantities.

Table 2-1. The expressions of the two types of multi-hazard risk assessment.

Type	Expression	Reference of examples
I	$R = \sum f_i(H_i, V_i, E_i)$	(Arnold et al., 2006; Dilley et al., 2005; Grünthal et al., 2006; Kameshwar and Padgett, 2014; Mosquera-Machado and Dilley, 2009; Schmidt-Thomé, 2006; Shi, 2011; Wipulanusat et al., 2009)
II	$R = f(\sum H_i, \sum V_i, \sum E_i)$	(ARMONIA, 2006; Carolina and Management, 2006; ESPON, 2006; Mardfekri and Gardoni, 2015; Ming et al., 2015; Munich Re, 2003; Olfert and Greiving, 2006; Schmidt-thomé et al., 2003; Thierry et al., 2008; Yin and Li, 2011)

The result of multi-hazard risk analysis can provide comprehensive information on the regional disaster risk, which is especially interesting for decision-makers and stakeholders like government departments, insurance and consultancy companies. These organizations supported or invested in some large-scale assessments of multi-hazard risk, including international research projects like the Global Natural Disaster Risk Hotspots (Dilley et al., 2005) and the ESPON program (Schmidt-thomé et al., 2003), and operational platforms for automated evaluation of multi-hazard risks, for instance, HAZUS (FEMA, 2011) and RiskScape (Schmidt et al., 2011). The large-scale assessment typically has the following features:

- A large research area, like a big country (FEMA, 2011; Shi, 2011), a continent (ESPON, 2006; Fleming et al., 2014), or the whole world (Dilley et al., 2005; Shi and Kasperson, 2015)
- A large assessment unit, typically the second or the third administrative district of the research region like country, state, and province
- A number of considered hazards, trying to cover all the influential dangers inside the evaluation domain, for example, 15 natural and technical hazards appraised in ESPON (2006), 12 natural hazards evaluated in Shi and Kasperson (2015)
- Simplified interrelations and interactions between different types of disasters, regarded as independent or linear relations with specific proportions of contribution to the total risk (Mosquera-Machado and Dilley, 2009)

Unlike the large-scale project, some small-scale assessments focus on relatively smaller regions and thus can be more targeted on the local disaster mitigation and risk management. The main characteristics of this research include:

- A small research area, like a city (Marzocchi et al., 2012), a community (Li et al., 2009), or a village (Bell and Glade, 2004)
- High-resolution assessment, the assessing unit can be fine grid cells with hundreds or tens of meters wide (e.g. Westen et al. 2014)
- A few considered hazards, concentrating on the most critical dangers to the local region
- More quantitative integrating methods, like statistical method (Ming et al., 2015), engineering experiment (Lee and Rosowsky, 2006), and hazard simulating models (Lian et al., 2013)

The large-scale assessments were prevailing in the early stage of disaster risk research to provide a common and comprehensive view of the multi-hazard risk level. Recently, more and more small and regional studies appeared to make the objectives and the methods of multi-hazard risk assessment become more diverse. Some cases of the multi-hazard risk assessment in the past decade are summarised in Table 2-2. It lists seven recent multi-hazard risk studies with the considered hazards, the types of exposure, the measures of risk, the outputs of assessment, the study area with assessing unit, and the key features. A significant trend of the multi-hazard risk research is that the quantitative risk assessment is becoming widespread. The typically quantitative measure of risk is the expected loss. But the object of loss is varied between different methods, including the direct economy (Selva, 2013), human life (Lung et al., 2013), infrastructure (Westen et al., 2014), agriculture (Wipulanusat et al., 2009), and so forth. Those quantitative risk assessments can provide more detailed information on the possibility of loss and have been the first choice of many recent studies.

Table 2-2 Cases of multi-hazard risk assessment in the recent decade.

Reference	Hazards	Exposure	Risk	Outcome	Study area	Features
(Lozoya et al., 2011)	storm, erosion, river floods, jellyfish, tourism overuse, hinterland urbanization	beach	surface area reduction, quality reduction	annual economic loss	S'Abanell beach, Spain. Divided into two parts: north and south	considered both natural and human hazards; direct addition for all kinds of risks; interactions are not considered
(Li and van de Lindt, 2012)	Hurricane, wind, earthquake, snow, flood	light-frame wood buildings	damage condition	expected annual loss	four cities in the USA	fully quantitative; engineering methods; direct addition of independent hazards
(Lung et al., 2013)	heat stress, river flood, forest fire	human	human health	risk ranks (5 ranks)	NUTS-2 regions, 26 of the Member States of the European Union (EU)	weighted aggregation; the influence of climate change is considered; adaptive capacity is considered
(Selva, 2013)	volcanic ash in seismic, local earthquakes in tsunami	economy	direct economic loss	loss-probability risk curve	Naples, Italy	fully quantitative; interactions considered in limited hazard scenarios

(Kameshwar and Padgett, 2014)	Earthquake, hurricane (storm surge and wave loading)	highway bridges	bridge damage	annual probability of damage	concrete girder bridges located in South Carolina, USA	engineering methods; fully quantitative; only comparison without aggregation
(Westen et al., 2014)	landslides, debris flows, rockfalls, snow avalanches and flood	building	building loss	expected losses due to each hazard	Barcelonnette, France, Pixel 1:25,000	GIS-based; uncertainty analysis; non-aggregation; interactions are not considered
(Ming et al., 2015)	Heavy rain, strong wind	crops	crop loss ratio	loss ratio-probability risk curve	Yangtze River Delta region, county level	fully quantitative; statistical analysis; dependence quantified; vulnerability curve

In general, the multi-hazard risk is a complicated system with a lot of interactive elements and inner-relationships to be clarified. The quantitative risk assessment that can reflect the interrelations is facing some difficulties, including the estimation of the joint frequency of hazards, and the quantification of hazard interactions. It is essential to develop an integrated framework of multi-hazard risk assessment that can estimate the joint frequency based on the dependence and various marginal distributions of the hazards and use physically-based models to simulate the hazard interactions.

2.2 Dependence analysis for multiple hazards

When thinking about multiple-hazard issues, a key concern is the potential inter-relationships of the occurrence of different hazards in a given spatial region or temporal period. As the 'Butterfly Effect' reveals, the natural phenomena on earth are potentially interrelated with each other. Some of the interrelations are evident and can be explained by the current studies, i.e. the dependent relationship between seawater temperature in the east and the west Pacific (known as El Niño-Southern Oscillation (ENSO)) (Neelin et al., 1998) . Some interrelations can be statistically detected but are yet to be physically illustrated like some types of earthquakes are found to be correlated with heavy rainfall but the reason is still unclear (Hainzl et al., 2006).

The dependence widely occurs among natural hazards sharing the same initial trigger(s), and its intensity varies according to the local geographical environment and the categories of the

hazards. For example, heavy rainfall, strong wind and storm surge are highly related to each other in coastal zones influenced by tropical cyclones but less relevant in regions with fewer severe convective weather systems. For hydrometeorological hazards that result from the same regional weather condition, the dependence among them can be even stronger. Multi-hazard analysis needs to consider the potential dependence between the considered hazards as it matters with the likelihood of hazards coincidence that may cause severer consequence compared with the outcome of individually happening of hazards (Leonard et al., 2014; Wahl et al., 2015).

There were numerous studies that have concentrated on the dependence between hydrometeorological hazards, including the variables from the same hazard, such as the volume and discharge at the same gauges during a flood event (Zhang et al., 2006); or from different hazards, like the extreme discharge and the height of storm surge in coastal regions (Klerk et al., 2015).

A lot of studies have concentrated on the dependence between hydrometeorological hazards including heavy rainfall, extreme river flow, and sea surge. In coastal areas, extreme rainfall and surge are two of the main natural hazards that may co-occur and lead to flooding greater than from either in isolation. The dependence between heavy rainfall and storm surge are investigated for coastlines around the world. Zheng et al. (2013) quantified the strength of dependence between daily maximum surge and daily rainfall for the coastal regions of the Australian continent and concluded that these two hazards must be considered jointly with their dependence if flood risk is to be assessed correctly. Wahl et al. (2015) evaluated the likelihood of joint occurrence of storm surge and rainfall at major cities along the US coastline and demonstrated the importance of assessing compound flooding and its linkages to weather and climate. Van Den Hurk et al. (2015) used an ensemble of regional climate model simulations to demonstrate that the combined occurrence of the heavy precipitation and storm surge is physically related in the Netherlands.

The extreme river flow from upstream catchments is another potential hazard that may exaggerate flooding when it occurs together with extreme rainfall or sea surge. The dependent interaction of sea level and river flow was found to increase the flood risk in low lying floodplain zones and can be quantified by joint probability analysis (White, 2007). Kew et al. (2013) analysed the concurrence of surge and river flow extremes for the Rhine delta with climate ensemble and concluded that the extreme surge and discharge probabilities are not independent for the current climate. Moftakhari et al. (2017) proposed a bivariate hazard

assessment framework for compound flooding from river flow and coastal water level in three estuarine systems along the coasts of the US and found that the correlation between river flows and surges is spatially diverse in different regions. Ward et al. (2017) assessed the dependence between observed high sea-levels and high river discharge for deltas and estuaries around the globe and illustrated how the dependence may influence the joint probability of flood.

In addition to the double-hazard dependence analysis, a few studies also consider all the three hazards that are potentially concurrent in river estuaries. For example, the paired dependence between extreme sea surge, river flow, and precipitation are evaluated in south and west Britain and the strength of different paired dependence is compared (Svensson and Jones, 2004). Paprotny et al. (2018) investigated the probability of joint occurrence of storm surges, precipitation, and river discharges for a pan-European assessment of compound flood potential and identified the areas at risk from different types of compound flooding.

The presence of dependence among multiple hazards is not only analysed based on the physical process but also revealed as the stochastic behaviour of their indicating variables. Many attempts have been made to quantify the strength of the dependence by applying different statistical tools. An asymptotic dependence measure was introduced by Buishand (1984) to estimate the dependence of inter-station rainfall data in the Netherlands. It was then further developed by Coles et al. (1999) to evaluate both the asymptotic dependence and independence of extreme value data. A Bayesian Network is developed to investigate the shoreline change rates accompanying sea level rise (Gutierrez et al., 2011). Zheng et al. (2013) proposed a bivariate extreme model to calculate the dependence between extreme rainfall and storm surge and estimate the coastal flood risk in a catchment near Sydney (Zheng et al., 2014). Apart from those bivariate models, many nonparametric and rank-based approaches were introduced by statisticians while Spearman's rho and Kendall's tau are the two most widely used statistics (Genest and Favre, 2007) that are also able to measure the multivariable dependence, and methods developed based on them can be found in literature (Hult and Lindskog, 2002; Lall et al., 2016; Schmid and Schmidt, 2007).

The aim of quantifying the dependence between multiple variables is to investigate the statistical character of their combinations, which is often illustrated by the joint probability distributions. The bivariate distribution functions, like bivariate normal, lognormal, gamma, and extreme value, are commonly used to generate joint distributions for two variables that have the same univariate distributions (Tawn, 1988). With respect to a wider application in

multiple variables that might have various individual statistical behaviours, Copula is a prevailing and powerful tool for joint probability analysis.

Copula function is a link that connects the multivariate distribution functions with their univariate marginal distribution functions. The basic theory and main concepts of Copula were presented by Nelson (1999) and a detailed step-by-step introduction for constructing a copula model is given by Genest & Favre (2007). In the recent decade, an extensive literature in the field of quantitative hydrology uses copula functions to deal with multivariate flood frequency issues (Corbella & Stretch, 2013; Favre et al., 2004; Kao & Govindaraju, 2008; Liu et al., 2018; Salvadori & De Michele, 2015; Wang et al., 2009; Zhang et al., 2006) to accompany the development of software computing packages (Kojadinovic and Yan, 2010; Yan, 2007). The majority of the applications were performed with bivariate copula while only limited cases managed to utilize high-dimension (3D or higher) copula analysis (Kao and Govindaraju, 2008; Zhang and Singh, 2007).

In flood frequency analysis, the notion of return period is widely used for flood estimation. For the single hazard with univariate analysis, the return period can be clearly identified from the cumulative distribution function of one quantity. However, the joint return period with multiple quantities tends to be ambiguous and its calculation is closely related to the structure of copula (Salvadori et al., 2011).

In Britain, Atlantic depressions from the southwest often bring extreme winds and rainfall that result in hydrometeorological disasters, such as storm surge, wave, pluvial and fluvial floods. A quantitative investigation of bivariate inter-station and cross-variable dependence among extreme sea surge, river flow and precipitation using asymptotic dependence and independence measures has been applied in eastern Britain (Svensson and Jones, 2002) and south and west Britain (Svensson and Jones, 2004), respectively, which gives a general assessment of the multi-hazard dependence across the UK. White (2007) then combined the asymptotic dependence measure with joint probability analysis and put it into practice at Lewes, East Sussex, UK, for the hazard assessment of joint tidal and fluvial flood.

However, the three main sources of flooding: precipitation, river flow, and surge, have not been analysed in terms of joint probability with their trivariate dependence in the UK. Moreover, a comprehensive comparison between different dependence measures is also required to appropriately evaluate the statistical relations among multiple hazards.

2.3 Multivariate, multi-source, and multi-hazard flood modelling

Flooding is probably the most frequently occurring and significantly damaging natural disaster throughout human history (Teng et al., 2017). According to the EM-DAT International Disaster Database (Guha-Sapir et al., 2015), the affected population and the direct economic loss due to floods have been growing over the past century. Flooding is the dominant type of natural disaster, occupying a large ratio of the reported natural disaster events in the recent 30 years (Freer et al., 2013). Multi-hazard flooding is caused by several different types of water sources such as heavy rainfall over the local region, extreme river flow from the upstream area, and sea water from the coast, corresponding to pluvial, fluvial, and coastal flooding, respectively. As the result of the coincidence of multiple water sources that can be relevant to each other (Lewis et al., 2013; Svensson and Jones, 2002), multi-hazard flooding may lead to severer threats to human society compared to single-hazard flood (Klerk et al., 2015). The simulation and assessment of multi-hazard flooding is a vital task for flood management and disaster mitigation.

2.3.1 The types of single hazard floods

Pluvial flooding usually occurs in urban areas when an extremely heavy downpour of rain saturates drainage systems and the excess water cannot be absorbed. The threat of an increase in the frequency and severity of high-intensity rainfall events is recognised in many regions in the world (Falconer et al., 2009; Mallakpour and Villarini, 2015), which is attributed to both climate change and urbanization (Ashley et al., 2005; Schreider et al., 2000; Zhou et al., 2019). Daily or hourly precipitation is the indicating variable to analyse the intensity and frequency of the pluvial hazard.

Fluvial flooding happens when rivers burst their banks as a result of extreme high flow that may be caused by the upstream rapid snowmelt, dam failure, or sustained/intense rainfall. River floods usually occur suddenly and cause not only direct severe destruction and casualties, but also long-term economic damage (Koks and Thissen, 2016). Human activity has amplified both river flooding hazard (Munoz et al., 2018) and the risk of human and economic losses (Dottori et al., 2018). Flow rate or water level recorded in river gauge stations is generally used as the indicating variable in pluvial hazard analysis.

Coastal flooding is caused by extreme seawater level conditions including high tides, storm surges and waves, leading to overtopping of coastal defences and inundation of low-lying

coasts, which can potentially result in damage or loss (Wolf, 2009). The threat of coastal flooding has also increased globally because of sea level rise and the dramatical growth of total population and the economic value of material assets located in coastal zones (Jongman et al., 2012; Woodruff et al., 2013). The sea water overtopping in coastal flooding is directly triggered by the total water level, which consists of storm surge and the astronomical tide. Astronomical tides are caused by the gravitational pull of the sun and the moon. Storm surge is the abnormal rise in seawater level during a storm, measured as the height of the water above the normal predicted astronomical tide. Besides surges and tides, waves may also contribute to coastal flooding but the impacts vary in different geographical locations (Hawkes et al., 2002). For the Thames estuary, waves have no significant effect on the total water level (Spencer et al., 2015) and is therefore not considered in this research of multi-hazard assessment and simulation. In frequency analysis of coastal flooding, the height of storm surge is the indicating variable. In hydrodynamic modelling, storm surge is added with a normal astronomical tide to create total water level as boundary conditions.

2.3.2 Multivariate flood and multi-source flood simulation

The understanding of multi-hazard floods can be confused with some close concepts like the multivariate flood and the multi-source flood. In general, the multivariate flood refers to the multiple variables measuring the same event such as the volume, the peak flow and the duration (Wyncoll and Gouldby, 2013; Zhang et al., 2006). The prediction model of multivariate flooding typically focuses on the interrelationship between the variables from one type of flood (Goel et al., 1998; Xu et al., 2017; Zhang and Singh, 2007), which completely differs from the multi-hazard flooding. However, it is the multivariate flood studies that first introduced some statistical techniques in the multivariate frequency analysis (Adamowski, 1985; Krstanovic and Singh, 1987; Sackl and Bergmann, 1987; Yue et al., 1999), which are further applied in the multi-source and multi-hazard flood assessment.

The multi-source flood indicates the flooding due to multiple water sources that may or may not form the same type of hazard. It can be divided into the multi-hazard flood that the water sources refer to more than one hazard and the single-hazard multi-source flood. The latter kind of flood was investigated for the coincidence of river flows (Chen et al., 2012; Pingel and Watkins, 2010; Wang et al., 2009), and the flood due to rainfall in different sub-basins (Jiang et al., 2013).

Statistical methods are widely used to quantify the dependence between the single-hazard water sources, which is typically significant and easy to be detected. Pingel and Watkins (2010) summarised the options for computing the damage due to the confluence of multiple flooding sources and emphasised that the hydrological and hydraulic conditions may be complicated in the region subjected to flooding as the result of different extreme streams. Chen *et al.* (2012) analysed the coincidence of flood flows from four upstream tributaries of the Yangtze River and its impact on the Three Gorges Reservoir. Schulte and Schumann (2015) investigated the correlation of the peak discharges of three adjoining catchments and the analysis of 178 flood events found a very strong dependence of the cross-catchment flood peaks. Serinaldi and Kilsby (2016) estimated the collective flooding risk using a large dataset of recorded daily flow time series across the central and eastern European rivers. The estimation considered the impact of the spatial and temporal correlation structures not only from the extreme events but also on the continuous flow observations. Regrettably, most of the studies of multi-source flooding only concentrated on the statistical analysis of the concurrent water sources but ignored the simulation of the physical process of the joint water flows.

2.3.3 Multi-hazard flood simulation

The multi-hazard flood involves water sources from different hazards typically including rainfall (pluvial flood), stream flow (fluvial flood), and surge. Coastal regions and urban areas with river networks are likely to suffer from multi-hazard flooding (Lian et al., 2013). The multi-hazard flood studies are not as numerous as the multi-source flood from the same hazard, but a few cases can still be found.

a) Statistical modelling

Lamb *et al.* (2010) carried out a method to evaluate the risk of concurrent flooding on rivers and coasts. The joint probability of recorded data between gauge stations is analysed separately for flow, tide and surge based on a statistical conditional exceedance model. The time lags of the hazard at different locations are quantified by an asymptotically justified dependence model. This research produced a statistical approach to assess concurrent multi-hazard flood but failed to consider the cross-hazard dependence.

Zheng *et al.* (2014) made a comparison of three types of statistical method for quantifying the dependence between extreme rainfall and storm surge. The methods were applied in a coastal area to estimate the multi-hazard frequency of coastal flood and to demonstrate the

implications of the two hazards with the various strength of correlations for flood prediction. The statistical behaviour of the two hazards was investigated thoroughly but the dynamic process from rainfall to overland flow and its interaction with storm surge were not considered in this study.

Examples can also be found for the statistical assessment of flooding due to rainfall and extreme river flow, such as statistical assessment of coastal flooding from hurricane-induced storms and heavy rainfall presented by Thompson and Frazier (2014). The assessment was aiming to produce probabilistic results and employed a series of discrete scenarios with linear regression analysis.

Unfortunately, all the above-mentioned studies only applied statistical methods in the multi-hazard flood assessment. The statistical methods can estimate the frequency of single or joint hazards but not afford to predict the resulted flooding in terms of inundation and water velocities. The physical process of the concurrence of multiple water-related hazards is much more complicated than the simple overlay of single-hazard flooding results. Therefore, physically-based flood simulation is essential for complete multi-hazard flood analysis.

b) Hydrological modelling

Breinl *et al.* (2017) presented a joint framework for simulating flood events due to extreme river flow and rainfall in urban areas. The relationship between river discharge and urban rainfall was investigated in the framework that can produce dependent time series of the two hazards. A hydrological model is employed to simulate the flooding process accompanied by a site-based weather generator. The selected hydrological model is conceptual rather than a physically-based distributed model to ensure it is fast enough to run numerous simulations. Because of this, the result of the flooding is only displayed as river discharges and rainfall predictions. The method cannot produce an inundation map of the flooding nor investigate the concurrent process of the multiple hazards.

Klerk *et al.* (2015) have undertaken studies of coincident flooding from storm surge and extreme river discharge in the Rhine-Meuse Delta. The statistical relationship between the high sea levels and the extreme river flow is evaluated by the asymptotic dependence measures. The impact of future climate change is included in the assessment of the hazards coincidence by employing a regional climate model to give sea level predictions. The river discharge is estimated by a hydrological model implemented in the Rhine sub-basins. The limitations of this study include: the interaction between sea level and river discharge is not

simulated, and the hydrological model cannot generate the inundation maps that are essential for risk analysis.

Chen *et al.* (2010) have proposed a modelling approach for combined outcomes of fluvial and pluvial flooding and applied it in a small community of the UK. An integrated 1D sewer and 2D overland flow modelling system is employed in flood simulation. The rainfall-runoff process is simulated by a hydrological model that produces discharge hydrographs. The overland flow is derived from a 2D non-inertia model. The modelling system has generated inundation maps for the research area with limited scenarios. However, the physical process of the flooding is greatly simplified by neglecting the inertial terms in the 2D model and using weir equations to reflect the interactions between the river and flooded area.

The first limitation of applying hydrological models in multi-hazard flood modelling is the model itself typically cannot produce inundation depth of the flooded area. For this reason, hydrological models are widely coupled with some hydraulic inundation models to predict flood extent. However, replicating the high fluid motion and the physical interactions between the water sources is another constraint of hydrological models, which leads to the application of full hydrodynamic models (Kumbier et al., 2018).

c) Hydrodynamic modelling

The advantages of hydrodynamic models have been demonstrated by many studies in simulating the water dynamics and the interactions between different flooding drivers and providing comprehensive assessment of inundation depth, extent and water velocities (Dutta et al., 2007; Liang, 2010; Liang and Smith, 2015; Sanders et al., 2010). The hydrodynamic model can be categorised into 1D, 2D, and 3D models according to their spatial representation of the model domain.

The 1D model simulates water flow along the central line of the river channel and is typically computational efficient. Lian et al. (2013) applied the 1D hydrodynamic model in the joint frequency estimation of flood due to rainfall and tide level in the river network of Fuzhou, China. The interactions between the rainfall-induced flow and sea level are simulated in the 1D river network. To probabilistically analyse the joint impact of the two hazards, the 1D hydrodynamic model is run many times with boundary conditions generated from the joint probability distribution of the rainfall and the downstream tidal level. Apart from the common drawbacks of the 1D model that cannot reproduce the lateral diffusion of flood wave (Teng et al., 2017) and the floodplain inundation over complex topography (Zhang, 2014), this study

employs a hydrological model to convert the rainfall to boundary flows and estimates the hydrographs over-designed rainfall process, which means the physical process of rainfall-runoff and its interaction with tidal water outside the river channel are not appropriately simulated.

The 2D hydrodynamic model is probably the most prevailing model for flood simulation that aims to produce inundation maps and represents the current state-of-the-art (Teng et al., 2017). However, regarding the multi-hazard flood simulation, very few studies can be found to focus on the hydrodynamic modelling of multi-hazard interactions. Three typical cases of 2D hydrodynamic modelling for multi-hazard flooding are analysed below.

Apel *et al.* (2015) presented a framework of multi-hazard analysis with combined pluvial and fluvial flooding and put it into practice in a riverine city in the Mekong Delta. A 2D hydraulic model based on shallow water equations is selected to simulate the flood inundation due to heavy rain and extreme river flow. The model is run many times with rainfall and flow inputs generated from hazard frequency analysis. Probabilistic inundation maps for both single-hazard and joint-hazard scenarios are produced with estimated exceedance probabilities. However, the joint probability is calculated on a rough assumption that the rainfall and flow are independent. The study area is a very small part of the city and clipped according to the DEM data availability rather than the hydrological catchment. Therefore, the potential water exchange on the boundaries of the model domain apart from the river channel is actually neglected in the simulations. It is also worth noting that the applied hydrodynamic model is a simplified model that is only applicable for subcritical flow in order to save the simulation runtime, which means it is not suitable for extreme flood simulation on complex topography that may experience high-speed flows.

Kumbier *et al.* (2018) have undertaken a study of concurrent flooding with drivers from storm surge and river discharge in an estuary of Australia. A 2D hydrodynamic model developed based on a finite difference method is employed to simulate the physical processes induced by two interacting hazards. A storm event is simulated by the model in a 25 m-resolution grid over the model domain with two open boundaries towards the sea and one boundary for the river flow. The interacting flooding process is demonstrated by the comparison modelling with and without riverine flow. The paper concludes that neglecting the interaction between different flooding drivers may significantly underestimate the flood risk, which is a supportive view of the objective of the literature review in this section. One limitation of this study is that the river flow boundary position is moved about 25 km downstream from its

original river gauge station to avoid the model domain extending too large. However, the downstream part of the rives can be greatly impacted by the over-sized interaction that makes the flow in the model boundary significantly different from upstream observed discharge time series.

Apart from the two uniform grid-based models, Olbert *et al.* (2017) proposed a 2D high-resolution and multi-scale modelling system for multi-hazard flooding triggered by river flow and coastal tide and surge. The modelling system is applied in Cork City next to the Cork Harbour in the south west of Ireland with three different spatial resolutions cascading from 90 m to 30 m, 6m, and 2m over four nested grids. A historic flooding event is simulated by the multi-scale model to investigate the impact of the riverine extreme flow and the high tide level from the coast. An inundation map in the urban area is produced and used to estimate the flood risk to people. The multi-scale resolution is an attractive attempt to reduce the computational burden in hydrodynamic modelling. However, the model presented in this study is applied in a small region and for only one event while the multi-hazard flood assessment typically requires numerous simulations. One more concern is whether the modelling system can consider rainfall over the entire model domain and keep stable on the interface of grids with different resolutions.

The application of 3D models for the simulation of multi-hazard floods is rare in the literature. One example can be found in Chen *et al.* (2014) investigating the joint impact of freshwater discharge and storm surge over a river catchment in Taiwan, China. A 3D hydrodynamic model is employed on an unstructured grid with resolutions ranging from 1000 m to 40 m. The study shows good performance when simulating historical events but does not demonstrate the necessity of applying a 3D model while 2D shallow water model is widely believed to be adequate in flood simulation (Teng et al., 2017). And the high-dimensional model can lead to the compromise in spatial resolution to control the computing cost, like in this case, the highest 40 m-resolution may not be fine enough for flood simulating in urban areas with a complex land surface.

As a summary, the basic requirements of a model for multi-hazard flood simulation and assessment can be concluded as follows

- The model must be able to simulate multiple water-related hazards including rainfall, stream flow, and coastal surge. Some cases have undertaken double-hazard

simulations, but unfortunately, there is no model found to investigate the joint impact of all the three water-related hazards.

- The model must be physically-based and fully hydrodynamic such that the physical interactions of multiple hazards in extreme condition can be well simulated without significant dynamic loss.
- The model must be fast and efficient enough to run numerous simulations in a large catchment. This is because the impacted region completely covering all of the three hazards especially rainfall is usually an entire hydrological basin that is much bigger than the small application area in most current hydrodynamic models. Moreover, the joint frequency analysis of multiple hazards relies on numerous Monte Carlo simulations, requiring high-speed hydrodynamic models.

2.4 Vulnerability analysis for flooding

For the quantitative assessment of disaster risk, it is vital to quantify not only the hazard process but also the vulnerability of elements at risk. The assessment of vulnerability is related with so many internal and external factors (Adger, 2006) and can be generalized into physical vulnerability and social vulnerability according to the scope of considered attributes. Social vulnerability pays attention to the social and economic characteristics and circumstances that may contribute to the state of susceptibility to harm from hazards (Cutter and Boruff, 2003; Cutter et al., 2000). In general, a wide range of variables can be included in social vulnerability analysis and thus the results are expressed by indicator-based measures like the Social Vulnerability Index (Ge et al., 2013). Physical vulnerability focuses on the status of loss due to physical forces (Uzielli et al., 2008), and it can also be influenced by social aspects, such as the hazard warning system and the actions of disaster prevention from the government. In contrast, the evaluation of physical vulnerability usually constrains the number of considered variables and scenarios to produce more quantitative results such as damage curves (Khanduri and Morrow, 2003; Quan Luna et al., 2011; Shinozuka et al., 2000), which is more valuable in the full quantitative risk assessment.

The typical tool to quantitatively illustrate vulnerability is the vulnerability curve that links the magnitude of a specific hazard to the expected loss. Examples include the seismic fragility curves showing the damage of structure at given ground motion levels (Singhal and Kiremidjian, 1996), the debris flow vulnerability functions for different types of buildings in Austria (Fuchs et al., 2007), and the vulnerability curve for crop loss due to flooding (Dutta et

al., 2007). The historical loss data during disaster events is the principle of the estimation of vulnerability curves. A more specific investigation, such as survey to properties and household, is sometimes necessary for the region without enough recorded disaster data (Smith, 1994; Thieken et al., 2005). Loss models and damage experiments are also used to estimate loss for some types of the element at risk like crops (Wang et al., 2013) and buildings (Khanduri and Morrow, 2003).

A vulnerability curve usually employs one indicator as the representation of the magnitude of hazards, such as the ground motion for earthquakes, the water depth for flooding, and the wind speed for hurricanes. However, the destructiveness of some types of hazard can be decided by more than one variable, for example, both water depth and velocity can contribute to the damage of buildings during flooding (Kelman, 2002). A typical way to deal with this problem is to develop a series of vulnerability curves rather than a single one to denote the vulnerability function with one continuous variable and some other discrete variables with limited states (Schwarz and Maiwald, 2012). The series of vulnerability curves can be expanded to vulnerability surface with two continuous variables. Nadal et al. (2010) integrate the depth-damage curves and velocity-damage curves to the vulnerability surface illustrating the damage function of both depth and velocity in the riverine and surging flood.

For multi-hazard risk assessment, the vulnerability analysis can involve multiple indicators representing different hazards, which also requires multivariate vulnerability functions. Lee and Rosowsky (2006) proposed a bivariate vulnerability function of woodframe buildings in consideration of snow and earthquake loading and generated several fragility curves with limit state probabilities. Schwarz and Maiwald (2012) presented a discrete trivariate vulnerability function to estimate the fragility of building due to three hazards including flood, earthquake, and wind. The damaging process during multi-hazard disaster events can be dynamic and significantly change with the temporal and spatial overlay of the hazards (Gill and Malamud, 2014). Some experimental or physical model-based approaches have attempted to investigate the physical process of multi-hazard vulnerability for simple objects in small areas (Ellingwood et al., 2004). But the most typical and feasible way in large-scale application is the empirical regression with historical loss data and insurance data. For example, a continuous vulnerability surface considering the concurrence of strong wind and heavy rain was developed to estimate crop loss ratio in the Yangtze River Delta according to empirical loss assessment (Ming et al., 2015). The physical damaging process is more or less neglected in statistical approaches, but the outcome can be estimated by the multivariate vulnerability function. However, the high data requirement of the statistical approach makes it

only applicable in the multi-hazard disaster events with widespread consequences and to areas with a high quantity of loss data survey and collection (Kappes et al., 2012).

The vulnerability analysis of multi-hazard flooding is less complicated compared with the vulnerability issue related to different disaster groups. Because all the hazards can point to the same direct stress to the elements at risk, namely the water inundation. Therefore, the loss estimation of multi-hazard flooding can follow the general procedure of traditional flood vulnerability analysis. For quantitative risk assessment, it is critical to employ the hazard-loss functions that appropriately reflect the local attributes of the objects to be assessed (Nasiri et al., 2016).

In the UK, a lot of efforts have been put into the vulnerability analysis of flooding. For example, Kelman (2002) analysed the physical vulnerability of residential properties for flooding in two small regions in coastal, eastern England. The field survey methods are employed to identify the characteristics regarding the physical vulnerability of residences. The failure modes of the prominent concerns in the flooded properties are appraised in detail using a first-order analysis method. This type of particularised assessment requires comprehensive surveyed data and must be renewed with up to date local information when it is put into practice in new flooding events.

Multi-Coloured Manual (Penning-Rowsell et al., 2013) provides many types of vulnerability curves that are acquired by historical loss analysis and comprehensive household survey. The vulnerability investigation was based on the data from England and Wales and recently renewed in 2017. In consideration of the timeliness and regional applicability that are the key concerns of flood vulnerability analysis, the Multi-Coloured Manual is a prevailing choice to assess flood damage in England and Wales.

In general, the vulnerability analysis involves lots of physical and social factors and is therefore very complex especially when it is in a multi-hazard context. The physical vulnerability represented by the loss function of hazard intensities is the feasible choice in quantitative risk assessment. The application of vulnerability functions must consider the regional applicability and timeliness of the data used to produce the functions.

2.5 Hazard and risk forecasting of multi-hazard flood

Due to climate change, the precipitation is expected to be concentrated into more intense events in the warmer future (IPCC, 2014b) and consequently result in more extreme rainfall-

induced flooding. A lot of effort has been put into the construction of flood forecasting systems that aim to predict different types of flooding events, such as storm flood, coastal flood (Saleh et al., 2017), flash flood (Hapuarachchi et al., 2011), and snowmelt flood (Blöschl et al., 2008).

A reliable flood forecasting system, especially for the short-range and intense flooding, can provide timely hazard warning to decision makers and the residents at risk, being extremely important to the reduction of both tangible and intangible disaster damages (Carsell et al., 2004). A complete forecasting system, no matter for what type of flood, can at least consist of two major components: a module of simulating flooding processes including the flow in the riverbed and floodplain, and a module of predicting flooding sources like rainfall, river flow, and storm surge.

The module of simulating flooding processes involves a wide variety of approaches including statistical model, hydrological model, hydrodynamic model, and the combination of them (Campolo et al., 1999; Chau et al., 2005; Chiang et al., 2007; Nayak et al., 2005). The hydrological models, mainly the distributed hydrological model is widely used to predict the long-term and large-scale flooding (Garrote & Bras 1995; Liu et al. 2005; Li et al. 2017). However, the application of the simple hydrological model is limited when facing the short-range and intense flooding as it cannot reflect highly transient and fast-moving water at the slope, floodplain and riverbed of the regional catchment. Also, the hydrological model has typically many parameters must be calibrated either at a large-scale domain or using less-extreme events because of the limited availability of observations for extremes in the small region, which means the scarcity of data can restrict the model calibration for the small domain. For example, the Grid-to-Grid (G2G) distributed hydrological model (Bell et al., 2007) is currently playing a vital role in the UK's National Flood Forecasting System (NFFS) configured in the 1 km^2 grid covering England and Wales. But as suggested in the Environment Agency (EA)'s report about the performance of flood forecasting models (Environment Agency, 2017), the G2G model is not expected to perform as well as local models due to the limitation of model calibration.

As an alternative, the hydrological model is sometimes coupled with a 1D or 2D hydrodynamic model calculating the flow propagation inside the watercourse (Paiva et al., 2011; Saleh et al., 2017). Thus, the physical process on riverbed can be reflected in the flood simulation, but it is still inadequate to represent the interaction mechanism between the riverbed and the floodplain (Dutta et al., 2007). Moreover, it is unreasonable to neglect the

dynamic outside the riverbed, which can be significantly high during a severe flood event like the pluvial flooding caused by a strong rainstorm. The 2D hydrodynamic models based on the principles of Mass Conservation and Momentum Conservation are the realistic approach to consider the dynamic covering the whole model domain and particularly suitable for simulating extreme floods in favour of understanding the precise physical processes and mechanisms (Carrivick, 2006).

However, very few cases can be found to apply full hydrodynamic models in the entire catchment for flood simulation due to the high demand of computational capacity and the high-resolution DEM and bathymetric data. A combined 1D & 2D hydrodynamic modelling system is used to simulate the flood inundation in the lower Mekong river basin at a 1×1 km uniform grid that is applicable only for the flat floodplain with a level surface in each cell (Dutta et al., 2007). As a high-resolution case, a full 2D hydrodynamic model is applied to simulate the high-magnitude outburst flood with an excessive long model time for a short event at a small mountainous region of Iceland (Carrivick, 2006), which is not feasible for flood forecasting that requires enough lead time. In general, the current practice of the full hydrodynamic model is limited either at a coarse grid or in the small domains. To simulate the intense flooding in the forecasting system, most of the applied hydrodynamic models are yet too expensive to reach a decent level of spatial resolution and lead time at a large river catchment.

As another critical module of the flood forecasting system, the prediction of flooding sources relies typically on numerical weather prediction (NWP) models that use numerical methods to solve 3D partial differential equations based on physical laws and quantify the sub-grid physical processes in the atmosphere (de Roo et al., 2003). The large-scale (global or continental) NWP models are widely run through supercomputers and supported by the government at tens or hundreds kilometre spatial resolutions. Examples include the European Centre for Medium Range Weather Forecasts (ECMWF) (Palmer et al., 1990), the Meteorological Service of Canada (MSC) (Gauthier et al., 2007), the Weather Research and Forecasting (WRF) Model (Done et al., 2004), and the US National Weather Service (Fread et al., 2002). Those NWP models have been developed since the 1980s and are now widely used for the large/medium-scale and long-term flood forecasting platforms, such as the European Flood Awareness System (EFAS) (Bartholmes et al., 2009; Thielen et al., 2009) and the Advanced Hydrological Prediction Services (AHPS) (Mcenery et al., 2005) giving hydrologic forecasts for Europe and the United States, respectively. However, to deal with the short-range and intense flooding sources like the heavy rainfall brought by intense storms, more

spatially precise weather prediction is required to give local-scale forecasting information based on the regional atmospheric and geographical conditions.

Although it is still challenging to run global NWP models at 1 km horizontal resolution that is an order of magnitude greater resolution than the current models (Bauer et al., 2015), some regional and short-range models have been performed at kilometre scale grids using the output from the global model as the boundary conditions. For example, in the UK, a unified model (UM) covering the British Isles has been run by the Met Office at low resolution for climate modelling and high resolution for regional NWP for decades (Davies et al., 2005). One version of the UM is the UK Variable resolution model (UKV) with a grid length of 1.5 km. The high resolution means the impact of the local domain like enhanced rain over mountains can be reflected in the model, which is critical for intense rainfall forecasting. The performance of the UKV model has been proved to be significantly improved in terms of rainfall prediction compared with other coarser models (Kendon et al., 2012; Mittermaier and Csima, 2017).

With scientific and technological development, it comes to be possible for hydrodynamic modelling with both high-resolution grid and large model domain in support of super-computers and parallel computing (Sanders et al., 2010). More recently, the GPU-based acceleration techniques create a new possibility for large-scale hydrodynamic modelling without super-computers (Smith and Liang, 2013), suggesting that it can significantly reduce both the time and financial cost of full hydrodynamic flood simulation at regional scale.

Flooding does not necessarily result in the loss of human lives or properties if it happens in an area without human activities. Therefore, the final concern of the public and the government is the outcome of flooding rather than the flooding itself. While most of the current forecasting system focuses on flood prediction, few cases can be found to estimate the disaster loss due to the predicted flooding in advance. However, it is necessary to extend the flood forecasting system with vulnerability models to predict the outcome of flooding that is more valuable to the residents and the authorities of disaster prevention and mitigation.

2.6 Summary

According to the literature reviews in the previous sections, the research gaps of multi-hazard risk assessment and forecast are identified as follows

- Most of the current multi-hazard assessments ignore the dependence of the occurrence of hazards or only focus on the bivariate correlations. However, it is essential to consider the dependence of all the related hazards and quantify the joint frequency of the concurrence of multiple hazards in the risk assessment framework. Therefore, the first objective is to analyse the dependence and joint probability of the three water-related hazards.
- The hazard interactions are ignored or over-simplified in most of the existing analyses of multi-hazard risk. Physically-based models like the hydrodynamic model for water-related hazards are needed in the simulation of the interaction processes. Therefore, the second objective of this thesis is to simulate the physical process of multi-hazard flooding via a 2D hydrodynamic model.
- Few cases of multi-hazard risk assessment can produce fully quantitative results with the proper consideration of hazard dependence and interactions. But the quantitative assessment shown as risk curves is more valuable than the qualitative risk ranks and semi-quantitative risk indexes in the practice of disaster risk management. Therefore, the third objective is to develop a quantitative assessment framework to calculate multi-hazard disaster risks.
- The current flood forecasting systems tend to be complicated with a series of models with various empirical parameters and assumptions that can limit their application in unprecedented events with high physical dynamics and raise the uncertainties across the different modules. Few applications can be found to provide flood risk forecasting according to the predicted inundation and vulnerability functions, which are very meaningful to flood-prevention and risk management. Therefore, the fourth objective of this study is to extend the application of the proposed risk assessment framework to real-time risk forecasting.

These research gaps will be investigated and addressed in this thesis.

Chapter 3. Methodology

3.1 Introduction

This chapter is to introduce the structure of the proposed multi-hazard risk assessment framework and all of the involved methods. As shown in Figure 3-1, the multi-hazard risk assessment framework consists of four integrated modules including hazard frequency analysis, hydrodynamic flood simulation, vulnerability analysis, and multi-hazard risk assessment. The framework aims to provide an integrated methodology for quantitative assessment of multi-hazard risk that can consider the dependence and physical interactions between the associated hazards.

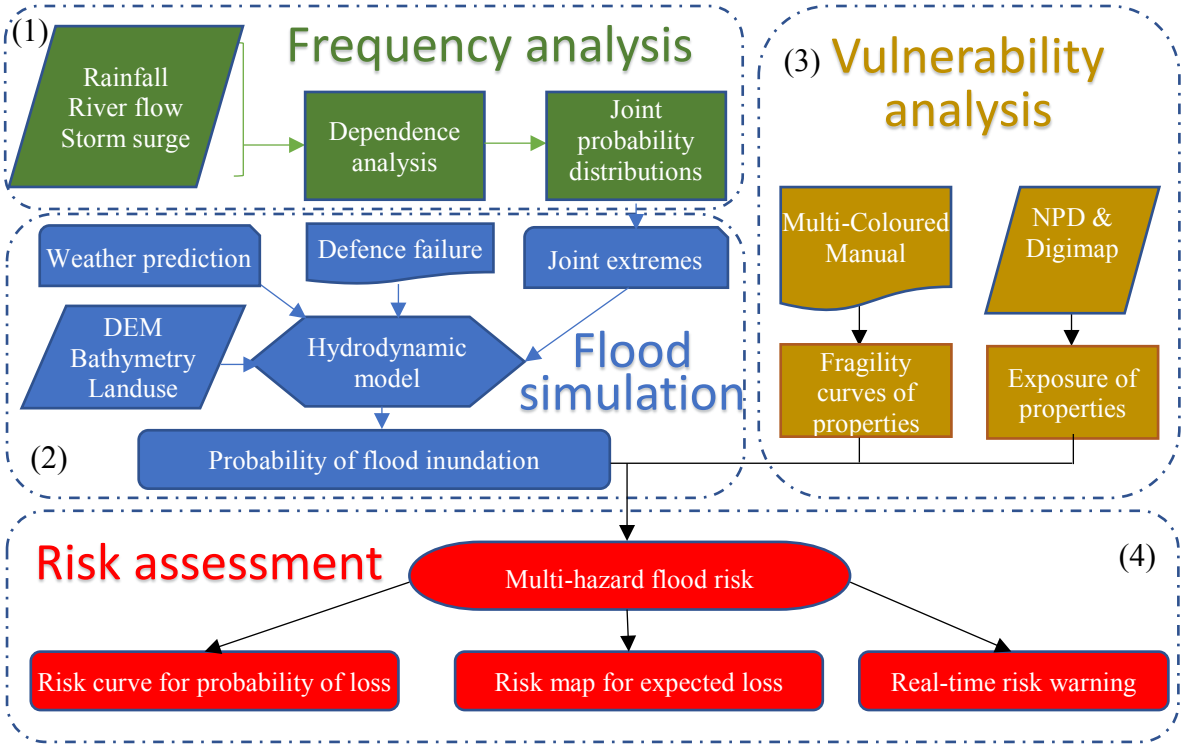

Figure 3-1. The structure of methodology for multi-hazard risk assessment

Heavy rainfall, extreme river flow and storm surge are the three identified hazards that may lead to potential flood disasters in the coastal and riverine regions. The dependence of the three individual hazards is evaluated to generate the joint multi-hazard probability distribution of the multi-hazard. Asymptotic dependence (Coles et al., 2000) and Copula theory (Nelson, 1999) are applied in this module. A high-performance 2D hydrodynamic model (Liang, 2010;

Xia et al., 2017) is employed to simulate flood inundations associated with designed multi-hazard events to produce probabilistic inundation maps. The vulnerability module will provide the hazard-damage function of properties and their exposure, supported by loss data from the Multi-Coloured Manual (MCM) (Penning-Rowsell et al., 2013) and the property data from the National Property Dataset (NPD) and the Digimap. The risk assessment module combines the results of hazard and vulnerability analysis to predict the potential loss and generate quantitative risk curves and maps for use by decision-makers and at-risk residents.

3.2 Measuring dependence

Dependence is the statistical relationship between two or more random variables, indicating the extent to which the value of one variable is affected by or reliant on another variable. As the positive or negative dependence between variables may increase or decrease the probability of occurrence of joint extremes, dependence analysis is an essential step for estimating joint probability distributions of multivariate events.

3.2.1 Asymptotic dependence

Asymptotic dependence is a general and quantitative measure for the whole dataset and facilitates the selection of an extreme threshold to generate the joint extreme sample. A method for investigating bivariate asymptotic dependence is developed by Coles et al. (2000), which is capable of quantifying the dependence level at various extreme thresholds. The asymptotic dependence measure χ is defined as the probability of one variable exceeding a certain limit given that the other is over that limit. For paired random variables (X, Y), χ may be given by equation (3-1)

$$\chi = \lim_{u \to 1} P(G(Y) > u | F(X) > u) \qquad (3\text{-}1)$$

where $F(X)$ and $G(Y)$ are the marginal distributions of X and Y respectively, u is the probabilistic extreme threshold within the interval $[0,1]$. The degree of dependence between X and Y increases when the value of χ moves from 0 to 1, with $\chi = 1$ indicating total dependence and $\chi = 0$ being full independence (Svensson and Jones, 2002). If a quantity $\chi(u)$ is defined as a function of threshold u as

$$\chi(u) = 2 - \frac{\ln(P\{F(X) \leq u, G(Y) \leq u\})}{\ln(P\{F(X) \leq u\})} \qquad (3\text{-}2)$$

the dependence measure $\chi = \lim_{u \to 1} \chi(u)$. The properties of dependence measures χ and $\chi(u)$ are summarized by Reiss and Thomas (2007, p75), as follows:

- χ and $\chi(u)$ are asymmetric in X and Y;
- the range of χ is between 0 and 1;
- if X and Y are stochastically independent, $\chi(u) = 1 - u$ and $\chi = 0$; therefore, independence implies tail independence or extreme independence;
- if $X = Y$, then $\chi(u) = 1$ and $\chi = 1$.

However, when analysing χ based on observations, the empirical estimation χ always tends to be zero as the threshold approaches one because of the decreasing sample size when the extreme threshold gets higher. The left panel of Figure 3-2 shows the estimated $\chi(u)$ of a series of random samples derived from the bivariate standard normal distribution with correlation values $\rho = 0.9, 0.8, \ldots, -0.9$, respectively. A higher correlation value corresponds to a higher $\chi(u)$ estimation line towards the positive vertical axis in the figure. For all the lines with positive dependence, $\chi(u)$ experiences a sudden drop when u approaches 1. Moreover, $\chi(u)$ for negative dependence is converging to zero much quicker than for positive dependence as u is getting higher. Minimal gaps between different negative lines can be observed when $u > 0.9$, making it hard to distinguish the different levels of negative dependence.

In order to avoid the aforementioned limitations of χ, Coles et al. (2000) introduced a second dependence measure $\bar{\chi}$ based on survivor functions, defining

$$\bar{\chi}(u) = \frac{2\ln(P\{F(X) > u\})}{\ln(P\{F(X) > u, G(Y) > u\})} - 1 \qquad (3\text{-}3)$$

then $\bar{\chi} = \lim_{u \to 1} \bar{\chi}(u)$. When $u \to 1$, $\bar{\chi}(u)$ converges to 1, indicating the increase of dependence degree, and $\bar{\chi} = 0$ means the asymptotic independence. The properties of $\bar{\chi}$ and $\bar{\chi}(u)$ are summarised by Reiss and Thomas (2007, p323) as:

- $\bar{\chi}$ and $\bar{\chi}(u)$ are symmetric for X and Y;

- $\bar{\chi}$ and $\bar{\chi}(u)$ range between -1 to 1;
- if $X = Y$, then $\bar{\chi} = 1$.

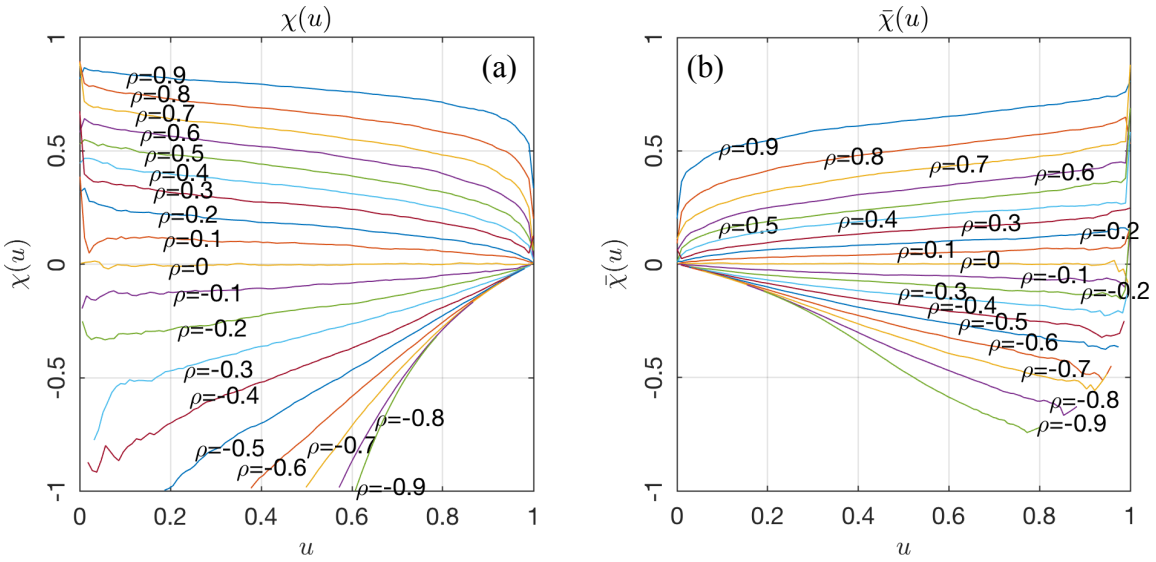

Figure 3-2. The dependence measures $\chi(u)$ (a) and $\bar{\chi}(u)$ (b) for bivariate standard normal distribution with various correlation values $\rho = 0.9, 0.8, \ldots, -0.9$

The dependence measure $\bar{\chi}(u)$ for the random sample from bivariate standard normal distributions with correlation values from $\rho = 0.9$ to $\rho = -0.9$ is illustrated in Figure 3-2 (b). $\bar{\chi}(u)$ is converging to 1 as $u \to 1$ but remains stable and it is almost linear at the high threshold level. In comparison with Figure 3-2 (a), the difference between the negative dependence lines and the independence line ($\rho = 0$) becomes more prominent.

In general, the measures $(\chi, \bar{\chi})$ can be paired to quantify the dependence between variables. $(\chi > 0, \bar{\chi} = 1)$ represents the asymptotic dependence utilizing the value of χ to measure the dependence. $(\chi = 0, \bar{\chi} < 1)$ indicates the asymptotic independence using the value of $\bar{\chi}$ to measure the dependence (Coles et al., 2000). In equations (3-2) and (3-3), u is the non-exceedance probability threshold of the two random variables, and $(\chi, \bar{\chi})$ can be estimated based on any threshold value. The selection of threshold should ensure that the sample size of observations above the threshold is large enough for statistical analysis and the observations exceeding the limit are rare enough to be treated as extreme or hazardous events (Svensson and Jones, 2002). For dependence analysis of daily data, the characteristic of annual maximum series and daily point-over-threshold (POT) series are often used as a reference for threshold selection (Petroliagkis, 2018; White, 2007).

The dependence measures $(\chi, \bar{\chi})$ are estimated based on empirical observations. The significance testing is performed with a permutation method (Anderson and Braak, 2003). The method randomly generates a large number of datasets for which the independent

variables would hold. And the dependence measure, for instance, χ, is calculated based on the new datasets to obtain a sample of χ that may appear from the independent dataset. If the χ derived from the original observations is significantly different from the sample of randomly obtained χ, the original observations are recognised as not independent. To maintain the seasonality of variables, the observations are divided into year blocks and the sequence of records inside a year is kept intact. Then the record series of one variable is fixed while the year blocks of record from the other variable are resampled without replacement and combined with the first series to generate a paired dataset. The resampling is duplicated a certain number of times and a χ value for each resample can be estimated. All the estimated values based on resampled observations are regarded as the random sample of variable χ. Then, the 5% non-exceedance value of the random sample is the 5% significance level of χ. If the original χ is higher than the 5% non-exceedance value, the dataset is regarded to be asymptotic dependent at 5% significance level, and vice versa.

It is also necessary to compute the confidence interval of the dependence measures to provide more information about the randomness of dependence. The calculation of confidence interval for $(\chi, \bar{\chi})$ is similar to the significance testing. A resample procedure based on yearly blocks of observation is performed with the replacement of each variable, which means some years can be selected more than once and some are not chosen in a sample. All the values of the dependence measure derived from resampled datasets are sorted, and their 2.5% and 97.5% non-exceedance probability points correspond to the lower and upper limits of the 95% confident interval respectively.

3.2.2 Rank-based measures of dependence

The asymptotic dependence measures provide a general view of dependence at continuous thresholds that are identical for each variable. However, the magnitude values derived from the same limit for different hazards may represent the distinct degree of threat. The rank-based measures are generally used to extract extreme samples from the whole observation set, and the selection of extreme events can be based on different threshold levels for each variable. Spearman's ρ and Kendall's τ are the classic nonparametric measures that can quantify the statistical dependence between the ranks of different variables and do not rely on any assumptions of their marginal or joint distributions.

The detailed introduction of these two measures is given by Genest and Favre (2007). Suppose that $\{(x_1, y_1) \dots, (x_n, y_n)\}$ represents a random sample with n observations given

from a pair of the continuous random variable (X, Y). The corresponding ranks of (x_i, y_i) are denoted by (R_i, S_i). Then Spearman's ρ is defined as

$$\rho = \frac{\sum_{i=1}^{n}(R_i - \bar{R})(S_i - \bar{S})}{\sqrt{\sum_{i=1}^{n}(R_i - \bar{R})^2 \sum_{i=1}^{n}(S_i - \bar{S})^2}} \tag{3-4}$$

where $\bar{R}$ and $\bar{S}$ are the average value of R_i and S_i respectively. The range of ρ is $[-1,1]$ and the value closer to 1 or -1 means higher positive or negative monotonic dependent relationships between the random variables. If the null hypothesis is the independence between X and Y, then the distribution of Spearman's rho should be close to normal with zero mean and variance $1/(n-1)$. So, the test statistic for Spearman's rho is $\sqrt{n-1}|\hat{\rho}|$.

Kendall's tau is defined based on the concept of concordance that indicates the relation of two pairs of observations. The pairs (x_i, y_i) and (x_j, y_j) are regarded as concordant if $(x_i - x_j)(y_i - y_j) > 0$ and discordant if $(x_i - x_j)(y_i - y_j) < 0$, assuming the probability of appearance of ties is zero as the variables are continuous. Then Kendall's tau can be defined as

$$\tau = \frac{P - Q}{n(n-1)/2} \tag{3-5}$$

where P and Q are the numbers of concordant and discordant pairs respectively. The range of Kendall's tau is also from -1 to 1, $\tau = 1$ means the perfect agreement of paired rankings, and $\tau = -1$ means complete disagreement of the paired rankings. The test statistic for τ under the null hypothesis of independence is given as $\sqrt{\frac{9n(n-1)}{2(2n+5)}}|\hat{\tau}|$.

3.3 Joint probability analysis and copula function

3.3.1 Copula function

Joint probability distribution provides the quantitative information about statistical behaviour between multiple variables, which is crucial for multi-hazard analysis. Let $X_1, X_2, \dots, X_d$ be d continuous random variables with marginal distribution functions $F_1, F_2, \dots, F_d$ respectively. The joint cumulative distribution function of those multiple variables can be denoted by

$$H(x_1, x_2, \dots, x_d) = P\{X_1 \leq x_1, X_2 \leq x_2, \dots, X_d \leq x_d\} \quad (3\text{-}6)$$

If the random variables are fully independent between each other, then

$$H(x_1, x_2, \dots, x_d) = \prod_{i=1}^{d} F_i(x_i) \quad (3\text{-}7)$$

When the hazard variables are not independent, which is more natural in the real world, the combination from all the marginal distributions to the joint distribution is not as straightforward as equation (3-7) shows. Instead, a function called copula (Nelson, 1999) is introduced to build the relationship of the combination as follows:

$$H(x_1, x_2, \dots, x_d) = C[F_1(x_1), F_2(x_2), \dots, F_d(x_d)] \quad (3\text{-}8)$$

According to Sklar's theorem (Sklar, 1959), the copula function is uniquely determined when the joint and marginal distribution are given. The copula is a widely used tool for multi-variable modelling in many fields. The main advantage of applying copula in the multi-hazard analysis is that the univariate distribution of each hazard variable is not necessarily from the same parametric family. A well-fitted copula function together with marginal distributions of a single hazard make it possible to generate an analytical joint distribution function for multiple variables and then use it for joint frequency analysis.

3.3.2 Joint probability distribution based on copulas

To build the joint probability distribution of multiple variables with a Copula function, the typical procedures are

- Fit the marginal distribution of each variable,
- Test multivariate independence,
- Construct Copulas,
- Perform Goodness-of-fit test for Copulas,
- Select the best-fitted copula and generate joint distribution function.

The first step is to find the appropriate univariate distribution function to fit the observations from every single hazard. Step 2 is to estimate whether it is necessary to apply non-independent copula functions for the multiple variables. A test process for multivariate mutual

independence is introduced by (Genest and Rémillard, 2004), and the test statistic is defined as

$$I_n = \int_{[0,1]^d} n[C_n(\boldsymbol{u}) - \prod_{i=1}^{d} u_i]^2 \, d\boldsymbol{u} \tag{3-9}$$

where $\boldsymbol{u} = [u_1, u_2, \dots, u_d]$ is the vector of marginal distributions, $u_i = F_i(x_i)$, n is the number of observations for each variable, d is the dimension of the variable, and C_n is the empirical copula. The null hypothesis for the test of independence is that all the components of the vector of random variables $X_1, X_2, \dots, X_d$ are mutually independent, which means the copula function of these variables is $C(\boldsymbol{u}) = \prod u_i$ based on Equation (3-7). If the null hypothesis is rejected, it is necessary to explore a suitable copula with a certain degree of dependence to fit the joint probability distribution of the multiple variables.

Normally, a copula function has at least one or more parameters. There are several non-parametric approaches to estimate the parameters of copulas relying on the ranks of observations, including the inversion Kendall's Tau estimator, the inversion Spearman's Rho estimator, and the maximum pseudo-likelihood estimator. The last one is especially efficient and widely used in parameter estimation for multidimensional copulas (Genest and Favre, 2007). Suppose that a one-parametric copula C_θ with density function c_θ is selected in the joint probability analysis for trivariate random variables (X, Y, Z) with a sample of n observations (x_i, y_i, z_i) and their ranks are (R_i, S_i, T_i). The likelihood function is defined as

$$L(\theta) = \sum_{i=1}^{n} ln\left[c_\theta\left(\frac{R_i}{n+1}, \frac{S_i}{n+1}, \frac{T_i}{n+1}\right)\right] \tag{3-10}$$

As there are many different families of copulas available, such as Gaussian copula, Placket copula, Student's t copula, and Archimedean copulas. The one-parameter Archimedean copulas are most widely used in joint probability analysis as they are easy to construct, and serval software packages are available for their parameter estimation. The expressions of four types of Archimedean copulas are given in Table 3-1 with bivariate and trivariate cumulative distribution functions. Figure 3-3 illustrates the bivariate CDF distributions of the four types of Archimedean copulas.

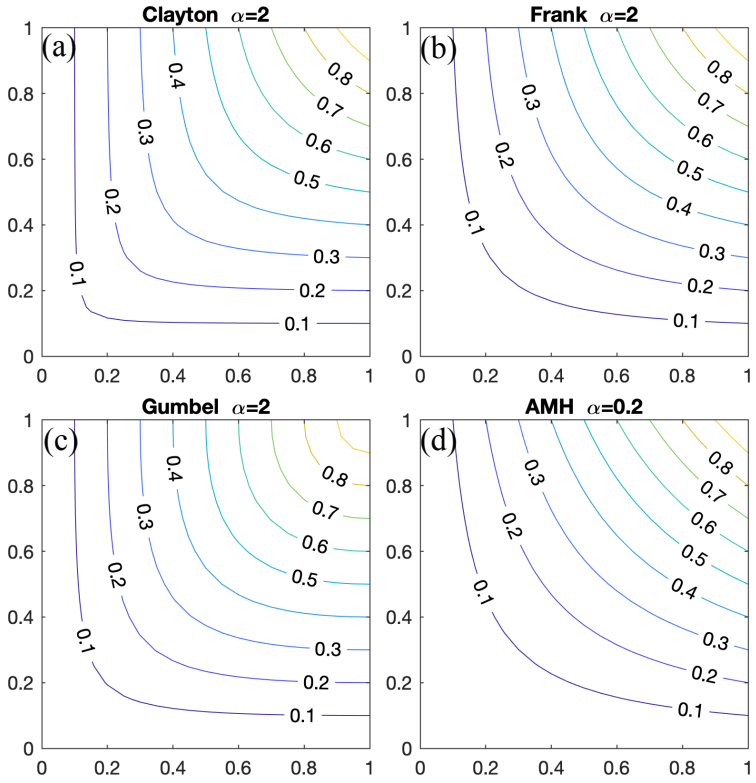

Figure 3-3. Contour plots of four types of bivariate Archimedean copulas.

Table 3-1. One parameter bivariate and trivariate Archimedean copulas.

Copula family	Bivariate CDF $C_\alpha(u,v)$	Trivariate CDF $C_\alpha(u,v,w)$	Range of parameter
Clayton	$(1 + (u^{-\alpha} - 1 + v^{-\alpha} - 1))^{-1/\alpha}$	$(u^{-\alpha} + v^{-\alpha} + w^{-\alpha} - 2)^{-1/\alpha}$	$[1, +\infty)$
Frank	$-\frac{1}{\alpha} ln(1 + \frac{(e^{-\alpha u} - 1)(e^{-\alpha v} - 1)}{(e^{-\alpha} - 1)})$	$-\frac{1}{\alpha} ln(1 + \frac{(e^{-\alpha u} - 1)(e^{-\alpha v} - 1)(e^{-\alpha w} - 1)}{(e^{-\alpha} - 1)^2} - 2)$	$(-\infty, 0) \cup (0, +\infty)$
Gumbel	$\exp(-[(-lnu)^\alpha + (-lnv)^\alpha]^{1/\alpha})$	$\exp(-[(-lnu)^\alpha + (-lnv)^\alpha + (-lnw)^\alpha]^{1/\alpha})$	$[1, +\infty)$
AMH	$\frac{uv}{1 - \alpha(1-u)(1-v)}$	$\frac{uvw}{1 - \alpha(1-u)(1-v)(1-w)}$	$[-1,1)$

Note: α is the parameter and $u, v, and\ w$ are the marginal distributions

The goodness-of-fit test is a necessary step to judge whether the selected copulas are fitted well enough at a significance level. The test is based on a null hypothesis that the selected copula is the valid one for the observations. There are several approaches (Genest et al., 2009) available for the goodness-of-fit test while the one based on multiplier central limit theorems introduced by Kojadinovic and Yan (2011) has the best efficiency. A copula R package is developed for modelling multivariate distributions with functions including the test of

multivariate independence, estimation of parameters, goodness-of-fit test, and random number generation (Kojadinovic and Yan, 2010; Yan, 2007).

However, it is still possible that more than one type of copulas can pass the goodness-of-fit test. The most straightforward way of copula selection is to compare the average Euclidean square distance between the empirical copula and the fitted copula. The type of copula with the minimum error distance is regarded as the best-fitted one (Zhang et al., 2006).

3.3.3 Joint return period and extreme scenarios

The return period, which means a measure of the rarity of an event and sometimes referred to as the recurrence interval, is often used to quantify the probability of occurrence of hazards above a specific magnitude. For a single hazard indicated by a random variable X, the return period $T(x)$ is the expected recurrence time of the event that X is larger than x, defined as

$$T(x) = \frac{M_t}{P\{X > x\}} = \frac{M_t}{1 - F_X(x)} \tag{3-11}$$

where M_t is the average reoccurrence time of the hazard event (typically given in years) that equals the time span of the events divided by the number of events.

When dealing with concurrent events with multiple hazards, the different types of hazard combinations should be considered. Normally, sample points located at the upper set of the variable(s) are regarded as extreme events that may cause disasters. For bivariate analysis, the relation of the hazard combinations is categorized as three scenarios according to the extreme methods (Zheng et al., 2014). When extended into the multivariate analysis, Salvadori et al. (2016) used a copula-based framework to deal with the extreme scenarios of the hazard combinations. The trivariate extreme scenarios can be illustrated in Figure 3-4 as four types: (a) “And” scenario that each variable should be larger than the threshold; (b) “Or” scenario that either one of the variables is larger than the threshold; (c) “Kendall” scenario that the sample points located in the upper set defined by a Kendall distribution function layer; and (d) “Survival Kendall” scenario that sample points located in the lower set defined by a survival Kendall distribution function layer. A narrow definition of multi-hazard disaster is that the disaster is contributed to by all the related hazards exceeding the extreme level, but any single extreme hazard does not necessarily lead to a disaster, which corresponds to scenario (a) or (d). However, single hazard events can be more frequent than joint events in reality. Thus, a generalised multi-hazard issue that considers all of the combinations of hazards including the

single-hazard events, as shown in scenario (b) or (c), is more worthwhile in disaster risk analysis.

The type of critical surface in scenario (c) is the precise layer to distinguish the extreme events from normal observations. However, to obtain this 3D layer requires numerous observations or simulations for multi-hazard events, which are not usually available in practice. Instead, the critical layer in scenario (b) can be simply represented by analytical equations and can include both single and multiple extreme hazards. The extreme events defined by the "Or" scenario can be decomposed into six subsets, including one trivariate extreme set (X, Y, Z), three bivariate extreme subsets$\{(X, Y), (X, Z)\ and\ (Y, Z)\}$, and three univariate extreme subsets $\{X, Y, and\ Z\}$. Thus, the return period of three variables can be represented by a 3D step function consisting of seven sub-functions.

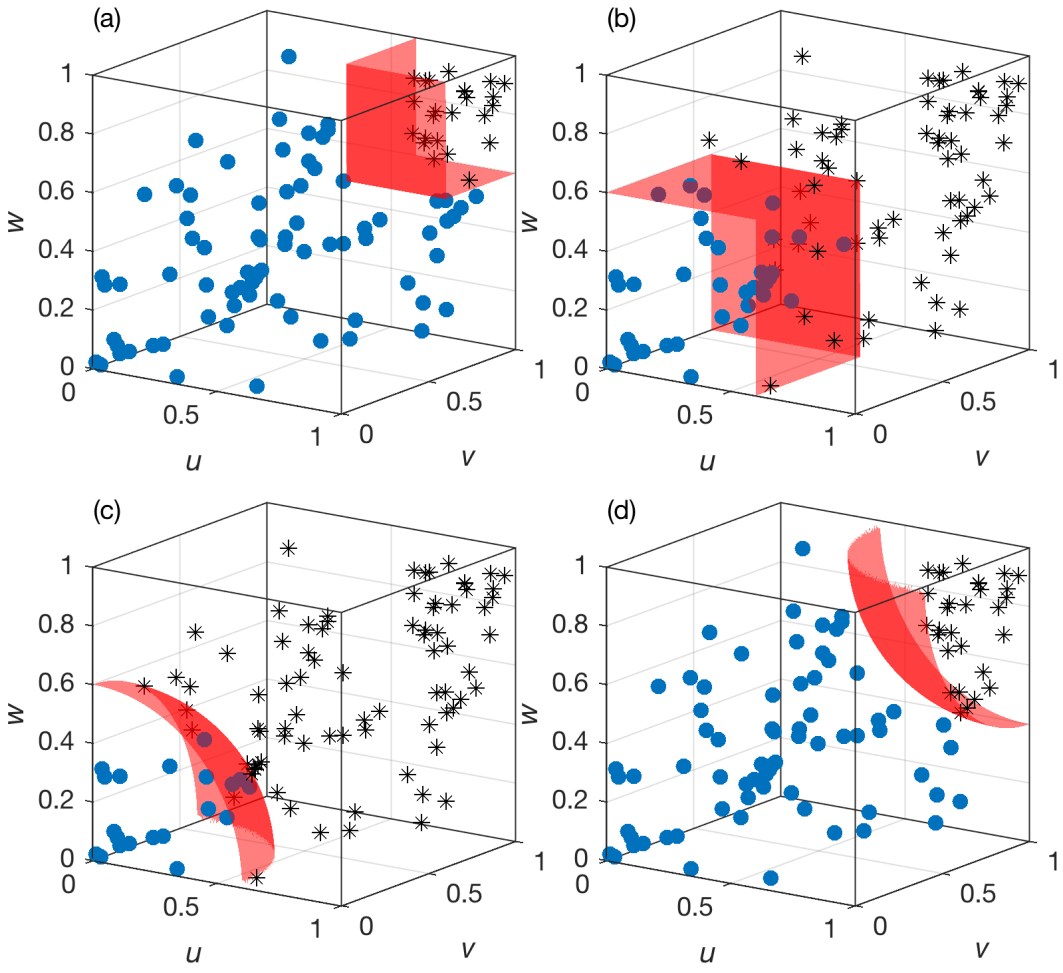

Figure 3-4. Extreme scenarios of trivariate combination for multiple hazards. Red surface is the division layer between normal (blue dot) and extreme (black star) events. The sample points are randomly generated from a trivariate standard normal distribution with 0.5 correlation between each variable.

The form of a univariate return period is as Equation (3-11) shows with M_t and $F_X(x)$ derived from single-hazard extreme observations. Let (X, Y) and (X, Y, Z) be random variables

representing the bivariate and trivariate extreme combinations, respectively. An example of the bivariate joint return period function is as below

$$\begin{aligned} T_{XY}(x,y) &= \frac{M_t}{P\{X > x \cap Y > y\}} \\ &= \frac{M_t}{1 - F_X(x) - F_Y(y) + F_{X,Y}(x,y)} \\ &= \frac{M_t}{1 - F_X(x) - F_Y(y) + C(F_X(x), F_Y(y))} \end{aligned} \tag{3-12}$$

where $F_X(x)$ and $F_Y(y)$ are the marginal distribution of $X\ and\ Y$ respectively, M_t is the average recurrence interval of bivariate extreme events, and $C(..)$ is the bivariate copula of $F_X(x)$ and $F_Y(y)$. Similarly, the trivariate joint return period of (X, Y, Z) can be defined as

$$T_{XYZ} = \frac{M_t}{P\{X > x \cap Y > y \cap Z > z\}} = \frac{M_t}{1 - \bar{F}_{XYZ}(x,y,z)} \tag{3-13}$$

where $\bar{F}_{XYZ}(x,y,z) = F_X(x) - F_Y(y) - F_Z(z) + F_{XY}(x,y) + F_{XZ}(x,z) + F_{YZ}(y,z) + F_{XYZ}(x,y,z)$, $F_X(x), F_Y(y), F_Z(z)$ are the univariate margins, $F_{XY}(x,y), F_{XZ}(x,z), F_{YZ}(y,z)$ are the bivariate margins, $F_{XYZ}(x,y,z)$ is the trivariate joint distribution, and M_t is the recurrence interval of the three-hazard events. Both the bivariate margins and trivariate distributions can be obtained based on their corresponding bivariate and trivariate copula functions and the univariate margins.

For a given return period, according to Equations (3-11), (3-12) and (3-13), a number of random events can be generated with the same return period but various strengths for every single variable. Those events can be used to do risk analysis under the framework of multiple hazards. Therefore, the joint return period based on copula plays a vital role in multi-hazard risk assessment.

3.4 Hydrodynamic model for multi-hazard flood simulations

Among the different types of flood simulation models, hydrodynamic models are considered to provide high simulation accuracy and require less effort in model calibration. However, it is also acknowledged to be computational demanding for large-scale simulations. Thus, the application of hydrodynamic models is normally restricted to small catchments or operated on coarse spatial resolutions. With the recent technical progress in high-performance computing, it has now become realistic to employ hydrodynamic models to support large-scale flood

modelling across an entire catchment or city with required performance and accuracy, especially after GPU-based acceleration techniques are introduced to hydrodynamic modelling. As a large number of simulations and quantitative results of flood depth and extent for the whole research domain are needed to support risk assessment in this thesis, the recently developed High-Performance Integrated hydrodynamic Modelling System (HiPIMS) (Liang and Smith, 2015; Xia et al., 2017) is adopted for flood modelling, which is implemented using the NVIDIA CUDA platform to achieve multi-GPU high-performance computing.

3.4.1 Governing equations and numerical scheme

In a flood event, the water depth is generally much smaller than the horizontal inundation extent. The 2D depth-averaged models based on Shallow Water Equations (SWEs) provide a rigorous mathematical framework for the simulation of regional flood inundation. A matrix form of the SWEs can be written as

$$\frac{\partial \mathbf{q}}{\partial t} + \frac{\partial \mathbf{f}}{\partial x} + \frac{\partial \mathbf{g}}{\partial y} = \mathbf{R} + \mathbf{S}_\mathrm{b} + \mathbf{S}_\mathrm{f} \tag{3-14}$$

where t denotes the time, x and y are the Cartesian coordinates, $\mathbf{q}$ is a vector containing the conserved flow variables, $\mathbf{f}$ and $\mathbf{g}$ are the flux vectors in the x and y direction, and $\mathbf{R}$, $\mathbf{S}_\mathrm{b}$ and $\mathbf{S}_\mathrm{f}$ are the source terms representing the rainfall/infiltration rate, bed slope and friction effect, respectively. The vector terms are given by

$$\mathbf{q} = \begin{bmatrix} h \\ uh \\ vh \end{bmatrix}, \mathbf{f} = \begin{bmatrix} uh \\ u^2h + \frac{1}{2}gh^2 \\ uvh \end{bmatrix}, \mathbf{g} = \begin{bmatrix} vh \\ uvh \\ v^2h + \frac{1}{2}gh^2 \end{bmatrix} \tag{3-15}$$

$$\mathbf{R} = \begin{bmatrix} R + I \\ 0 \\ 0 \end{bmatrix}, \mathbf{S}_\mathrm{b} = \begin{bmatrix} 0 \\ -gh\frac{\partial b}{\partial x} \\ -gh\frac{\partial b}{\partial y} \end{bmatrix}, \mathbf{S}_\mathrm{f} = \begin{bmatrix} 0 \\ -\frac{\tau_{bx}}{\rho} \\ -\frac{\tau_{by}}{\rho} \end{bmatrix} \tag{3-16}$$

where h is the water depth; u and v denote the two depth-averaged velocities in x- and y-direction, respectively; $\mathbf{R}$ is the rainfall rate; I is the infiltration rate; ρ is the water density, g is the acceleration of gravity, and τ_{bx} and τ_{by} are the frictional stresses estimated using the Manning formula:

$$\tau_{bx} = \rho C_f u\sqrt{u^2 + v^2} \text{ and } \tau_{by} = \rho C_f v\sqrt{u^2 + v^2} \quad (3\text{-}17)$$

where $C_f = gn^2/h^{1/3}$ is the coefficient of bed roughness with n being the Manning coefficient.

A Godunov-type finite volume scheme presented by Liang (2010) is used initially to solve the above SWEs in HiPIMS. Recently, the numerical scheme is improved by Xia et al. (2017) with the application of an innovative surface reconstruction method (SRM) for computing slope source terms more accurately, and a novel implicit discretisation method for handling the highly nonlinear friction terms, to maintain numerical stability at small water depth.

Compared with the traditional CPU-based approaches, the GPU-accelerated models have been proved to be far more efficient in solving the SWEs for large-scale simulations (Smith and Liang, 2013). HiPIMS was developed to run on multiple GPUs for computationally efficient high-resolution simulation of multi-source flooding across large domains. The device available for executing HiPIMS in this work are four NVIDIA K40 and two NVIDIA K80 GPUs.

3.4.2 Model parameters and basic assumptions

The simulation results of a hydrodynamic model are sensitive to the grid resolution. For flood simulation in urban areas, the resolution should be as high as possible to reflect buildings, walls, embankments, and kerbs that may affect the overland flow. However, as HiPIMS is based on uniform grids and a self-adaptive time step, to halve the grid size can result in an eightfold increase in simulation time. Therefore, it is necessary to test the sensitivity of grid size in the research domain to find the largest acceptable grid size to ensure simulation accuracy but reduce the computation expense.

The initial conditions of water depth and velocity at each grid resolution may have an impact on the result of flood simulation, especially for short-time flooding. To set up the model, appropriate initial conditions need to be generated. For real-world modelling, the initial conditions can be obtained by running the model with observed rainfall/boundary conditions for several days before the events.

Unlike hydrological models, there are not many parameters to be calibrated in HiPIMS. The most critical parameter is the Manning coefficient that represents the roughness of the ground surface resisting flood flows. The selection of Manning coefficient is generally based on the

landuse types but also influenced by many detailed characteristics of domain surfaces. The Manning coefficient in HiPIMS will be selected by following the guidelines suggested by Chow (1959) and be further adjusted by comparing simulation results with observations.

Infiltration rate is another parameter that can be defined in HiPIMS. As surface soil usually becomes wet and saturated quickly during extreme events, the infiltration rate is assumed to be zero in the HiPIMS simulations to avoid extra parameter adjustment. Surface flow can be reduced by a well-designed and functional drainage system during a flooding event. HiPIMS is a one-layer surface model that uses permeable DEM cells implemented underneath street networks to conceptually represent the underground drainage pipes.

3.5 Vulnerability and multi-hazard risk analysis

Apart from hazard analysis, the appraisal of vulnerability and exposure are the other two essential modules of the complete risk assessment. The approaches to evaluate the vulnerability can be varied with the object of risk assessment, such as the experimental method for wooden construction (Yin and Li, 2011), the past damage or loss survey method for infrastructure (Kelman, 2002), and the index-based statistical method for social vulnerability (Ge et al., 2013). In this thesis, we use the vulnerability data and analysis techniques from the Multi-Coloured Manual (MCM) to quantitatively measure the potential loss of elements at risk. Exposure analysis is conducted to provide information about the types, characters, and values of the buildings and roads that are under threat from flooding. The data on exposure is from the national property database and Digimap. The risk analysis gives the probability of potential loss of a specific object or a group of objects in a defined spatial range. The risk can be estimated according to the hazard curve and the vulnerability attribute of the exposure.

An example of a virtual property exposed to flood can show the relationship between hazard, vulnerability, exposure, and risk (Figure 3-5). We suppose that the exposure is a house located in an area that is likely to be flooded. The hazard curve in Figure 3-5 shows the hazard quantification in that area by the annual exceedance probability (AEP) of inundation depth. The vulnerability curve illustrates the potential loss of the house as a result of flooding. Each inundation depth corresponds to an AEP value from the hazard curve and a loss value from the vulnerability curve. These two variables are linked for all the hazard values to generate the risk curve that is a loss function indicated by the AEP. The area below the risk curve is the expected average annual loss of the house due to flood.

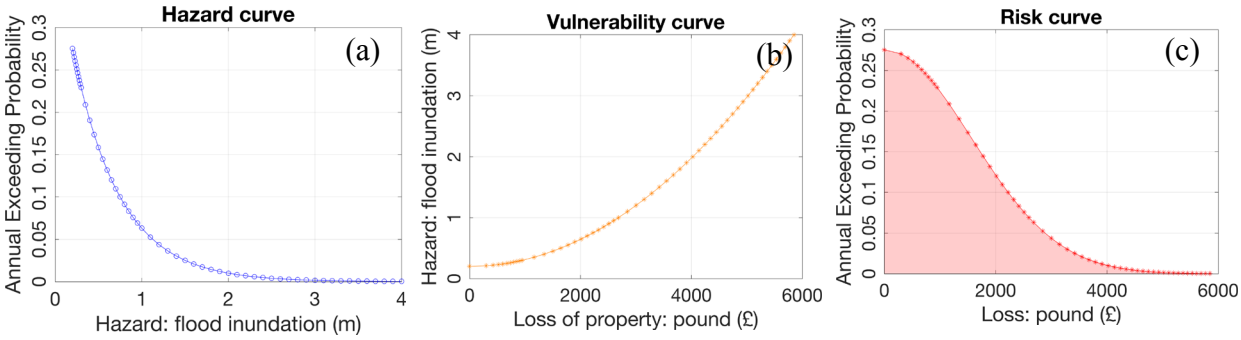

Figure 3-5. Examples of (a) hazard curve, (b) vulnerability curve, and (c) risk curve for a property exposed to flooding

3.5.1 Multi-Coloured Manual for vulnerability analysis

MCM is the synthesis of a series of manuals produced by the Flood Hazard Research Centre (FHRC) to summarise the information on the influence of flooding and coastal erosion in the UK. It mainly consists of the "Blue Manual" providing the assessment of flood hazards, the "Red Manual" appraising the indirect impact of the flood, and the "Yellow Manual" analysing coastal erosion and its intangible effects. The MCM was updated in 2013 by a more comprehensive manual with new data and improved techniques. The new version is Flood and Coastal Erosion Risk Management – A Manual for Economic Appraisal (Penning-Rowsell et al., 2013) but still known as MCM.

MCM provides detailed vulnerability data about residential properties, non-residential properties, and transportation networks. The hazard variable of the vulnerability analysis primarily uses the inundation depth but sometimes also considers the duration of immersion, and the water velocity. The depth/damage functions are appraised according to many internal and external characteristics of the exposure, such as the house types, the building ages, the standard of protection, and the lead time of flood warning. The different kinds of vulnerability curves will be applied to the corresponding types of the exposure. The extent of detail of the curves used is decided by the quality of exposure data.

3.5.2 National property dataset for exposure analysis

The objectives of the risk assessment framework can be varied, such as human life, infrastructure, agriculture and so on. In this thesis, the case study focuses on buildings and transportation networks. The national property dataset (NPD) delivered by the Halcrow Group Limited in accordance with the EA aggregates the information on the geographical position and category of built properties in England and Wales. The detailed usages of all types of properties are given, and the values of non-residential properties are provided. The dataset is

built on the base of Address point from Ordnance Survey (OS) and Rating List from the Valuation Office (VO). The code system of the property types is made compatible with the MCM codes that are associated with the typical depth/damage functions.

As the NPD does not hold information on transportation networks, we use OS Open Roads as a supplement to the exposure data. OS Open Roads provides the topological and geographical information of the links and nodes of the UK's road network that is made up of the significant national roads and the regional or county level roads. The associated attributions of the road link include the identification and classification information and are used to find the corresponding vulnerability function in the MCM.

3.5.3 Multi-hazard risk calculation

The risk is widely recognised as the function of hazard, vulnerability, and exposure or some more related risk components. The calculation method of risk is varied with the understanding of the concept and the purpose of the risk assessment. A simple way is to count the sum or the product of all risk components, which is usually found in the qualitative or semi-quantitative assessment that is only applicable for comparing the risk level (Kappes et al., 2012). The full quantitative risk is not just a fixed value but rather a function curve to show the probability of loss in accordance with the mathematical definition of risk. And this curve can surely be interpreted to a single value like the annual expected loss for comparing and mapping.

The typical procedure to generate single-hazard risk curves is illustrated in Figure 3-5. For the multi-hazard issue, the hazard is a function of multiple variables. In this thesis, rainfall, river flow and storm surge are the three primary hazards considered, and they all lead to flood inundation that is the direct trigger of damage and loss. So, a trivariate hazard function of three primary hazards is first constructed and then the hydrodynamic model is used to find the relationship between the primary hazards and the terminating hazard. According to these two steps, the probability/inundation curve can be obtained as the final hazard function. The multi-hazard disaster risk curve is generated based on the last hazard function, vulnerability curves and exposure data.

3.6 Summary

This chapter has introduced the structure of the risk assessment framework and all the related methodologies. The framework consists of four modules. The frequency analysis module and flood simulation module give the probabilistic appraisement of multiple hazards. The

vulnerability module provides the hazard/damage curves and the information on exposure. The risk module combines the results from hazard and vulnerability to generate risk curves and provide real-time disaster loss forecasts.

The dependence between multiple hazards is measured by asymptotical dependence and rank-based dependence. A copula function is applied to generate the joint probability distribution and joint return period of multiple hazards. A GPU-accelerated 2D hydrodynamic model is introduced to simulate flood with the multi-hazard inputs in the large-scale and high-resolution grid and produce inundation values for each grid cell. The exposure data of valuation and spatial distribution of properties is derived from NPD. The vulnerability analysis uses damage/depth curves from MCM to calculate disaster loss in different vulnerability scenarios. The quantitative multi-hazard disaster risk can be obtained by connecting the hazard curve and vulnerability curve.

The multi-hazard risk assessment framework is fully quantitative and able to estimate the probability of loss in the research area. The framework addresses the research gaps of current methods regarding the analysis of dependence and the simulation of physical interactions of triple hazards. It provides a novel and comprehensive tool to estimate the disaster risk and can be applied in any region potentially impacted by fluvial, pluvial, and coastal flooding.

Chapter 4. Dependence and joint probability analysis for multiple hazards

4.1 Introduction

This chapter corresponds to the section of frequency analysis in the adopted framework of multi-hazard assessment (Figure 3-1), aiming to generate a joint return period function for the three main hazards (i.e. rainfall, river flow, and storm surge) that may cause flooding in Greater London, UK and its adjacent downstream region. The geographical information of the research area and the associated hazards are first analysed to give a general view of the hazard environment in the research area. Then, the asymptotic and rank-based dependence measures introduced at Section 3.2 are employed to investigate the potential correlation among the three hazards, both for the same-hazard inter-station correlation and the cross-hazard dependence. The joint probability distribution of the three hazards is fitted based on the marginal distribution of each hazard and the cross-hazard dependence using copula function. The joint return period can be derived from the probability distribution, which is the quantitative measure of the multi-hazard frequency. It can be further utilised to generate random multi-hazard events with a given probability of occurrence, which will provide the main inputs required for multi-hazard flood simulations in Chapter 5.

4.2 Data source and pre-processing

The main sources of flood water to the Greater London catchment are river flows from the upstream of River Thames and River Lee, seawater from the east coast, and rainfall over the entire region. As shown in Figure 1-1, the locations of the gauge station are ideal for flood frequency analysis, with river flow recorded at Kingston and Feildes Weir, tide height at Sheerness, eight stage gauges along the river showing the interactions between tide and flow, and many weather stations inside the catchment recording daily or hourly rainfall data.

4.2.1 River flow

The flow from the Thames upstream basin in the west of Kingston is the main river water source of the study area, accompanied with the relatively lower flow from the upper

catchment of the River Lee gauged at Feildes Weir (see their locations in Figure 1-1). The River Lee is a tributary of the Thames, and the upstream catchment is about 1036 km^2 in the north of Feildes Weir. The area of the upper Thames Catchment is around 9948 km^2. Both Kingston and Feildes Weir gauges have long flow records that can be dated back to the 1880s. The daily average flow rate observations for each station and the information about the catchment boundary can be downloaded from the UK National River Flow Archive (https://nrfa.ceh.ac.uk). A summary of the daily average flow data is given in Table 4-1, suggesting that the daily flow at Kingston is approximately an order of magnitude higher than it is at Feildes Weir.

Table 4-1. A summary of daily flow data for river gauge stations, Kingston in the Thames and Feildes Weir in the Lee.

Station	Period of record	Daily average flow (m^3/s)				
		Mean	Q95	Q70	Q50	Q10
Kingston	1883-2016	65.67	7.54	22.1	40.5	161.6
Feildes Weir	1879-2016	4.46	0.60	1.73	2.78	8.62

Note: Q95 means 95% exceedance probability and similar hereinafter.

Figure 4-1 displays the monthly average of daily flows at Kingston and Feildes Weir. At both of the two stations, a strong seasonality is shown and the mean daily flow in winter half-year from November to April is significantly higher than it is in the summer-half year from May to October, similar to the seasonality of flood events in the wider England (Macdonald, 2012). Therefore, the investigation of statistical behaviour of daily flow data should consider the influence of seasonality.

4.2.2 Precipitation

In the UK, the Met Office Integrated Data Archive System (MIDAS) archives and provides meteorological observations including daily and hourly precipitation with controlled quality. The rainfall records can be downloaded from the Centre for Environmental Data Analysis (CEDA) (http://www.ceda.ac.uk). A total number of 348 weather stations with daily precipitation records can be found inside the research area, and 15 of them have hourly precipitation recorded (see Figure 4-2). However, most of the stations have very limited time coverage while only 37 of them have daily rainfall records equal to or longer than 40 years as the typical requirement of reliable statistical analysis. These stations are categorised as “good stations”. A summary of the daily rainfall completeness from good stations is illustrated in

Figure 4-3. Although the majority of the rainfall stations seem to start recording from the 1960s, there are still some stations like Kew and Cross Ness providing rainfall records for more than 100 years.

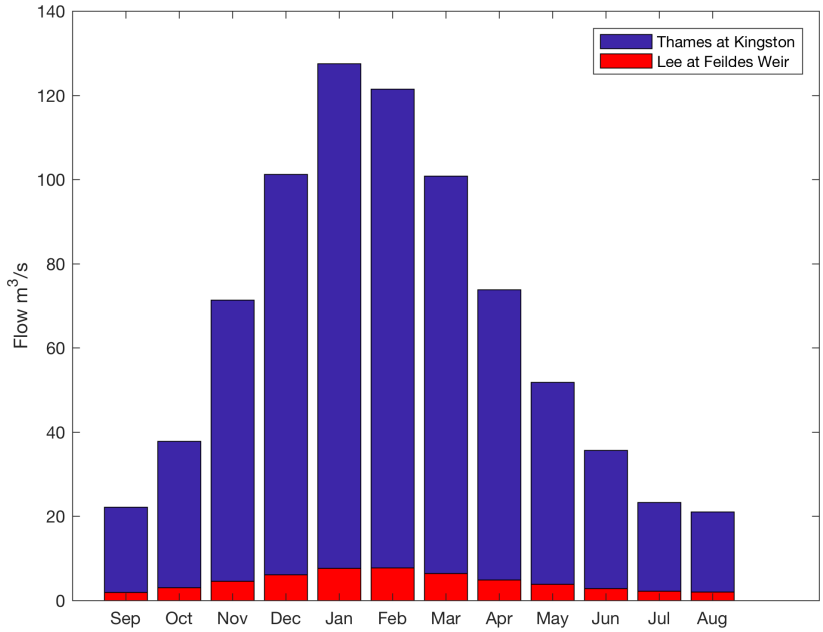

Figure 4-1. Monthly average of mean daily flow at the Kingston and Feildes Weir river stations.

To analyse the general spatial distribution of rainfall at the research area, the annual average precipitation for every "good station" is derived from the daily records. Then the station-based yearly averages are interpolated using the Inverse Distance Weighted (IDW) method to generate a raster and contour map for the research area as shown in Figure 4-4. The contour map shows that the annual rainfall accumulation is generally similar at the west, the central, and the east regions of the research domain, except for the higher rainfall values at the south and northwest corners with higher altitudes (see Figure 1-1).

4.2.3 Tide and Surge

As the total sea level changes periodically under the combined influences of the gravitational forces exerted by the Moon, the Sun, and the rotation of the Earth, it is not reasonable to measure the dependence between astronomical tide and other extreme events directly. Instead, the tide level can be decomposed into its tidal and non-tidal components via harmony analysis (Pugh, 1996). The non-tidal part of sea level called surge is usually created by suitable meteorological conditions and therefore more likely to be correlated to other hydrometeorological hazards.

The tide station Sheerness is located at the south bank of the Thames river mouth and is approximately 35 km away from the east border of Greater London. It provides 1-hour or 15-min tide and surge observations for about 38 years from 1953 to present with missing data in several periods (data available at the website of British Oceanographic Data Centre https://www.bodc.ac.uk/data/hosted_data_systems/sea_level/uk_tide_gauge_network/). The monthly average height of the maximum daily surge and mean daily tide are illustrated in Figure 4-5. Both the tide and the surge show strong seasonality but different trends in that the surge tends to be higher in the cold half-year from October to March while the tide is higher in the second half-year from July to December.

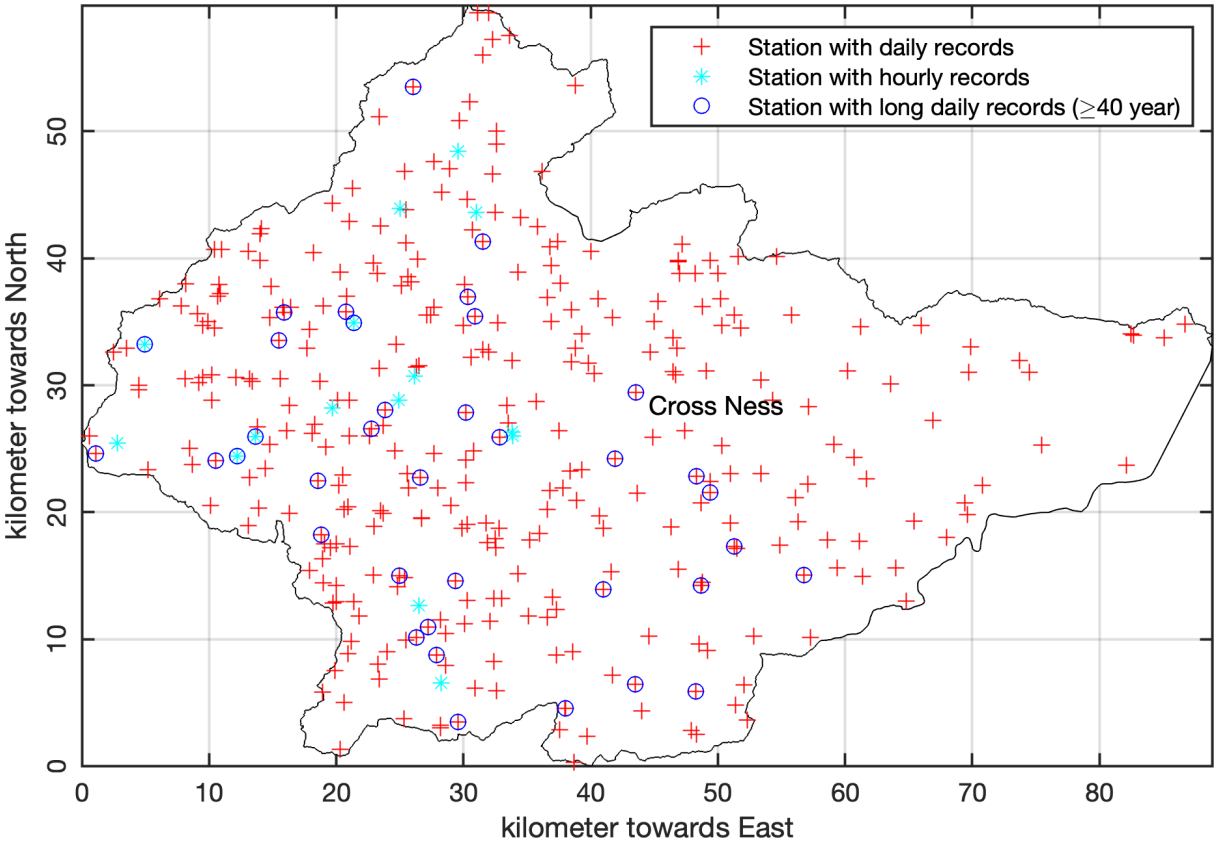

Figure 4-2. MIDIAS weather station with daily and hourly rainfall records in the research area.

The location of Sheerness is ideal to provide sea level data as the boundary conditions for flood simulations in the model domain. However, compared with the observations of rainfall and river flow, the time series for tide and surge observations at Sheerness is relatively short which is the limitation in joint statistical analysis. Therefore, another tide station at Dover, located 52 km southeast of Sheerness, is considered as a supplementary choice to expand the time-coverage of tide and surge observations. Dover has approximately 58-year valid tide and surge records that can be dated back to 1924. The regression analysis is performed between observations in Dover and Sheerness for the max daily total water level as shown in Figure

4-6. The maximum daily total water level is well fitted by a linear equation from Dover to Sheerness but the fitting for surge experiences a greater uncertainty. In general, both the tide and the surge at the two stations show strong and almost linear correlations between Sheerness and Dover. Therefore, total water level data in Sheerness is expanded based on the valid observations at Dover via linear regression analysis.

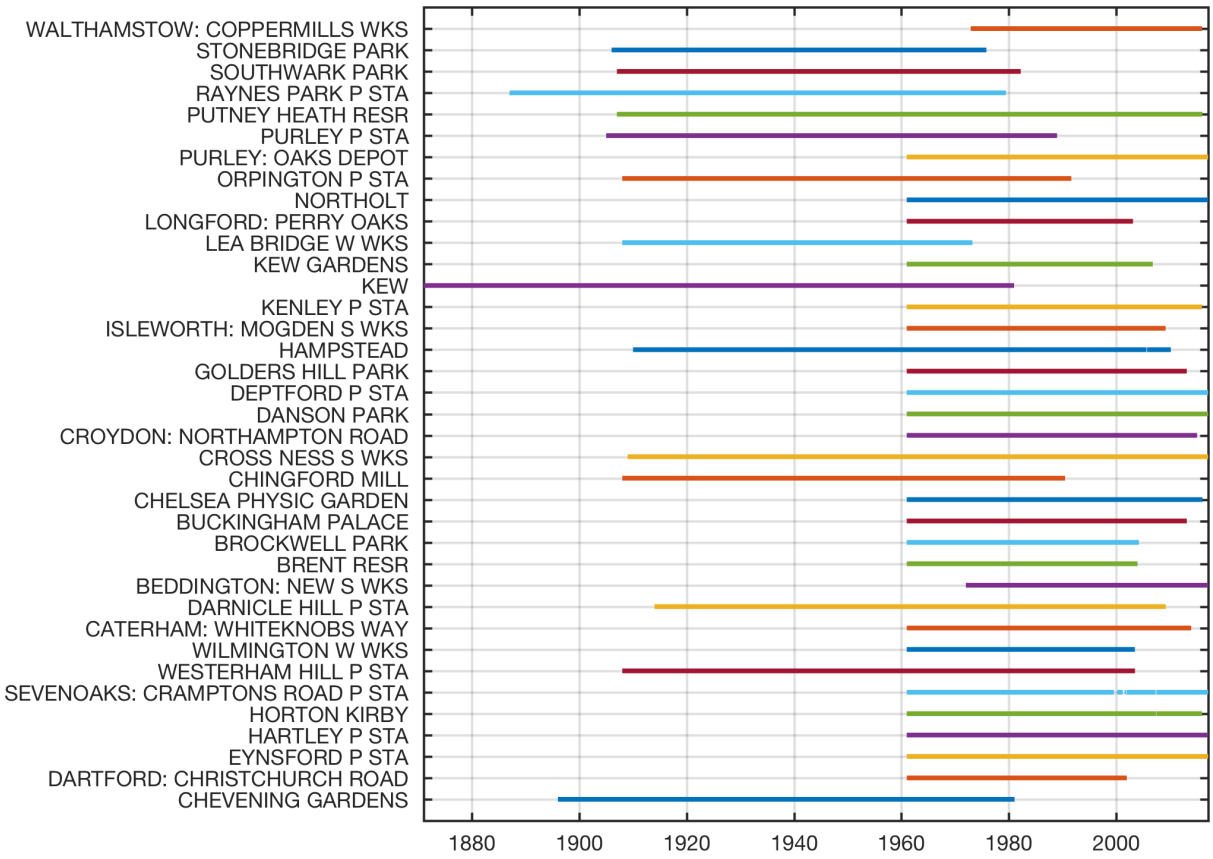

Figure 4-3. Durations of daily rainfall observations for the "good stations" in the research area.

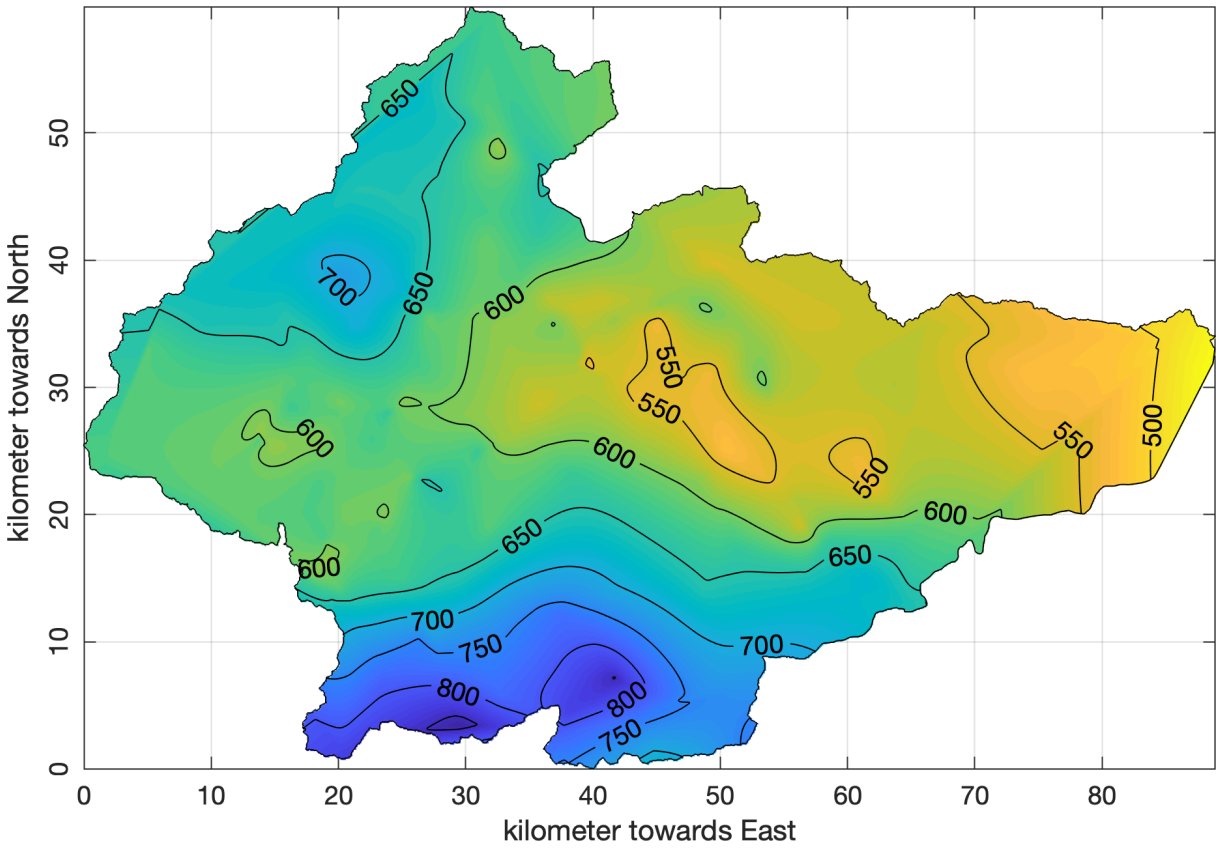

Figure 4-4. Contour map of annual average rainfall in the research area.

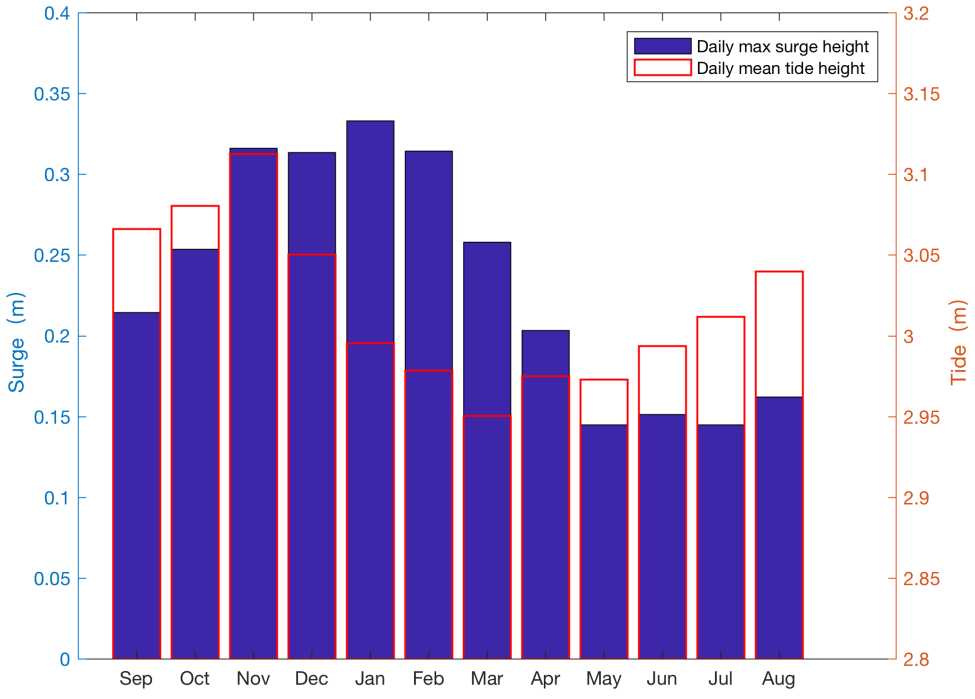

Figure 4-5. Monthly means of daily max surge and daily mean tide at Sheerness.

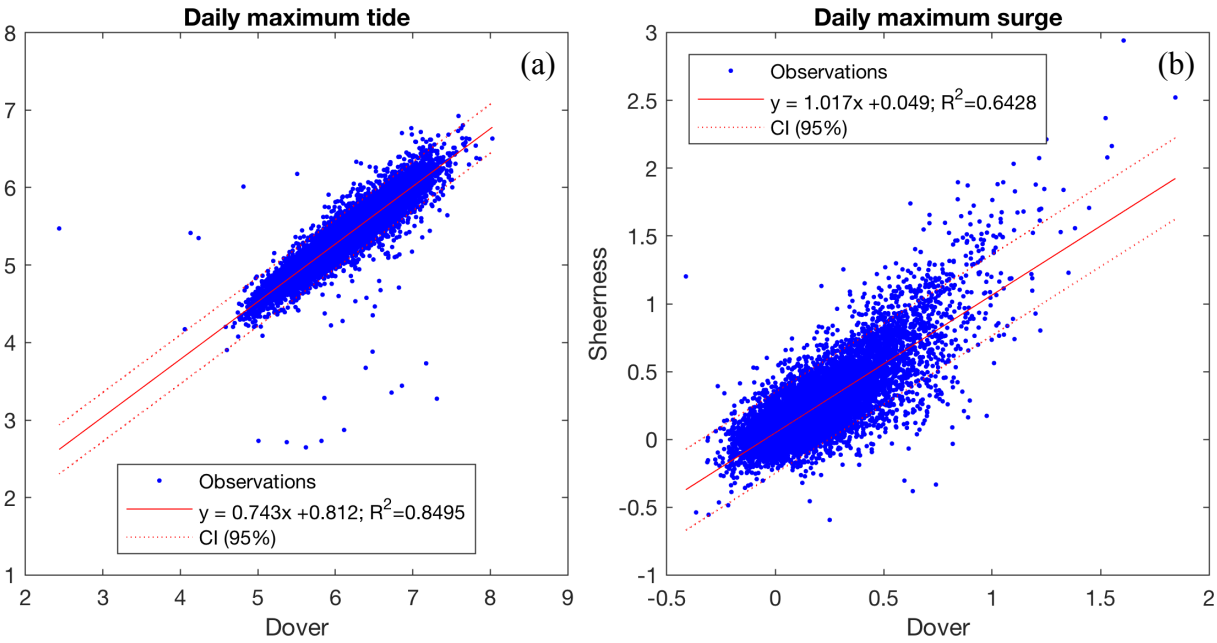

Figure 4-6. Linear regression between the observations at Dover and Sheerness for daily maximum tide (a) and daily maximum surge (b).

4.3 Inter-station dependence for single hazard

In this section, the inter-station dependence of the same hazard variable is explored, including river flow at gauges in the Thames and the Lee, rainfall recorded inside the research area with long enough time series. As Sheerness is only one tide station close to London, no inter-station dependence for tide or surge will be considered.

4.3.1 Dependence of river flow gauges

The reason to investigate the dependence between Kingston and Feildes Weir is that they are the two main river gauges that measure the flows into the research area from west and north respectively. A potential positive dependence would exaggerate the severity of fluvial flooding in London.

At first, the asymptotic dependence measures χ and $\bar{\chi}$ are applied to quantifying the dependence of the daily river flows recorded in the two gauges. The results are presented in Figure 4-7. The red line denotes χ or $\bar{\chi}$, the black dashed line plots the values of 5% significance level, and the dotted blue lines present the 95% confidence intervals. The significance test is performed based on the methodology described in 3.2.1 with 500 times of resampling with replacement, indicating that the line of $\chi(u)$ is considerably higher than the line of 5% significance level at most of the range. The confidence interval is calculated based on the resampling without replacement for 500 times and the results show that the variance of

$\chi(u)$ and $\bar{\chi}(u)$ is convergent as $u \to 1$, suggesting a strong dependence of daily flows in the two flow gauges.

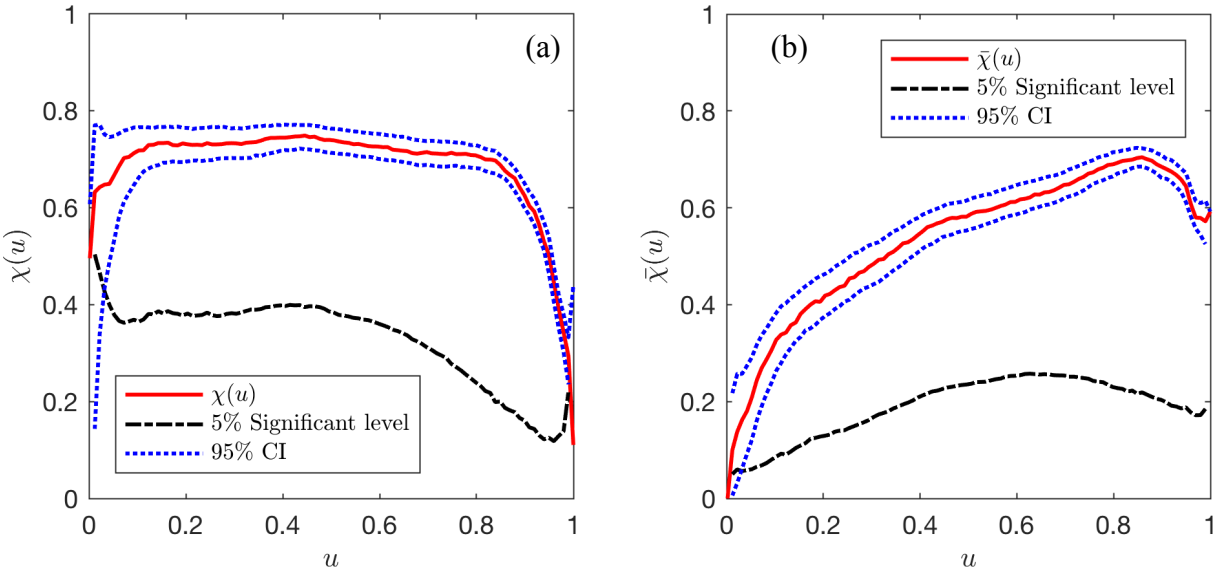

Figure 4-7. Dependence measures χ and $\bar{\chi}$ for daily flow data at Kingston and Feildes Weir.

If the threshold u for χ and $\bar{\chi}$ is set to be the 1% exceedance probability ($u = 0.99$), $\chi = 0.340$ and $\bar{\chi} = 0.579$, and an extreme sample containing 138 paired values over the threshold can be extracted from the observation in the two gauges. The threshold $u = 0.99$ corresponding to one-year return period makes the selected events be rare enough as extremes, and the sample size is reasonably large for statistical analysis. Therefore, this sample is used to further analyse the extreme dependence based on rank-based measures.

A scatter plot in the left panel of Figure 4-8 provides a general view of the extreme sample points. The right panel of Figure 4-8 is called Chi-plot, which is a graphic tool for detecting dependence (Fisher and Switzer, 2001). The horizontal coordinate λ shows the distance of each point to the median point of the whole sample and the vertical coordinate χ indicates how far a point is away from the null hypothesis (the two variables are independent) illustrated by the black dotted line. If the null hypothesis is true, around 95% of the χ values should lie between the two red dashed lines. According to the Chi-plot, a weak dependence from the extreme sample can be observed. This is also supported by the values of the two rank-based measures Spearman's Rho $\rho = 0.18$ and Kendall's Tau $\tau = 0.12$ that show a positive dependence under the 95% significance test.

4.3.2 Dependence of rainfall stations

As stated in Section 4.2.2, there are 37 rainfall stations with daily records of no less than 40 years, the daily rainfall at these stations are selected to perform dependence analysis. Every

station is paired with all the other stations and calculated one by one for asymptotically dependence measures $\chi(u)$ and $\bar{\chi}(u)$ at the extreme level $u = 0.99$, corresponding to around 1-year return period for a single rainfall station. Then the values of inter-station dependence are compared against the horizontal and vertical distances between the stations respectively. In Figure 4-9, the top left and right plots illustrate χ and $\bar{\chi}$ values against the horizontal distance between the stations respectively while the bottom-left and bottom-right plots depict the relationship between dependence measures and the vertical distance between the stations.

From the figure, we may conclude that 1) the inter-station asymptotically dependences are generally high as the measure χ is generally over 0.4 and $\bar{\chi}$ over 0.6; 2) χ and $\bar{\chi}$ decrease when the horizontal distance between stations increases but they do not significantly change with the vertical distance; and 3) the interpolation method for rainfall based on horizontal distance will not spatially omit the extreme character as the existence of high dependence for extreme thresholds.

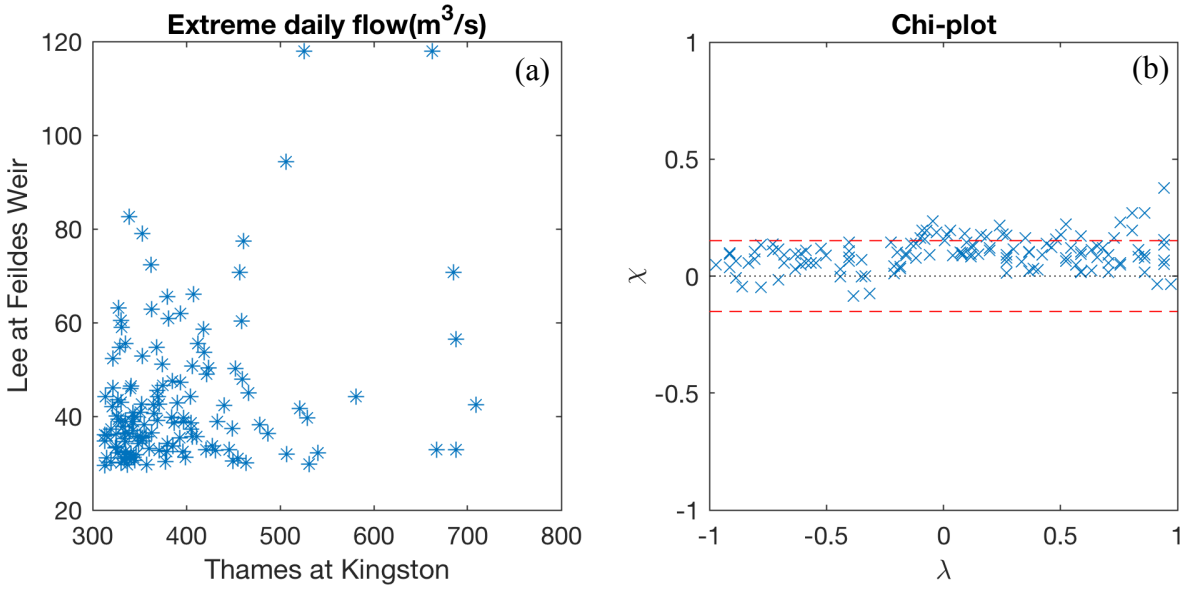

Figure 4-8. Scatter plot (a) and Chi-plot (b) of joint extreme flow at Kingston and Feildes Weir.

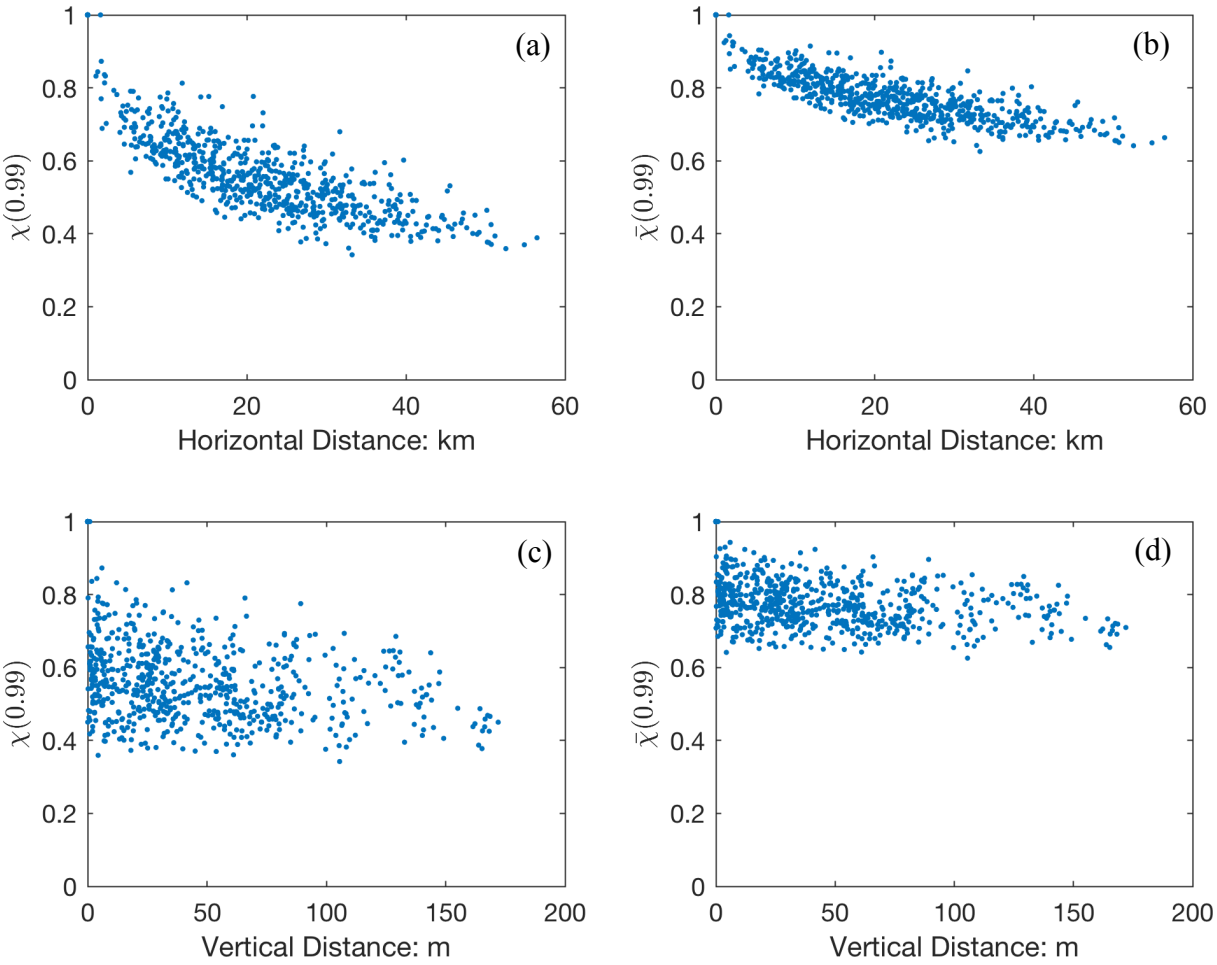

Figure 4-9. Inter-station dependence for daily extreme rainfall at stations of London. The X-axis represents the horizontal or vertical distance between stations and Y-axis represents the dependence measures χ and $\bar{\chi}$ estimated at level u=0.99.

4.4 Dependence between multiple hazards

Rainfall, river flow, and storm surge are the three hazards in consideration, and both rainfall and river flow have more than one recording station to provide data for analysis. According to the results of the inter-station analysis for the single hazard, the rainfall station has a strong dependence on the nearby stations and daily average flows at the two river gauges are also correlated to each other. Meanwhile, the flow rate at Kingston is much higher than that at Feildes Weir and more likely to cause flood events. So, the daily records at Kingston are selected as the representative variable of river flow. For rainfall, the station Cross Ness is chosen as the representative gauge because it provides recorded observations for a very long time-series and its annual amount is also close to the median rainfall value of the whole research area. Additionally, daily maximum surge observations at Sheerness with expanded records from Dover provide the only available but appropriate representative variable for coastal flooding. The cross-hazard dependence is investigated for the bivariate combinations

of rainfall vs flow, rainfall vs surge, and flow vs surge. Each pair of the variables is matched based on the same day observations.

4.4.1 Asymptotic dependence

For a given sample of bivariate random variables, the estimation of asymptotic dependence varies between different thresholds (White, 2007). It is essential to investigate the changing trend of dependence strength due to the threshold values. The asymptotic dependence measures χ and $\bar{\chi}$ are applied to give a general view of the degree of dependence at continuous threshold levels from 80% to 99% for all of the three hazard pairs.

The representative rainfall station Cross Ness is around 32 km away from the river gauge station Thames at Kingston (see Figure 4-2). The weather systems like mild cyclones traversing from Wales to east England might bring simultaneous extreme observations for both of the stations as the catchment area of Kingston is in the west of the gauge. In contrast, concurrent extreme events are unlikely caused by weather systems moving from east England to the west. The asymptotic dependence measures χ and $\bar{\chi}$ between rainfall and river flow over 80% percentile are illustrated in Figure 4-10. For the value of $\chi(u)$, it decreases slowly as the threshold approaching to 1 while the uncertainty indicated by 95% confidence interval grows as fewer observation pairs can surpass the thresholds for both variables. The value of the other measure $\bar{\chi}(u)$ keeps stable and is always higher than the 5% significance level. The $\bar{\chi}(u)$ line is almost linear until the threshold value exceeds 98%. The results demonstrate that a significant and positive dependent relationship exists between daily rainfall in Cross Ness and daily average river flow at Kingston.

The hazard pair of rainfall and surge is represented by the observations from rainfall station Cross Ness and tidal station Sheerness respectively, being around 40.5 km away from each other. Figure 4-11 shows the value of asymptotic dependence measures χ and $\bar{\chi}$ between them. For χ, it decreases, and its uncertainty increases as u approaching 1. When the threshold becomes larger than 95%, χ is getting closer to zero and cannot significantly indicate the dependence as the estimated value of χ going below the black dashed line. In contrast, $\bar{\chi}$ drops slightly with the increase of the threshold value and its uncertainty does not enlarge until u becomes larger than 96%. The results indicate a weak but statistically significant dependence between daily rainfall at Cross Ness and maximum daily surge at Sheerness.

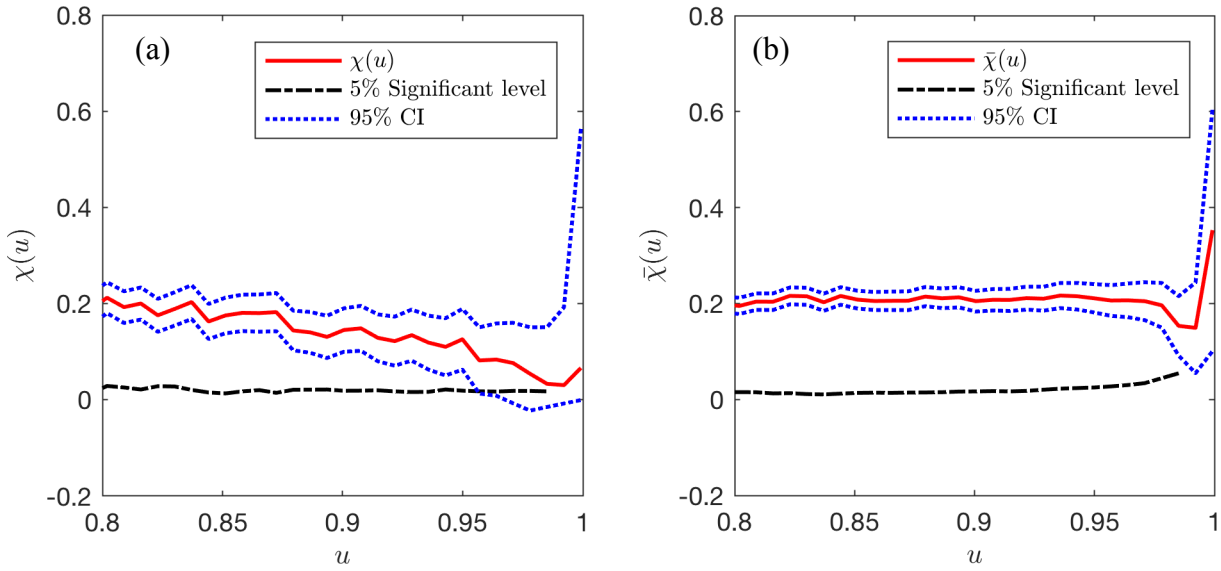

Figure 4-10. Asymptotic dependence measures (a) χ and (b) $\bar{\chi}$ for daily extreme rainfall at Cross Ness and extreme daily Thames flow at Kingston.

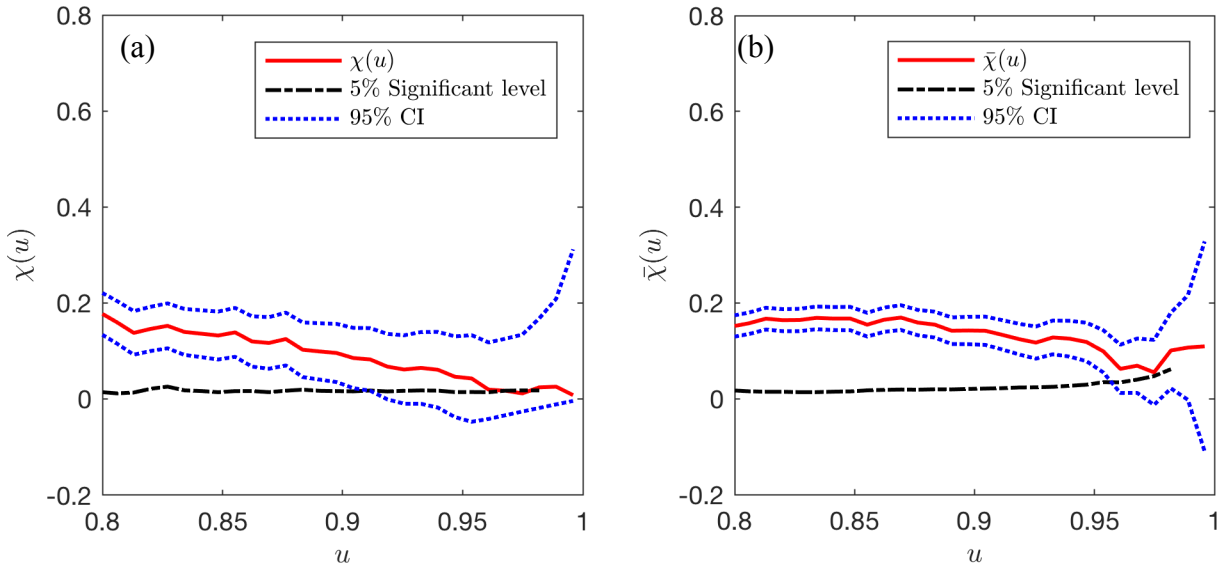

Figure 4-11. Asymptotic dependence measures χ and $\bar{\chi}$ for daily rainfall at Cross Ness and daily maximum surge at Sheerness.

The concurrence of extreme river flow and storm surge is the third hazard pair to be analysed. The distance between the river flow station Kingston and the tide station Sheerness is 71 km, larger than the distances between the observation stations of the other two hazard pairs. The asymptotic dependence between the river flow and the surge is illustrated in Figure 4-12. The value of χ equals to 0.21 when $u = 0.8$ and then decreases to zero with a slightly enlarging uncertainty as u becomes closer to 1. When $u > 0.95$, the estimation of $\chi(u)$ is not significant at 5% level. The value of $\bar{\chi}(u)$ starts from a similar value to χ and does not obviously decrease until u becomes close to 0.95. The 95% confidence interval of $\bar{\chi}(u)$ is convergent and the estimation of $\bar{\chi}(u)$ can pass the significant test when u is not larger than

0.97. The results can suggest that the dependent relationship between daily average river flow at Kingston and daily maximum surge at Sheerness is significant.

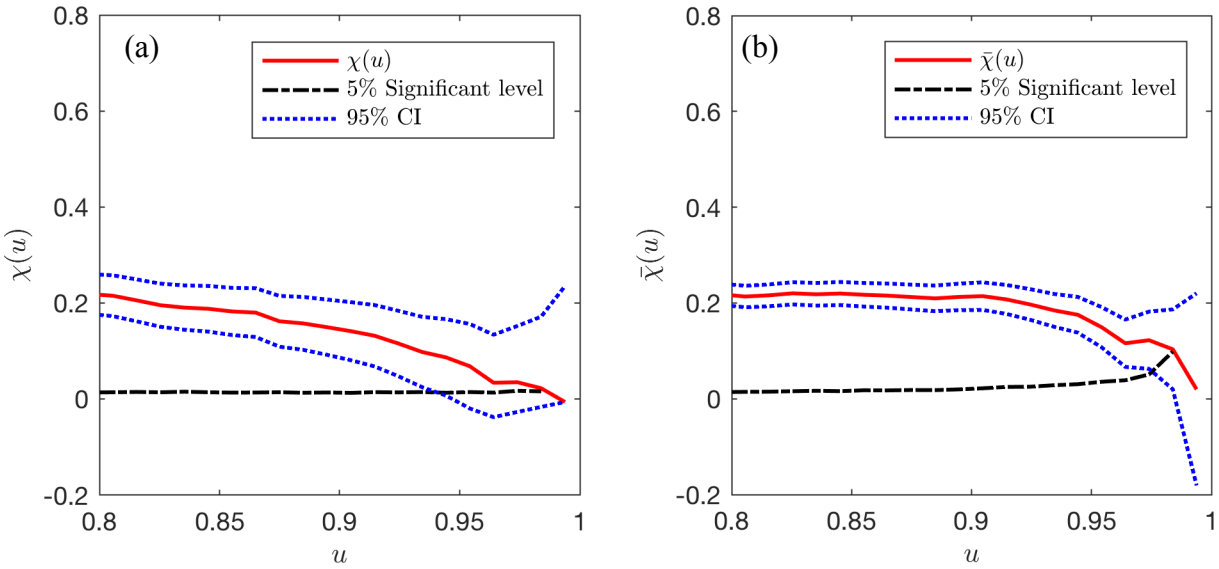

Figure 4-12. Asymptotic dependence measures χ and $\bar{\chi}$ for daily average flow at Kingston and daily maximum surge at Sheerness.

In summary, although the cross-hazard bivariate dependence is much lower than the value of inter-station and single-hazard dependence, different degrees of dependence obviously exist in the three hazard pairs. The dependence between rainfall and storm surge is the weakest among the three hazards pairs. The other two hazard pairs have a similar degree of dependence. However, the rainfall and river flow seem to be more reliant on each other at the high threshold ($u > 0.95$) compared with the hazard pair of rainfall and storm surge.

4.4.2 Selection of extreme threshold

The extreme part of each set of variables, instead of the entire time-series records, is of interest for natural hazard analysis because only the extremes are responsible for disasters. A certain level of threshold needs to be given to define extreme events for each hazard. Both the asymptotic and rank-based dependence measures are performed for any of the thresholds following two rules: 1) high enough to be treated as extreme, and 2) low enough to retain a suitable sample size. For multivariate extreme analysis, the selection of threshold should obey these rules for all of the component variables.

While the time coverage of rainfall and flow records are longer than 100 years, the Sheerness tidal station, with expanded observations from Dover, only has valid surge records for approximately 60 years. Therefore, to guarantee enough extreme observations for statistical

analysis, the extreme threshold for each hazard combination is not identical, and neither is the resultant extreme sample size. Specifically, the threshold for joint rainfall and river flow can be high as long time-series of observations are available. In contrast, if any of them is paired with the surge, the threshold value needs to be lower to ensure a suitable sample size of observation pairs due to the relatively short time coverage of the surge data.

In flood frequency analysis, two main types of extreme data series are generally used: the annual maximum (AM) series and the peaks-over-threshold (POT) series (Robson and Reed, 1999). The AM series consists of the largest observed data in each year, which means only the single largest value is recorded. A POT series contains all distinct high records that are greater than a selected threshold. The resulting POT series is irregular; in some years there may be many extreme records, in other years there will be no extremes. POT is a more entire extreme dataset to depict flood regime than AM but is also more difficult to extract and not always available. Therefore, although POT is more recommended, AM is still a popular and pragmatic choice in many cases of flood frequency analysis when data is not adequate. In this research, POT series is adopted, but the selection of abstraction threshold is also assessed with AM series data. Five POT thresholds are defined for each hazard pairs as

- The minimum value of the AM series (POT_{AMmin}), which is the smallest annual maximum value, suggesting that each year has at least one event, but some years may have many;
- The 5th percentile of the AM series (POT_{AM05}), a high threshold representing 5% of the years having no extreme events;
- The 90th percentile of the POT series (POT_{90});
- The 95th percentile of the POT series (POT_{95});
- The 98th percentile of the POT series (POT_{98}).

All the above five thresholds are applied to each pair of hazards to investigate the resultant univariate critical values, the extreme sample size, and the frequency of joint extreme events.

For hazard pair of rainfall and river flow, the length of matched daily records is 103 years (a natural year with no more than one-third of missing daily records). Table 4-2 shows the selections of the threshold for daily rainfall at Cross Ness and daily average river flow at Kingston and lists the corresponding univariate threshold of each hazard, the number of single and joint extreme events, and the average annual frequency of joint extremes. It is clear that for any universal threshold, the number of joint extreme events is much smaller than the

number of extreme observations for every single hazard. As the time-series of matched daily records is long, even the high thresholds like POT_{AM05} and POT_{98} can generate joint extreme events with considerable sample size (64 and 51 respectively) for statistical analysis. According to the value at the last column, the threshold of POT_{90} seems too low to be regarded as extreme in that more than 8 joint extreme events can be expected per year.

Table 4-2. Extreme threshold selection for dependence analysis between rainfall at Cross Ness and river flow at Kingston.

Universal probabilistic threshold	Threshold for each variable		Single exceedance records		Joint exceedance records		Joint exceedance records per year
	Rain (mm)	Flow (m^3/s)	Rain	Flow	Number	Rate (%)	
POT_{AMmin}	12.4	86.5	757	9341	362	0.89	3.2
POT_{AM05}	17.23	192.55	367	2838	64	0.17	0.6
POT_{90}	4.8	169	3769	3713	831	2.26	8.1
POT_{95}	7.9	223	1883	1861	275	0.75	2.7
POT_{98}	12.4	280	757	741	51	0.14	0.5

The matched daily records between rainfall at Cross Ness and surge at Sheerness have stretched approximately 66 years, which means a smaller number of annual maximums can be obtained. The extreme threshold selections for dependence analysis between rainfall and surge are summarized in Table 4-3. The limitation of short annual maximum series is reflected by the number of the joint exceedance records at the different threshold levels. The selection of any of the annual max thresholds or POT_{98} may lead to a very small size of the joint extreme sample, which is inapplicable for further analysis. The threshold of POT_{90} appears to be too low as the average frequency of the joint extremes is over 5 events per year. Nevertheless, the joint sample size and frequency derived from POT_{95} is a reasonable choice for the joint extreme hazard analysis.

The hazard pair between the river flow and the storm surge has matched daily records for 64 years, similar as the rain-surge pair, suggesting the main limitation of the number of multi-hazard joint records is due to relatively short time series of the surge data. Table 4-4 gives information on the single and the joint extreme sample size for the five types of thresholds. It shows that the threshold of POT_{AMmin} and POT_{90} are too low while the POT_{98} is too high to

obtain enough joint extreme records. The other two thresholds, POT_{AM05} and POT_{95}, can generate an appropriate joint extreme sample for statistical analysis.

In summary, the threshold of POT_{95} is suitable for all three hazard pairs, and the only acceptable one among the five choices for the rain-surge pair. The threshold of POT_{AM05} can be applied to both the rain-flow and the flow-surge pair while POT_{98} is only reasonable for the long time-series pair rain versus flow.

Table 4-3. Extreme threshold selection for dependence analysis between rainfall at Cross Ness and surge at Sheerness.

Universal threshold	Threshold for each variable		Single exceedance records		Joint exceedance records		Joint exceedance records per year
	Rain (mm)	Surge (m)	Rain	Surge	Number	Rate (%)	
POT_{AMmin}	12.4	0.93	419	406	15	0.07	0.2
POT_{AM05}	16.99	1.04	209	286	5	0.02	0.1
POT_{90}	4.8	0.52	2087	2019	364	1.78	5.5
POT_{95}	7.9	0.69	1034	1008	95	0.47	1.4
POT_{98}	12.5	0.93	409	406	15	0.07	0.2

Table 4-4. Extreme threshold selection for dependence analysis between river flow at Kingston and surge at Sheerness

Universal threshold	Threshold for each variable		Single exceedance records		Joint exceedance records		Joint exceedance records per year
	Flow (m^3/s)	Surge (m)	Flow	Surge	Number	Rate (%)	
POT_{AMmin}	86.5	0.93	5094	436	181	0.88	2.8
POT_{AM05}	165.8	1.06	1958	288	45	0.21	0.7
POT_{90}	158	0.52	2137	2122	469	2.20	7.3
POT_{95}	215	0.69	1082	1069	122	0.57	1.9
POT_{98}	271	0.93	428	436	15	0.07	0.2

4.4.3 Dependence value

With a given threshold, the asymptotic dependence measures χ and $\bar{\chi}$ can be calculated. The extreme samples generated based on selected thresholds can be used to estimate the rank-based measures Spearman's Rho and Kendall's Tau. As summarised in section 4.4.2, the threshold of POT_{95} is applicable for all three pairs of hazards. In addition, as observed from the figures of asymptotic dependence measures (Figure 4-10, Figure 4-11, Figure 4-12), the estimation of χ and $\bar{\chi}$ are above the 5% significant line when $u = 95\%$ for all three hazard combinations.

The estimations of χ and $\bar{\chi}$ at threshold level $u = 0.95$ and the corresponding 95% confidence intervals are listed in The existence of tail dependence between rainfall and river flow is also supported by the value of Spearman's Rho and Kendall's Tau with significant positive values. The asymptotic dependence between flow and surge is higher than that between rain and surge, which is concordant to the general dependence of the two pairs as shown in Figure 4-11 and Figure 4-12. The lower bounds of 95% CI of χ for rain-surge and flow-surge pairs are below 0, which suggests that the dependence is relatively weak. It is also reflected by the rank-based dependence of the other two hazard pairs that are shown as negative values and cannot be verified by the test at 5% Significance level.

Table 4-5. With the joint extreme samples extracted based on that threshold level, rank-based measures Spearman's Rho and Kendall's Tau are calculated and listed in the last two columns of The existence of tail dependence between rainfall and river flow is also supported by the value of Spearman's Rho and Kendall's Tau with significant positive values. The asymptotic dependence between flow and surge is higher than that between rain and surge, which is concordant to the general dependence of the two pairs as shown in Figure 4-11 and Figure 4-12. The lower bounds of 95% CI of χ for rain-surge and flow-surge pairs are below 0, which suggests that the dependence is relatively weak. It is also reflected by the rank-based dependence of the other two hazard pairs that are shown as negative values and cannot be verified by the test at 5% Significance level.

Table 4-5. The results show that the dependence at threshold level $u = 0.95$ between the rain and the flow is the highest among all the hazard pairs at the same threshold level.

The existence of tail dependence between rainfall and river flow is also supported by the value of Spearman's Rho and Kendall's Tau with significant positive values. The asymptotic dependence between flow and surge is higher than that between rain and surge, which is

concordant to the general dependence of the two pairs as shown in Figure 4-11 and Figure 4-12. The lower bounds of 95% CI of χ for rain-surge and flow-surge pairs are below 0, which suggests that the dependence is relatively weak. It is also reflected by the rank-based dependence of the other two hazard pairs that are shown as negative values and cannot be verified by the test at 5% Significance level.

Table 4-5. Dependence value of hazard pairs at threshold u=0.95 for χ, $\bar{\chi}$, Spearman's ρ and Kendall's τ.

Hazard pair	u	χ	95% CI of χ	$\bar{\chi}$	95% CI of $\bar{\chi}$	Spearman's ρ	Kendall's τ
Rain vs Flow	0.95	0.12	[0.06, 0.18]	0.21	[0.18, 0.24]	0.07	0.05
Rain vs Surge	0.95	0.05	[-0.04, 0.14]	0.12	[0.08, 0.16]	-0.03	-0.04
Flow vs Surge	0.95	0.07	[-0.02, 0.16]	0.15	[0.11, 0.19]	-0.05	-0.08

Note: The values with an underline indicate fail of significance test at 5% level.

4.5 The probability distributions and return period

4.5.1 Single hazard return period

The prediction of the return period of a hazard variable requires its cumulative distribution function that can be fitted based on the sample observations. The return period is typically quantified in year. For a given extreme threshold, a POT series of daily data can be screened out from the whole set of daily observations. Then Equation (3-11) is applied to calculate the univariate return period of rainfall, river flow and storm surge, respectively. If a predicted return period is much longer than the duration of valid observations, the uncertainty of estimation can be too large to be meaningful in practice. According to the length of the observations time-series for all the three variables, the range of univariate return periods used in this chapter is ranged from 1 to 200 years for rain and flow and 1 to 100 years for surge.

At first, an extreme threshold is chosen for each variable based on their empirical one-year return period, which means the size of POT series is close to the number of years of observation. Table 4-6 gives the extreme threshold and the corresponding extreme sample size for rain, flow, and surge, respectively, showing that river flow has the largest extreme sample while surge has the smallest. The extreme sample is then utilised to fit the probability

distribution. Several types of distributions are tested, and the three-parameter Generalised Pareto (GP) distribution provides the best fit for all the three samples. The cumulative distribution function (CDF) is given as

$$F(x|\xi,\mu,\sigma) = \begin{cases} 1-\left(1+\dfrac{\xi(x-\mu)}{\sigma}\right)^{-\frac{1}{\xi}} & for\ \xi \neq 0, \\ 1-\mathrm{e}^{-\frac{x-\mu}{\sigma}} & for\ \xi = 0. \end{cases} \quad (4\text{-}1)$$

The fitted parameters of the univariate distributions are given in Table 4-6. All of the distribution fittings can be verified via a KS test at the 0.05 significance level. The cumulative distribution functions of the three hazards are illustrated with the 95% confidence interval bounds and the empirical distribution of the observations in the left panels of Figure 4-13. A wider confidence interval is observed from the bottom-left plot, indicating that a small sample size of the surge leads to a larger uncertainty in comparison to the other two hazards.

Table 4-6. Univariate extreme samples and probability distribution function.

Hazard variable	Extreme threshold	Extreme sample size	Probability distribution parameters		
			Shape (ξ)	Scale (σ)	Location (μ)
Rain	26.7 (mm)	105	0.36	4.50	26.7
Flow	393 (m^3/s)	131	0.02	86.26	393
Surge	1.56(m)	60	-0.03	0.30	1.56

With the fitted cumulative distribution functions, the return period for the given strength of a hazard is then calculated via Equation (3-11). The return period, with the 95% confidence interval, for each hazard is depicted in the right panels of Figure 4-13. The confidence interval of the return period is generated based on the confidence bounds of the CDFs. The red stars in the figure signify the return period value of sample points based on their empirical distributions. With the return period line, the expected frequency of a hazard over a certain quantity can be obtained. However, the uncertainty of the return period is enlarged from the uncertainty of the fitted probability distribution and increases sharply after the return period moving beyond the sample length. Therefore, the prediction of a large return period should be very careful especially for variables with short time-coverage.

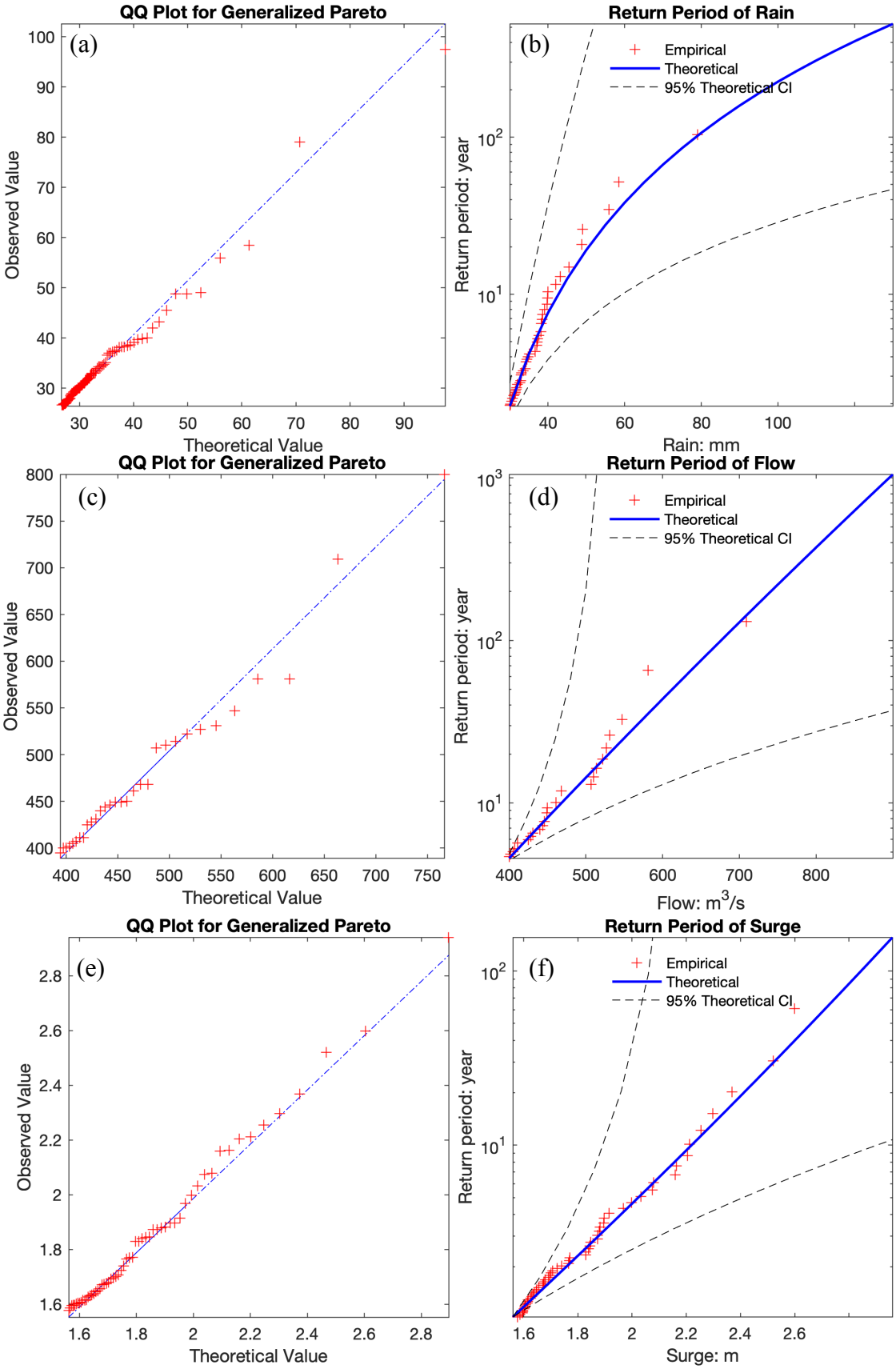

Figure 4-13. Univariate cumulative distribution functions (left) and return periods (right) of rainfall (top panel), river flow (middle panel), and surge (bottom panel).

4.5.2 Bivariate return period

The bivariate return period is the recurrence time of the event quantified by two variables, representing the frequency of joint events with different strength combinations. For fully independent variables, the joint probability distribution is simply the product of each marginal distribution, and similarly, the joint return period is also the product of the univariate return periods. For variables with reliant relationships, the calculation of bivariate return period should use Equation (3-12) with the dependent joint distributions.

As analysed in section 4.4, significant and positive dependence exists between the rainfall and the river flow at the two representative stations, and weak dependence can be found in the pairs of rain-surge and flow-surge. The POT_{95} threshold is identified to be appropriate for every hazard pair. A copula-based procedure introduced in Section 3.3 is applied to fit the bivariate joint distribution for each hazard pair with the bivariate extreme samples.

The first step is to fit the marginal distribution of the two variables using the joint extreme sample. The univariate probability distributions for each hazard have been fitted before based on the single POT series. However, these cannot be regarded as the marginal distributions in the bivariate case because joint sample only contains observation pairs in which both components exceed the extreme threshold. To maintain enough observations in the joint sample, a lower threshold is applied compared with the single-hazard extreme selection. Therefore, instead of using the previously defined univariate distributions, the marginal distributions of the bivariate probability distribution are fitted based on the joint extreme samples. After testing various types of probability distributions, the three-parameter Generalised Extreme Value (GEV) distribution is the best for all marginal distributions of each hazard pairs, which is expressed as

$$F(x|\xi,\sigma,\mu) = \exp[-\left(1+\xi\frac{x-\mu}{\sigma}\right)^{\frac{-1}{\xi}}] \tag{4-2}$$

Table 4-7 displays the parameters of all of the fitted GEV distributions in the last two columns. u and v respectively represent the marginal distributions of the first and the second variable for each hazard pair. The three numbers in each cell give the parameters of shape, scale, and location, respectively. All fitted marginal distributions can pass the KS test at the significance level of 0.05.

Table 4-7. Parameters of joint bivariate distribution and their marginal distributions.

Hazard pair	Copula type	Copula parameter	Marginal GEV distribution			Marginal function domain
			ξ	σ	μ	
Rain	Frank	0.397	0.60	2.34	10.00	>7.9
Flow			0.40	31.83	255.74	>223
Rain	Clayton	-0.153	0.72	1.80	9.44	>7.9
Surge			0.60	0.14	0.82	>0.69
Flow	Frank	-0.501	0.34	37.33	251.55	>215
Surge			0.65	0.10	0.78	>0.69

After deriving marginal distributions, the next step is to find the copula function that links the two margins to a joint distribution function. A test of independence is performed to verify whether it is suitable to use the direct product of margins for the variables. The result of the test shows that all three hazard pairs have rejected the null hypothesis of independence, meaning that it is necessary to find a copula function with a certain level of dependence. Four types of one-parameter Archimedean copulas are tested and compared based on the equations in Table 3-1. For the hazard pairs rain vs flow and rain vs surge, Frank copula is found to be the best fit while AMH copula is better than any other for the pair of flow vs surge. The parameter of each copula is estimated using maximum likelihood methods, and the result is shown in Table 4-7.

With the type of copula and the values of the parameters determined, a joint probability distribution is built to provide the non-exceedance value of the hazard combination at arbitrary intensities. Figure 4-14 displays the joint CDF of rain vs flow, rain vs surge, and flow vs surge via probability distribution surface and contours. For any given combination of intensity from the two hazards, a non-exceedance probability can be obtained from the joint distribution function in the left panel of the figure. Intensity combination of hazards locating closer to the upper-right corner of plots in the right indicates a lower probability of occurrence.

To calculate the bivariate return period, Equation (3-12) is applied to the fitted joint probability distributions. A surface plot illustrates the joint return periods of each hazard pair in Figure 4-15 (left panel). In theory, for each given intensity pair over each extreme threshold, a return period value can always be found. However, due to the huge uncertainty when the component variable becomes larger, a very long return period is not practically significant. Contours of joint return period are shown in the right panel of Figure 4-15,

illustrating the relationship between return period and hazard intensity in plane graphs. The red dots are the extreme observations that are used to fit the joint return period function. These graphs are useful for getting the value of return period with the given pair of hazards or observing what the intensity combination of hazards can be for a given return period.

However, the above fitted joint return period is only applicable for hazards that both surpass their extreme thresholds. For a scenario that one variable is over the threshold while the other is not, the return period functions for the single hazard described and fitted in Section 4.5.1 are then applicable. The thresholds of joint extreme events are lower than the value of each corresponding single extremes to maintain a large enough joint sample size. At bivariate return period analysis, for any hazard intensity pair lower than both bivariate thresholds, it will not be treated as an extreme or dangerous event and is not of interest for further hazard analysis. The domain of interest for bivariate hazards is based on the "Or" scenario that can be decomposed into two univariate extreme domains and one bivariate "And" scenario as discussed in Section 3.3.3. Then, the return period function is able to cover all the intensity combinations of the paired hazards that are acknowledged as "extreme" or "dangerous" events.

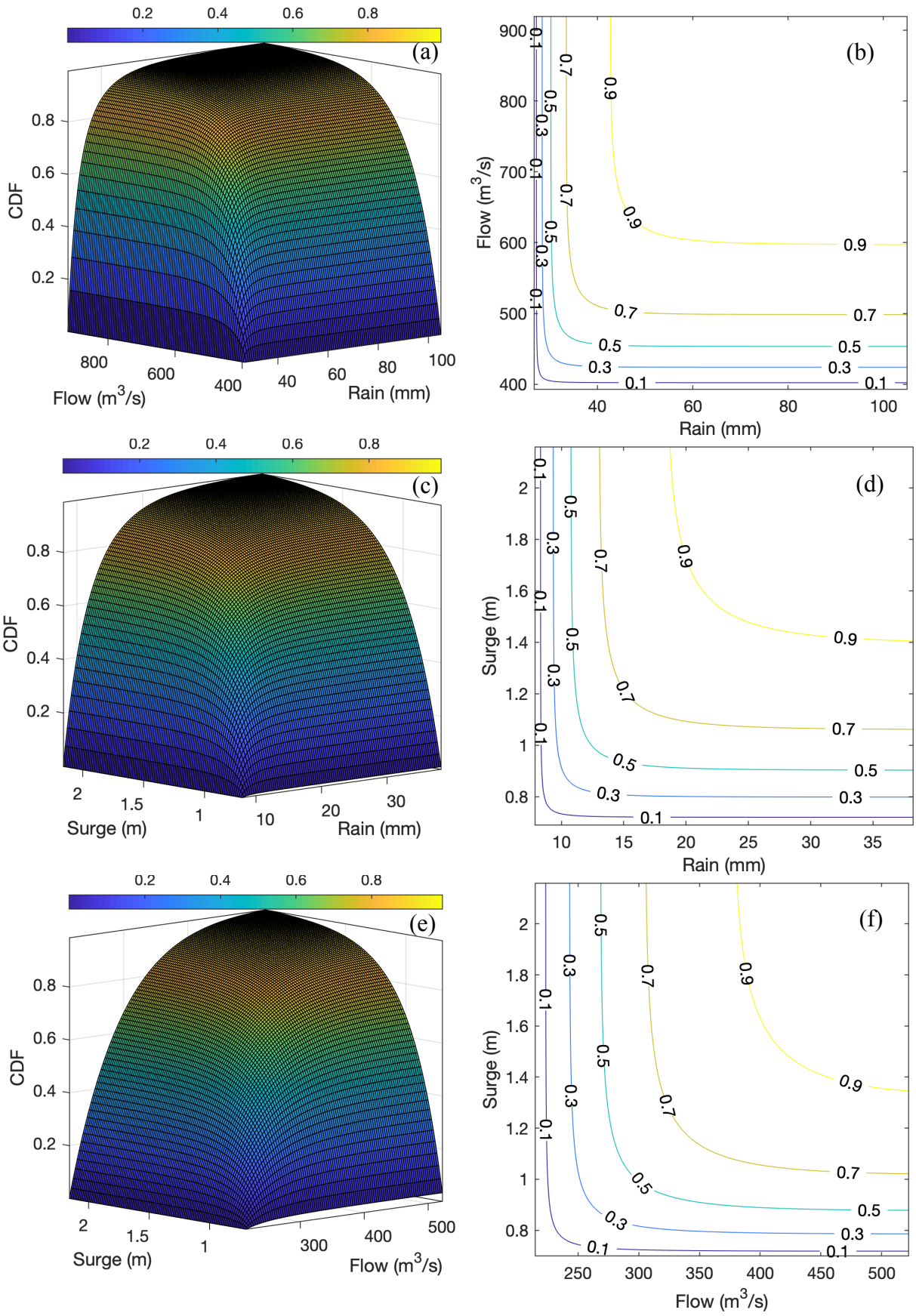

Figure 4-14. Bivariate joint CDF of hazard pairs: rain vs flow (a,b), rain vs surge (c,d), and flow vs surge (e,f).

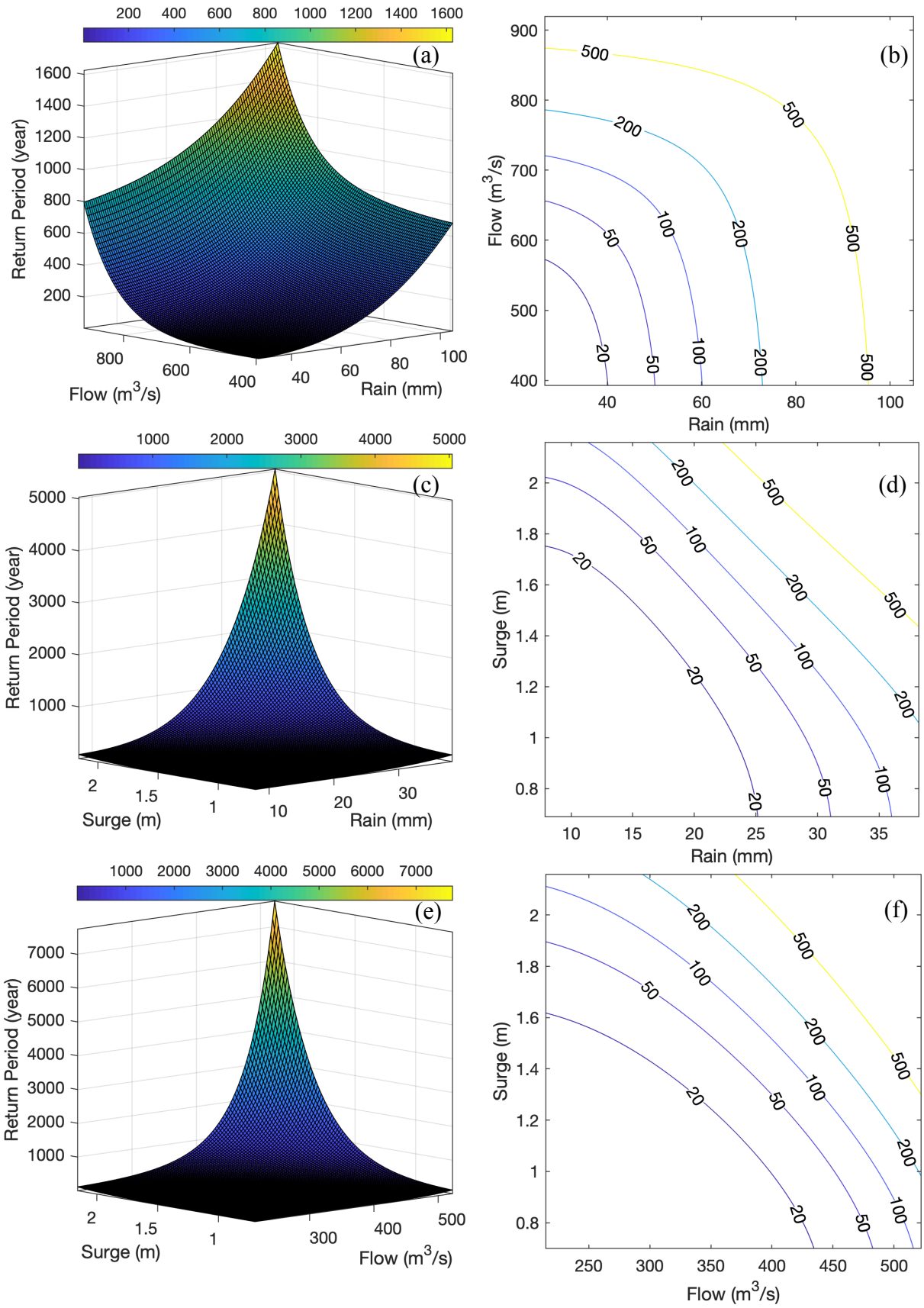

Figure 4-15. Bivariate joint return period of hazard pairs: rain vs flow (a,b), rain vs surge (c,d), and flow vs surge (e,f).

4.5.3 Trivariate return period

The occurrence of trivariate extreme events is even rarer than the bivariate ones. In order to retain a considerable sample size of the joint observations, a lower threshold (POT_{90}) is used to generate the trivariate extreme sample. A total number of 143 trivariate observations are obtained as Figure 4-16 shows. The left panel illustrates the spatial position of each of the extreme observations, and the right panel displays the tied rank of the observations.

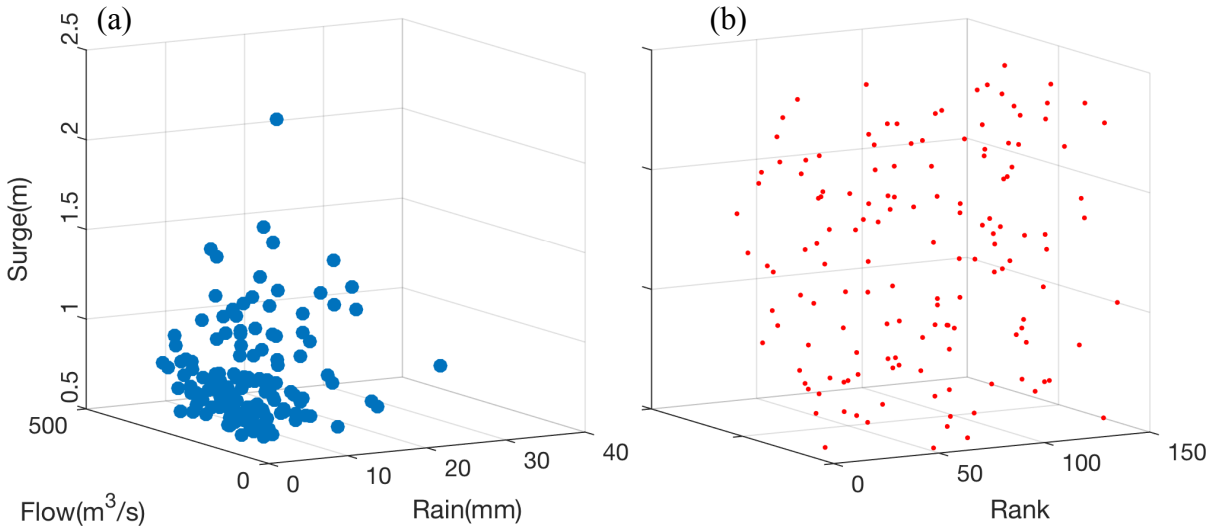

Figure 4-16. Trivariate extreme samples derived from POT_{90} observations for rain, flow, and tide. The left plot is the observed value and the right is the tied rank.

According to Equation (3-13), univariate and bivariate distribution functions are also essential for fitting trivariate return period. A matrix of plots for bivariate scatters and univariate histograms are depicted in Figure 4-17. The similar steps as those described in the previous sections but with a new dataset are used to fit the univariate and bivariate probability distribution functions. The GEV distribution is still the best-fitted margin for every hazard and the parameters are given in Table 4-8.

Table 4-8. Parameters and domains of estimated marginal distributions and for rain, flow and surge based on the POT_{90} trivariate extreme sample.

GEV parameters	Rain	Flow	Surge
Shape (ξ)	0.48	0.04	0.45
Scale (σ)	2.17	53.96	0.12
Location (μ)	7.07	225.51	0.65
Domain	>4.8	>160	>0.52

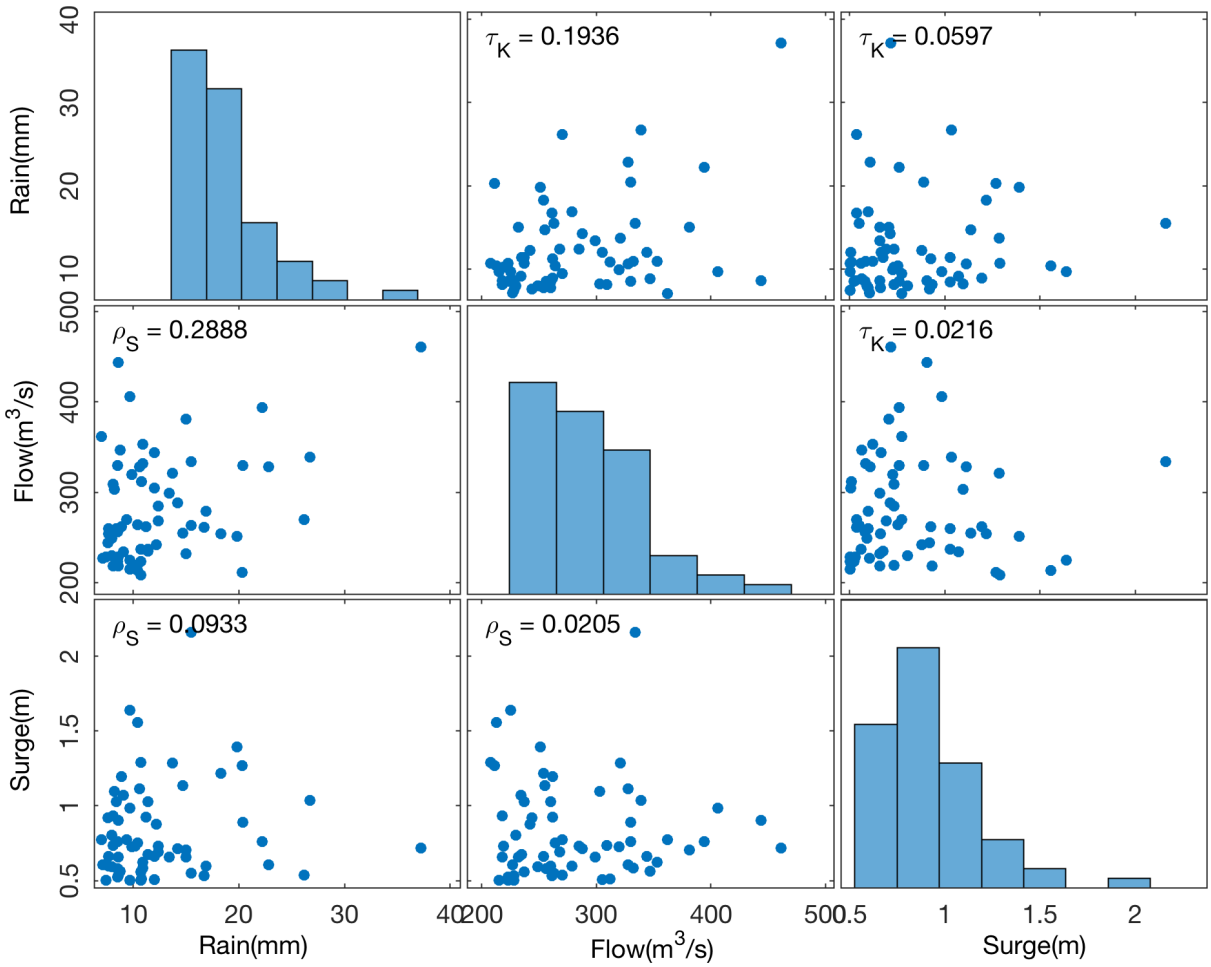

Figure 4-17. Bivariate Scatter plot of trivariate joint extreme events of daily rain, flow, and surge. Spearman's rho (ρ_S) and Kendall's tau (τ_K) are given.

While there are many families of copula functions and parameter estimation methods available for bivariate distribution, the choices of trivariate copula are very limited. Among the four types of Archimedean copulas listed in Table 3-1, the 3D Gumbel, Clayton, and Frank copula function can be estimated via maximum pseudo-likelihood method using the copula R package. Therefore, a goodness-of-fit test is performed for these 3D copulas based on the joint extreme observations. The results of best-fitted copulas with estimated parameters for trivariate and bivariate scenarios are given in Table 4-9.

Table 4-9. Best fit Copula types and estimated parameters for bivariate and trivariate distributions.

Copula	Rain & Flow	Rain & Surge	Flow & Surge	Rain & Flow & Surge
Type	AMH	Gumbel	Frank	Clayton
Parameter	0.2	1.09	0.70	0.13

With univariate margins, bivariate CDFs and trivariate copula function, a 3D joint return period function can be obtained according to Equation (3-13). A joint return period value can

be derived for any given values of rainfall, river flow and storm surge within the domain of the function. And a 2D return period distribution can also be generated if the value of one variable is provided. Figure 4-18 displays the contour lines of joint return period of rainfall and flow by given four different height of the storm surge.

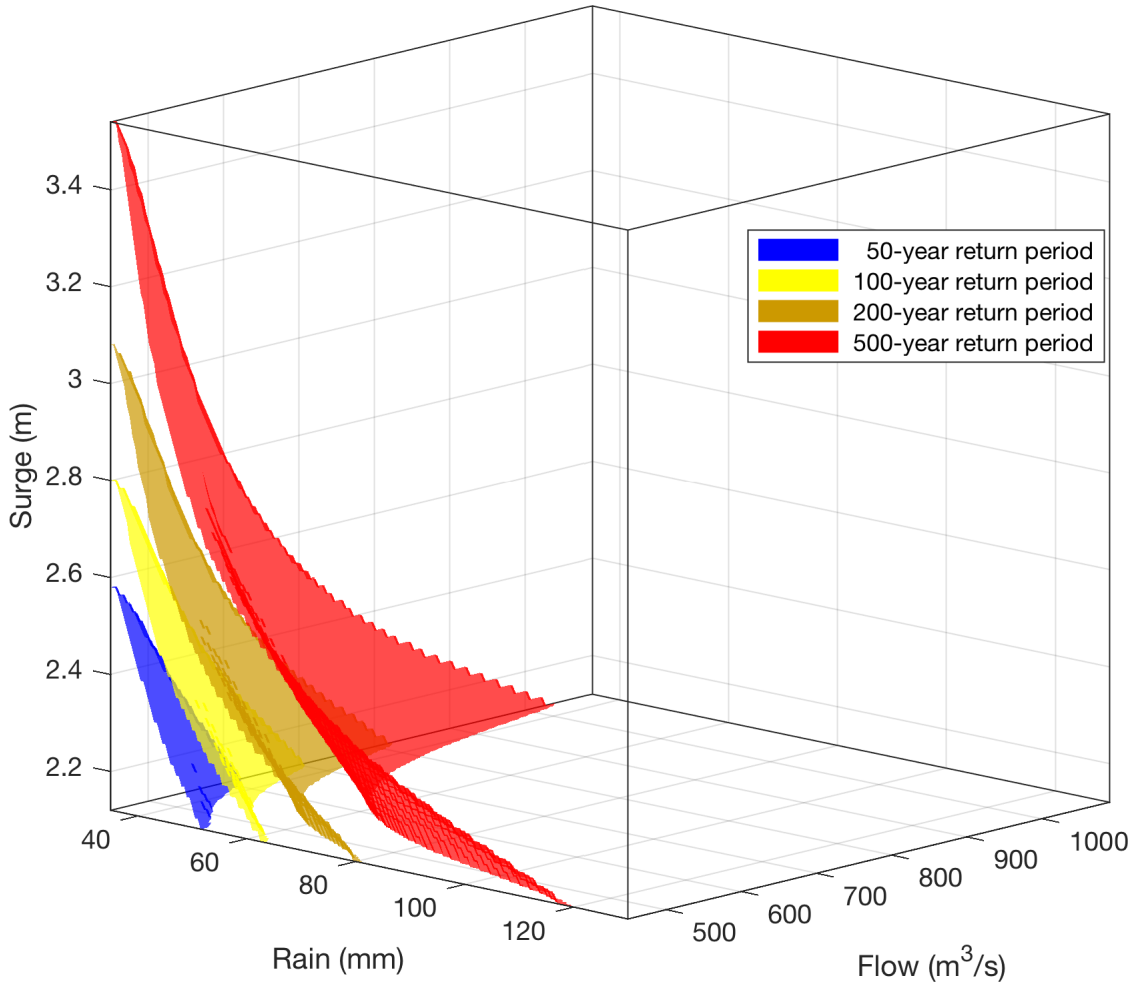

Figure 4-18. Trivariate return period surfaces of rainfall, river flow, and surge height at return level 50-year, 100-year, 200-year, and 500-year.

In the last, all the return period functions defined for the univariate, bivariate, and trivariate scenarios can be merged into a full return period function with domain covering the whole value space of rainfall, river flow and storm surge. Let X, Y, Z represent the strength value for the three hazards respectively, then the full function for their return period can be defined as below

$$T_{xyz}\begin{cases}\dfrac{Mt_{XYZ}}{\bar{F}_{XYZ}(x,y,z)}, & (x,y,z)\in\Theta_{XYZ},\\ \dfrac{Mt_{XY}}{\bar{F}_{XY}(x,y)}, & (x,y,z)\in\Theta_{XY},\\ \dfrac{Mt_{XZ}}{\bar{F}_{XZ}(x,z)}, & (x,y,z)\in\Theta_{XZ},\\ \dfrac{Mt_{YZ}}{\bar{F}_{YZ}(y,z)}, & (x,y,z)\in\Theta_{YZ},\\ \dfrac{Mt_{X}}{\bar{F}_{X}(x)}, & (x,y,z)\in\Theta_{X},\\ \dfrac{Mt_{Y}}{\bar{F}_{Y}(z)}, & (x,y,z)\in\Theta_{Y},\\ \dfrac{Mt_{Z}}{\bar{F}_{Z}(z)}, & (x,y,z)\in\Theta_{Z},\\ 0, & else.\end{cases} \tag{4-3}$$

For the above equation, Mt is the average reoccurrence time of the extreme events calculated by the number of years divided by sample size. $\bar{F}_{XYZ}(x,y,z)$ is the survival function of $F_{XYZ}(x,y,z)$ defined as

$$\begin{aligned}\bar{F}_{XYZ}(x,y,z) = 1 &- F_{XYZ}(x,+\infty,+\infty) - F_{XYZ}(+\infty,y,+\infty)\\ &- F_{XYZ}(+\infty,+\infty,z) + F_{XYZ}(x,y,+\infty)\\ &+ F_{XYZ}(x,+\infty,z) + F_{XYZ}(+\infty,y,z) + F_{XYZ}(x,y,z)\end{aligned} \tag{4-4}$$

Similarly, $\bar{F}_{XY}(x,y)$, $\bar{F}_{XZ}(x,z)$, $\bar{F}_{YZ}(y,z)$ are the survival functions of $F_{XY}(x,y)$, $F_{XZ}(x,z)$, $F_{YZ}(y,z)$, respectively. For example, $\bar{F}_{XY}(x,y) = 1 - F_{XY}(x) - F_{XY}(y) + F_{XY}(x,y)$. $\bar{F}_X(x), \bar{F}_Y(y), \bar{F}_Z(z)$ are the 1D survival functions simply denoted like $\bar{F}_X(x) = 1 - F_X(x)$. Θ_{XYZ} is the domain of variables X, Y, Z given in Table 4-8. The domains Θ_{XY}, Θ_{XZ}, Θ_{YZ} for bivariate return period functions are defined as the domain of the corresponding two variables given in Table 4-7 excluding Θ_{XYZ}. For the domains of the univariate return period, Θ_{XY}, Θ_{XZ}, Θ_{YZ} are derived from the threshold of each variable given in Table 4-6 excluding all the upper dimensional domains Θ_{XYZ}, Θ_{XY}, Θ_{XZ}, Θ_{YZ}.

For a given event with an intensity of each hazard, it is firstly located in the rightful domain signifying whether it is a single-hazard, paired-hazard or triple-hazard event. Then the corresponding return period function can be applied to calculate the reoccurrence time for that event. In reverse, if a return period value is given, a number of events can be generated based on this return level and those events can be derived from either single-hazard or multi-hazard scenarios.

4.6 Conclusions

In this chapter, multivariate statistical approaches have been applied to derive the probability distributions and the return period distributions of different combinations of the heavy rain, extreme river flow and storm surge. Dependence analysis is performed to investigate the inter-station dependence of the single hazard and the cross-hazard dependence. The inter-station dependence in extreme rainfall measured by asymptotical dependence value (χ) ranges between 0.4 and 0.99, decreasing with the horizontal distance between stations. The asymptotical dependence (χ) in extreme daily flow in the two river gauges is 0.34. In contrast, the cross-hazard dependence is much lower ($\chi = 0.12$ for rain & flow, $\chi = 0.05$ for rain & surge, $\chi = 0.07$ for flow & surge) but still statistically significant, which means the joint probability of multi-hazard variables should consider the correlations between marginal distributions.

The bivariate and trivariate joint probability distributions respectively for the concurrence of two and three hazards are fitted based on the copula theories and then used to generate joint return period distributions of different hazard combinations. The frequency of arbitrary hazard intensities in a three-dimensional variable space for rainfall, river flow and storm surge is fully quantified by synthesizing all the trivariate, bivariate, and univariate return period distributions. This method applied in London provides a quantitative and straightforward way to calculate and visualise the probability of occurrence of multiple hazards with consideration of their correlation. The joint probability and return period distributions can be further applied in disaster risk assessment to evaluate the potential loss of human life and properties in the research area.

Chapter 5. Hydrodynamic simulation of multiple hazards

This chapter is to perform flood simulations with various multi-hazard inputs and generate. hazards curves under different scenarios and for different areas in the Greater London catchment. The chapter begins with an introduction of the process of the hydrodynamic modelling, followed by the validation of HiPIMS that is thereupon applied in investigating the impact of flood defence facilities. Then, the results of single-hazard, double-hazard, and triple-hazard flood simulations are shown and discussed in three sections, respectively. At last, conclusions are made for the hydrodynamic multi-hazard simulations.

5.1 Introduction

Flood frequency analysis estimates the probabilistic occurrence of the flood magnitude measured by rainfall, discharge, or total seawater level that are normally recorded at gauge stations or simulated from climate models and hydrological models. However, none of these three measurements is the direct trigger of damage during a disaster event. Instead, the resulting inundation is the final physical process determining the impact or loss. Therefore, it is necessary to investigate the frequency of flood inundation involving the interaction of flood depth and extent and the elements at risk inside a spatial domain.

Chapter 4 has analysed the joint probability and return period distributions of the three flood-related hazards, rainfall, river flow, and storm surge in Greater London. The Monte Carlo method is applied to stochastically generate a series of multi-hazard events with frequencies quantified by the joint return period distribution. Each event is simulated by the hydrodynamic model (HiPIMS) introduced in Chapter 3, with the three hazard components used as inputs. Specifically, storm surge is added to the peak part of the astronomical tide height at Sheerness to create a periodic total water level time series. HiPIMS is capable of predicting the flood inundation process driven by the inputs of specific return periods and generating the hazard curves (frequency versus inundation) for the areas of interest.

However, the three flood-related hazards are not the only factors determining the final flood inundation pattern in Greater London and the defence systems also play a crucial role in the flood prevention and management. The hydrodynamic model should consider the function/operation of these flood defence systems and the effect of the potential defence failure on the hazard curves.

5.2 Data for HiPIMS

The fundamental data required in HiPIMS includes topographical data, river bathymetry, and land cover. Inputs of water sources such as gridded rainfall data, river flow rate, and tide height on the boundary are also essential for specific type of flood simulation and introduced in Section 4.2. Besides the data to setup and drive HiPIMS, some observed datasets such sub-hourly river gauge data, rainfall radar data, and historic flood extent maps are valuable to calibrate and validate the model.

Digital Terrain Model (DTM) representing height of bare earth surface is the background topographical data and can be acquired from Digimap OS Terrain 5 m DTM dataset (https://digimap.edina.ac.uk). LIDAR Composite Digital Surface Model (DSM) is needed to merge with the DTM to reflect buildings and other infrastructure, which may be downloaded from the UK Environment Agency (EA) (https://data.gov.uk/dataset/fba12e80-519f-4be2-806f-41be9e26ab96/lidar-composite-dsm-2m). River bathymetry data is not included in either the DTM or DSM datasets but is essential to support accurate hydrodynamic simulation in river channel. So, the surveyed river cross-section data from EA for downstream sections of River Eden is also merged into the topographical dataset to obtain the final DEM to set up HiPIMS for hydrodynamic flood prediction.

Land cover information is useful for estimating and adjusting friction and infiltration coefficients in HiPIMS. Land cover information in the study area can be subtracted from the UK Land Cover Map 2015 provided by the Centre for Ecology & Hydrology (CEH) (https://www.ceh.ac.uk/services/land-cover-map-2015). It is a parcel-based land cover map created by classifying satellite data into 21 classes (Rowland et al., 2017), available at a spatial resolution of up to 25 m for the whole UK.

The Met Office NIMROD system provides gridded radar rainfall data that is calibrated to give the best possible estimation of surface precipitation rate at 1 km spatial resolution and 5 min temporal resolution (available in CEDA archive http://badc.nerc.ac.uk). It is produced based

on radar records and processed using optimised quality control and correction procedures (Met Office, 2003).

River gauge observations and post-event investigations provide crucial data to evaluate the performance of the hydrodynamic model. Unlike the long-term daily river flow from UK National River Flow Archive, the EA flood-monitoring API provides sub-hourly and near real-time measurements of water level and flow rate for rivers across England (https://environment.data.gov.uk/flood-monitoring/doc/reference), which can be used to evaluate model performance for recent floods. Historic Flood Map is a GIS layer showing the maximum extent of all individual Recorded Flood Outlines from river, the sea and groundwater springs and shows areas of land that have previously been subject to flooding in England. Records began in 1946 when predecessor bodies to the Environment Agency started collecting detailed information about flooding incidents, although we may hold limited details about flooding incidents prior to this date (https://data.gov.uk/dataset/76292bec-7d8b-43e8-9c98-02734fd89c81/historic-flood-map).

5.3 Hydrodynamic model validation

As the inputs of the hydrodynamic model include rainfall, river flow and total water level on the coast, it is necessary to assess the model performance for simulating extreme events related to the three hazard components. Therefore, HiPIMS is firstly validated against three different events, i.e. a rainstorm flood, a flow interaction between the seawater and the river flow, and a coastal flood.

5.3.1 Rainfall-runoff process

Flow or stage observations from the gauge stations at the main watercourses are required for validating the rainfall-runoff progress in the model domain. In the Greater London catchment, most of the river gauges along the River Thames are greatly influenced by the periodic tidal level and therefore the flow/stage records do not entirely reflect the rainfall-caused peak flow. Therefore, the upper River Lee Catchment located in the north of Greater London is selected as the validating domain for rainfall-runoff progress (see Figure 5-1). The flow observations for the rainfall-runoff validation are available from the Lee gauge station located at Feildes Weir, which is in the south of the catchment and free from tidal influence.

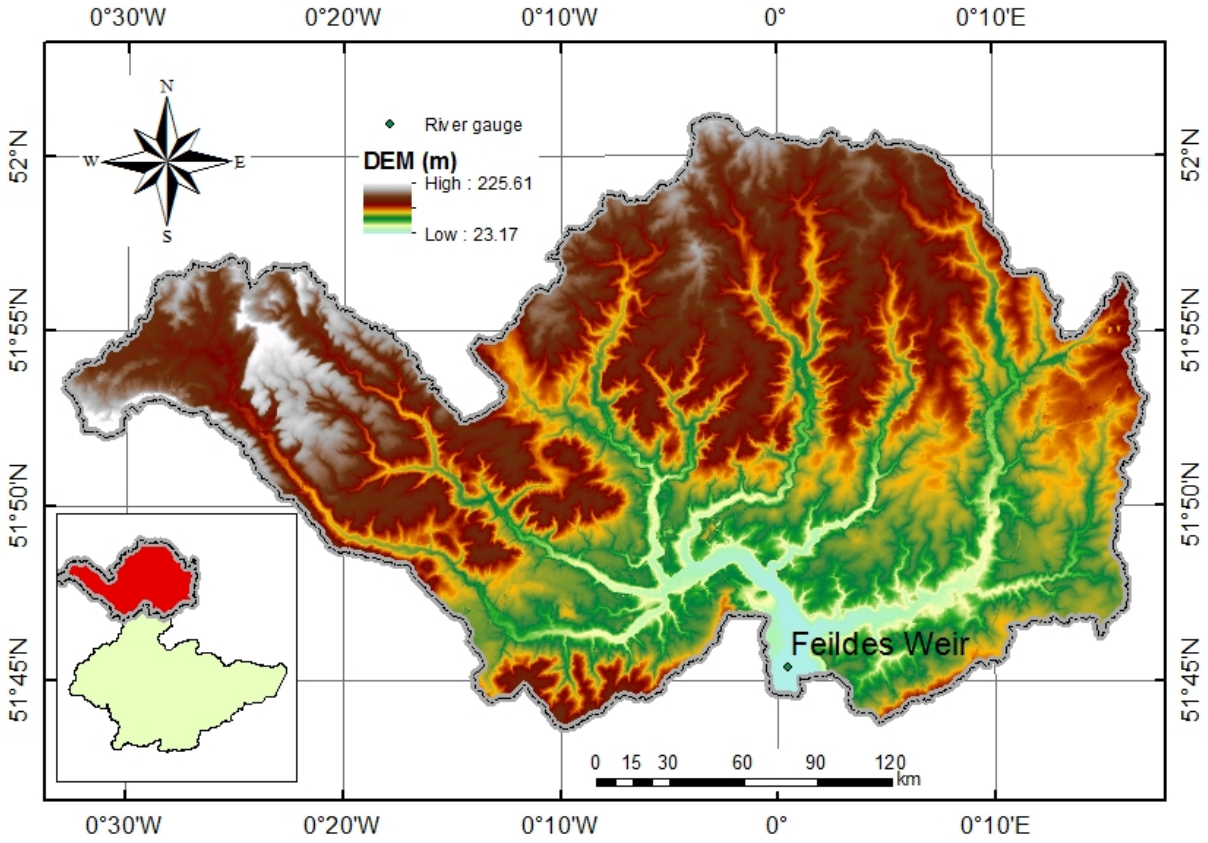

Figure 5-1. Map of the 1049 km^2 Upper Lee catchment. In the embedded map, the area in red shows the location of the Upper Lee catchment relative to Greater London in the bottom.

The river gauge at Feildes Weir records the outlet discharge of the catchment, and the quarter-hourly observations are made available by the Environment Agency (EA). The rainfall input for the hydrodynamic model is generated from the Met Office NIMROD system that provides rainfall rate at 1-km spatial and the 15-min temporal resolutions (available in CEDA archive http://badc.nerc.ac.uk). The heavy rainfall event between 5 and 8 Feb 2014 is chosen in this work. Figure 5-2 illustrates the average rainfall rate of the whole catchment for this event. The rainfall peak occurred in the morning of 6 Feb 2014, but there is some rainfall before the peak. So, a two-day simulation is pre-run to generate initial conditions with the 48-hour rainfall data before 5 Feb 2014. The output flow depths and velocities are used as the initial conditions to set up HiPIMS for the simulation of the main event starting at 0:00 on 5 Feb 2014.

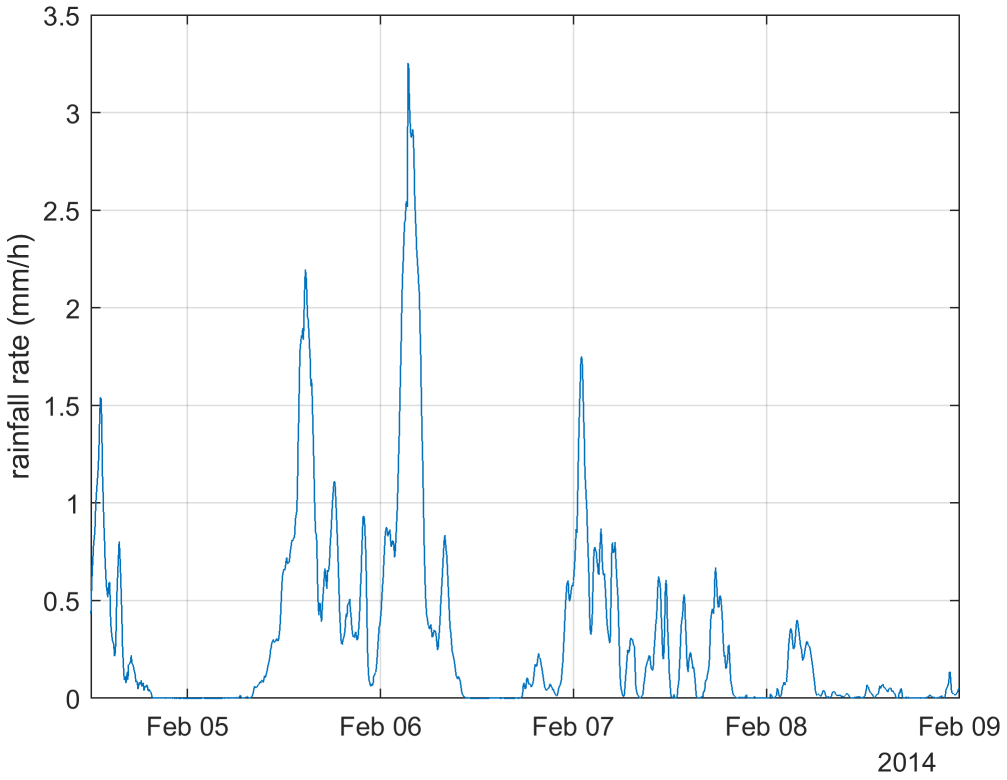

Figure 5-2. Average rainfall rate (mm/hour) at the upper Lee Catchment from 5 Feb 2014 to 8 Feb 2014.

The model is run on a uniform grid of 20 m resolution. Two sets of Manning coefficient are used in the simulations, i.e. 0.055 for rivers/channels and 0.075 for other areas, assigned according to the suggested values in hydraulics text books (e.g. Chow (1959)). As there was a medium-scale rainfall before the main event, the soil is assumed to be fully saturated and the infiltration is not considered. The simulated time-series of unit-width discharge is output based on the gridded cross-section line across River Lee at Feildes Weir. Then, the unit-width discharge is converted to total discharge by multiplying by the river width. Figure 5-3 compares simulated hydrograph with the measurements at the Feildes Weir gauge. Although the simulated peak retreated a few hours earlier than the observed peak, the simulated results generally agree well with the observations regarding the time to peak and also the shape of the discharge hydrograph. The root-mean-square-error (RMSE) of the simulated discharge with respect to observations is 12.14 m^3/s, which demonstrates that HiPIMS is able to reliably simulate fluvial floods for the upper Lee catchment and further infers that it is capable of simulating the rainfall-runoff process across the whole Greater London catchment.

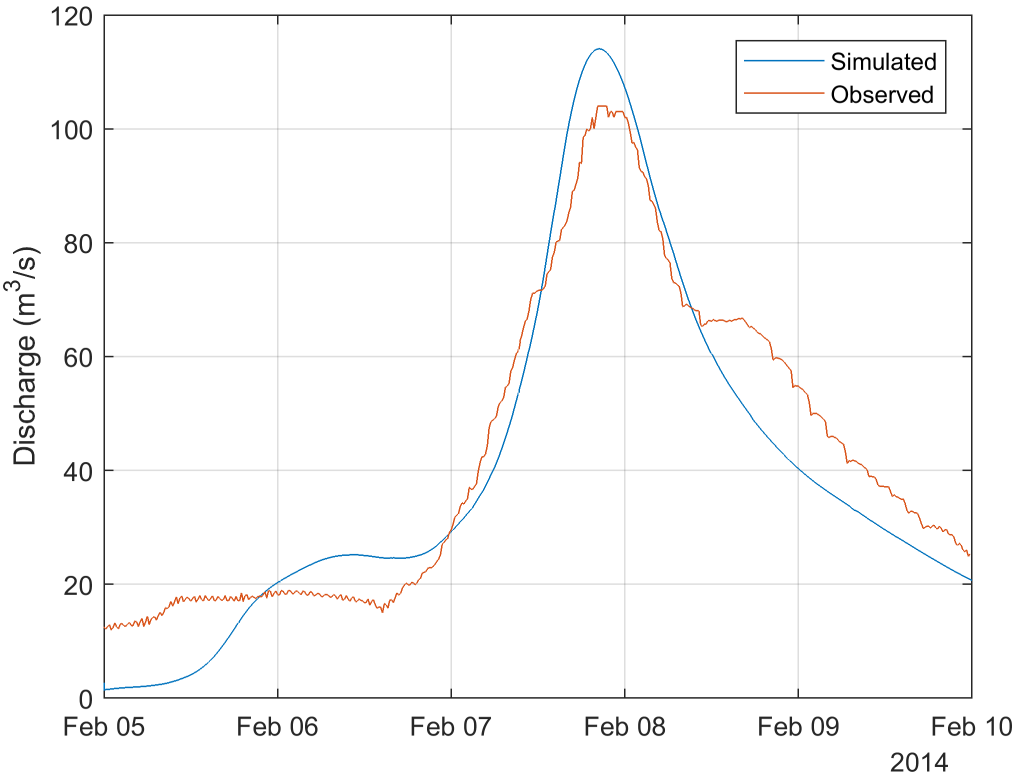

Figure 5-3. Simulated and observed discharge of Lee at Feildes Weir.

5.3.2 Tide and flow interactions

Herein, the capability of HiPIMS for flood modelling is further verified against a flood even driven by the interaction between total water level and upstream high flow. The area along the River Thames between Kingston and Southend is selected as the model domain, as shown in Figure 5-4. Water level records from 8 gauges along the River Thames are available for evaluating the simulation results.

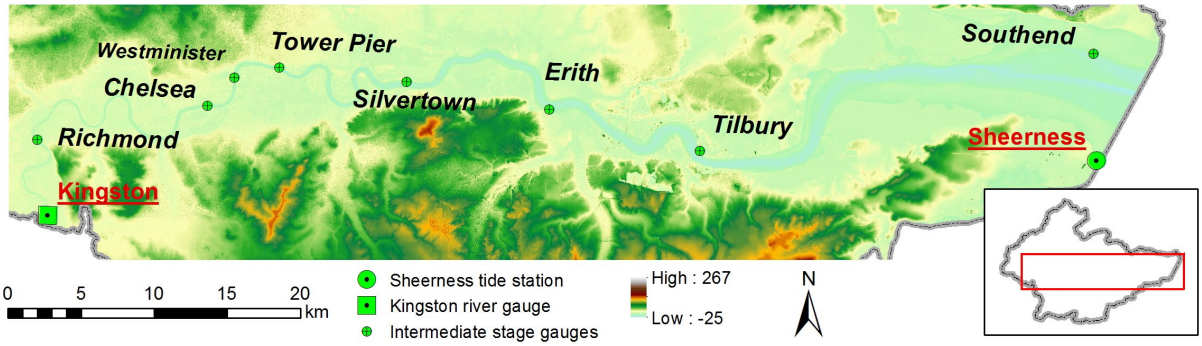

Figure 5-4. Model domain for the validation of tide and flow in the Greater London.

The DEM of the domain and the bathymetric data of the River Thames are both downloaded from Digimap and merged for use by HiPIMS. The observed sub-daily river flow at Kingston and tidal level at Sheerness from 31st March to 2nd April 2014 are used as the boundary conditions. Considering the dominant effect from the sea at this part of the river, the initial

water depth for the simulation is set based on the average sea level (0 m above Ordnance Datum), and the initial velocity was set to be zero. Different Manning coefficients (n), in the range of $0.015 \leq n \leq 0.045$, are tested for the river bed roughness.

The value of $n = 0.020$ is found to be the best for the model performance. The simulated and observed water levels at the eight river gauges are compared in Figure 5-5, where the red curves indicate the observed water level and the blue dotted lines denote the simulated values. The results show that the peak stage value and changing trend are well matched between the simulations and the observations at every station except the Erith, where there are some questionable observed values. The result in Richmond does not perform as well as the other downstream gauges, which may be attributed to the narrower river channel whose topography is over-simplified on the 20 m DEM grid. However, in general we can conclude that HiPIMS is capable of accurately predicting the interaction between flow and tide in the River Thames in the research region.

5.3.3 Coastal flooding

A flood event, which happened in 1953 at the estuary of the River Thames, is used to further test the performance of HiPIMS for coastal flood modelling. The event is known as the 1953 North Sea Flood, it was caused by a very large storm and occurred between the night of 31st January and the morning of 1st February. It was one of the most devastating natural disasters striking the east coast of London in history and made the government decide to invest in constructing new flood defence facilities, such as the Thames Barrier. The process and the damage of the flood were described by Steers (1953), and the detailed tide and surge data from their study can be used as the boundary conditions for hydrodynamic modelling. The maximum surge of 2.44m was recorded in Southend, a region where the flood embankments did not exist before the event.

The DEM data from Digimap represents the current or recent topographic status. However, a lot of flood walls, embankments and other defence facilities were built after the flood. To reflect the defence conditions during the North Sea Flood of 1953, the DEM is rectified by removing the walls and embankments in the model domain. The event is reproduced by a three-day simulation (two days before the peak surge and one day after). The simulated maximum inundation depth is illustrated in Figure 5-6 and compared with the investigated flooding extent according to the Historic Flood Map from the EA. The simulated flood extent

is consistent with the surveyed extent indicated by the red lines, confirming that HiPIMS is able to reliably predict coastal flood in the Thames Estuary.

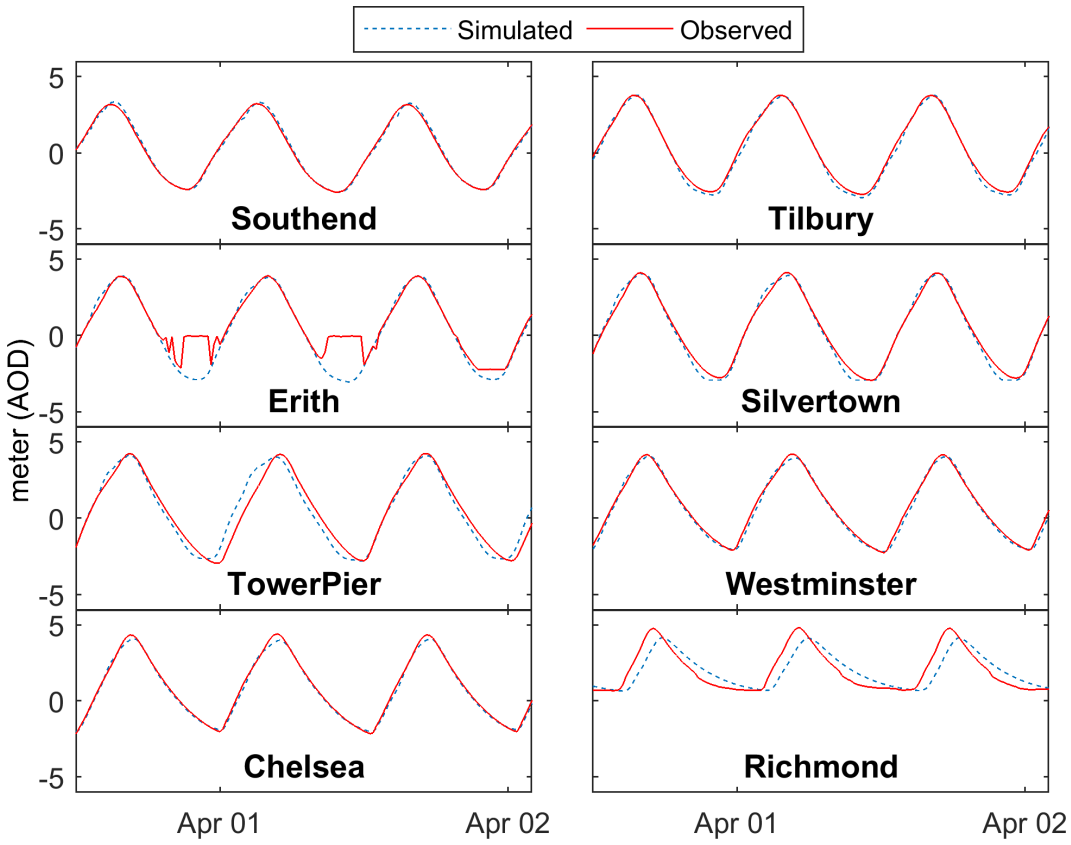

Figure 5-5. Comparison of the simulated and observed water levels at the eight gauges along the Thames River.

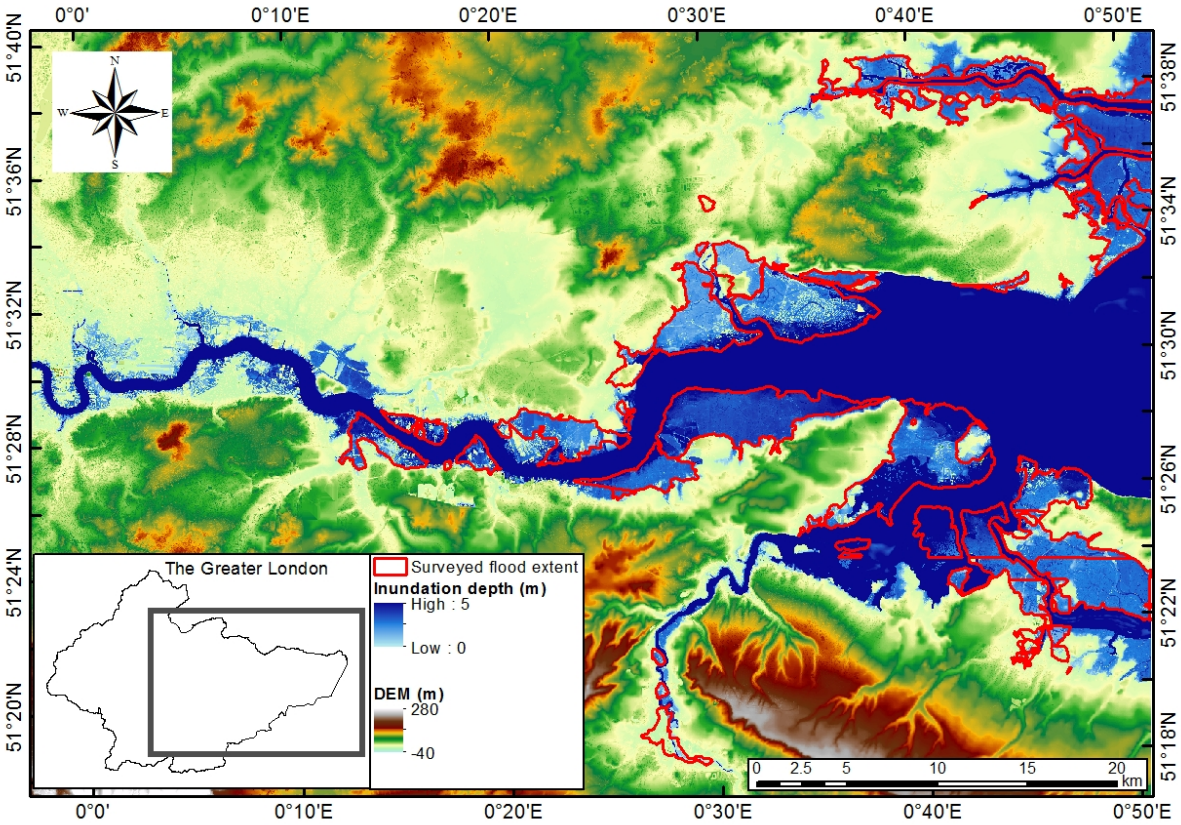

Figure 5-6. The simulation of the North Sea Flood 1953 at the Thames Estuary. The simulated inundation depth is indicated by light blue area and the red lines outline the surveyed inundated area.

5.4 Impact of flood defences along the Thames River

In England, around 8% of the land area, containing properties and agricultural land worth approximately £105 billion (NAO, 2001), is protected by flood defence facilities with a total length of 3300 km. As the most populated and well-developed region in the UK, Greater London is protected by a high-standard of flood defence walls, dykes and embankments along the River Thames. Moreover, the Thames Barrier, which is designed to protect the city centre of London from flooding caused by storm surges from the North Sea (see the red lines in Figure 5-7) was built in the 1980s. However, according to the assessment of the EA, not all the dykes and embankments are currently in functional status. Instead, some parts of the flood defences are appraised as “poor” or “very poor” as indicated by the blue lines in Figure 5-7. The poor facilities are found even in the central region of London, such as Chelsea, and are very likely to lose efficacy when facing extreme events.

Significant damages due to defence failures have been reported across England during the 1998 Easter Floods, 2000 Autumn Floods, and 2015 Storm Desmond Floods. For the metropolitan area of the Greater London, it is essential to evaluate the effectiveness of the

flood defence systems and consider the impact of potential failure scenarios. As the dykes and embankments along the River Thames were designed to defend from fluvial and coastal floods, the historical records of river flow and storm surge are selected as the boundary conditions of the hydrodynamic model to test the role of defence systems. The historical maximum daily average flow (800 m^3/s) at Kingston and the historical highest storm surge (2.94m) at Sheerness are combined as the extreme multi-hazard scenario corresponding to the approximate 2000-year joint return period, 213-year return period for river flow, and 117-year return period for the storm surge.

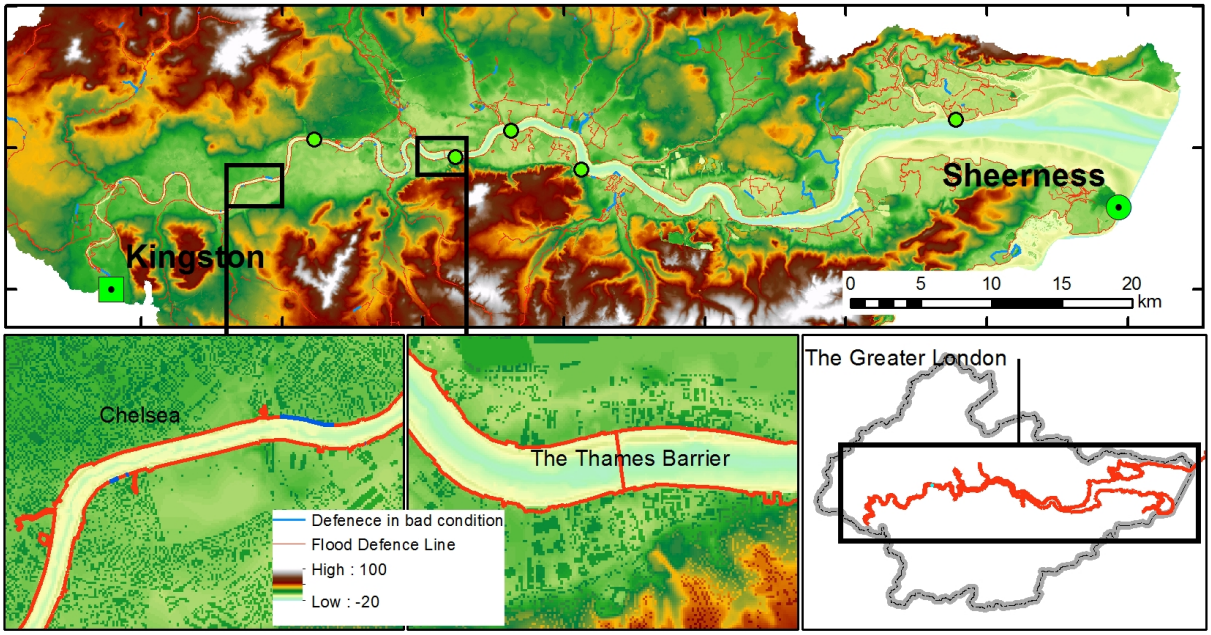

Figure 5-7. Flood defences along the River Thames in Greater London. The green circles show the assumed defence failure locations.

Four failure scenarios of the flood defences along the Thames River are designed: 1) no breach at any point and the Thames Barrier is closed (active to protect); 2) no breach at any point but the Thames Barrier is open (failed to protect); 3) defence failure at five assumed positions before the flooding arrives; 4) defence failure at the five places during the flooding. The locations of the defence failures are shown in Figure 5-7 with green circle points, and the detailed information is given by Table 5-1.

The designed joint extreme events of the river flow and total water level is simulated for the four defence scenarios. The results are illustrated in Figure 5-8 for the first and the second scenarios. Five regions noted from A to E are specified to evaluate the impact of the different status of the Thames Barrier with no defence failure in other locations. Region A is normally influenced by fluvial flood, and regions B and C are in the city centre. The Thames barrier is

located between regions C and D. Region E is exposed to coastal flooding and was seriously damaged during the 1953 North Sea Flood but now is well protected by the sea walls.

Table 5-1. The locations of the assumed defence failure points along the River Thames.

Location	Type	Defence level (mAOD)	Defence length (m)
Southend	wall	6.86	1469.92
Erith	wall	7.01	357.11
Woolwich	wall	7.19	118.24
Thamesmead	embankment	7.18	1873.42
London Bridge	wall	5.48	93.13

Figure 5-8 (a) shows that even the 2000-year joint extreme event cannot threaten the city centre of London with all the current flood defences being functional. If the Thames barrier is opened but all the other defences are active (Figure 5-8 (b)), the city centre, region C, can be flooded as shown in the bottom panel. The closure of the barrier also affects region A, in which a larger inundated area is predicted in the simulation without the Thames Barrier. However, not all the regions benefit from the existence of the Thame Barrier. For example, the northwest area of region D is predicted to be flooded when the barrier is closed but safe when the barrier is open. It is because tidal water is accumulated at the downstream side of the barrier by stopping the peak surge.

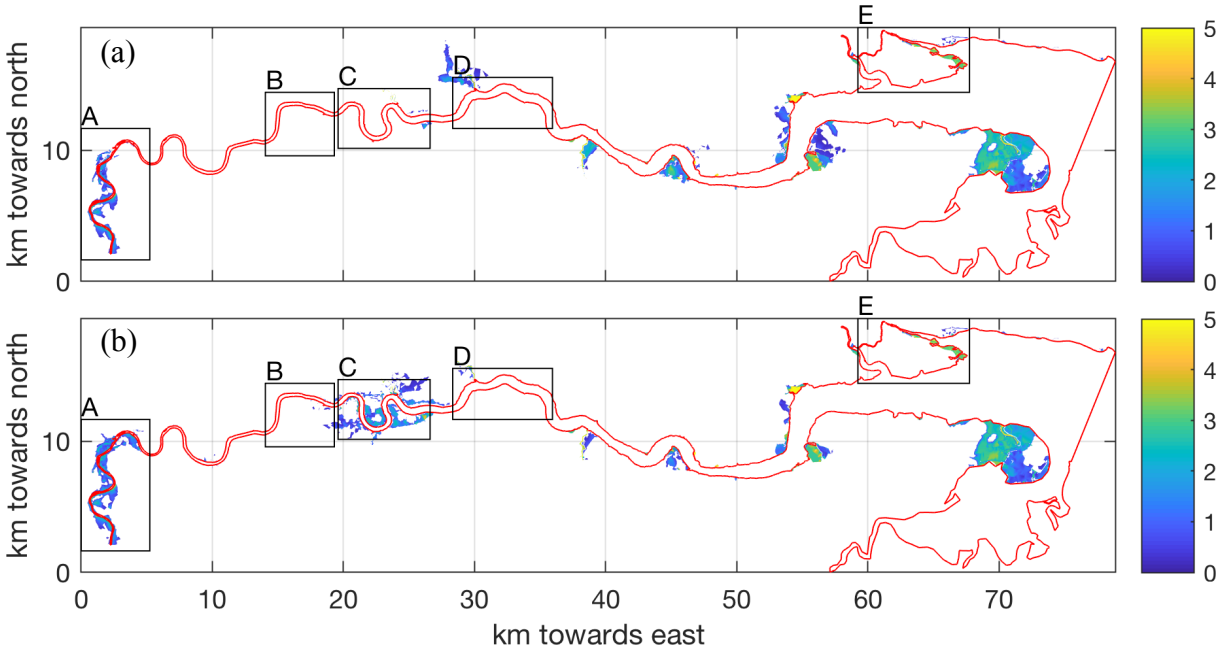

Figure 5-8. Maximum inundation extents predicted for a 24 hour joint event with highest recorded flow(800 m^3/s) and surge(2.94m) when Thames barrier is closed (a) and open (b).

Further flood simulations are run for different failure scenarios to investigate the resulting potential inundations. The failure is more likely to happen under high hydraulic loading during a flood event. Figure 5-9 shows the results of defence failure before flood arrival (a) or after the water level reaches 4 m AOD (b) in the simulation of the highest recorded flow and surge with the open Thames Barrier. Some differences of the inundated area can be observed in region B between the two failure conditions, which suggests that the assumption of pre-occurred defence failure could lead to a slight overestimation of the flood. In comparison with the result in Figure 5-8 (b), region C is less flooded even with the defence failure, which can be attributed to the defence failures at its adjacent regions B and D that effectively become flood diversion areas.

In general, Greater London, apart from the upstream region A, is very safe under the current flood protection schemes and the Thames Barrier plays a critical role in protecting the city centre of London from storm surge. However, a defence failure can lead to serious flooding along the River Thames and the seaside area. Some regions heavily rely on the defence facilities, e.g. region C, which can be entirely flooded if the sea wall is damaged. The central and downstream parts are more influenced by the coastal surge while the upstream area is under the threat of both fluvial and the coastal floods. The failing time of the flood defences has a small impact on the results in the flood inundation in the city centre.

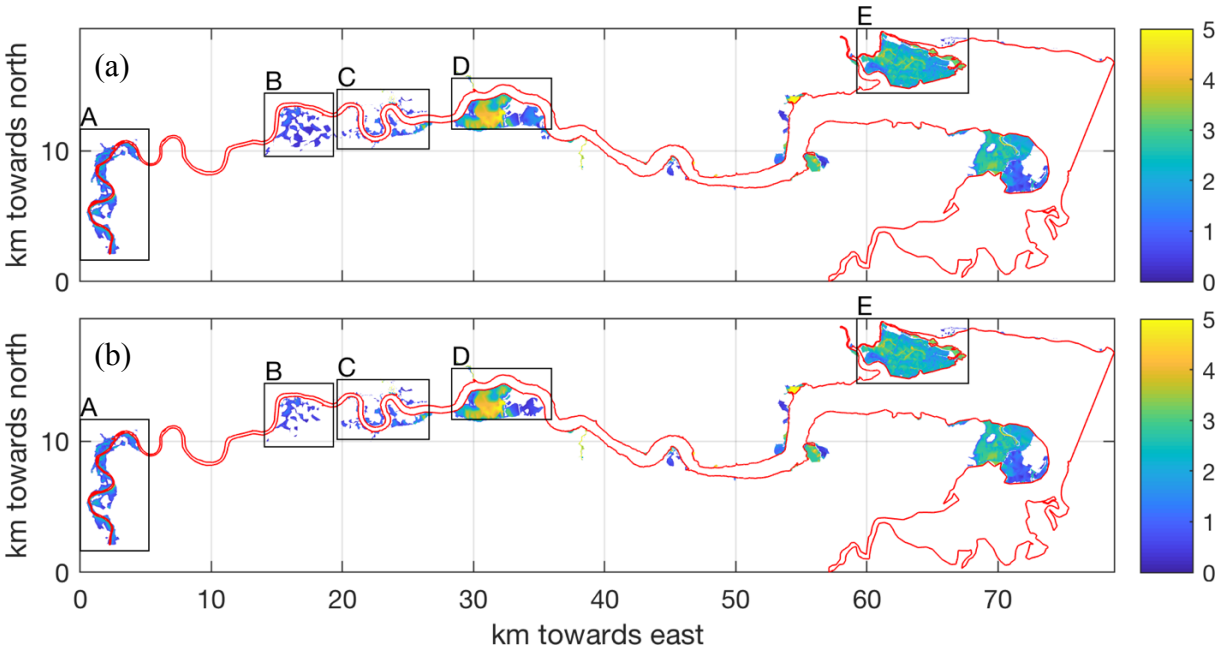

Figure 5-9. Maximum inundation extents for a 24 hour joint event with highest recorded flow (800 m3/s) and surge (2.94m) for (a) defence failure in advance and (b) during the flood event.

5.5 Single-hazard simulations

This section is to simulate the flooding driven by a single water source, either extreme rainfall, river flow or storm surge, with assumed defence failure in bad condition sections. Failures are assumed to happen before flooding, and the Thames Barrier is set as not active during the events. HiPIMS is pre-run for 72 hours with no rainfall. The resulting average river flow of 75 m^3/s at Kingston, and total seawater level (15-min data with peaks and valleys) at Sheerness are used as initial conditions over the model domain to initiate the simulations.

Hydrodynamic simulations are performed for single hazards of various intensities corresponding to different return periods. A peak inundation map is generated for each simulation of one hazard with a specific load. Then, the single-hazard curves are generated by connecting inundated areas with the probability of occurrence (return period).

According to the single-hazard return period functions fitted in section 4.5.1, the return periods of hazards at any specific intensity can be obtained and shown in Table 5-2. A series of simulations are conducted for each hazard of different return periods including the listed ones ranging from 10 years to 500 years. The simulation results are then used to estimate the hazard curves. Based on the assumption that the higher intensity (longer return period) of one hazard can result in more severe flooding compared with the lower intensity of the same hazard, the linear interpolation method is used to generate hazard-inundation curves with the discrete hazard intensities and the simulated inundation.

Table 5-2. The intensity of single hazard rainfall, flow, and surge at various return periods.

Hazard	Return period (year)						
	10	20	50	100	150	200	500
Rainfall (mm)	41.67	47.7	60.53	76.46	89.59	101.19	156.17
Flow (m^3/s)	470.61	523.29	602.38	682.46	740.90	788.82	987.23
Surge (m)	2.24	2.39	2.64	2.88	3.04	3.17	3.68

5.5.1 Hazard curves of extreme rainfall

The rainfall rate is used to drive HiPIMS to create potential floods. The daily accumulative rainfall height is converted to rainfall rate according to the duration of rain. The temporal distribution of rainfall in one day may vary, even with the same daily accumulation. To reduce the number of simulations as required for one given daily rainfall, the rainfall rate is

simplified as homogeneous during the rain process and the rain is assumed to be happening during the first-half of every 24-hour simulation.

The results of rainfall-runoff simulation for 50, 100, 200, and 500 years return period are shown in Figure 5-10. Any cell with no less than 0.3m peak water depth is defined as the inundated cell and portrayed as blue. The general inundation maps illustrate a clear increasing trend of inundation areas from lower to higher rainfall. The impacted regions are mostly located in the lower land close to the river as identified in the topographic map in Figure 1-1. London city centre, situated in the middle-left of the map, is generally safe under the one in 50-year or 100-year rainfall, but starts to be flooded by the 200-year rainfall, and is seriously flooded by the extreme rainfall of 500-year return period.

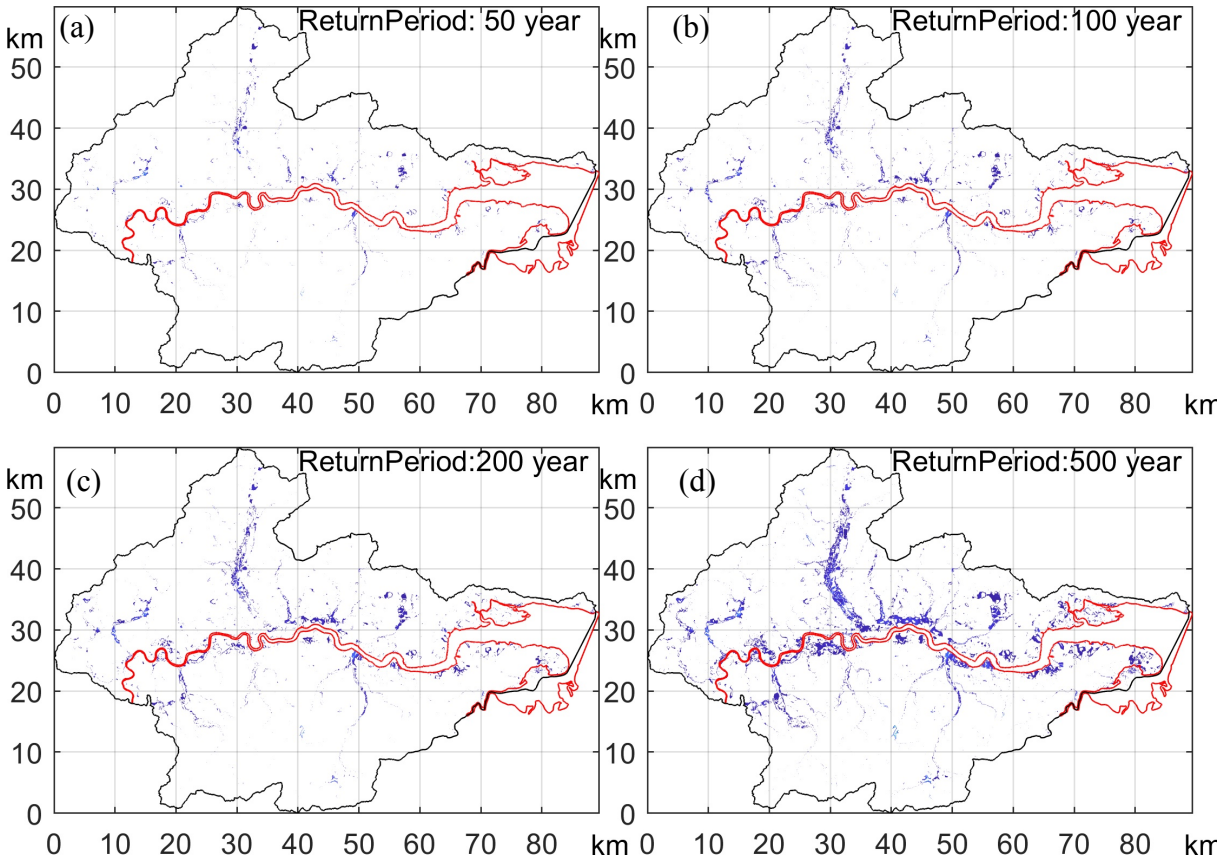

Figure 5-10. Inundation map of extreme rainfall at four return periods. The black line is the boundary of the model domain, and the red line is the river bank or coast line.

The hazard-inundation curves are portrayed in Figure 5-11 to quantitatively show the continuous relationship between the severity of flooding and the rainfall loads. The X-axis is the daily rainfall amount, and the Y-axis is the total flooded area and flooded water volume inside the model domain. The total flooded area is the sum of the area of all the inundated cells, and the total flooded water volume is calculated by adding up the peak water volume in each inundated cell. The curve of the total inundated water volume is almost linear while the

curve of the total flooded area is slightly convex, signifying that the latter has a lower increasing rate and is less sensitive to the changing of rainfall amount.

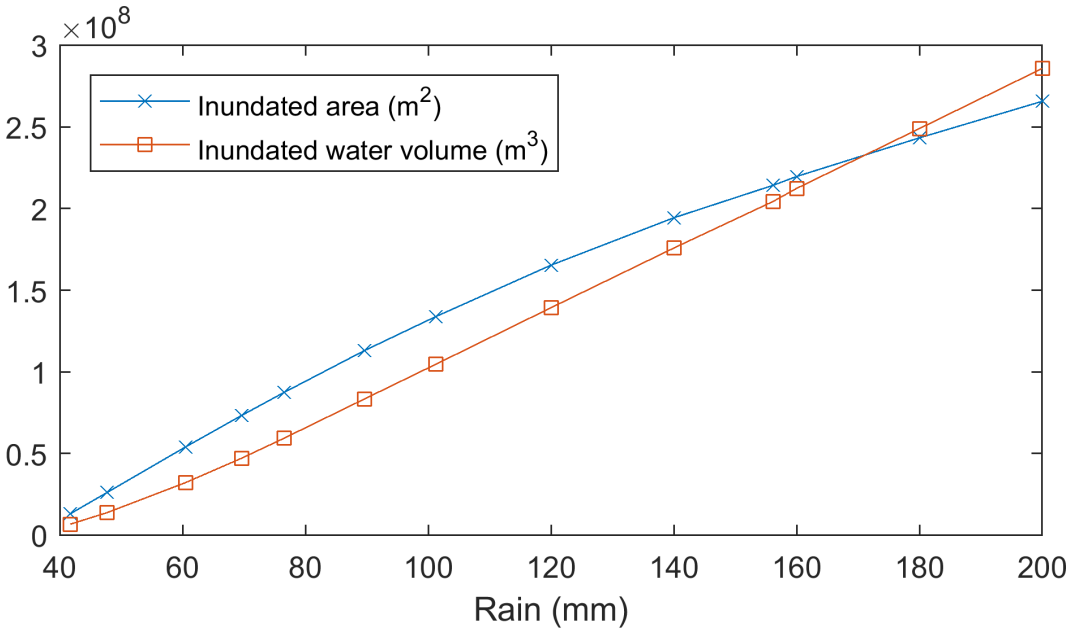

Figure 5-11. The total flooded area and the total flooded water volume at Greater London due to extreme rainfall.

To give a more detailed analysis of the inundated area, the inundation depth is classified into four grades according to the inundation depth: 0.3~0.5 m, 0.5~1.0 m, 1.0~2.0 m, and larger than 2m. The curves of the inundated area at the four grades against the rainfall amount are shown in Figure 5-12. It shows a increasing trend of the inundated area for each depth grade. The curve of the highest grade (deeper than 2 m) is concave, and its changing rate is rising with the increase of rainfall, suggesting more sensitivity to extreme rainfall.

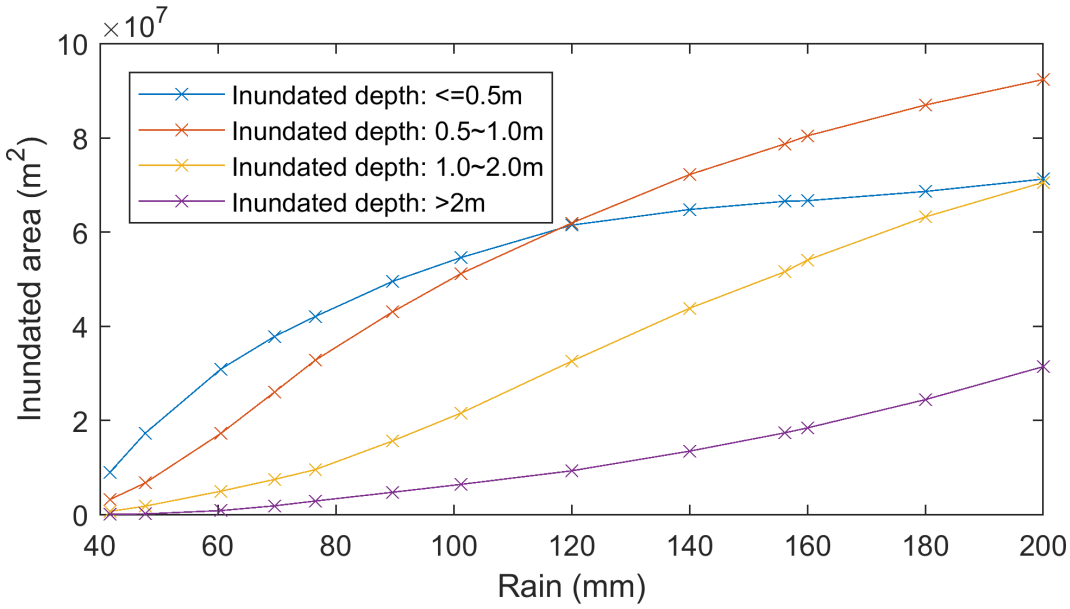

Figure 5-12. The inundated area with different depth grade due to extreme rainfall.

With the hazard-inundation curve defining the quantitative relationship between the flooding and the hazard intensity in the model domain, the hazard-frequency curves are derived from the single-hazard return period function. Figure 5-13 illustrates the relationship between the total inundated area and its estimated frequency of occurrence using the return period and the annual frequency of exceedance, respectively. The blue line shows the increasing trend of the flooding area with the return period while the red line shows the negative relationship between the flooding area and the annual frequency of exceedance. This type of hazard-frequency curve can be generated for any region defined inside the model domain. They are necessary for quantitative assessment of single-hazard risk.

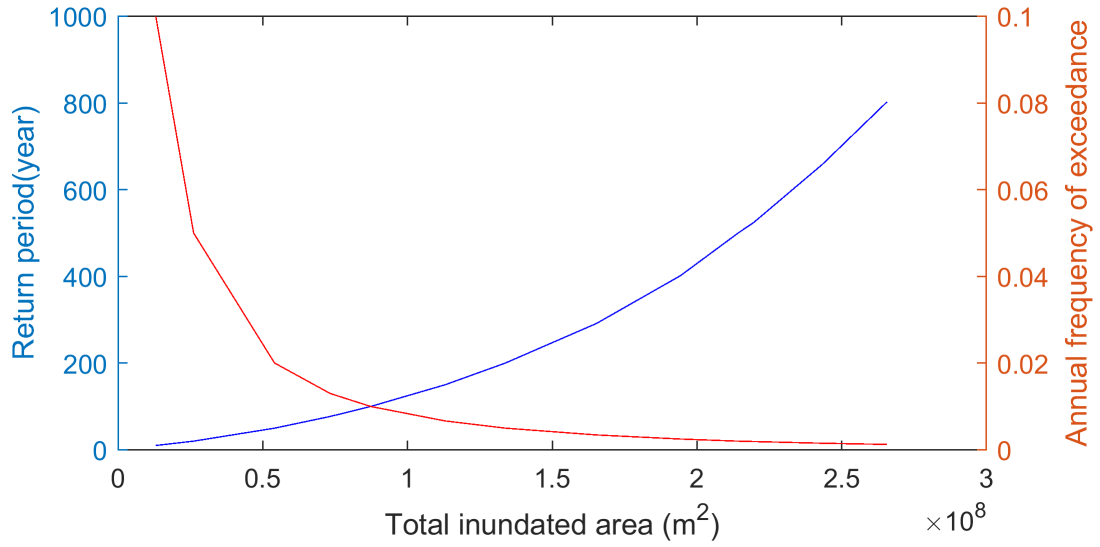

Figure 5-13. Hazard-frequency curve of the overall inundated area at Greater London due to extreme rainfall.

5.5.2 Hazard curve of extreme flow

The river flow is added to HiPIMS as boundary conditions of water velocity in Kingston, which is the entrance of the River Thames to the model domain. The velocity at the boundary cells is equal to the cross-sectional area divided by the discharge. During the flood simulation, the discharge at the boundary is simplified as steady throughout the event. The east boundary of the model domain uses the normal astronomical tide height as boundary conditions.

A series of 24-hour extreme flows as listed in Table 5-2 are used. The results of fluvial simulations corresponding to 50, 100, 200, and 500 years return periods are shown in Figure 5-14 as maximum inundation maps. Areas with flood depth equal to or over 0.3m are marked in blue in the maps. Unlike the pluvial results in Figure 5-10, the influenced region is limited to the upstream area of the Thames River. The inundated area increases when the intensity of river flow rises from one-in-50 years to one-in-500 years. But the flooding does not affect

areas further than 10 km from the inlet point of the Thames River. These inundation maps suggest that for up to one-in-500 years' extreme flow, the city centre of London is unlikely to be threatened by a one-day event with the current defence facilities and the predefined failure scenarios.

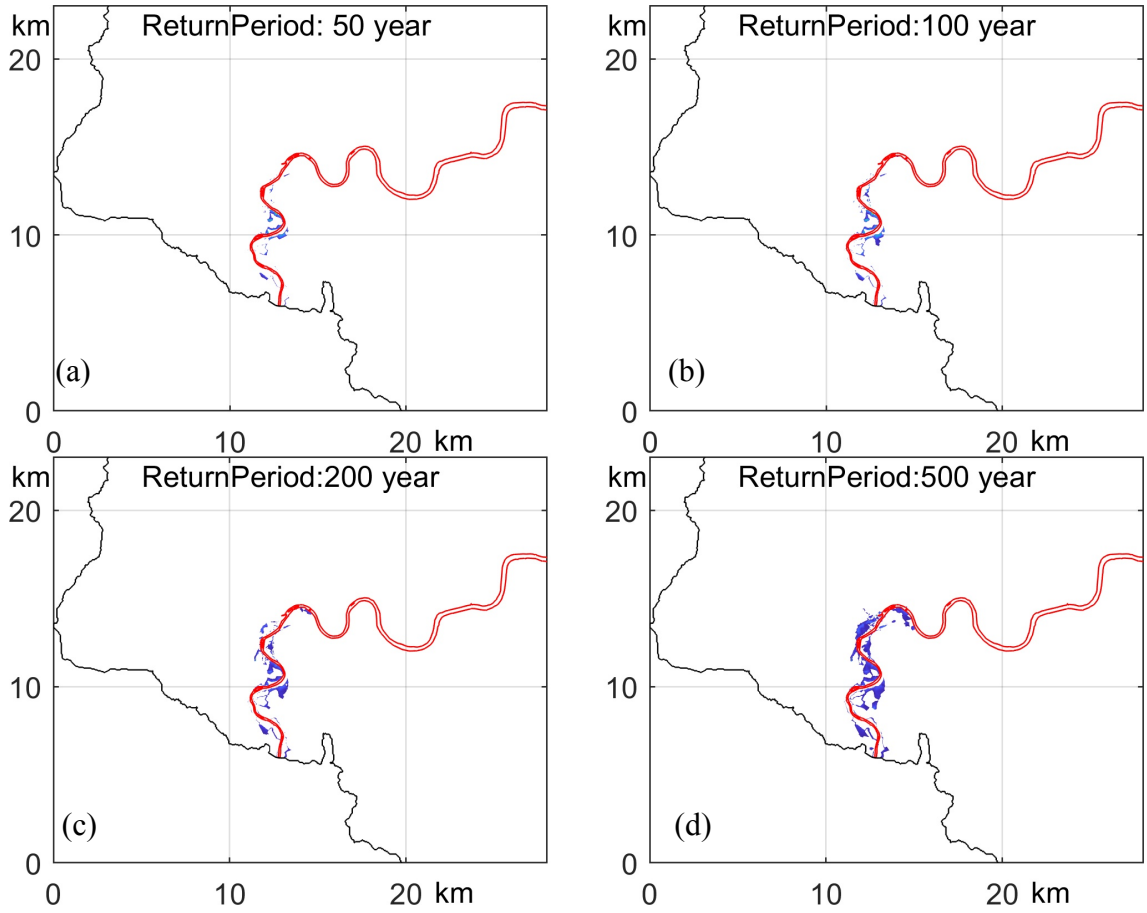

Figure 5-14. Inundation map of extreme river flow at four return periods. The black line is the boundary of the model domain.

To quantitatively show the relationship between the intensity of flow and the resulting flooding, two curves are depicted in Figure 5-15 respectively for the total inundated area and the total inundated water volume in the model domain. The blue curve (inundation area) is almost linear while the red curve (water volume) has a slightly higher increasing rate when the flow rate goes beyond 800 m^3/s.

We use the inundation grades defined in the previous section to show the hazard-inundation curves for four grades in Figure 5-16. The number of inundated cells with peak water between 0.5 m and 1m is highest among all the depth grades when the flow rate is lower than 1100 m^3/s. With a higher discharge, the cells become most likely flooded on the third inundation grade (1 m to 2 m).

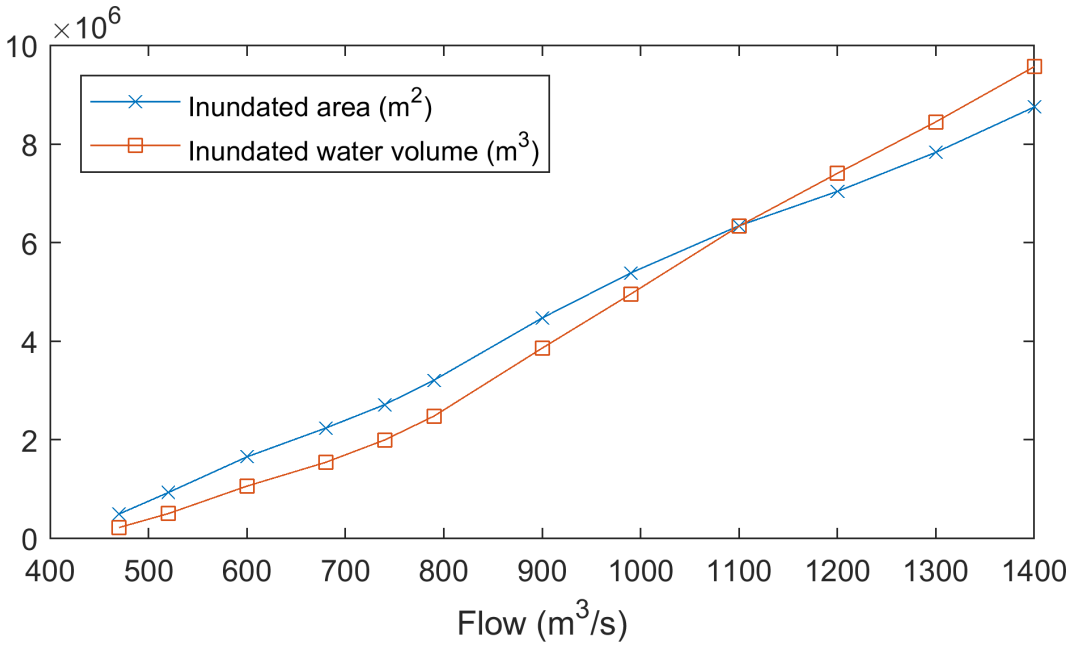

Figure 5-15. The total flooded area and the total flooded water volume in Greater London due to extreme flow.

By connecting the return period function of extreme flow with the simulated inundation results, the hazard curves showing the relation between inundated area and frequency are illustrated in Figure 5-17. The total inundated area in Greater London catchment due to Kingston extreme flow is probabilistically estimated with return period and annual frequency of exceedance. Similarly, this type of hazard curve can be generated for any smaller region of interest inside the model domain.

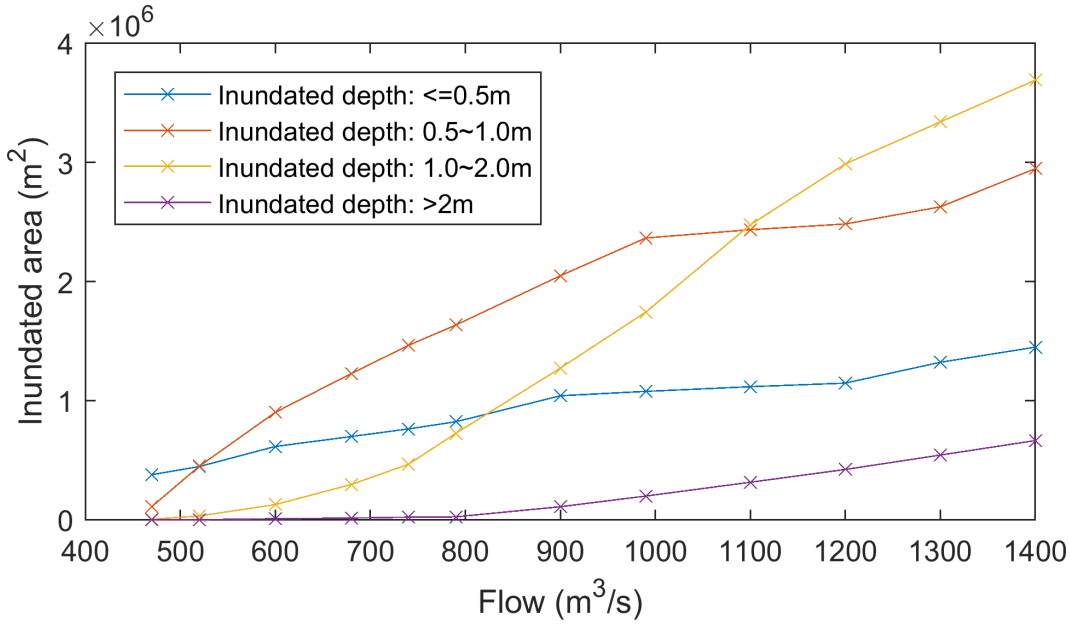

Figure 5-16. The inundated area with different depth grades due to extreme flow.

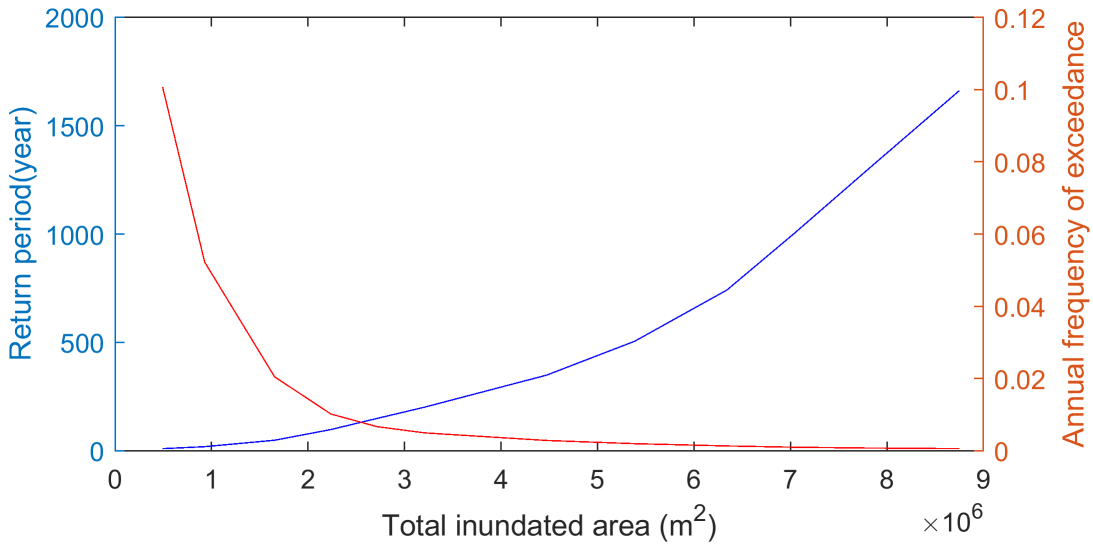

Figure 5-17. Hazard curve of the overall inundated area in Greater London due to extreme river flow.

5.5.3 Hazard curve of extreme surge

The storm surge from the North Sea is another main threat to the research area. The height of storm surge is added to the peak part of the normal astronomical tide height at Sheerness. The time series of surface water elevation is used to drive HiPIMS in the east boundary cells of the model domain. The model simulates a series of 24-hour events with surge height ranging from 1.6m to 3.8m under the assumed flood defence scenarios.

Figure 5-18 shows the results of flood simulations driven by storm surge at 50, 100, 200, and 500 years return periods, respectively. The inundated area is also defined by maximum water depth being no less than 0.3m and plotted with varying colours representing the inundation depth on the maps. Generally, the inundation extents are not distinguished for the different levels of the surge. This may be because the assumed defence failure is the main contributor to flooding in the riverine areas. When zooming in at the city centre area, the four localised maps indicate a clear increasing trend of both flood area and inundated depth accompanied with the rise of the surge height. Even for the one-in-50-year surge, serious flooding can be possible in the city centre of London if the hypothesised defence failure occurs.

The curves in Figure 5-19 quantitatively show the relationship between the severity of flooding and the height of surge at the whole London catchment. Unlike the more or less linear curves in Figure 5-11 and Figure 5-15, the surge-inundation curves have concave shapes herein, indicating that the inundation rises sharply when the surge height increases, especially for the total flood volume.

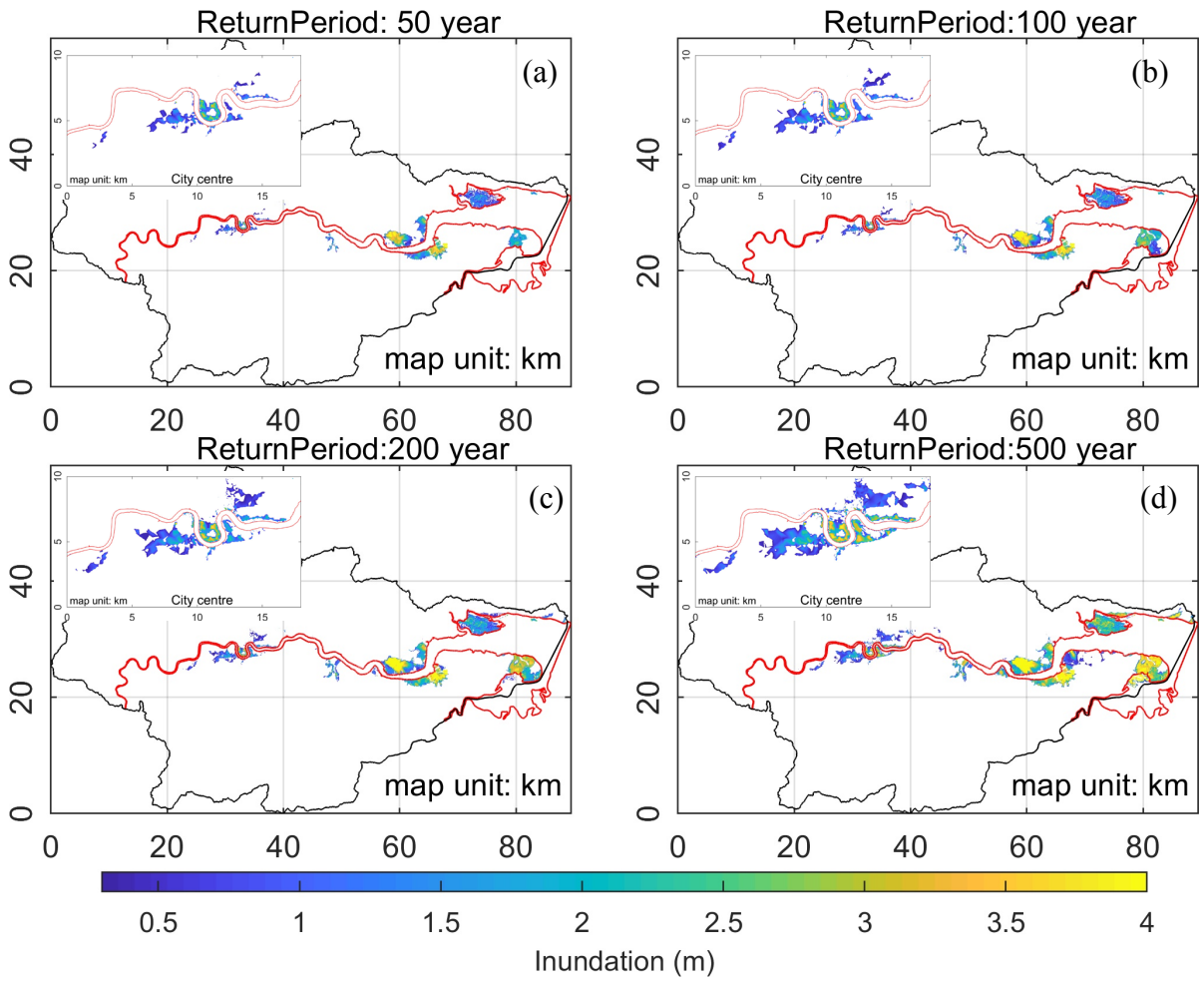

Figure 5-18. Inundation map of extreme surge at four return periods. The black line is the boundary of the model domain, and the red line is the river banks or coast line.

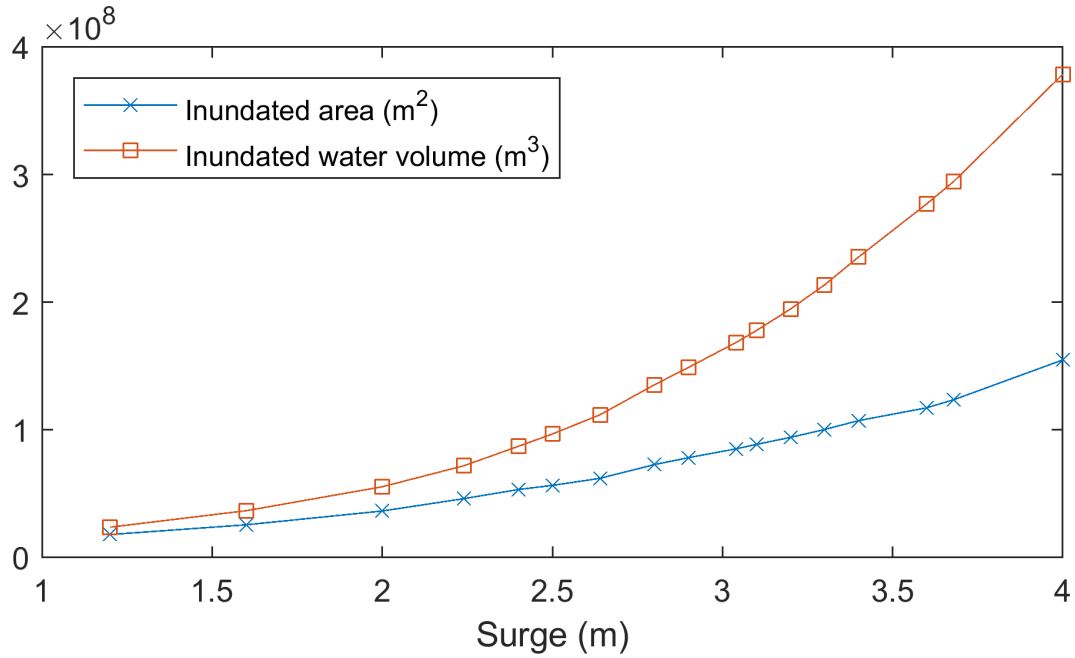

Figure 5-19. The total flooded area and the total flooded water volume at Greater London due to extreme surge.

Figure 5-20 illustrates the curve of the flooded area against the surge height for different levels of inundation. The hazard curves of the first and the second grades are relatively flat while the areas of the most severe classes move up sharply when the surge is getting higher. The curve of the third class fluctuates, which can be attributed to the transformation of the flooding region between grade 3 and 4 with the increase of the surge.

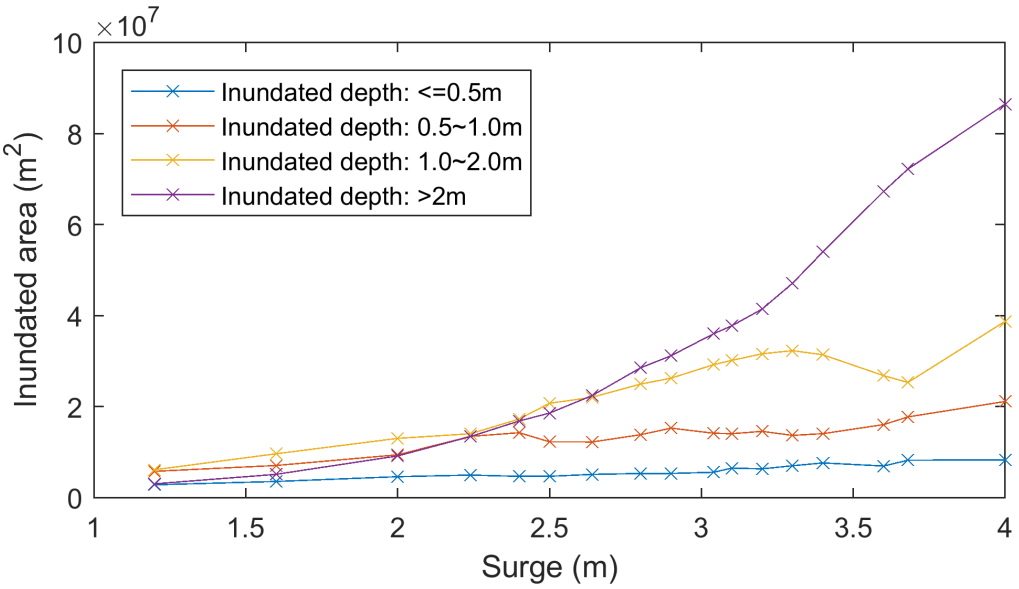

Figure 5-20. The inundated area with different depth grade due to extreme surge.

Figure 5-21 shows the hazard curves of the total flooded area due to the extreme surge in the London catchment. These curves are generated by connecting the return period distribution of extreme surge as shown in Figure 4-13 with the surge-inundation curve as shown in Figure 5-19. The curve for the annual frequency of exceedance is calculated according to the return period and estimates the probabilistic inundated area in the whole model domain. The similar hazard curves can also be generated for any defined area inside the domain.

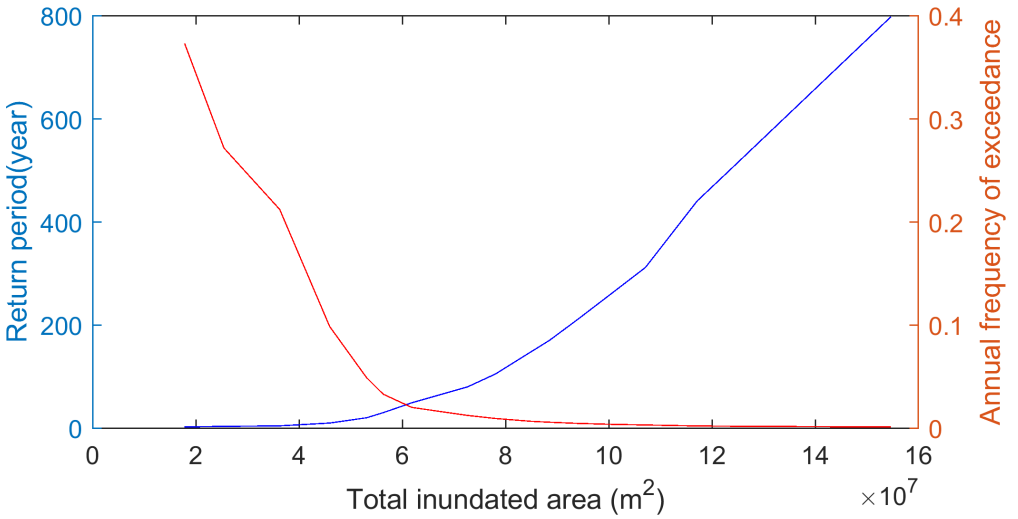

Figure 5-21. Hazard curves of the overall inundated area of the Greater London catchment due to extreme surge.

5.5.4 Comparison between the single hazard curves

The single hazard curves of inundated area and water volume in the Greater London catchment are compared respectively in Figure 5-22 and Figure 5-23 for the three hazard components. The storm surge can result in the most extensive flooded area, and the rainfall is likely to cause the biggest amount of flood volume when the three hazards are in the same return period of 100 years. For the current case study, the extreme river flow is relatively less dangerous than the other two hazards. Both figures suggest that rainfall and surge are the two main threats to the whole research area.

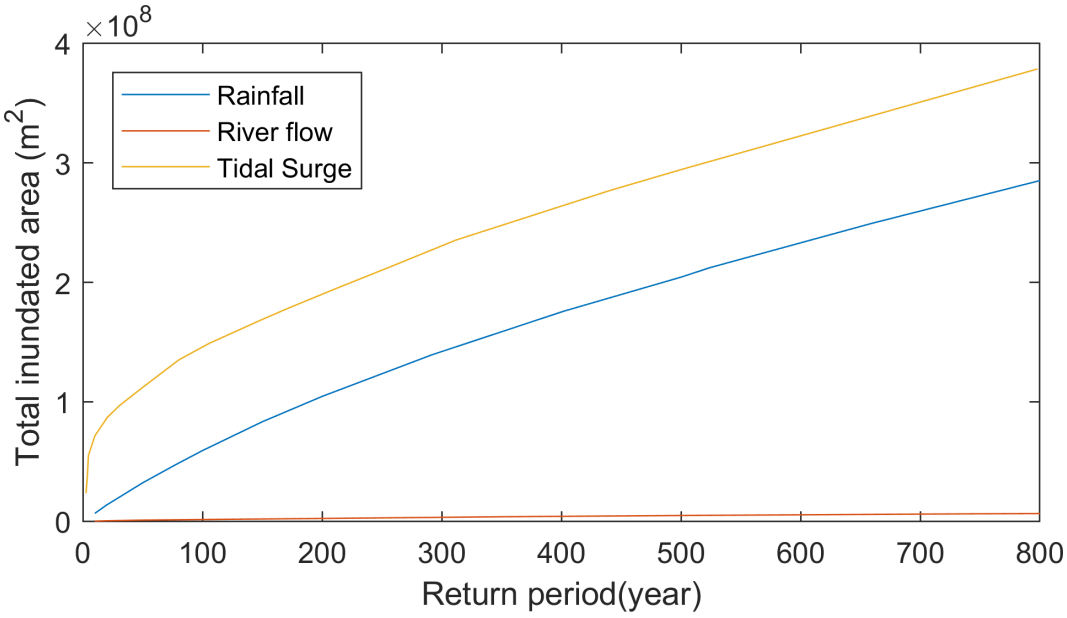

Figure 5-22. Comparing the inundated area frequency curves for the three single hazards.

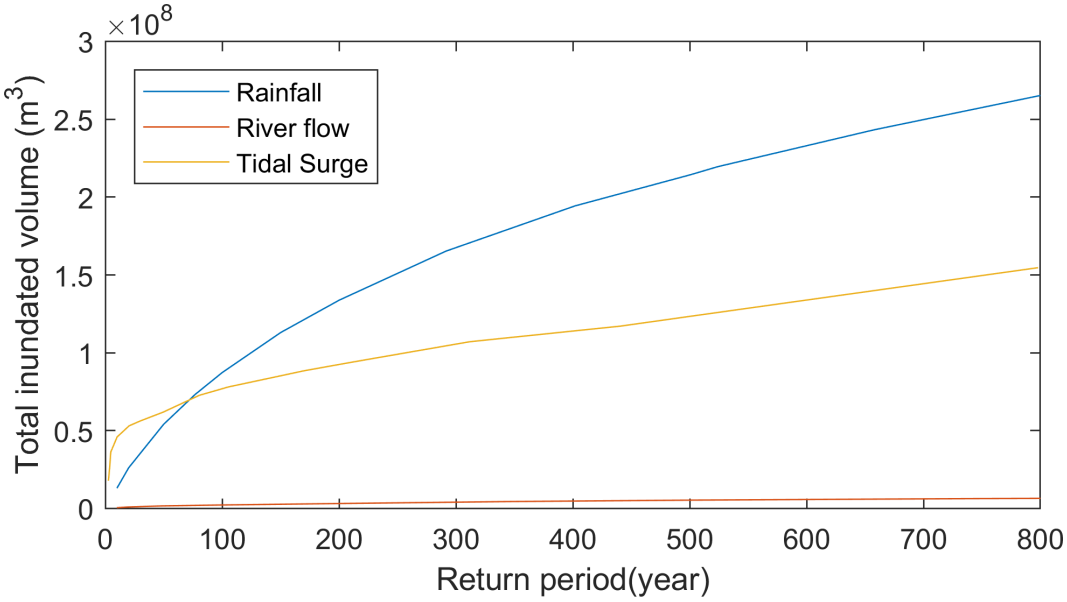

Figure 5-23. Comparing the inundated water volume frequency curves for the three single hazards.

However, Figure 5-22 and Figure 5-23 provide only the general assessment for the whole catchment but do not reflect the effect of the three hazards on smaller regions with the various geographical environments. To obtain more specific hazard curves for local area, the simulated flooding results are calculated inside the five small regions as defined in Figure 5-8. The total inundated areas of each of the regions due to the three hazards are illustrated respectively in Figure 5-24. In region A, the river flow and rainfall are the main drivers of flooding while the sea surge only slightly contributes to the flooded area, which is because region A is far away from the seaside and its average elevation is higher than the normal sea level. From region B to region E, the storm surge has a more significant impact on the inundated area, especially in region E which faces the North Sea surge at the very front. In contrast, the effect of the extreme river flow can be neglected in the downstream regions. For all the five regions, the extreme rainfall is a significant hazard that can cause serious inundation.

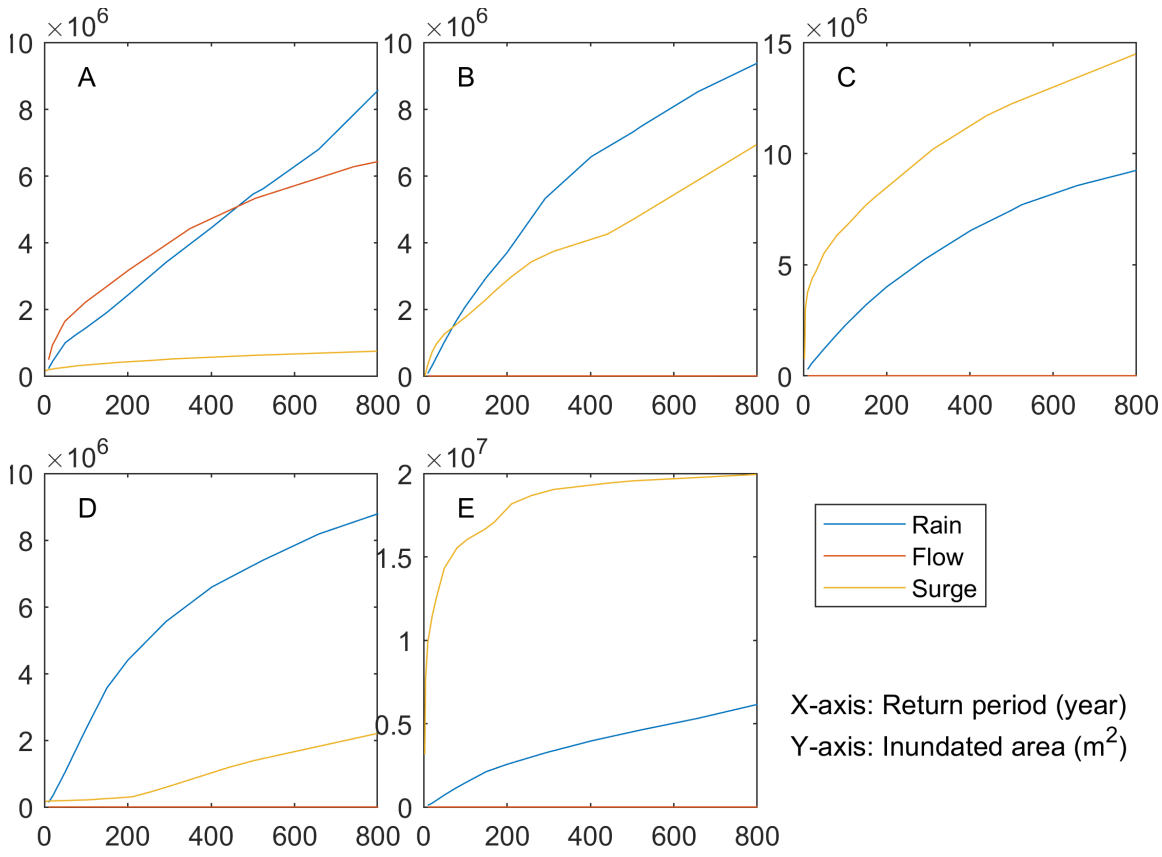

Figure 5-24. The frequency curves of inundated area for rainfall, flow and tide at the five localised regions.

5.6 Double-hazard simulations of joint extreme river flow and total water level

The 1928 Thames flood was one of the most disastrous flood of the River Thames that affected much of riverside London as well as places further downriver, which was caused by the concurrence of extreme river flow and total water level from the Thames estuary. In this section, we investigate the joint impact of these two hazards on the riverside and seaside region along the River Thames. Extreme flow and surges with different single and joint return periods are given in Table 5-3 with the estimated single and joint return periods. Due to the dependence between the two hazard components, their joint return period is much lower than the product of the two single-hazard return periods, suggesting that the joint hazards curve can be significantly different from the single-hazard curve as displayed in the previous section.

All the double-hazard combinations of flow and surge as listed in Table 5-3 are simulated using HiPIMS in the Greater London catchment. The flow hydrograph is imposed to provide flow boundary conditions for the Thames River and the surge level is added to the astronomical tide at the east boundary of the catchment close to Sheerness. Results will be shown by inundation maps of several joint events for Greater London. Then the hazard curves of the inundated area for the whole catchment and selected small regions are displayed, respectively.

Table 5-3. Joint return period (year) of the concurrence of extreme river flow and storm surge compared with the single hazard return period (year).

Surge m (year) / Flow m^3/s (year)	2.2 (8)	2.4 (20)	2.6 (43)	2.8 (80)	3 (135)	3.2 (211)	3.4 (312)
500 (14)	17	38	78	144	241	375	553
600 (49)	52	100	196	352	582	902	1325
700 (114)	118	221	424	756	1246	1926	2828
800 (213)	219	406	773	1374	2262	3495	5128
900 (349)	358	659	1254	2224	3659	5651	8291
1000 (525)	537	987	1873	3321	5462	8433	12372
1100 (742)	759	1392	2640	4678	7692	11875	17420

5.6.1 Inundation maps

For each combination of the extreme flow and surge, the results of the 24-hour simulations are illustrated as inundation maps. The maximum water depths of the three joint events are shown in Figure 5-25 and the estimated return periods are found in Table 5-3. With the increasing magnitude of the flow and surge from top to bottom, the joint return period of the event rises sharply, accompanied by the change of total inundation area in the catchment.

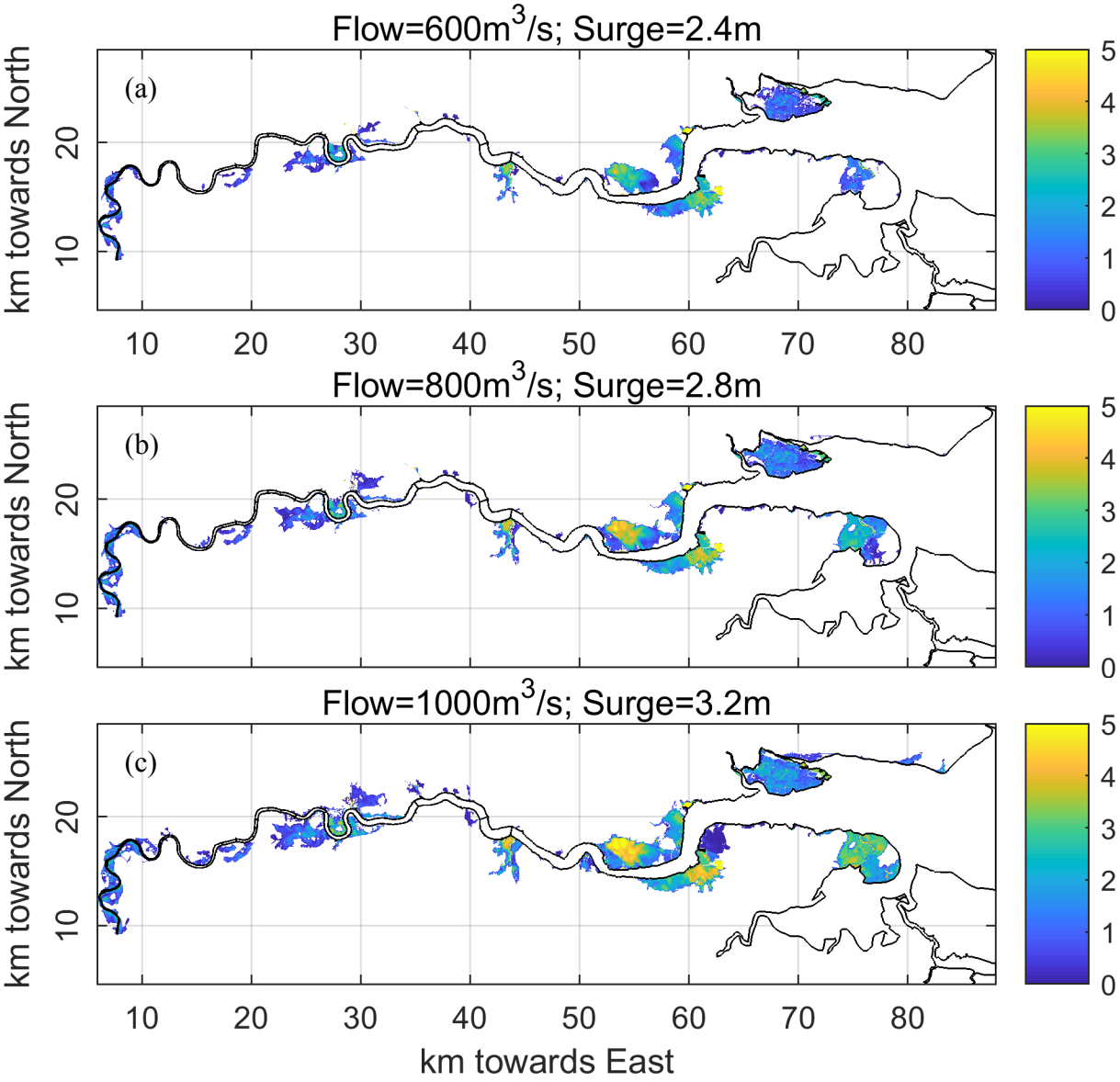

Figure 5-25. Inundation maps due to the concurrence of extreme flow and surge with return periods of 100-year (top panel), 1374-year (medium panel), and 8433-year (bottom panel).

The underlying assumption of the defence failure scenario has a critical effect on the flooding areas in the middle and east catchment. All of the flooded areas from London city centre towards the east coast are caused by the short or long breaches of the defensive walls or embankments adjacent to the river or coast. However, most of the low land along the Thames

remains safe, even in the highly extreme events like the bottom plot in Figure 5-25, which can be attributed to the high design level of the defence facilities. It is also the reason why the general inundated area does not show obviously expand from 100-year event to 8000-year event. As the decisive result, the multi-hazard inundation map can display the outcome of various hazard intensities as well as defence failure scenarios. But for risk analysis, the result needs to be given a meaning of probability that is estimated by a large number of simulations and random sampling.

5.6.2 Hazard curves for the total inundated area

For any given intensity of flow and surge, the joint return period can be estimated, and the inundation map can be generated using HiPIMS. Thus, it becomes possible to construct the functional relationship between the return period and the flooded extent or water volume. However, a certain return period of multiple hazards can infer to various multi-hazard combinations, as shown in Figure 4-15, which means the same return period can result in different flooding outcomes. As the return period is defined as positive-going, we choose the most severe result from it as the representative outcome.

The inundated area is a bivariate function of input flow and surge with all the other parameters and geographical background settings to be the same. The geometry of this function should be a continuous 2D surface in the positive quadrant. By randomly selecting hazard pairs to determine flood simulations, we can generate numerous discrete 3D points to depict the surface using the simulation results. The trend of the surface should be generally flat without peaks or valleys because the function is monotonically non-decreasing on the assumption that either a higher flow or a higher surge can result in an outcome of equal or more severe inundation. Therefore, instead of performing a large number of simulations, we evenly selected a set of hazard pairs as listed in Table 5-3 to estimate the double-hazard surface using spatial interpolation.

The hazard surface for the total flooded area in the whole research domain is illustrated in Figure 5-26. The bottom two axes represent the magnitude of the two hazards respectively, and the vertical axis displays the simulated total inundated area in the Greater London catchment. The red dots on the surface show the results from hydrodynamic simulation and are used to fit the whole surface. With the hazard surface, the possible flooded area can be estimated for any given flow and surge inputs and running the hydrodynamic model for each pair is no longer essential. The surface looks steeper in the axis of the surge than it is in the

axis of flow, meaning that the total flooded area is more sensitive to the storm surge than the river flow.

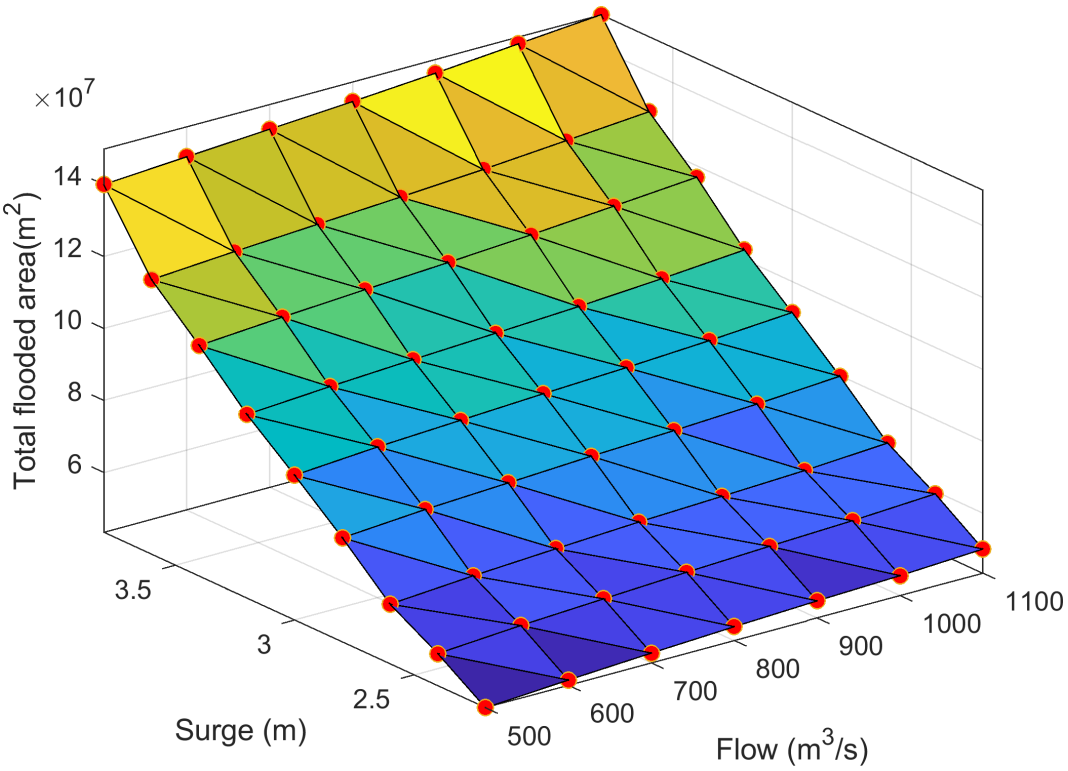

Figure 5-26. Total flooded area in Greater London due to joint extreme river flow and storm surge.

As each pair of flow and surge values can be associated with a certain return period, the contour lines of the return period can be directly depicted on the hazard surface, as shown in Figure 5-27. All points on the same line have the same return period, namely the same probability of occurrence. However, the total flooded area varies for the points on the same line. According to the concept of the return period, the most severe result should be the representing value in that level of return period.

Using the maximum value of inundated area for hazard pairs at each return period, a hazard curve is generated to measure the possibility of the total inundated area in the research domain (see Figure 5-28). The bottom axis is the flooded area in the whole research domain. The left and right vertical axes show the return period and annual frequency of exceedance of the specific inundated area respectively. Concerning the total inundated volume, the frequency curves can be generated by following the same steps. Thus, the severity of flooding is estimated quantitatively by the return period and the frequency of exceedance for the Greater London catchment. Since the hydrodynamic model can produce full 2D inundation maps, similar curves are also available for any small regions inside the catchment and make the specific risk analysis of target area and properties feasible and statistically reliable.

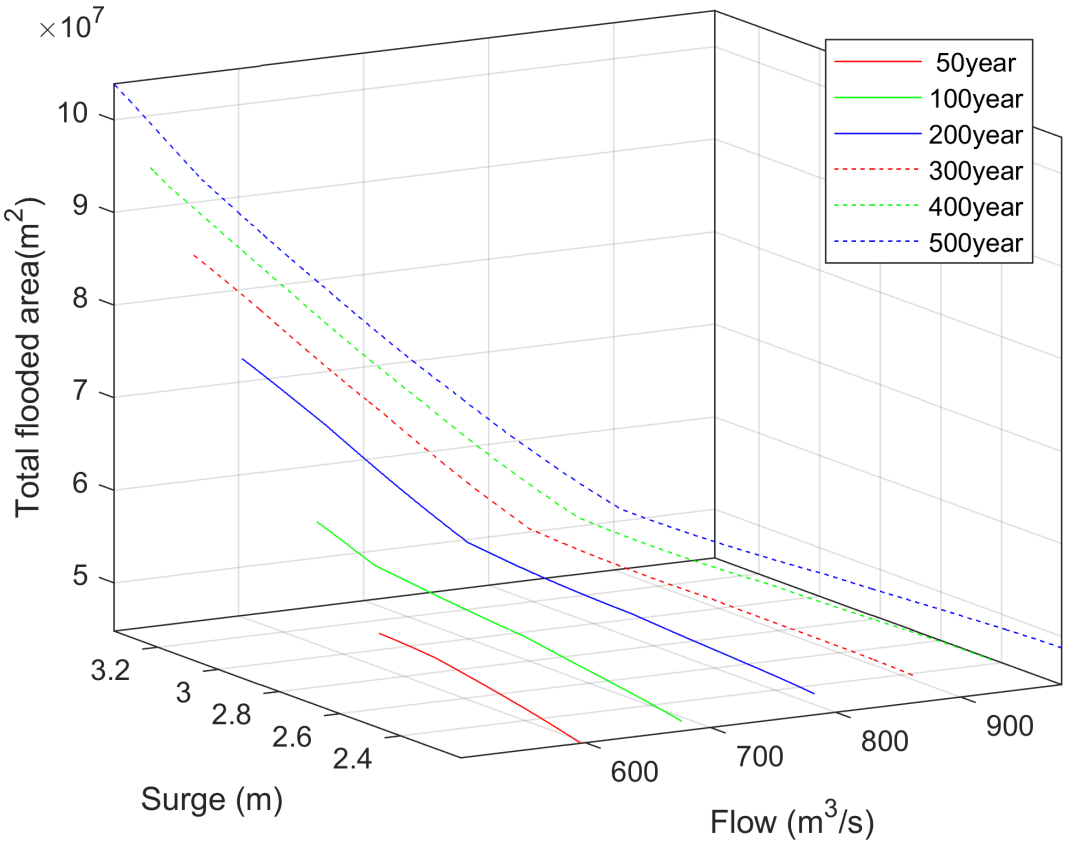

Figure 5-27. Contours of joint return period of flow and surge on the double-hazard surface.

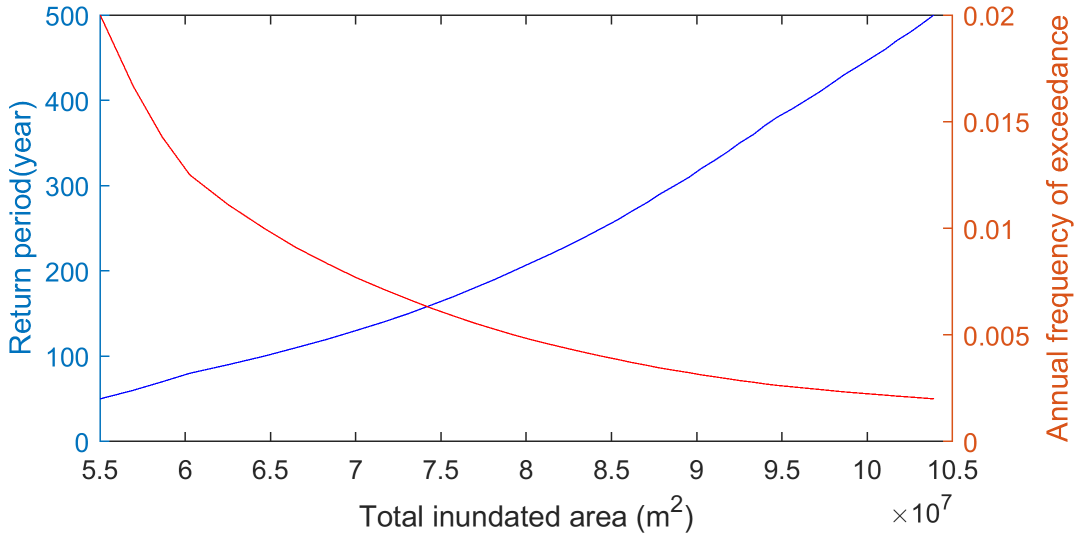

Figure 5-28. Hazard curves of flood inundation due to joint extreme flow and surge at the Greater London catchment.

5.7 Triple-hazard simulations

5.7.1 Hydrodynamic modelling with multiple inputs

The designed triple-hazard simulations involve three hazard components, and the range of the value for the three hazards is a 3D space of positive real number. A vast number of

simulations are required to adequately estimate all the possible outcomes from the different combinations of joint events in the whole range space. However, because of the limited computing resources, we choose values from a $3 \times 3 \times 3$ matrix to represent the range space of triple hazards in the hydrodynamic model. The values are listed in Table 5-4 with a total number of 27 triple-hazard simulations.

The initial conditions, parameters, and the assumption of defence failures are the same as the double-hazard flood simulations. The hydrodynamic model is run for 24-hour events in the Greater London catchment. The output of the model is the 24-hour maximum inundation depth at each grid cell and can be illustrated as triple-hazard inundation maps. Figure 5-29 shows the results of two of the triple-hazard simulations. The top panel depicts the outcome of a one-in-300 years event. The resulting flooding is limited along the River Thames and the east coast while only a few discrete regions away from the riverside are flooded due to the rainfall. The bottom map illustrates the result of an extremely infrequent event combining the highest values of the three hazards in all the simulations. The floodplain area along the Thames is mostly flooded, and severe pluvial flooding can be observed in many places outside the riverside region.

Table 5-4. Input values of triple-hazard simulations using the hydrodynamic model.

No.	Rain (mm)	Flow (m^3/s)	Surge (m)	No.	Rain (mm)	Flow (m^3/s)	Surge (m)
1	50	500	2.5	15	120	700	3.8
2	50	500	3.0	16	120	1100	2.5
3	50	500	3.8	17	120	1100	3.0
4	50	700	2.5	18	120	1100	3.8
5	50	700	3.0	19	200	500	2.5
6	50	700	3.8	20	200	500	3.0
7	50	1100	2.5	21	200	500	3.8
8	50	1100	3.0	22	200	700	2.5
9	50	1100	3.8	23	200	700	3.0
10	120	500	2.5	24	200	700	3.8
11	120	500	3.0	25	200	1100	2.5
12	120	500	3.8	26	200	1100	3.0
13	120	700	2.5	27	200	1100	3.8
14	120	700	3.0				

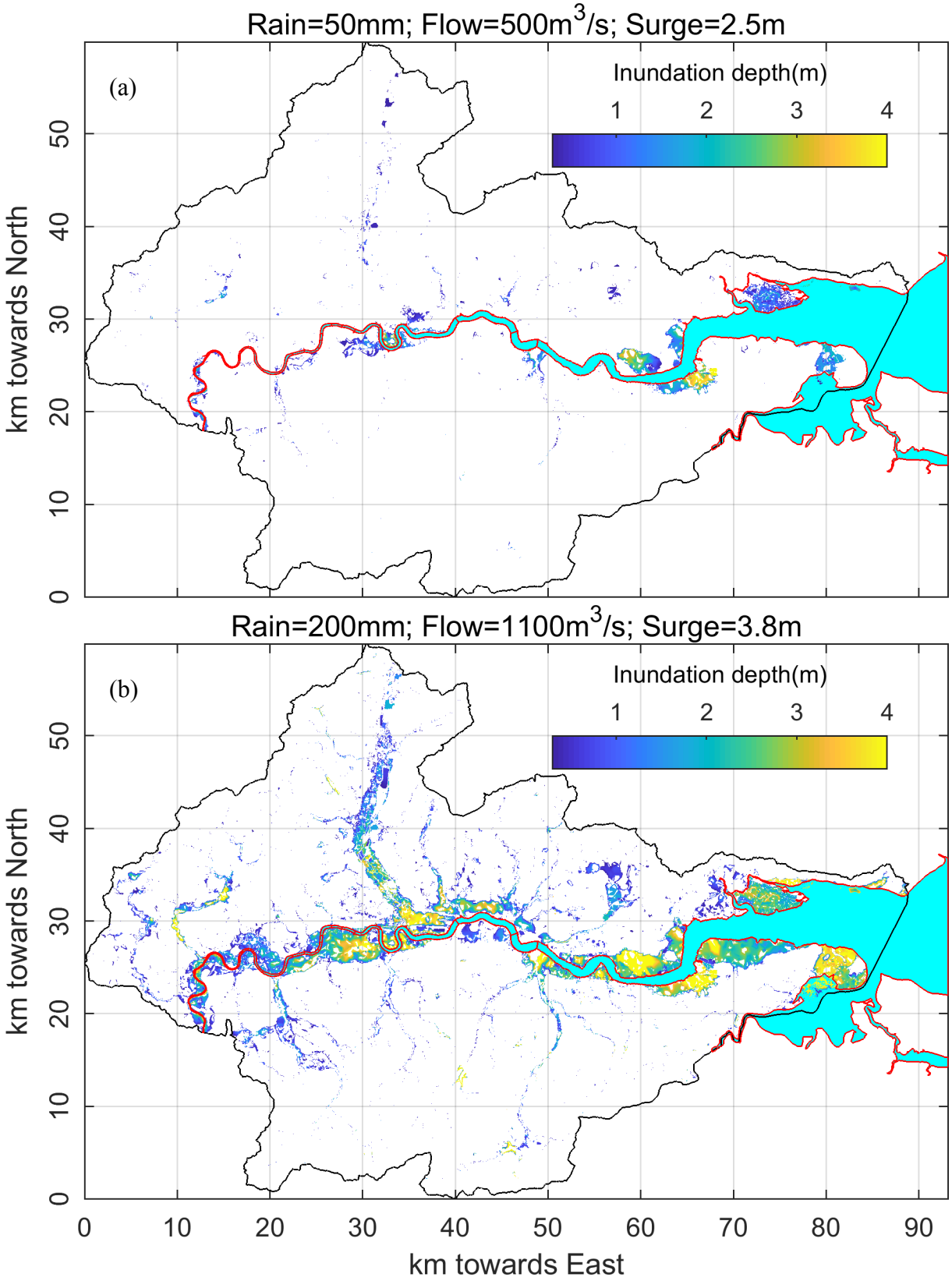

Figure 5-29. Inundation maps due to joint extreme events of rainfall, river flow and storm surge in the Greater London catchment.

5.7.2 Frequency curves of flooding due to triple hazards

For the triple-hazard simulation, the intensities of hazard are the decisive inputs that create flooding in the research domain. So, the inundated areas of any district inside the model domain should be a trivariate function of the three hazard components. Figure 5-30 indicates the geometry of the trivariate function for the total inundated area in the model domain. The three Cartesian axes represent the intensity of each hazard respectively. Different inundated areas are indicated by different colours and different sizes of dots. An increasing trend of the total inundated area can be observed at the direction of each axis. But the changing rate is relatively small in the axis of flow compared with the other two axes, signifying that the flow has the lowest effect on the total inundated area among the three hazards.

Based on the assumption that the increase of intensity of any hazard would result in a larger or equal size of inundated area, the trivariate function should be monotone non-decreasing for all variables, and its density in the 3D space is gradually varied in each direction. Therefore, it is reasonable to estimate the values of the function within its domain of definition based on the discrete points from the 27 simulations in Figure 5-30 using a linear interpolating method.

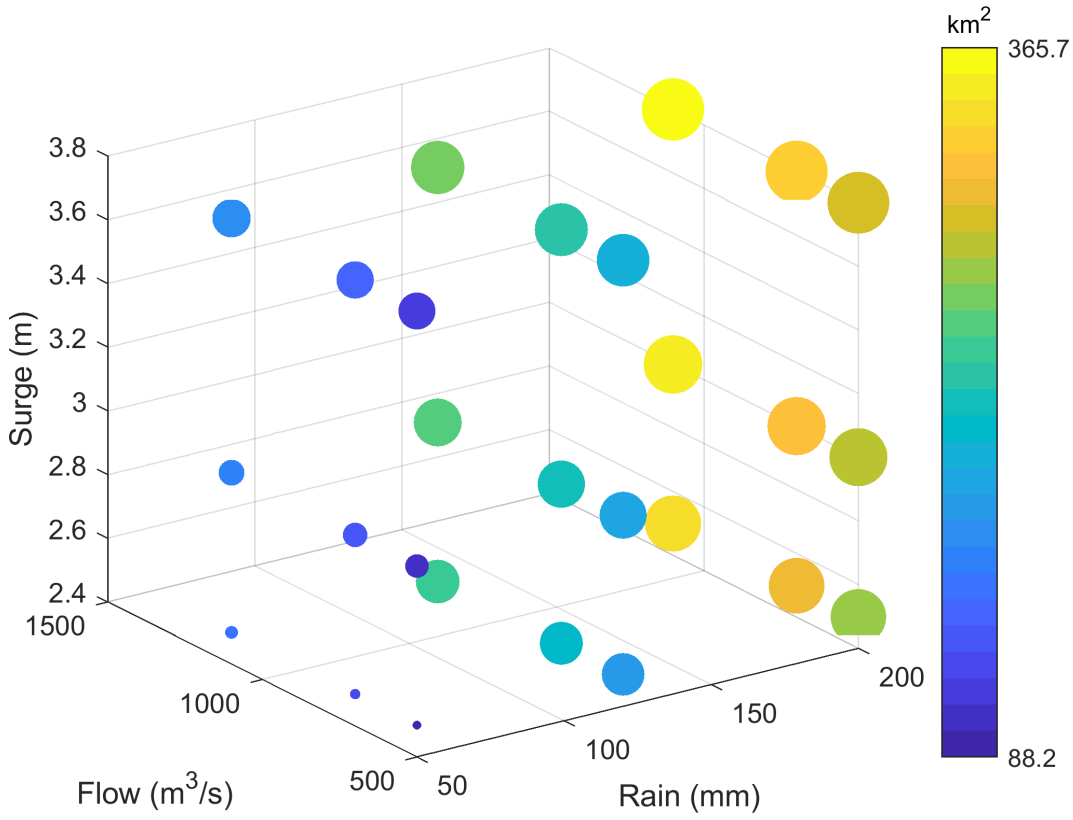

Figure 5-30. The total inundated area in the whole domain due to joint rainfall, river flow and storm surge. Varying inundated area is represented by different colour and size of the dot.

According to the trivariate return period distribution constructed in section 4.5.3, random joint events of the three hazards can be generated for any given return period. Thanks to the estimated trivariate function of the inundated area, the possible outputs of all the random events for a certain region can be worked out directly rather than running numerous hydrodynamic simulations. A specific return period corresponds to many random triple-hazard events and can produce the same number of inundation maps using HiPIMS. The most severe flooding from the inundation maps is chosen as the representation of that return period. Then, the frequency curve of flooding due to joint extreme rainfall, river flow and storm surge can be generated as shown in Figure 5-31. The bottom axis is the total inundated area inside the Greater London catchment. The left vertical axis represents the return period, and the right vertical axis shows the annual frequency of exceedance. Thus, the possibility of the inundated area in the whole catchment is quantitatively estimated, and the same procedures can be applied to any small district inside the model domain.

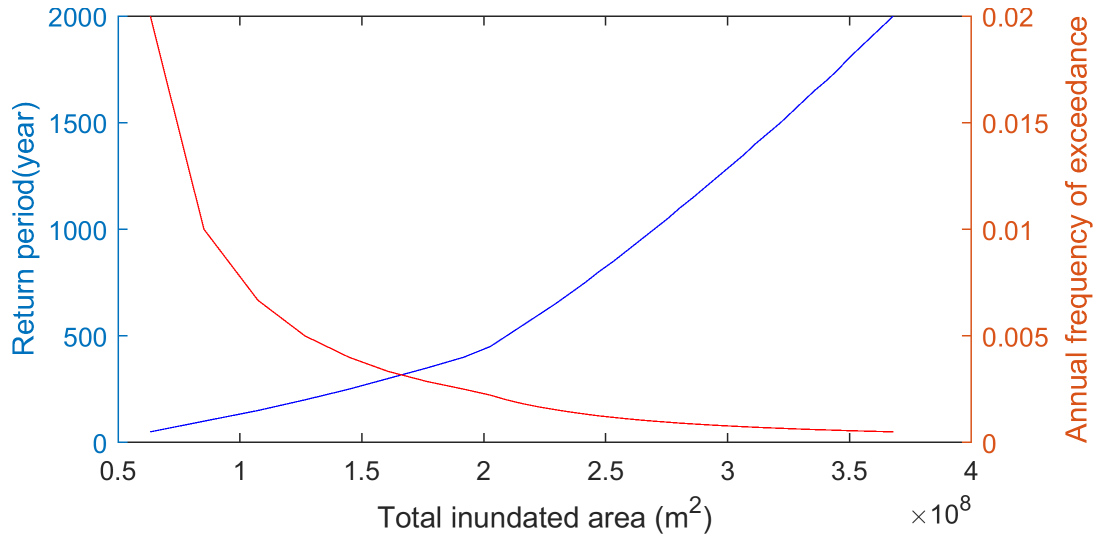

Figure 5-31. Hazard curve of flood inundation due to joint extreme rainfall, flow and surge at the Greater London catchment.

5.8 Conclusions

In this chapter, a 2D hydrodynamic model, HiPIMS, is applied to simulate flood inundation in the Greater London catchment. The model is firstly validated by reproducing three historical events to confirm model performance and estimate the essential parameters. The influence of the flood defence system is appraised with different failure scenarios and then considered in HiPIMS for the entire catchment. According to the return period distributions estimated in Chapter 4, random events regarding extreme rainfall, river flow and storm surge are generated at various return periods and then put into HiPIMS to simulate the potential floods. The

results from all the discrete simulations are used to estimate the relationships between the flooding and the input hazards. The frequency curves of flooding, also called hazard curves, are generated for single-hazard, double-hazard, and triple-hazard events to quantitatively depict the probability of occurrence of flooding at different scales.

The inundation-frequency curves for individual-hazard show that storm surge is the most dangerous hazard to the Great London Catchment, causing around 140 km^2 inundated area at 100-year return period, 90 km^2 larger than the rainfall-induced inundation. In contrast, the effect of river flow on London is much smaller, only flooding an area of 2.1 km^2 at the same return period. For local districts inside the Great London Catchment, the hazard curves may show totally different patterns as demonstrated in Figure 5-24. The frequency curves of inundation due to double-hazard (Figure 5-28) and triple-hazard (Figure 5-31) show the possible total inundated area with any given return period levels. For example, at 500-year return period, the expected inundated area in the Great London Catchment is 104 km^2 due to joint extreme flow and surge, and 210 km^2 due to joint rainfall, flow, and surge, respectively.

In the flood risk assessment, the small region with the same type of human properties is often selected as the spatial unit of analysis. Although the hazard curves are not demonstrated for many local districts in this chapter due to the length limit of the thesis, the procedures for generating the hazard curves are applicable to further risk analysis in the next chapter.

There are a lot of other factors affecting the simulated results apart from the intensity of the three hazard components, such as the model parameters, the temporal distribution of the hazards during a 24-hour event, and the scenario of defence failure. Due to the lack of data and computing capacity, it is unrealistic to consider all the variabilities and uncertainties of these factors. Instead, the framework of multi-hazard assessment is concentrated on dependence and interaction between the three hazards, which are the critical aspects of a multi-hazard issue.

Chapter 6. Vulnerability, exposure, and multi-hazard risk analysis

This chapter is to calculate multi-hazard flood risks. Firstly, integrated inundation maps are generated. Then, exposure of human properties is quantified, and vulnerability of the properties is analysis. Finally, risk curves and maps are generated based on the results from the three risk components.

6.1 Introduction

Apart from hazard, vulnerability and exposure are the other two essential components of disaster risk. The multi-hazard frequency and outcome have been appraised in Chapter 4 and Chapter 5. This chapter aims to accomplish the assessment framework of multi-hazard risk by coupling hazards with vulnerability and exposure analysis. The assessment framework is employed on a uniform grid of 100 m × 100 m resolution and produces results for every one-hectare square inside the research area. The objective of risk assessment in the framework can be various and relevant to the evaluation methods of vulnerability and exposure. Buildings and road networks are selected as the risk appraising objects to demonstrate the complete process of the assessment framework. The first step is to estimate the inundation-frequency curve for each grid cell and depict integrated inundation maps. Then the vulnerability curves of different types of building are derived from the Multi-Coloured Manual (MCM) (Penning-Rowsell et al., 2013). The exposure of buildings is analysed and illustrated in maps based on the data from the National Property Dataset (NPD) and Digimap. Finally, risk curves for each grid cell and risk maps are produced to show the probability of loss on each grid cell and the spatial distribution of risk in the Greater London catchment.

6.2 Integrated inundation map for multiple hazards

In the previous chapter, a hydrodynamic model is used to produce flood inundation maps, and the hazard curve of inundated-area against the probability of occurrence is estimated for the whole research domain. As the risk assessment unit is one-hectare square is this chapter, the hazard curve is generated for every cell of 100 m×100 m in the Greater London catchment.

The proportion of impact on a specific area from each hazard component may be various according to the geographical environment. The coastal region along the Thames estuary is more likely to be influenced by the surge. The extreme flow and surge can both lead to flooding on upstream riversides of the Thames. Regions far away from the river and the coastline are only exposed to extreme rainfall induced flooding. The hazard curve for a large region may not be able to reflect the real characteristic of hazards at the local areas, and a customised curve for each one-hectare cell is therefore necessary.

Following the same procedures introduced in section 5.7, a number of random events are generated for a series of return periods conforming to the joint return period function generated in Chapter 4. Then, the flood inundation at the specific cell for each event can be estimated by interpolation in accordance with the previous results from hydrodynamic modelling. The maximum estimated inundation of the events generated from the same return period is regarded as the non-exceeding inundation of that specific return period. Therefore, the paired data of inundation and return period can be obtained to illustrate the hazard curve for each grid cell.

For a specified return period is appointed, the corresponding inundation can be worked out based on the hazard curve of each cell and the inundation map associated with that return period can be generated to cover the whole domain. Figure 6-1 displays the inundation maps of 100-year and 500-year return periods for the Greater London catchment. The maps show the maximum possible inundation of each cell for the given recurrent time. We can observe the increase of both the flooded area and the inundation depth over the domain when the return period changes from 100 years to 500 years. However, the event from the same return period does not necessarily have the equal hazard magnitudes on each cell because the impact of hazards is various at the different locations of the catchment. We call this type of maps the integrated inundation maps in which the depth values are not obtained from the simulation of one single event.

The reverse of return period in years is equivalent to the annual non-exceedance probability. The function of the inundation against the return period can be transferred to an annual non-exceedance probability function of inundation for each grid. The mathematical expectation of the function is the yearly average inundation that is illustrated in Figure 6-2. It shows the expected inundation depth for each cell inside the Greater London catchment by integrating the possible flooding of the return period. The map gives a general and quantitative view of

the spatial distribution of flooding in consideration of all the three hazard components that are potentially destructive to this region.

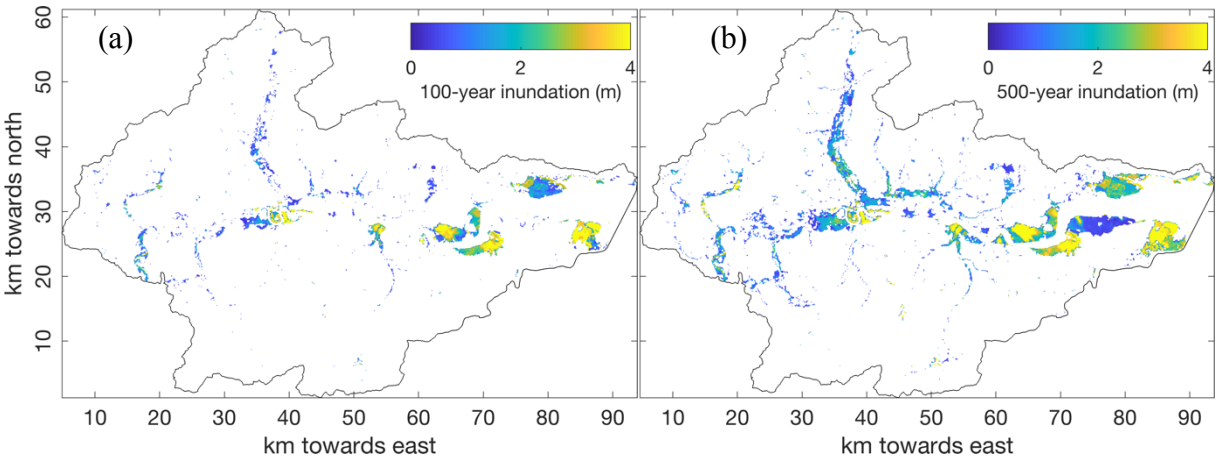

Figure 6-1. Integrated inundation maps on the 100 m-grid for 100-year and 500-year return periods.

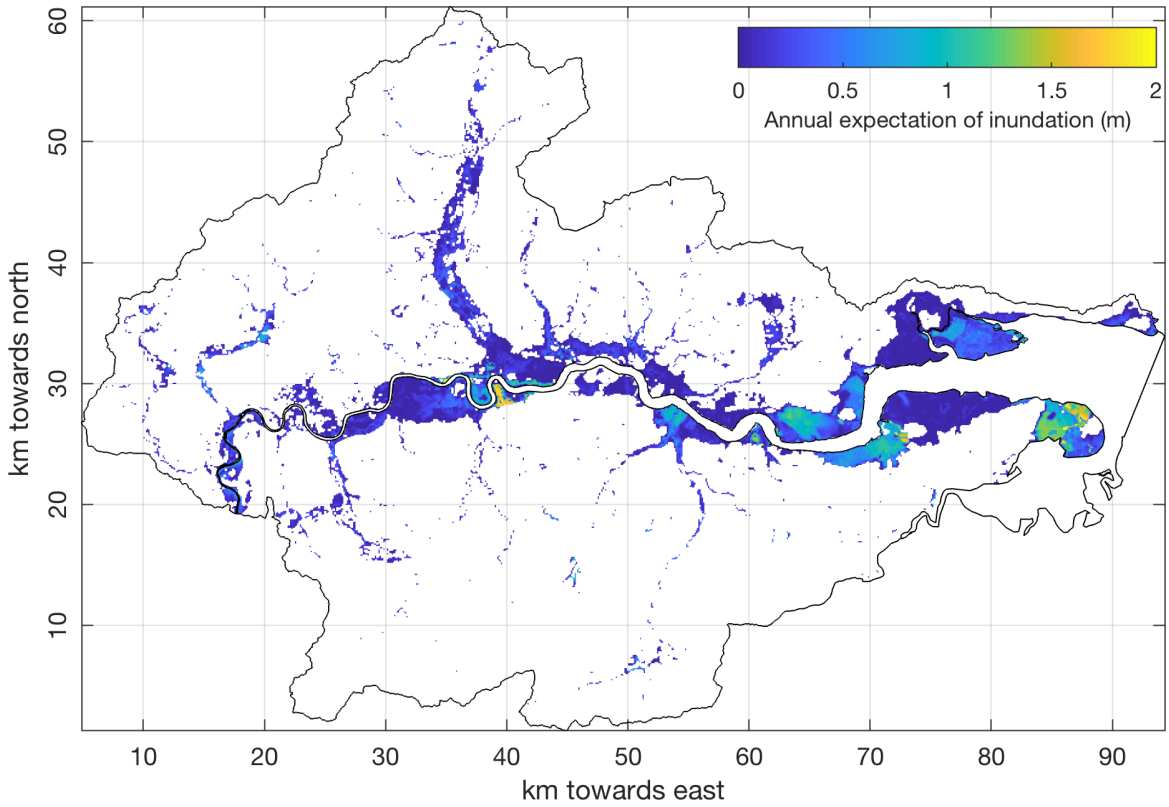

Figure 6-2. Expected average annual inundation due to multiple hazards in the Greater London catchment.

6.3 Exposure of human properties

The typical approach for exposure analysis is to assess the spatial distribution of the value or number of elements at risk. Elements to be evaluated are usually human life or properties, which are also the objects of the risk assessment, i.e. population, buildings, farmland,

transportation system, market, industry, and so on. Residential buildings, non-residential buildings, and road networks are chosen as the three types of exposure elements to be appraised in the framework of multi-hazard risk assessment in this thesis.

The selection of the exposure is based on the land cover map that gives a general view of main types of land use in the research area. According to the Land Cover Map 2015, the land use in the Greater London catchment is illustrated in Figure 6-3 with some of the close land categories merged into one type. Built-up areas, including urban and suburban areas, are the dominant type of land cover in the research domain. The Grassland is distributed sporadically in the built-up area and intensively in the northeast and southeast part of the catchment cover mainly by arable lands. Referring to the hazard map (Figure 6-2), flooding is more likely to happen in built-up areas rather than other landuse types. Therefore, we choose buildings and road networks from built-up regions as objects of exposure and risk assessment.

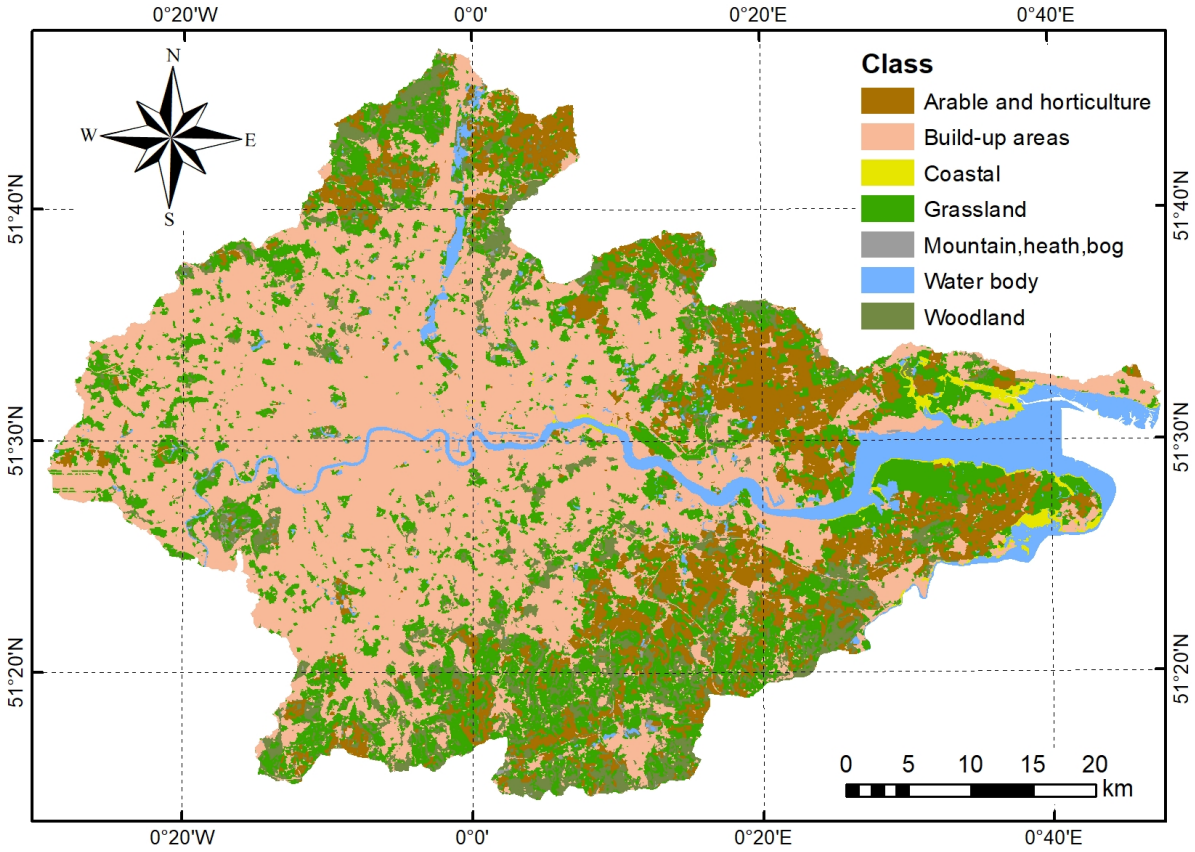

Figure 6-3. Landuse map of the Greater London catchment (Data source: Land Cover Map 2015, Centre for Ecology and Hydrology (CEH)).

NPD provides spatial points of properties while the building geometries can be obtained from OS MasterMap. Figure 6-4 illustrates zoomed-in maps of three small regions, Twickenham, Chelsea, and Canvey Island, which are located respectively in the upstream, midstream and the river mouth of the Thames. The background of each map is the land cover. Points of

buildings, geometry of buildings, and landuse types are matched well in these three local regions. Houses, terraces, and other large buildings can all be illustrated by polygons on the map. The high quality of the data makes it feasible to perform quantitative exposure and risk analysis at the catchment.

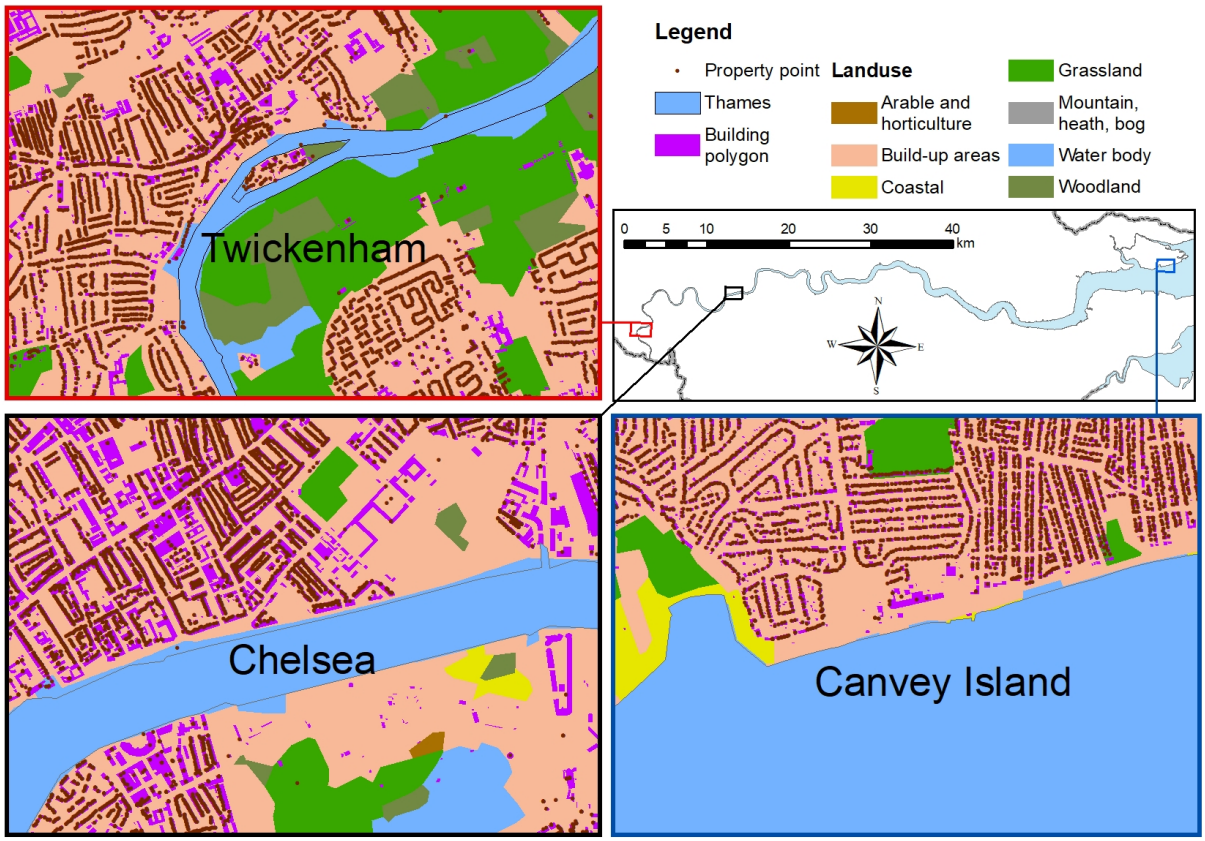

Figure 6-4. The position and shape of buildings in Twickenham, Chelsea, and Canvey Island

6.3.1 Residential buildings

For residential buildings, NPD has the geographical information of the property points but does not provide detailed categories and valuations. So, exposure analysis of the residential building is focused on the number of buildings in each cell. Based on the 100 m-grid defined for risk analysis in this chapter, the number of residential properties is calculated for each grid cell, and the result is displayed in Figure 6-5.

The residential buildings are mostly distributed in the middle and west parts of the Greater London catchment. In the city centre, the red colour indicates the dense residential buildings and also a high level of exposure to flooding in reference to the hazard map as presented in Figure 6-2. Apart from the city centre, regions with non-residential buildings along the downstream Thames and the coast are also worthy of attention as they are very likely to be flooded during extreme events, especially in the Gravesend, Canvey Island and Southend.

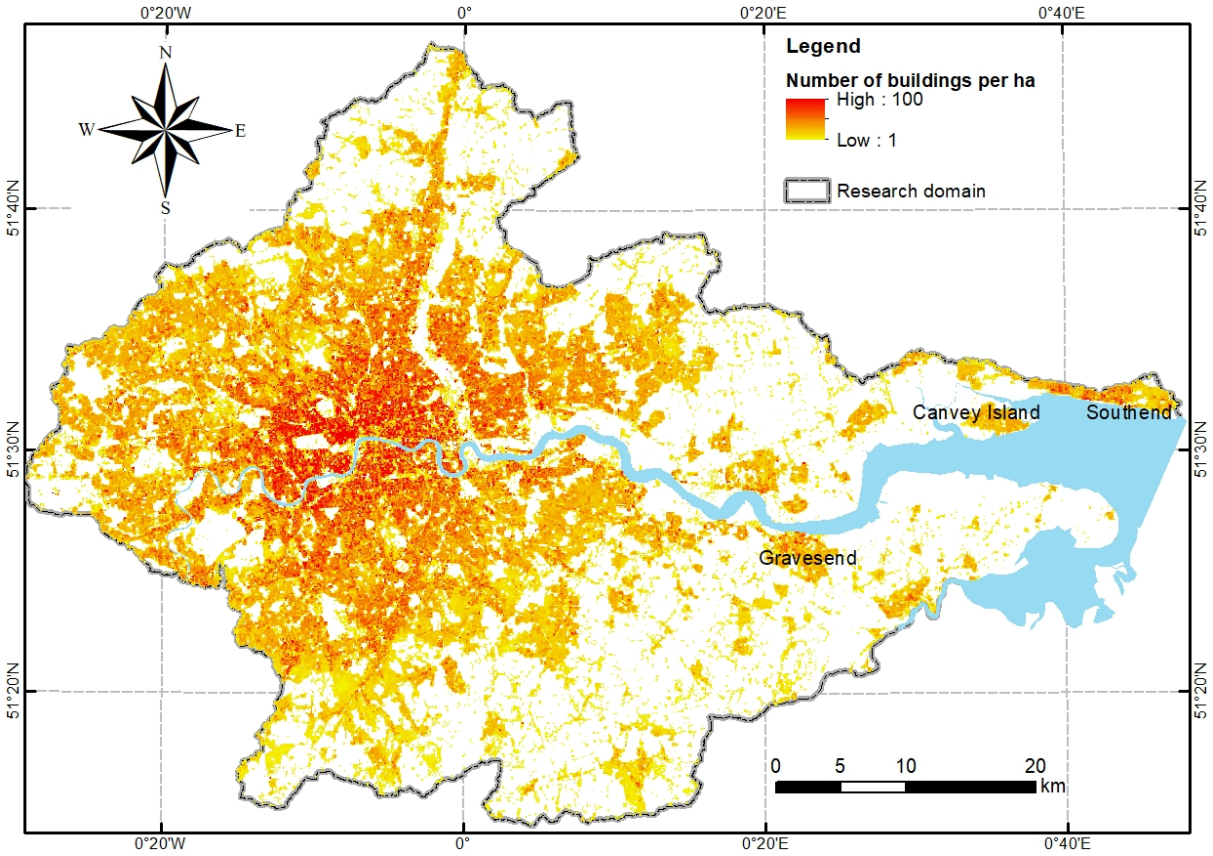

Figure 6-5. Density of residential buildings.

6.3.2 Non-residential buildings

Non-residential buildings are defined as the collection of all other types of building that are not used for living, including office, retail, warehouse, sports stadium, industrial buildings, and so on. NPD provides the information on the categories of non-residential property. As the value and the size of non-residential buildings can vary significantly from one to another, the exposure level at each grid cell is delivered by the total floor area of buildings based on the geometry data from OS MasterMap.

Figure 6-6 illustrates the total floor area of the non-residential buildings in each one-hectare cell for the Greater London catchment. The spatial distribution of the non-residential buildings is concentrated in the central and west part of the catchment, which is similar to the residential building. However, unlike the residential properties that spread across the research domain, the non-residential buildings distribute more intensively in city and town centres, or along the business streets that are indicated by the dark lines on the map.

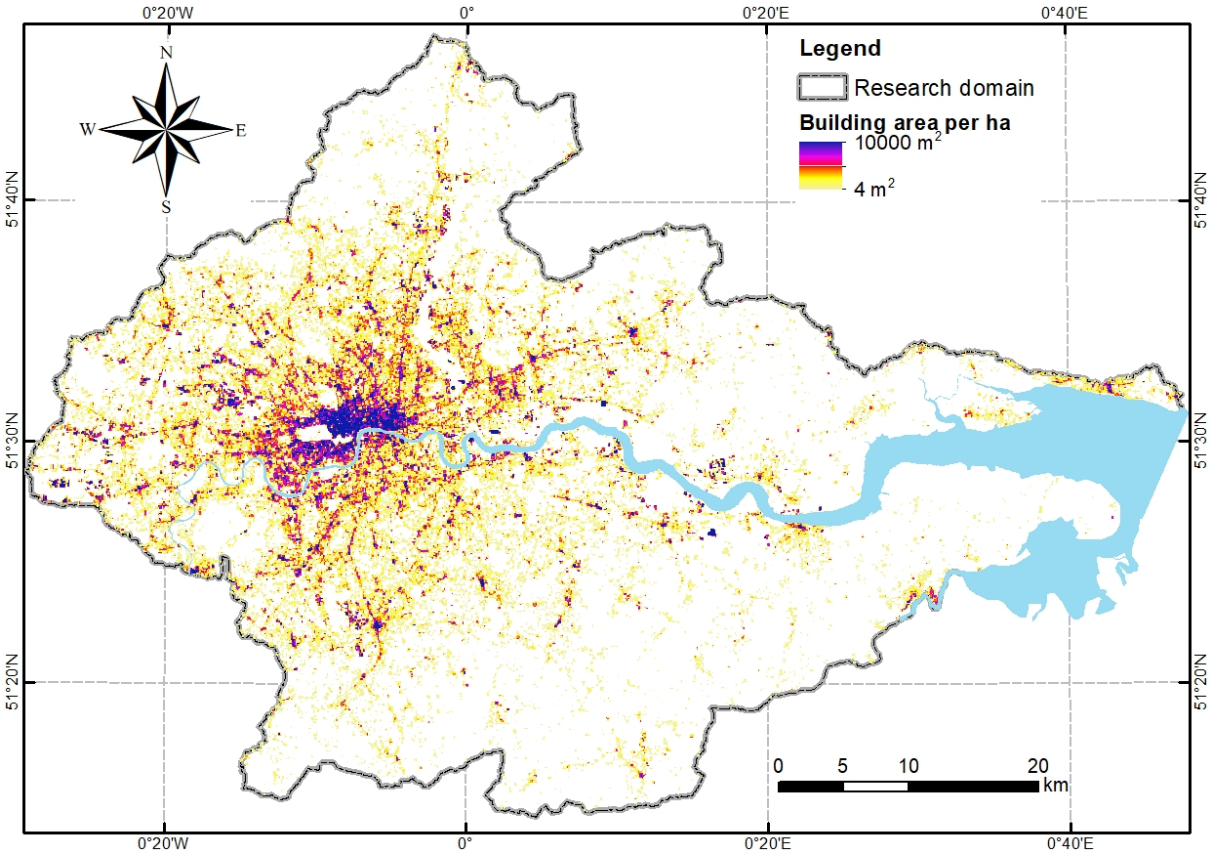

Figure 6-6. Total ground-floor area of non-residential buildings on the 100 m×100 m grid of the research area.

6.3.3 Road networks

Road networks play a crucial role in the social-economic system. The damage to buildings from flooding typically has a more localised impact while the disruption to road networks can result in widespread and system-wide disaster leading to substantially tangible and intangible losses. The data of road networks can be acquired from OS MasterMap, containing road links, nodes and junctions.

Road links in the Greater London catchment are shown in Figure 6-7. The roads are reclassified as two major types to display clearly in the map. The Major road (solid black lines) consists of the Motorway, A Road and B Road as defined by the Great Britain Road Numbering Scheme. The Local road (dotted yellow lines) includes all the other categories that are normally distributed in the smaller regions compared with the Major road. From a general view, the distribution of the Local road is in concordance with the distribution of residential buildings so that a more populated area commonly has denser road networks.

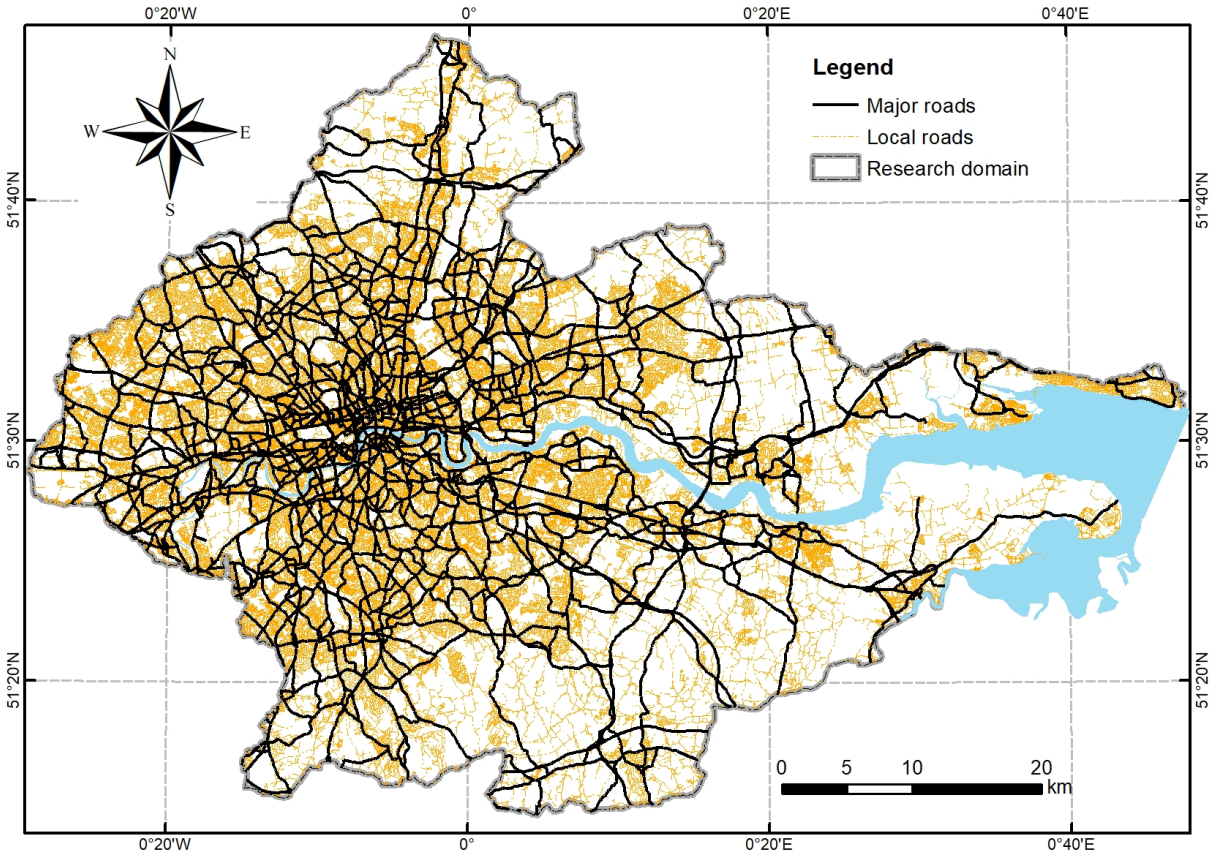

Figure 6-7. The road networks in the Greater London catchment.

6.4 Vulnerability curves for flooding

Vulnerability analysis of elements at risk is a big research topic that involves a lot of internal attributes of the elements and external environmental factors. This chapter attempts to apply some results of the current vulnerability approaches in the risk assessment framework of the thesis. MCM is selected in this work, which is widely employed in the UK for flood risk assessment, as the primary support of vulnerability data. A typical quantitative vulnerability function of flooding should be able to show the relationship between hazard (inundation depth or water velocity) and damage. The damage is referred to as loss of human lives, damage of buildings, blocking of roads, or economic loss measured in monetary term. Which way to be used to quantify the damage depends on the objects of risk analysis and the data availability.

6.4.1 Depth-loss curve of residential buildings

The MCM provides vulnerability data for five types of residential buildings as direct loss functions against inundation depth. These functions are given for several scenarios according to different levels of flood warnings, including no warning, 8-hour warning, and >8-hour warning. As the flood forecasting system is well established and operating in the UK (Ballard

et al., 2016), we assume that the Greater London catchment can receive the flood warning longer than 8 hours.

According to the damage data table of residential buildings for short duration flood with longer than 8-hour warning, the depth/damage curves of five types of house and the average residential building are illustrated in Figure 6-8. The damage measured as the economic loss in British Pound increases with the rise of inundation depth for all five types of house. As the exposure data does not contain detailed categories of the residential building in the research area, we only use the curve of residential sector average to generally represent the vulnerability of all residential houses in each of the appraising units.

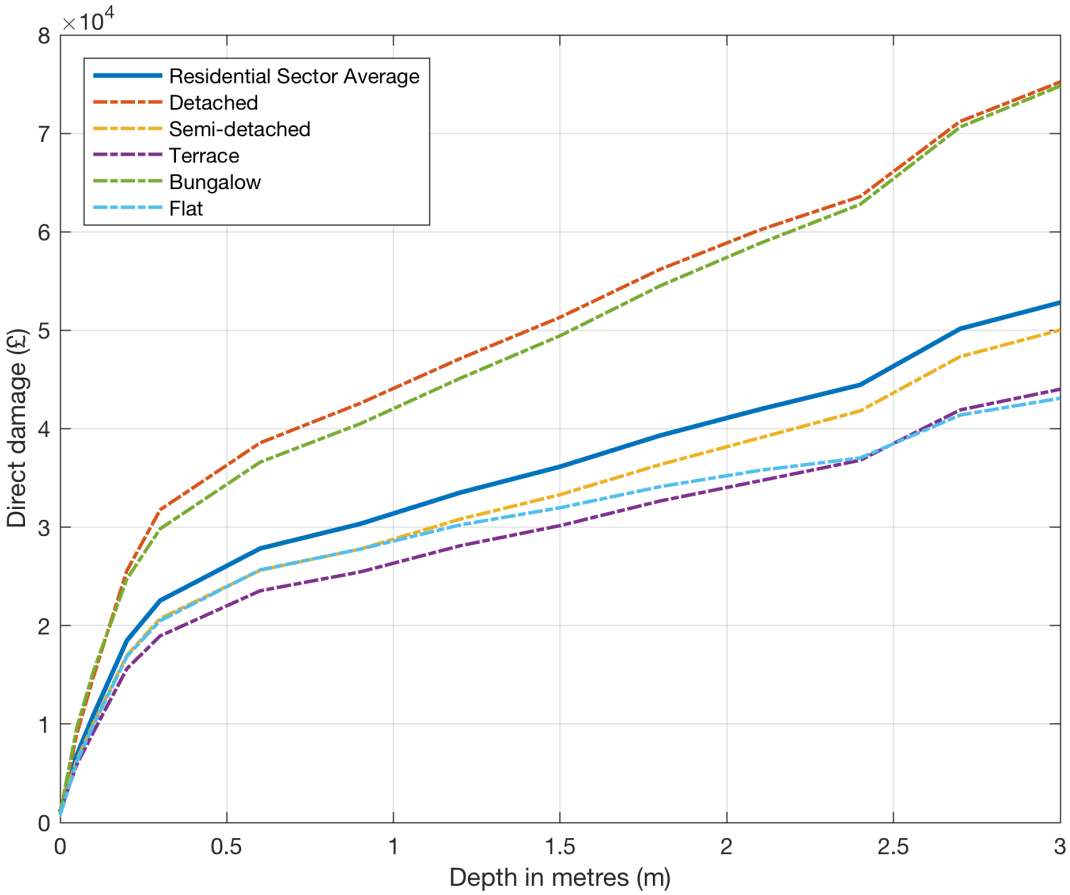

Figure 6-8. Depth-damage curves of residential buildingds due to flood inundation (Data source: MCM).

6.4.2 Depth-loss curves of non-residential buildings

The vulnerability data of non-residential properties from MCM provides depth/damage functions of 12 sector types for two flood warning scenarios (with or without warning). The damage is quantified by the economic loss as British Pound per square metre. As we assume that flood forecasting is available for the future flooding events, the vulnerability curves for

the scenarios with flood warning are selected to perform risk analysis for the non-residential buildings, as shown in Figure 6-9.

According to the vulnerability curves illustrated in Figure 6-9, the Sub-Station has a much higher economic loss per square metre compared with other types. The curves of Retail, Offices, Warehouses, and Leisure have similar shapes and are close to the curve of the NRP sector average while the other types have the relatively smaller loss when facing flood inundation. The curves also show that the damage becomes less sensitive to flood inundation when the inundation depth is deeper than 2 m. It may be because most valuable stuff inside the buildings would be fully submerged and badly damaged when the water depth reaches 2 meters. With the detailed depth-damage functions for a range of sectors, the risk of direct economic loss due to multi-hazard flooding can be evaluated for each sector by combining the exposure of property and the hazard curves.

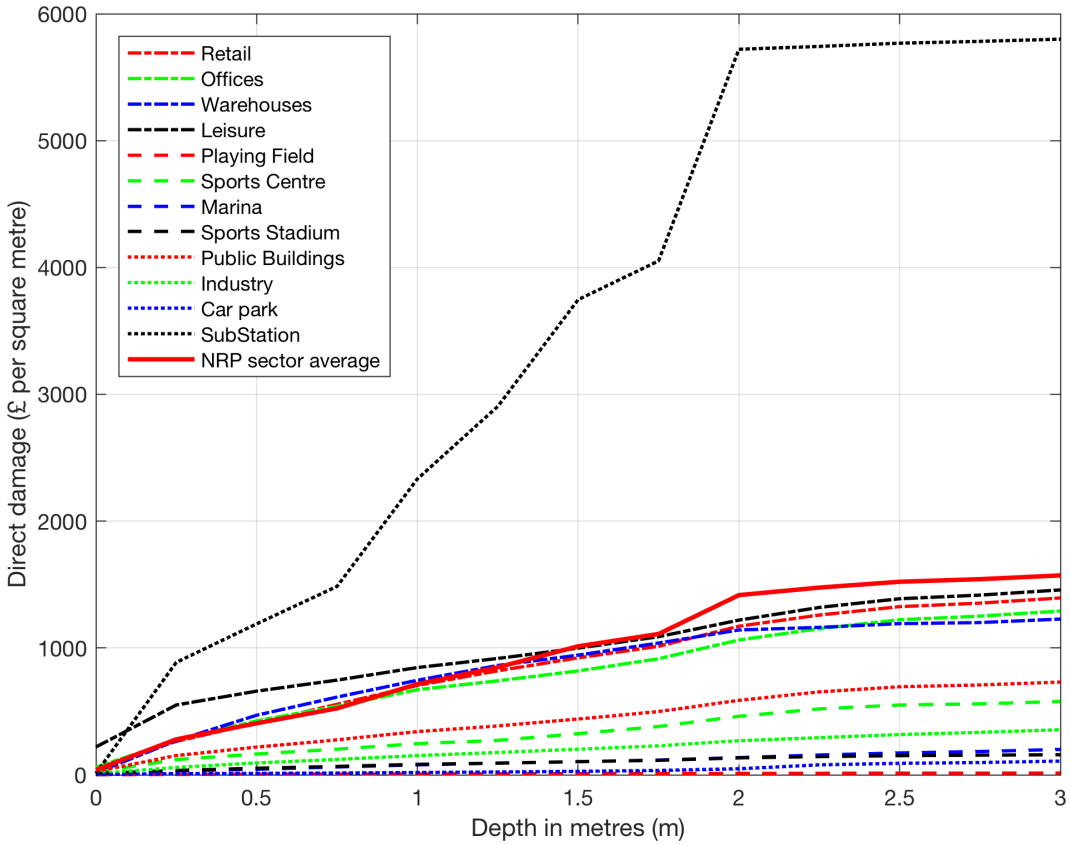

Figure 6-9. Depth-damage curves of non-residential buildings due to flood inundation inundation (Data source: MCM).

6.4.3 Depth-damage curve of road network

The vulnerability analysis of road networks is more complicated than buildings because the loss of road networks due to flooding can involve a larger number of factors that are very difficult to investigate. For example, the loss of a part of a submerged road may consist of the

money to repair the road, the effect of repairing the road during rush time, the economic loss due to traffic disruption that is related to the number of affected vehicles, and the influence on other roads. Because of the high complexity of road network disruption, the MCM does not provide specific loss function in the current version. However, with the current data of road networks, we can use the submerged distance as the representing variable of the road damage. Then the depth-damage curve can be illustrated by an indicator function,

$$D(h) = \begin{cases} 1, & if\ h > 0.3\ m \\ 0, & otherwise \end{cases}$$

where D is the damage of road, h is the inundated depth over the road. The threshold of road failing is set as 0.3 m as it is widely recognised as the maximum inundation depth for safe driving of ordinary vehicles (Pregnolato et al., 2017). The vulnerability function coupling with the exposure data of road length can be used to evaluate the risk of road damage signified by the road failing distance.

6.5 Multi-hazard risk

Risk analysis is performed for each grid cell by integrating the hazard curve, the vulnerability function, and the exposure for buildings and roads. A hazard curve quantifies the probability of occurring of flooding. A vulnerability function estimates the possible damage of elements at risk under the impact of inundation depth. A damage/ probability curve is calculated according to a shared variable (i.e. inundation depth) of the hazard and the vulnerability functions. Then, the damage/probability curve is multiplied by the exposure data to get the probability curve of total loss. The quantitative results of multi-hazard risk are produced for the buildings and road networks on the 100 m×100 m grid inside the Greater London catchment. The result of risk analysis can be shown as risk curves for individual grid cells and risk maps for the whole catchment.

6.5.1 Risk curves

As the fully quantitative result of risk analysis, risk curves provide the intact information about the occurring probability of disaster loss in the form of return period or annual non-exceedance probability. The risk curve is produced for every cell for properties inside the catchment. The vulnerability functions for the residential and non-residential buildings and the associated risk curves are both continuous curves. But the risk curves for the road networks will be presented as discontinuous lines with two stairs because the applied roads

vulnerability function is a step function. In this section, we only display the risk curves for the two selected types of buildings.

It is unrealistic to depict the risk curves of all of the one-hectare cells in the research domain as the number of valid cells will be around 0.27 million. The administrative district boundary can divide the research area into several smaller regions. We select eight cells that are from eight different administrative districts as examples. Figure 6-10 illustrates the risk curves for residential and non-residential buildings due to multi-source flooding on the eight cells. The vertical axis indicates the economic loss of buildings and the horizontal axis shows the return period of the potential flood events.

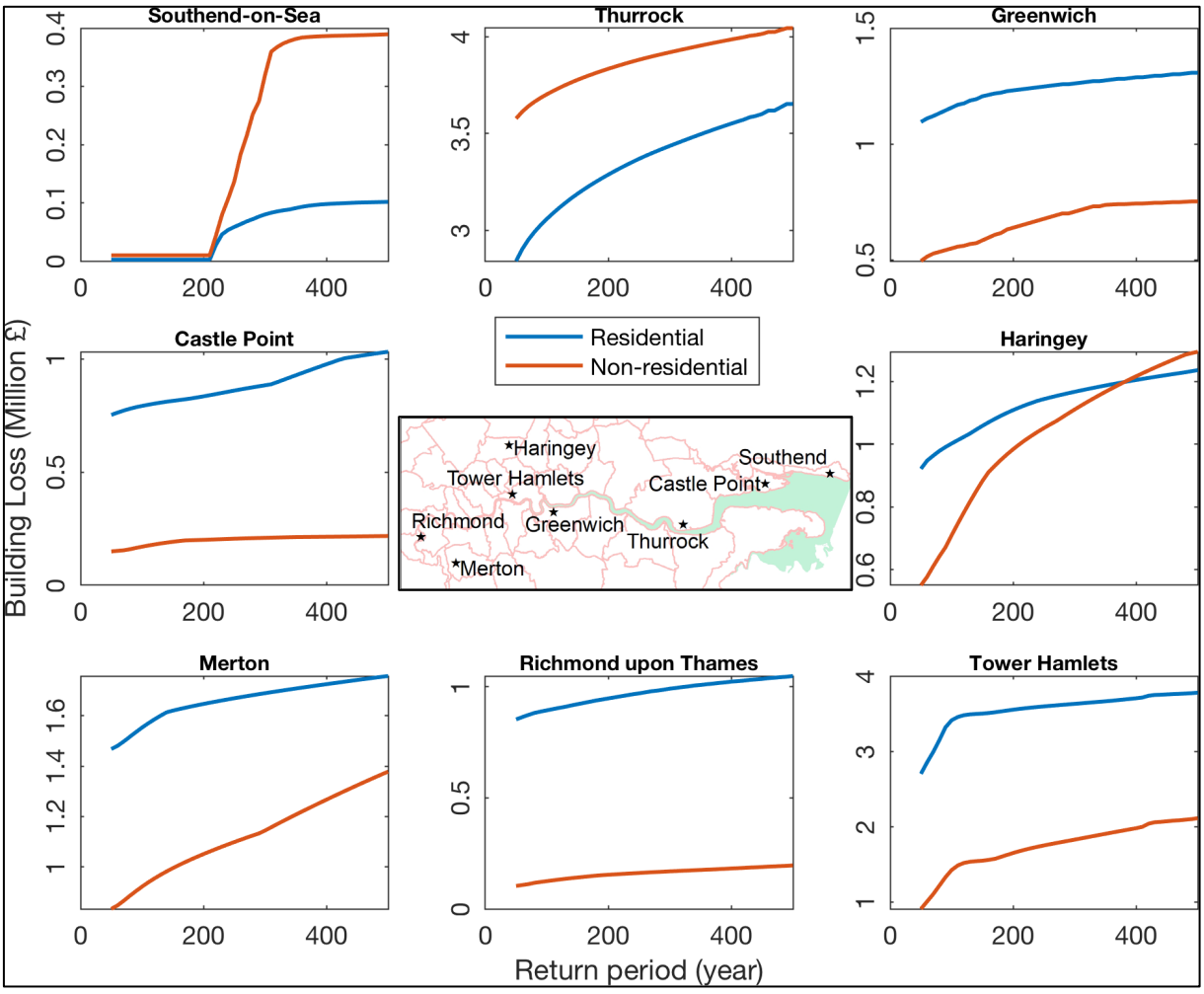

Figure 6-10. Risk curves for residential and non-residential buildings due to multi-source flooding at the eight grid cells as indicated on the map at the centre.

In the first plot of Figure 6-10, the risk of loss stays in zero until the return period getting higher than 200-year for both types of buildings in the cell in Southend. The reason may be that Southend is well protected from up to 200-year event but can be seriously flooded when a higher return period surge overtops the flood defence walls. The comparison between the risk

of residential and non-residential buildings can be made according to the position of the two types of the risk curve. For the cells from Southend and Thurrock, the non-residential buildings are at higher risk than the residential buildings. On the contrary, the residential buildings in the cells from Greenwich, Castle Point, Merton, Richmond, and Tower Hamlets are more likely to suffer from economic loss than the non-residential buildings. For the cell located in Haringey, the two risk curves across each other make it difficult to conclude which type of building is at higher risk, and it is, therefore, necessary to calculate the expected average loss.

6.5.2 Risk maps of average annual loss

A risk map depicts the spatial distribution of the risk levels on the whole research area. It is widely used for qualitative and semi-quantitative risk assessment by visualizing the risk rank or risk index of each assessing unit. In this thesis, we draw the risk map with the annual average loss (AAL) on each grid cell, providing both qualitative risk comparison and quantitative loss prediction. The AAL is derived from the risk curves indicating the annual non-exceedance probability of loss, which is the mathematical expectation of the risk function. Every cell inside the Greater London catchment with the AAL value larger than zero is displayed on the map with colour depth to reflect the value.

The risk map for residential buildings is illustrated in Figure 6-11. Each pixel in the map indicates the expected annual economic loss of the residential houses due to flooding. The value is a long-period expectation that does not suggest the specific quantity of loss can be expected every year. The south riverside area of the Thames in the city centre shows the very high AAL values, suggesting it is the most dangerous region exposed to flooding. According to the inundation map in Figure 6-2, the south coast of the Thame estuary is easy to be flooded. However, the AAL in that area is almost zero because of the lack of buildings there, which is a typical example to show the importance of exposure analysis in risk assessment.

Figure 6-12 is the AAL risk map for non-residential buildings. The pixel value is the aggregated AAL of all types of non-residential properties due to flooding. The spatial distribution of the AAL in the research area is similar to it in the risk map of residential houses. The significant differences between the two maps can be found in the Canvey Island and Southend located in the north of the Thames estuary. The AAL of non-residential properties is lower than that of residential buildings in those two regions. It is also because of the different exposure of the two elements.

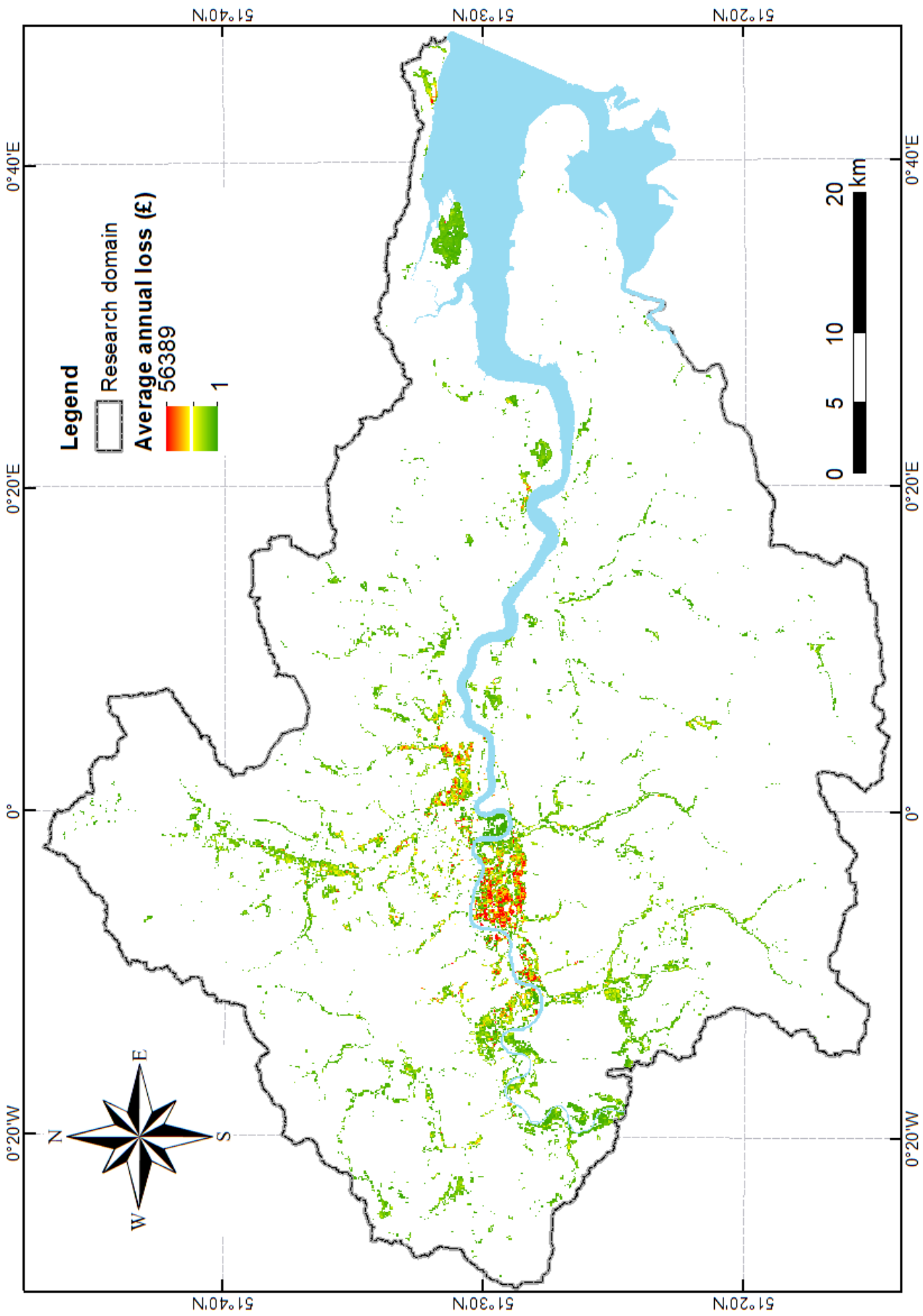

Figure 6-11. Average annual loss of residential buildings due to multi-source flooding.

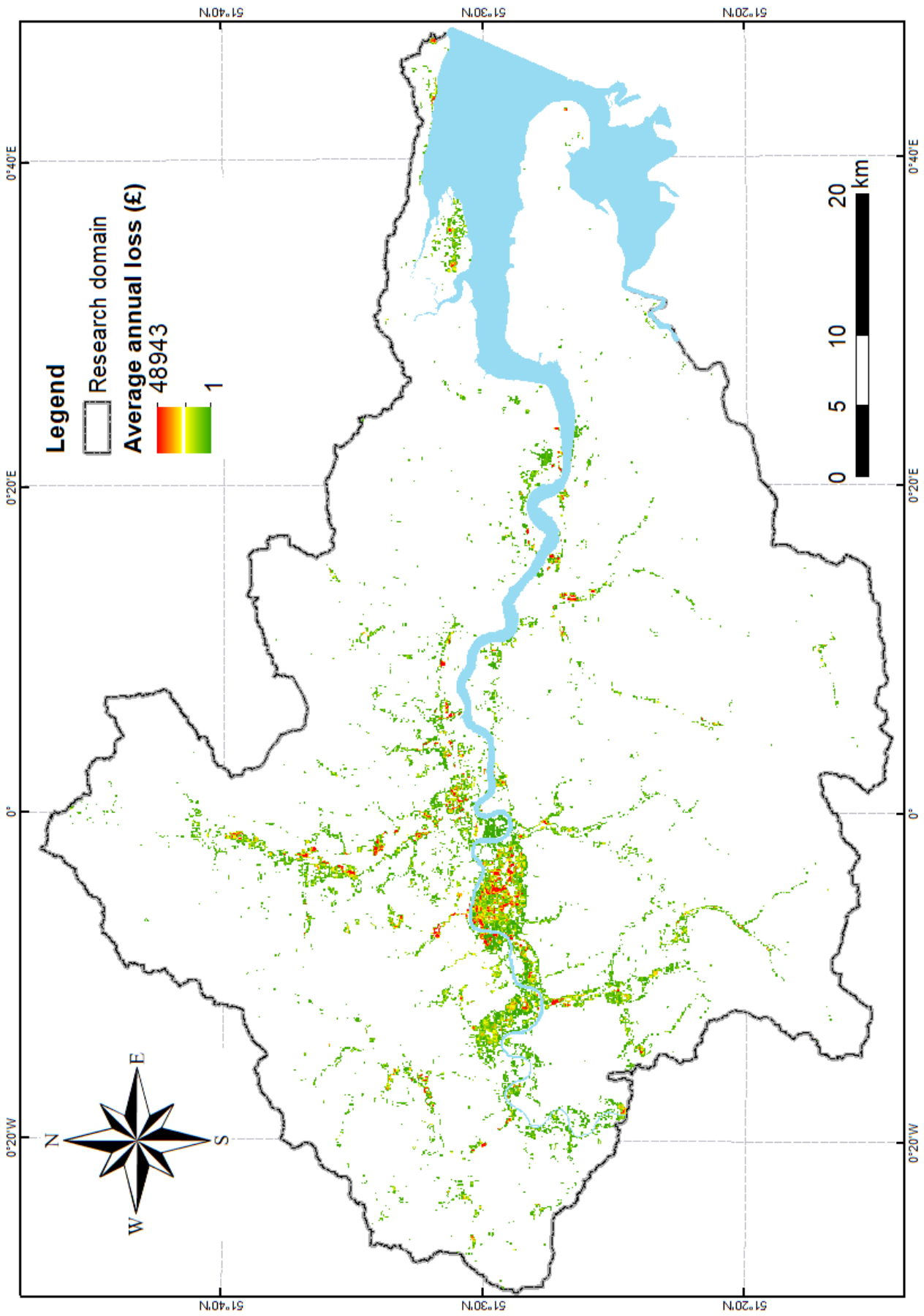

Figure 6-12. Average annual loss of non-residential buildings due to multi-source flooding.

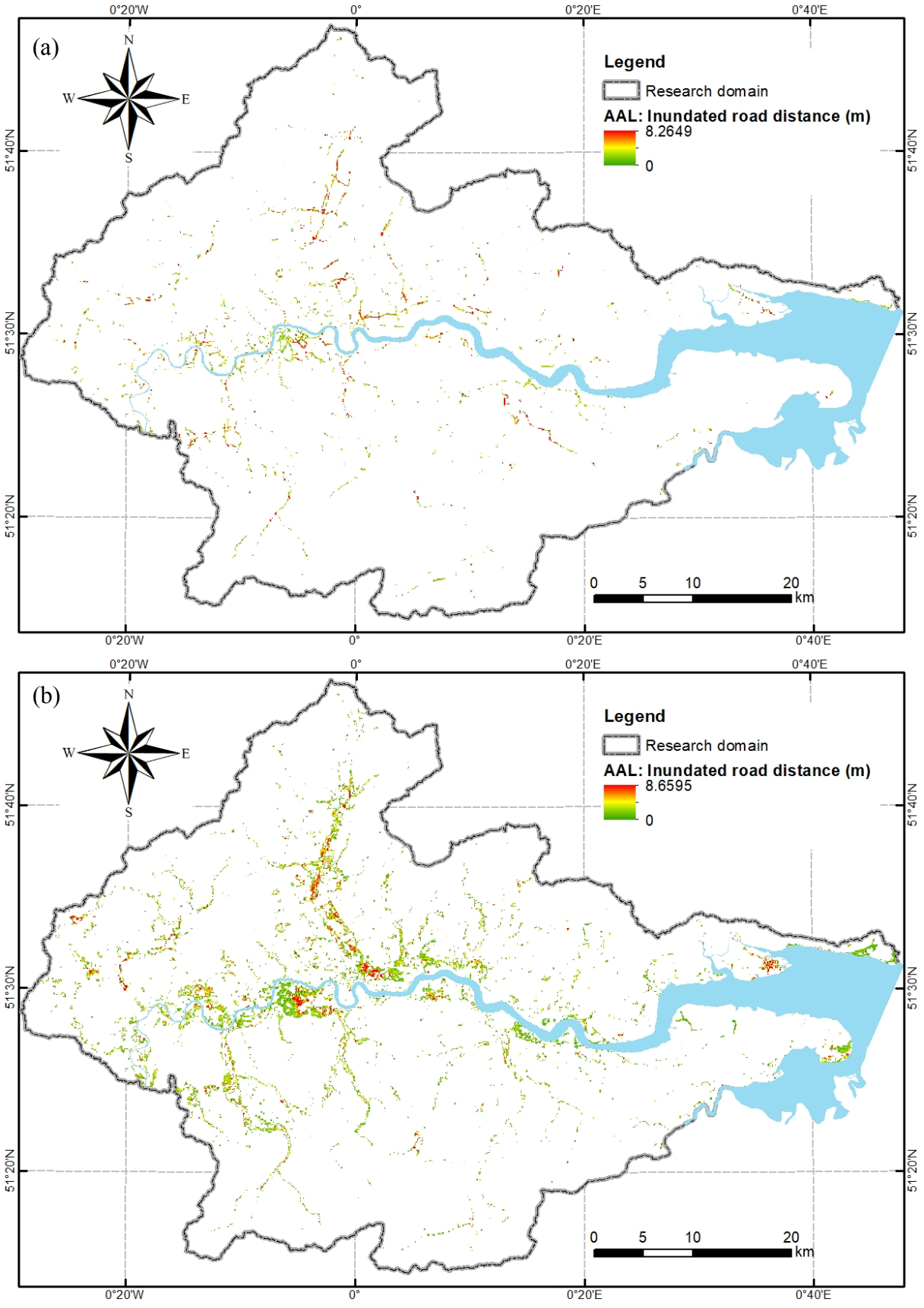

Figure 6-13. Average annual inundated distance for (a) major roads and (b) local roads.

The economic loss of road networks from flooding is not worked out in this work due to the high complexity of the transportation systems and the lack of traffic data. As a compromise,

we use the inundated length to measure the loss of road networks. Figure 6-13 shows the average annual inundated distance of major roads in the top panel and local roads in the bottom panel. Since the local road networks are denser than the major road networks, the area with high expected loss value is significantly larger in the risk map of the local road. The high-risk region of the local roads is generally in accordance with the distribution of residential properties. In contrast, the risky region of the major roads is discretely distributed over the entire research domain.

6.6 Conclusions

This chapter has comprehensively introduced the process of multi-hazard risk assessment and demonstrated the functions of the three components of risk analysis. Integrated inundation maps are produced for the Greater London catchment based on the hazard curves generated from the joint probability analysis and hydrodynamic modelling. The area with expected annual average inundation (shown in Figure 6-2) over 0.3 meter is 101.63 km^2 and mostly distributed along the Thames riverside. Risk curves are generated to quantify the possibility of disaster loss and illustrated in Figure 6-10 for buildings at eight different locations. Risk maps showing average annual loss are produced according to the risk curves on each grid cell for residential buildings (Figure 6-11), non-residential buildings (Figure 6-12), and road networks (Figure 6-13), respectively. The total expected average annual loss is £35.8m for residential buildings and £32.7m for non-residential buildings.

The risk assessment framework is able to produce fully quantitative results either as the risk curves of each assessing unit or the risk maps showing the average annual loss of elements at risk. Risk maps provide a general pattern of loss levels due to multi-hazard flooding for the whole Great London Catchment. It can be further calibrated with more detailed information about the exposure and vulnerability attributes in smaller regions. The risk assessment framework is an important reference tool to decision makers and residents for various flood risk reduction purposes.

Chapter 7. A forecasting system for multi-hazard flood and risk

This chapter is to extend the proposed risk assessment framework to a risk forecasting framework to predict floods and the resultant damage. The structure of the forecasting framework is firstly introduced. Then, it is applied to the Eden catchment as a case study followed by results analysis and discussion about model resolutions and uncertainties.

7.1 Introduction

With the rapid development of Numerical Weather Prediction (NWP) models (Bauer et al., 2015), short-term forecasting has become possible for certain water-related hazards like rainfall and storm surge. If an entire basin is used as the flood modelling domain, only two types of hazard need to be considered, i.e. rainfall over the entire domain and tide or surge imposed through boundary conditions. The risk assessment framework presented in the previous chapters can be extended to develop a risk forecasting system if the prediction of hazards is available. This chapter is to build a real-time forecasting system for intense rainfall-induced flooding and the resulting risk of economic loss. Two hazards are recognised as the potential drivers of flooding: extreme rainfall over the catchment region, and the total water level on the outlet of the catchment. The hazard simulation and vulnerability analysis modules are employed in the forecasting system to predict the flood inundation and potential loss. This chapter aims to 1) demonstrate the feasibility of applying the fully 2D hydrodynamic model for real-time forecasting of intense-rainfall triggered flooding over broad catchments, 2) investigate the effect of spatial resolution on the simulating results and lead time of the forecasting, and 3) evaluate the effect of cascading prediction errors from the NWP model to the hydrodynamic model.

7.2 The framework of the flood and risk forecasting system

The structure of the proposed flood forecasting system is illustrated in Figure 7-1, in which the hydrodynamic model HiPIMS is driven by the UKV rainfall forecasts to predict full-scale flooding processes across the pre-defined simulation domain (e.g. a catchment or a city). A

high-resolution digital elevation model (DEM) of the domain is needed to set up HiPIMS for flood simulation. Human-related interventions, e.g. flood defences, are considered when processing the topographic data to create the final DEM. Other relevant datasets including landcover information and soil properties are also required to estimate model parameters. Initial conditions (water depth and velocities in the domain) for starting a simulation may be generated by pre-running the model using antecedent rainfall data from observations or UKV predictions. The potential impact of the storm surge in catchment outlets is considered by imposing the sea level predictions as boundary conditions.

If available, river gauge and other field observations may be used to calibrate and validate the model. The HiPIMS-based forecasting system will produce tempo-spatial varying flood depths and velocities across the entire simulation domain, which can then be further processed to produce predicted inundation maps and other necessary flood information for issuing warnings. The simulation results can also be used to support flood risk analysis by superimposing the relevant exposure data and vulnerability curves.

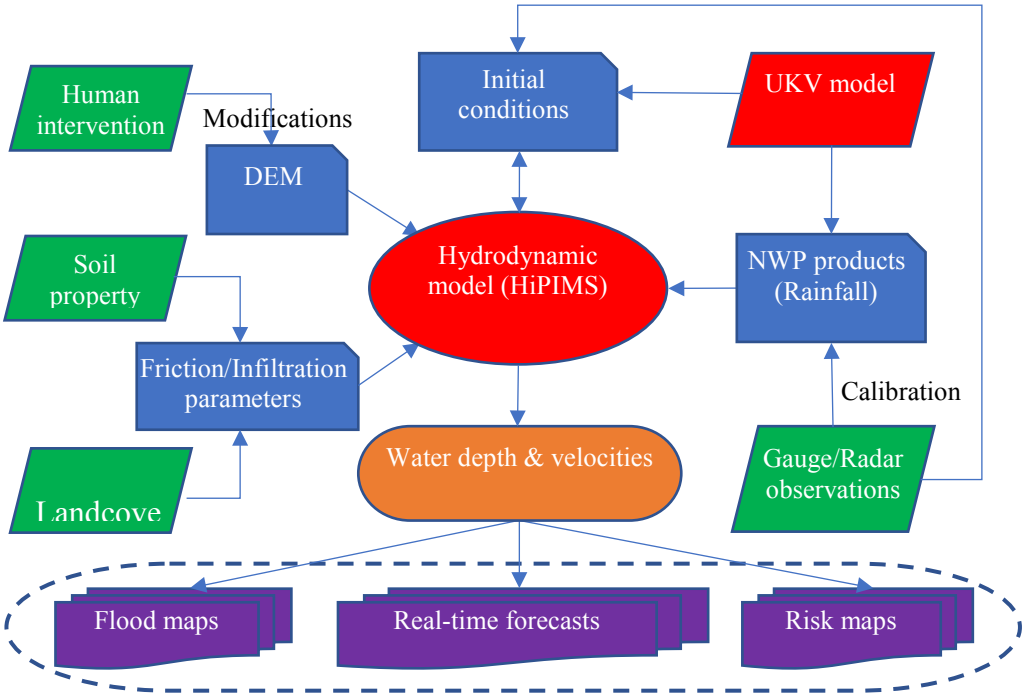

Figure 7-1. Real-time forecasting system for intense-rainfall induced flooding.

7.2.1 NWP model

NWP products from the UKV model (Davies et al., 2005) is used in this work to drive HiPIMS for real-time forecasting. The UKV model domain covers the entire Britain and Ireland (Tang et al., 2013) at a resolution of 1.5 km over its center and 4 km along its edges. It is the finest available resolution for short-range weather forecasting in the UK, which is able

to represent most convective dynamics without using a convection parameterization scheme (Lean et al., 2008). The operational UKV system has been running in real time since 2010 by the Met Office, using 3 hourly cycling 3D variational Data Assimilation (3D-Var) to generate weather forecasts up to 36 hours in every 6 hours (Ballard et al., 2016).

The UKV model outputs are deposited at the Centre for Environmental Data Analysis (CEDA) and stored as binary files in Met Office pp format which can be converted into the NetCDF format via an open software tool XCONV. The rainfall forecast data is output as gridded format on a rotated latitude-longitude projection and can be transformed to the Ordnance Survey National Grid (BNG) reference system at a spatial resolution of 1.5 km, which can be directly used as precipitation inputs to drive HiPIMS for flood simulation.

7.2.2 Real-time simulation and visualization

The UKV model is currently running at real-time by the Met Office and keeps producing forecasting outputs every 6 hours. A monitor module is running to download the weather prediction from UKV model once a new output is generated and monitor the predicted rainfall rate inside the system domain. The initial conditions of water depth and velocity are first created based on the previous rainfall forecasts and then daily calibrated with river stage observations. Once the predicted 36-hour accumulated rainfall is higher than the "warning" threshold, the hydrodynamic model is brought into operation with the prepared initial conditions and keeps running until the end of the rainfall event.

The simulated inundation depth and velocity can be output at any given time within the forecasting duration, typically 36 hours. The instant output is transferred into a KML file and visualised timely using Google Earth, showing the inundation on the local maps with surface details, like buildings, roads, and farmland. The predicted maximum flood depth throughout the forecasting period is generated once the simulation is finished and can be used to provide precise flooding forecasts for each cell inside the model domain. The threshold to release a flood warning is when a region with properties experiences inundation higher than 0.3 m in the hydrodynamic model. The risk prediction is issued together with the flood warning and visualised as risk maps.

7.3 Case study: the Eden Catchment

7.3.1 Catchment and data

The flood forecasting system is applied to the Eden catchment (see Figure 1-2) located in the northwest of England with an approximate area of 2500 km^2. The main rivercourse is the River Eden flowing from southeast to northwest with main tributaries including Caldew, Petteril, Eamont on its left and Irthing on its right. The predominant land-use in the catchment is rural, while only 1% of the area is urban. The largest settlement is Carlisle lying at the lower Eden with a population of 75000, around one-third of the whole population living in the catchment. The average annual rainfall in this area can exceed 2800 mm, which is three times of the average for the whole England.

Eden is a rapid-responding catchment to fluvial floods due to its steep topography in the upper areas. But there is no significant risk of tidal flooding within the region (Environment Agency, 2009). The lower catchment area like Carlisle suffers a lot from serious floods in history, especially the events in January 2005 and December 2015. Therefore, we choose this area as the pilot region to build and test the proposed flood forecasting system.

The terrain data (DEM) is from the Digimap for land surface and buildings with 5 m resolution. The river bathymetry is not reflected in the terrain data but is very important for accurate hydrodynamic modelling. So, the surveyed river cross-sections for part of Eden and its principal tributaries from available from EA are merged into the original DEM to setup the forecasting system.

Rainfall is the critical data to test and run the model. The rainfall rate with 1.5 km spatial resolution and 15 min time resolution from UKV model is the precipitation source. And the rainfall radar data from the Met Office NIMROD system is regarded as the ‘true’ observed rainfall to make a comparison with the flood predicted driven by the UKV outputs. This dataset gives the best possible estimation of surface precipitation rate with 1 km resolution based on radar sites and processed using optimum quality control and correction procedures (Met Office, 2003). Tide is not the direct threat to this area in the history but a high sea level during flooding may reduce the speed of river flow in the downstream basin and hence influence the flooding process. HiPIMS uses tide predictions from the National Oceanography Centre (NOC) as boundary conditions to reflect the tidal effect.

7.3.2 Model setup and validation

The model is validated against a flood event occurred in Eden catchment on 6th December 2015. It was caused by Storm Desmond that brought a period of heavy and prolonged rainfall from the 4th to the 7th of December. The amount of rainfall in one day and two consecutive days set new history records in the catchment, and so did the flow rate in River Eden (Environment Agency, 2016). Time series of the average and median rainfall across the whole domain is given in Figure 7-2, based on the NIMROD rainfall radar data. As the largest settlement within the catchment locating at the downstream, Carlisle was seriously flooded during the event. The surveyed flood extent is shown in Figure 7-3, which will be used to validate simulation results.

As the details about setting up HiPIMS in the Eden catchment has been described in Xia et al. (2018), herein the procedures are only briefly introduced with the results of model validation. HiPIMS is calibrated over a spatial resolution of 20 m for this case. The initial conditions of water depth and velocity, infiltration rate, and Manning coefficient in each grid cell inside the domain are required to set up and run HiPIMS. Three days of rainfall data before the 4th of December 2015 is run in advance over a dry DEM to generate the required initial conditions. The land was saturated at the beginning of the flood event as it had already recorded more than twice of the monthly average rainfall during November before Storm Desmond (Environment Agency, 2016). Therefore, the parameter of infiltration rate is set to zero. Manning coefficient for each type of land cover is given based on the values suggested by Chow (1959).

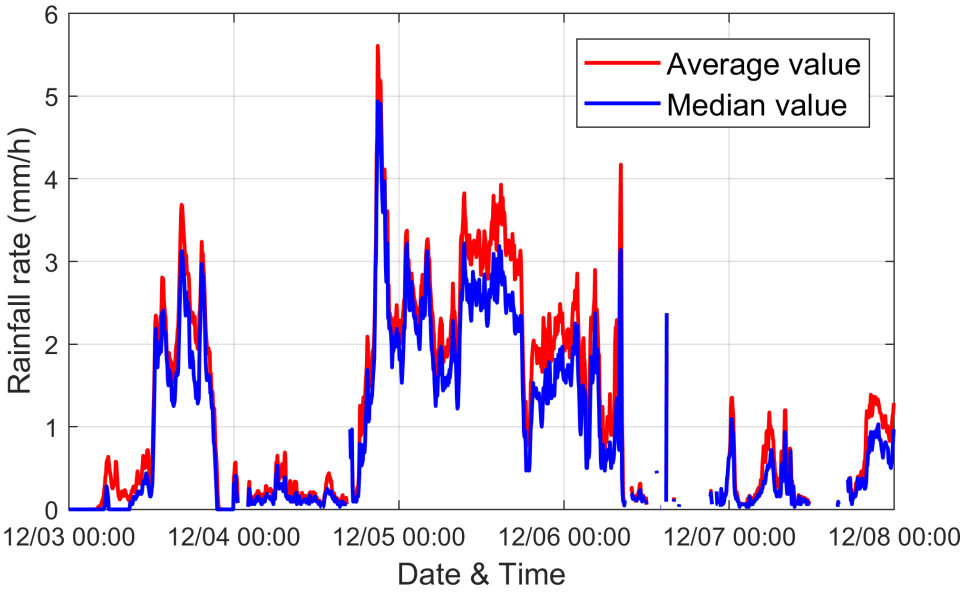

Figure 7-2. Average and median rainfall rate in Eden Catchment due to Storm Desmond in 2015

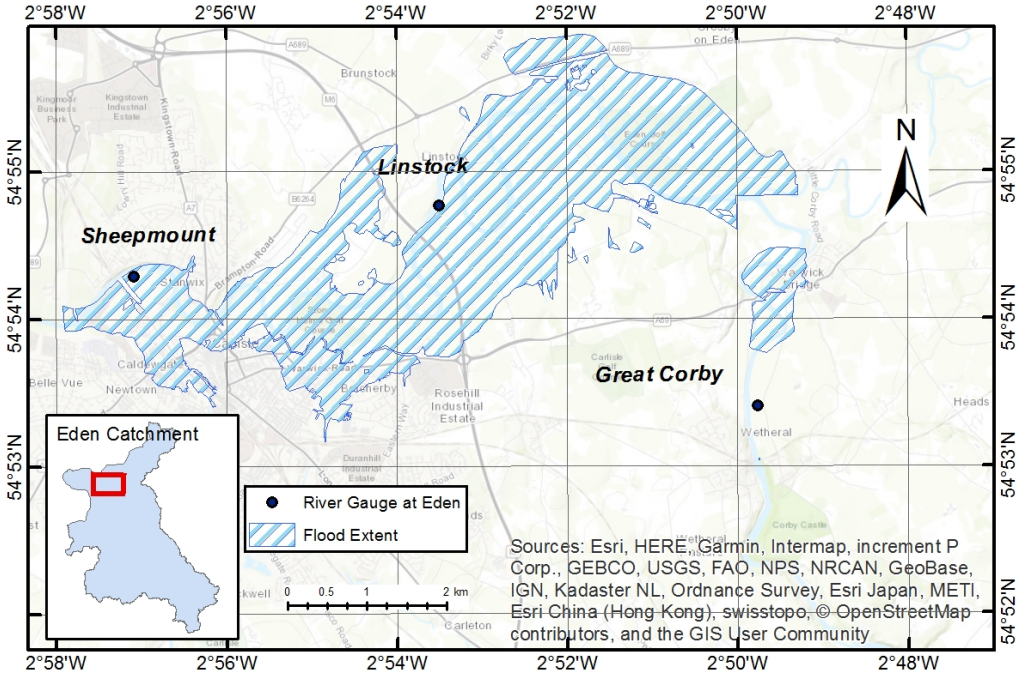

Figure 7-3. Flood extent map in Carlisle due to Storm Desmond on 6th Dec 2015 and the location of some river gauges.

Figure 7-4 presents the simulated and observed hydrographs at the three gauges located upstream (Great Corby), midstream (Linstock), and downstream (Sheepmount) in the Eden and the inundation extent around Carlisle for the two and half days flood caused by Storm Desmond. The red lines in Figure 7-4-(a) sketches the EA surveyed flood extent next to Carlisle and the blue area shows the simulated maximum water depth throughout the flood event. It can be observed that the surveyed flood extent is correctly reproduced by the current model to a large extent.

The Nash-Sutcliffe Efficiency (NSE) coefficient (McCuen et al., 2006) is used to assess the goodness of fit of the hydrodynamic model, which is denoted as

$$NSE = 1 - \frac{\sum_1^N (\hat{Y}_i - Y_i)}{\sum_1^N (Y_i - \bar{Y})} \tag{7-1}$$

in which $\hat{Y}_i$ and Y_i are the predicted and observed water depth, respectively, and $\bar{Y}$ is the mean of the measured values of Y. NSE will range from 0 to +1 if the predictions of linear model are unbiased. Otherwise, it may be negative. The closer the NSE is to 1, the better match between the predictions and observations.

The NSEs are respectively 0.82, 0.72 and 0.76 at Great Corby, Linstock and Sheepmount, confirming accurate forecasting of the water levels. The predicted peak water level is higher

than the observations. This may be because the radar rainfall data is underestimated compared to the real rainfall in the catchment. Generally, the temporal change of the water level is captured reasonably well in all of the three gauges although small underestimates appear in all hydrographs.

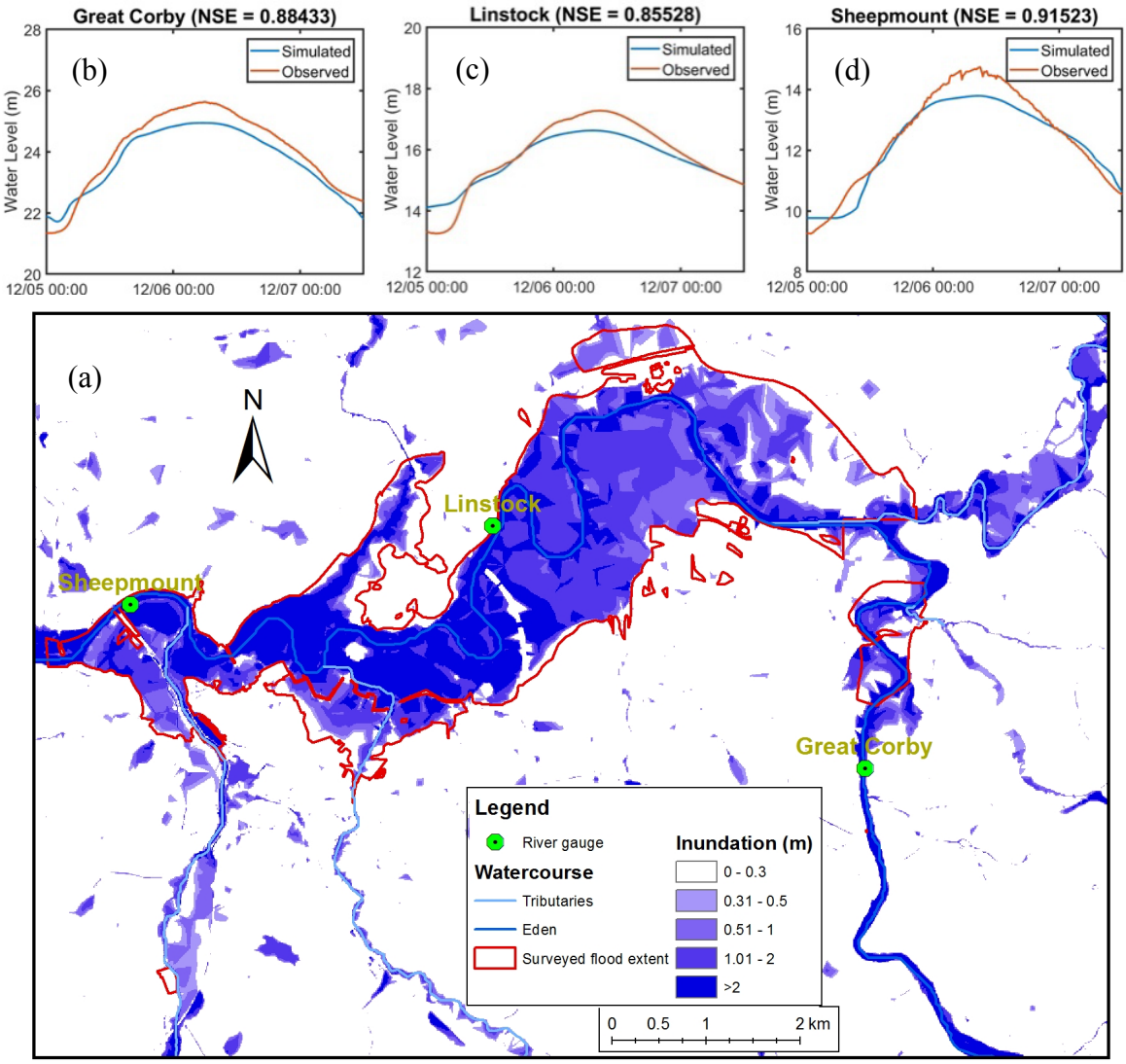

Figure 7-4. Simulated and Observed water level for different gauges at Eden with Nash-Sutcliffe Efficient (NSE) during the flood event caused by Storm Desmond.

7.3.3 Flood simulation with forecast rainfall

After HiPIMS is calibrated with suitable model parameters, the forecasted rainfall from UKV model can be used to drive HiPIMS for real-time flood forecasting. The lead time of the UKV forecasts is 36 hours, and the rainfall prediction is compared with NIMROD radar rainfall at Eden catchment. Figure 7-5 illustrates the maps of 36-hour accumulated rainfall outputs from NIMROD radar and UKV model throughout the event from 2015-12-04 21:00 to 2015-12-06 9:00 when the region experienced the most intense rainfall. NIMROD radar has a higher

resolution 1 km against the 1.5 km resolution of UKV. The spatial distribution of rainfall predicted by UKV is slightly biased to the northeast compared with radar rainfall, leading to the heavy rainfall belt (the yellow region in the maps) situated more inside the Eden catchment (shown by the red outline).

Figure 7-6 shows the comparison of bar plots between radar and UKV hourly rainfall at the grids within Eden Catchment. For the first 30 hours of prediction, the mean and median value of rainfall inside the domain from UKV forecast are generally higher than the values from NIMROD radar, which means the rainfall is overestimated. While in the last 6 hours, the UKV model underestimated the rainfall. Nonetheless, the rainfall prediction of UKV still compares reasonably well with the radar records in terms of spatial distribution, intensity and the temporal profile and is well suited for application in the flood forecasting system.

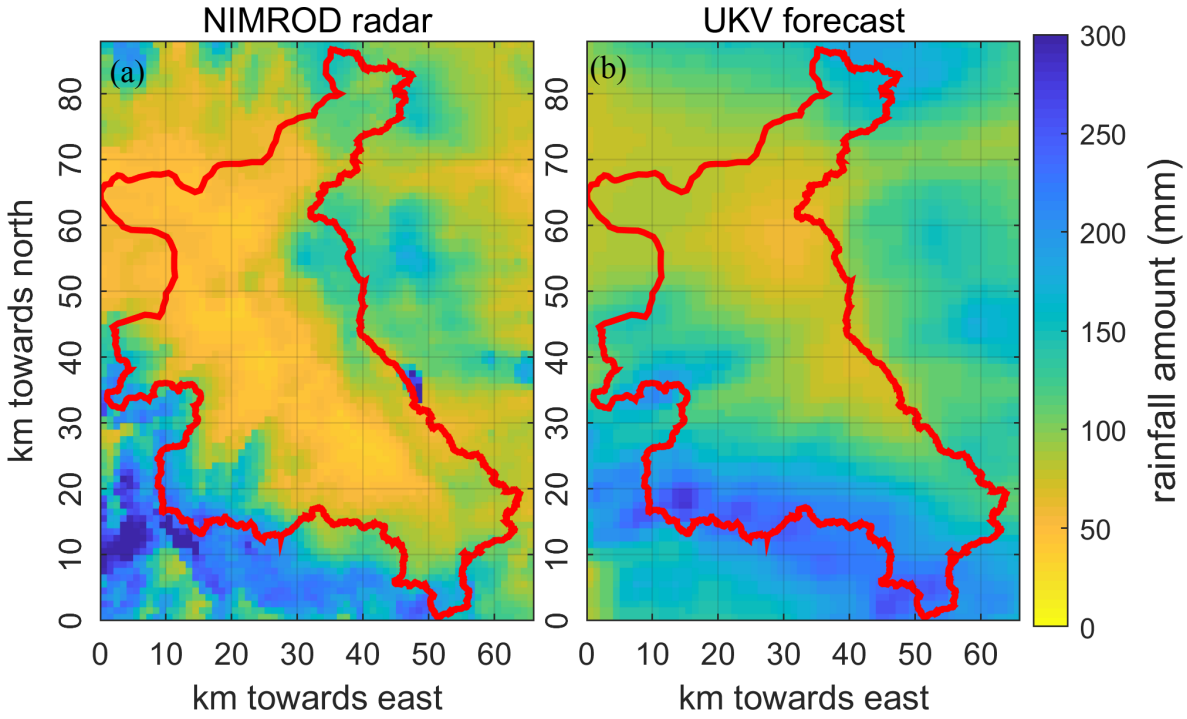

Figure 7-5. The grid-based maps of 36-hour accumulated rainfall from 2015-12-04 21:00 to 2015-12-06 9:00: (a). NIMROD radar rainfall, (b). UKV model forecast rainfall. Red line is the outline of Eden catchment.

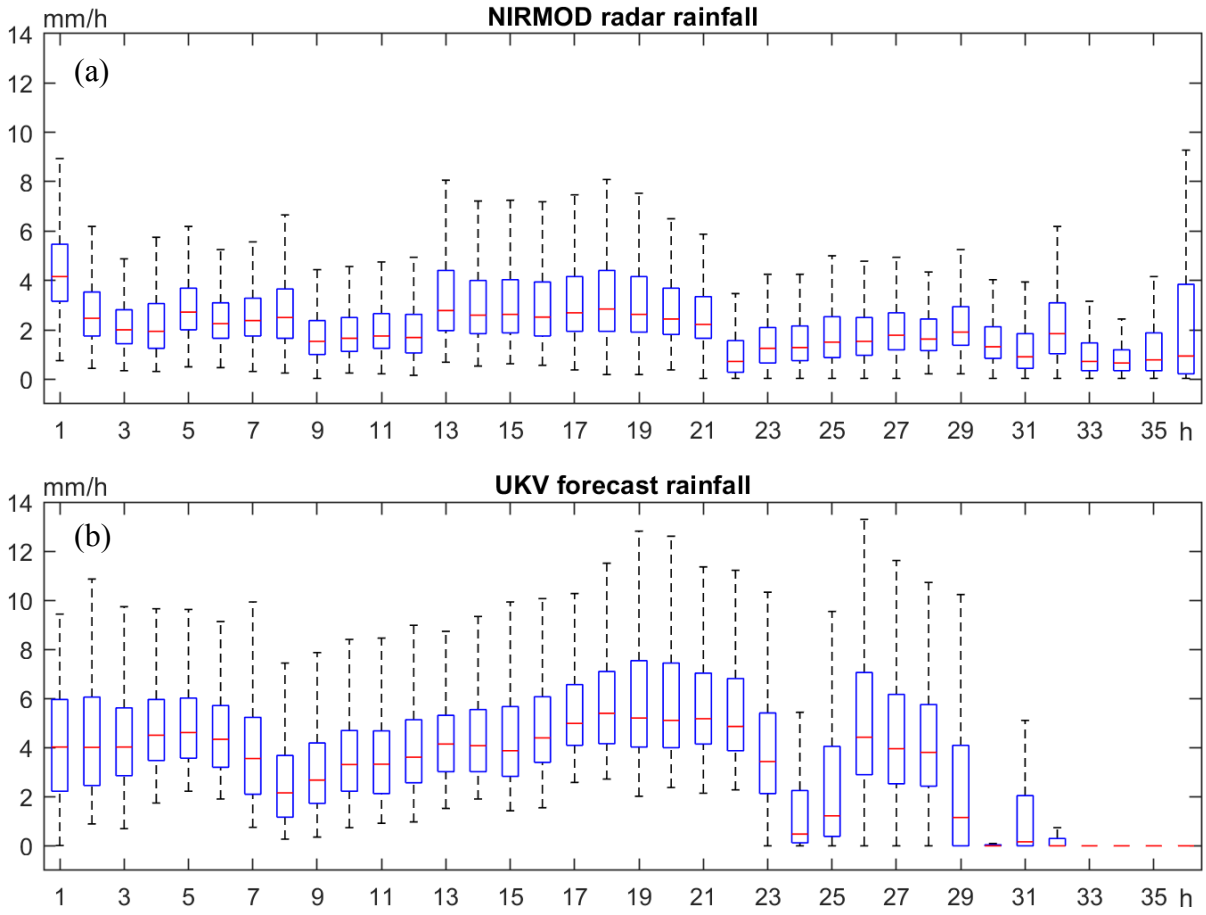

Figure 7-6. Bar plots of hourly rainfall.

In real-time operation of the flood forecasting system, rainfall predictions are imported to HiPIMS once it is released from UKV model, that is, rainfall in HiPIMS is updated every 6 hours and the model simulation time is 36 hours. But to test the forecast system with the flood event caused by Storm Desmond, we run the HiPIMS model for a longer duration covering the entire process, which is 84 hours (three and half day) starting from 2015-12-04 12:00 and ending at 2015-12-08 00:00.

A higher spatial resolution can result in a better accuracy of hydrodynamic modelling, but it also means the model is more computing-expensive, which may restrict the lead time when employed in a flood forecasting system. A 20 m grid was previously used to validate HiPIMS with radar rainfall data in the catchment. For flood forecasting, it is worth to test the efficiency and computing time of different spatial resolutions and find the optimal choice in consideration of the lead time. The forecast model is performed over several different DEM grids with resolutions of 10 m, 20 m, 30 m and 50 m. All the cases are executed on the same device so that the run time is comparable. The lead time of the whole forecasting system is then calculated based on the lead time of UKV model and the runtime of HiPIMS.

UKV model is a determinative model that produces one prediction in each output. Uncertainties from UKV model may propagate to HiPIMS and generate flood maps with uncertain errors. To evaluate the impact of the uncertainties, rainfall predictions with error levels of $\pm$10% and $\pm$20% are used to drive HiPIMS. The "error" results are compared with the result simulated with the original UKV forecast to assess the uncertainties in flood maps.

7.4 Results

A series of simulations with different grid resolutions and different rainfall sources (forecast or radar) are conducted at the whole Eden catchment. Results showing the water level at the three gauges at Eden and the flood extent at Carlisle are compared with observations.

7.4.1 Sensitivity of grid resolutions

Firstly, we use radar rainfall data to drive the flood forecasting system over various spatial resolutions and intend to select the most reasonable resolution for flood forecasting. Figure 7-7 shows the maximum inundation depths and area in the downstream of Eden near Carlisle as simulated at spatial resolutions of 50 m (Figure 7-7-(a)), 30 m (Figure 7-7-(b)), 20 m (Figure 7-7-(c)) and 10 m (Figure 7-7-(d)). In comparison with the surveyed flood extent indicated by red lines, the results from the simulation at 30 m resolution is better matched than the results of 50 m simulation. However, from a general point of view, there is no apparent difference from Figure 7-7-(b) to Figure 7-7-(d), suggesting that higher resolution above 30 m does not result in significant improvement in model performance in terms of flood extent.

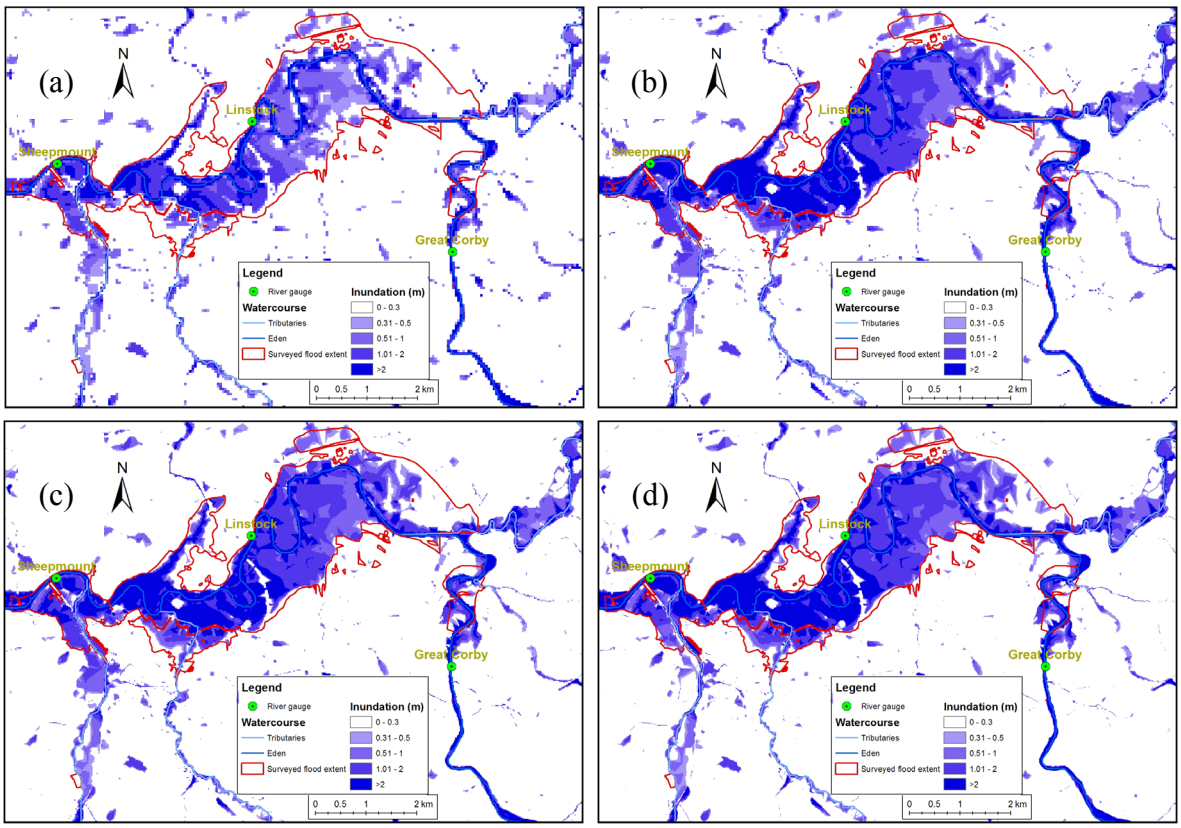

Figure 7-7. Simulated flood extent due to radar rainfall in comparison with investigated flood area. (a) simulation over 50 m grid; (b) simulation over 30 m grid; (c) simulation over 20 m grid; (d) simulation over 10 m grid.

For more quantitative evaluation, the water levels recorded at Great Corby, Linstock, and Sheepmount from different simulations are compared in Figure 7-8. It shows that the water level predictions from the 50 m simulation are far deviated from the corresponding observations while the water level hydrograph of 30 m simulation matches well at Great Corby and Linstock but not at the downstream gauge Sheepmount. The simulated hydrograph of 20 m and 10 m look quite similar and both well matched with the observations.

Looking at the model performance table (Table 7-1), it appears that the model performance indicated by NSE increases from the resolution of 50 m to 10 m. In contrast, the computing time of HiPIMS rises dramatically with higher spatial resolutions especially from 20 m to 10 m. The lead time of forecasting system is calculated based on the lead time of UKV model (36 h) and the runtime of HiPIMS. Table 7-1 shows that with the multi-GPU devices introduced in Section 3.4, the 20 m resolution forecasting system can give flood warning more than 34 hours in advance while the 10 m model system is capable for 20-hour forecast. As there is no significant improvement from 20 m to 10 m regarding the model performance, but 14-hour lead time can be gained if we choose 20 m instead of 10 m, we can conclude that

20 m is the reasonable choice for the flood forecasting system at Eden catchment with the current computing capacity.

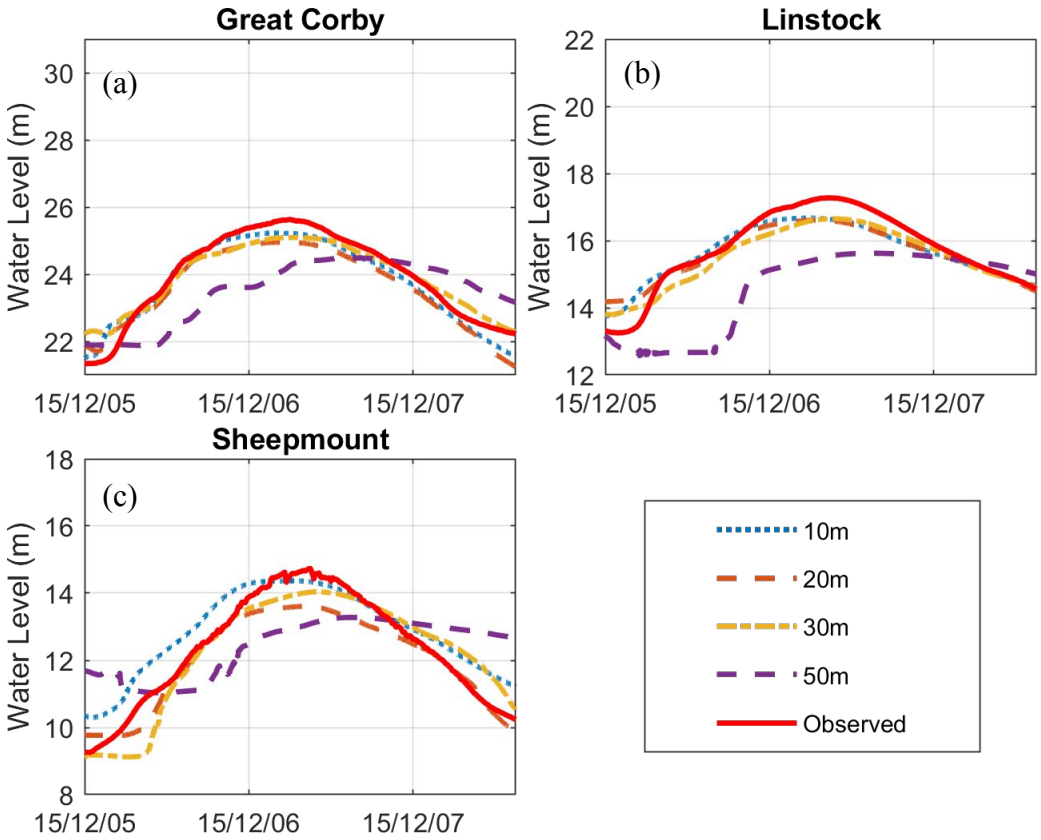

Figure 7-8. Water levels at (a) Great Corby, (b) Linstock, and (c) Sheepmount obtained the simulations of various spatial resolutions.

Table 7-1. Model performance (Nash-Sutcliffe Efficient) and lead time for various spatial resolutions.

Resolution	Nash-Sutcliffe Efficient				Computing Time (For 36h)	Lead Time
	Great Corby	Linstock	Sheepmount	Mean		
50 m	0.27	-0.31	0.31	0.09	6.5 min	35.89h
30 m	0.79	0.86	0.63	0.76	21 min	35.65h
20 m	0.91	0.84	0.90	0.88	1h 30 min	34.50h
10 m	0.95	0.93	0.85	0.91	15h 45 min	20.25h

7.4.2 Performance of forecasting system

From the previous results of sensitivity analysis for grid resolution, 20 m is proved to be a feasible and accurate enough resolution for flood forecasting system in consideration of the currently available data, models, and devices. Therefore, we use the results of 20 m-resolution model driven respectively by radar and NWP rainfall to evaluate the performance of the flood

forecasting system. Simulated flood extents and hydrograph for water level at river gauges are compared with investigations and observations in Figure 7-9. The left figure illustrates the simulated maximum water depth based on forecasted rainfall and the red line indicates the surveyed flood extent. The forecasted flooding is more severe than the flooding simulated using radar rainfall in Figure 7-4-a. It covers a higher ratio of the investigated flooding area but meanwhile exceeds the extent more outside the investigated flooding area. As the UKV rainfall forecast for Storm Desmond is demonstrated to be over-predicted versus the radar rainfall, a more severe flood is expected from the forecasting model, and we cannot judge whether it is better or worse than the simulated flood extent from radar rainfall.

However, the hydrographs of water level at the three river gauges (Figure 7-9 b,c,d) are helpful to provide more detailed information for model performance comparison. The forecasted water level is higher than the simulated results from radar rainfall and higher than the gauge observations, which can be attributed to the positive error of UKV rainfall prediction for Storm Desmond. Table 7-2 presents the NSE for water level simulation of radar and NWP rainfall at Great Corby, Linstock, and Sheepmount, respectively. It is obvious that the NSE from forecasting model is lower than the values from the model of radar rainfall, which is reasonable because the radar rainfall is believed to be more accurate than the forecasted rainfall. Nonetheless, the NSE values at each gauge are high enough to point to good model performance for flood forecasting.

Table 7-2. Model performance (Nash-Sutcliffe Efficient) for the simulation of water level.

Rainfall Data	Great Corby	Linstock	Sheepmount	Average
NWP	0.88	0.74	0.76	0.79
Radar	0.91	0.84	0.90	0.88

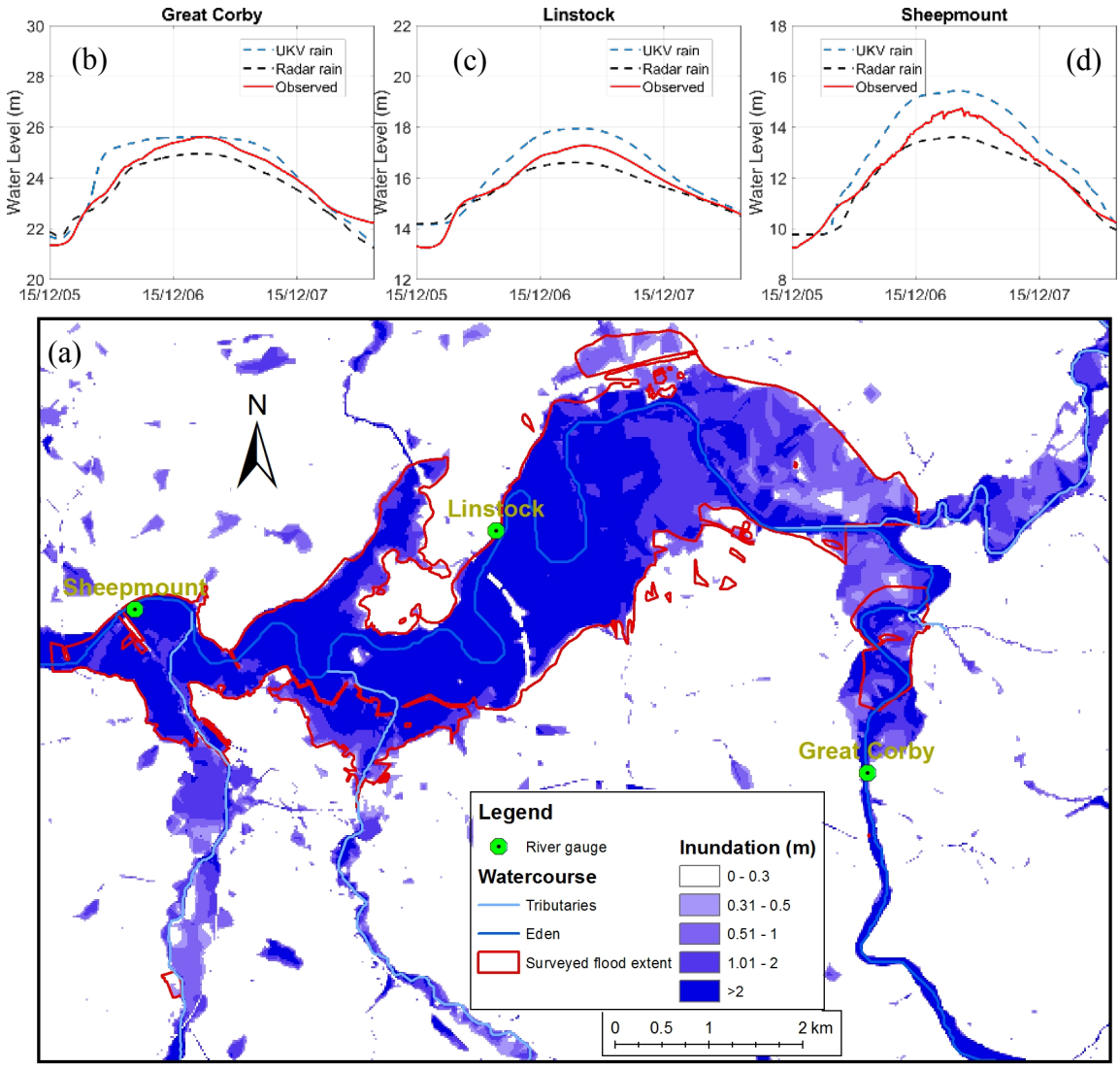

Figure 7-9. Bottom panel: (a) Comparison between surveyed flood extent and simulated flood extent due to forecasted rainfall of Storm Desmond. Top panel: Hydrographs of water level based on (b) observed values, (c) the simulation of forecast rainfall, and (d) the simulation of radar rainfall.

7.4.3 Risk analysis for buildings

According to the risk analysis procedures introduced in Chapter 6, the potential loss can be calculated from the hazard map, vulnerability curve and exposure data. Once the flood forecasting is issued, the predicted inundation depth is combined with the depth/damage function for specific exposures to produce the loss prediction result. Figure 7-10 illustrates the forecasted risk map of building loss due to Storm Desmond in Carlisle. The map gives damage prediction to the residential and non-residential building in Carlisle. Thanks to the high-resolution prediction of the flood from HiPIMS, the risk prediction is configured in each 20 m cell with buildings located. The urban area of Carlisle is in the south bank of the Eden River where two tributaries flow through. The damaged area is mostly situated along the two river branches.

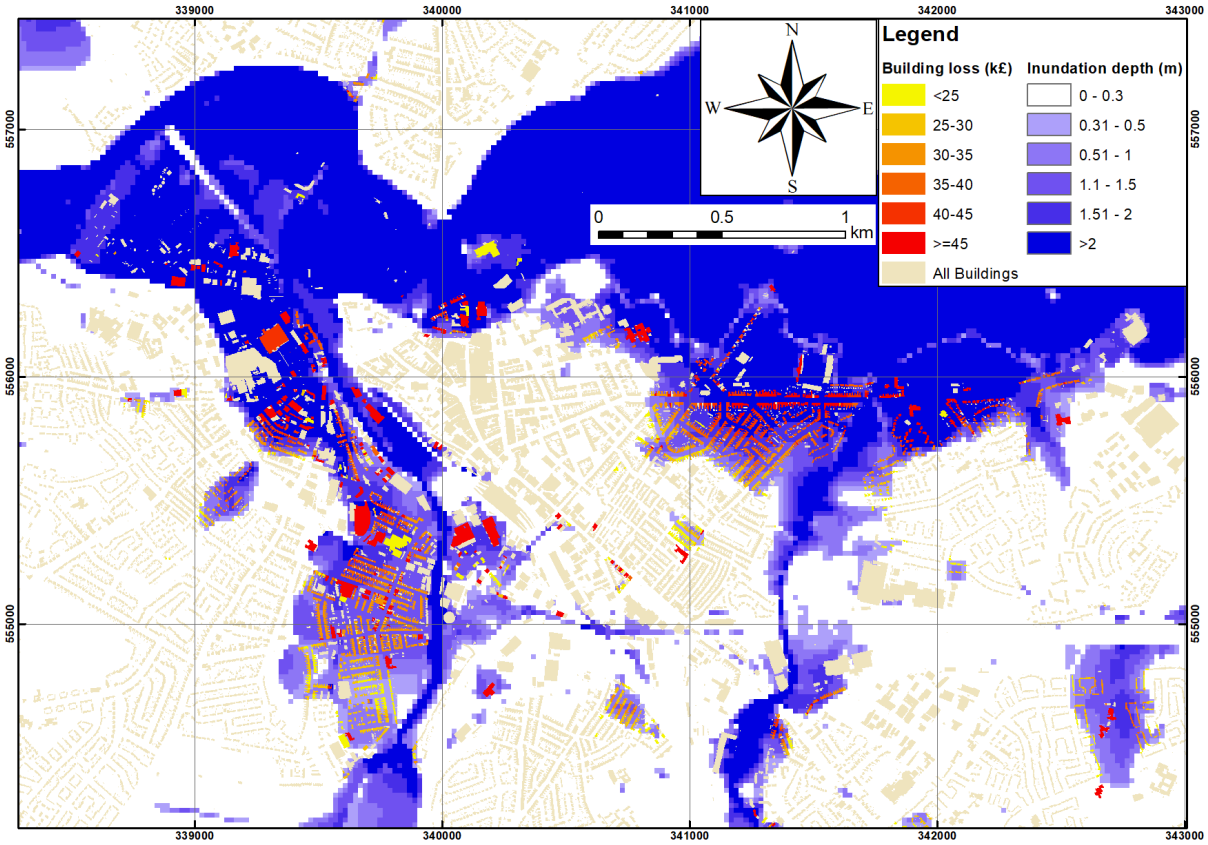

Figure 7-10. Predicted risk map of building loss due to Storm Desmond.

7.4.4 Error cascading

The flood forecasting system is further tested by the UKV predicted rainfall with added error levels of ±10% and ±20%. The hydrographs of water depth at river station Great Corby, Linstock, and Sheepmount from the four error scenarios are compared with the results of model driven by origin rainfall predictions (Figure 7-11). It shows that the error effect for simulated water depth increases from upstream to downstream gauges. But the error deviation from original prediction is relatively small, and even the most significant difference of water depth at Sheepmount locating in the very end of the whole catchment is still less than 1m on a 20% rainfall error level. The root-mean-square error (RMSE) is generally used to quantify the error level regarding the units of the variable calculated by the model, and it can be defined as

$$RMSE = \sqrt{\frac{\sum_{i=1}^{n}(\hat{y}_i - y_i)^2}{n}} \tag{7-2}$$

where $\hat{y}_i$ and y_i usually represent the sample of error predictions and original predictions respectively, and n is the sample size. The values of RMSE for water depth at each gauge are

given in Table 7-3. The relative mean error is calculated by the average RMSE at three gauges divided by their mean water depth respectively, which shows that the error from the rainfall prediction is not amplified by the hydrodynamic model in the forecasting system.

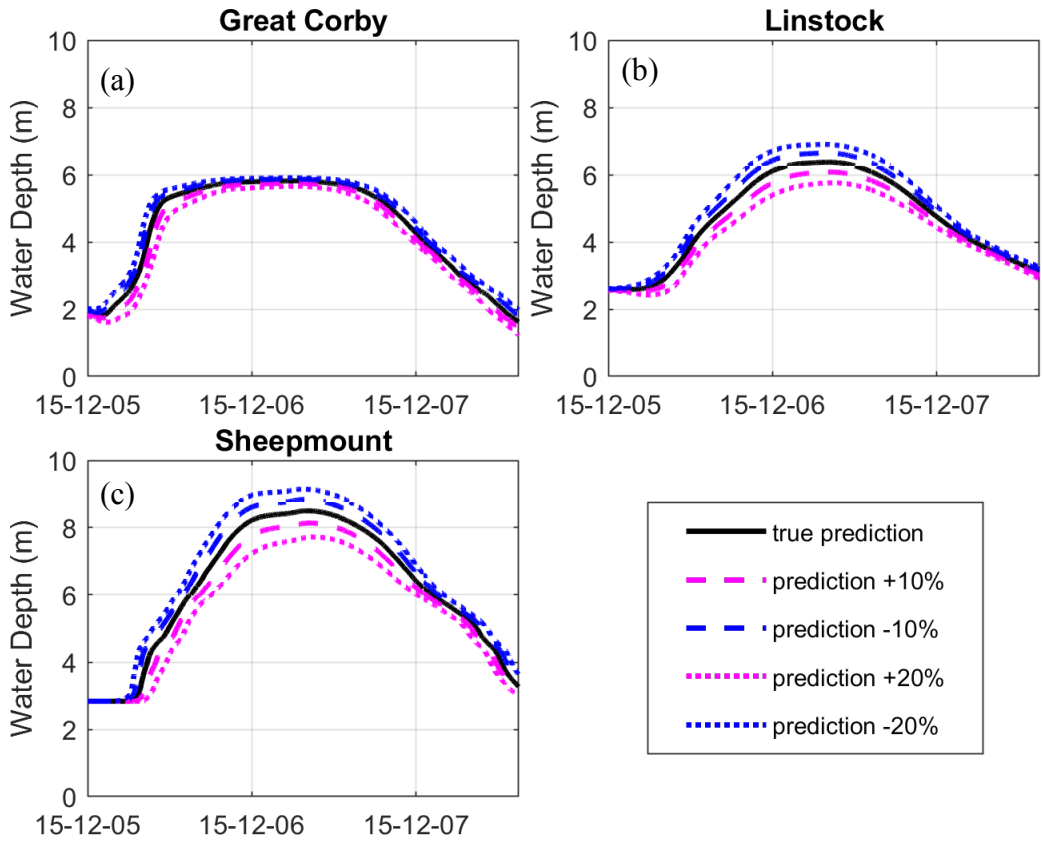

Figure 7-11. Water depth hydrographs from flood simulation model with forecasted rainfall at various error level.

Table 7-3. Error table for water depth with various rainfall error level.

Rainfall error level	**RMSE (m)**				**Relative mean error**
	Great Corby	Linstock	Sheepmount	Average	
+10%	0.18	0.22	0.33	0.25	+4.73%
-10%	0.16	0.22	0.31	0.23	-4.36%
+20%	0.38	0.47	0.69	0.51	+9.91%
-20%	0.30	0.42	0.59	0.43	-8.35%

7.5 Discussion

The situation of man-made flood defence or management facilities such as pumping station, sluice gate or embankment, has a great impact on the severity of the flood, especially in urban area. One limitation of the flood forecasting system in this paper is that the applied

hydrodynamic model sets the flood defence facilities as a static situation that cannot respond to defence failure or emergency management of flood immediately during an event. Hence, the next generation of the forecasting system will consider the 'human factors' in flood management by running a set of cases with various conditions of flood defence and regulation facilities and providing forecasts in corresponding with different scenarios.

Both the operational and research flood forecasting systems in the world are paying attention to the Ensemble Prediction System (EPS) by using ensemble NWP data rather than single deterministic forecast (Cloke and Pappenberger, 2009). Moreover, ensemble techniques are also applied in the application of hydrological modelling to deal with the uncertainty from model parameters, initial and boundary conditions (Jeong and Kim, 2005; Pagano et al., 2013; Seo et al., 2006). The ensemble forecasting system gives probabilistic flood predictions that can provide more detailed forecast information to the public and decision-makers. However, it obviously requires much more computing resources for running model multiple times with various data and parameters. In the UK, a short-range ensemble weather forecasting model called Regional Ensemble Prediction Systems (MOGREPS) is running by Met Office and produces weather prediction data available to be downloaded in real-time. Therefore, our next step is to employ the MOGREPS rainfall forecasts and HiPIMS with ensemble dressing to develop a hydrodynamic-driven ensemble flood forecasting system. And if the probabilistic prediction of inundation can be produced from the ensemble flood forecasting, the probabilistic risk prediction is also feasible for the exposure in the research domain.

7.6 Conclusions

Real-time flood forecasting is an effective means to mitigating the negative impact of flooding by providing timely and accurate flood forecasts and warnings to the public and relevant parties. Due to climate change, more extreme floods from intense rainfall have been observed in recent years across the world and the resultant floods may be amplified by other water-related hazards such as storm surge. The reliable simulation of this type of highly transient and multi-hazard flooding process requires the use of fully physically-based models. Most of the current flood forecasting systems are developed based on hydrological models or coupled hydrological and hydrodynamic models, which are not capable of modelling flood events induce by intense rainfall and interacted with other hazards to provide reliable and complete forecasts of inundation and potential loss. In this chapter, a new real-time flood forecasting system is developed by integrating a fully hydrodynamic model with the NWP

outputs produced by the UK Met Office's operational UKV model. By combining the flood forecasts with vulnerability and exposure data, a risk forecasting system is constructed to produce predictions of potential disaster loss. The performance of the flood forecasting system has been confirmed by applying to 'forecast' the 2015 Storm Desmond flood across the entire 2,500 km^2 Eden Catchment including City of Carlisle in the UK. Running on a uniform grid at 20 m resolution, the flood and risk forecasting system is able to successfully 'forecast' the event and provide 34 hours of lead time with the numerical weather prediction products released 36 hours in advance. Compared with the current flood warning service in Carlisle, the proposed flood and risk forecasting system can give 12 hours earlier flood warning to the public with a quantitative prediction of 4.19 km^2 inundated land and 4917 inundated buildings.

Chapter 8. Discussion and conclusions

The thesis has constructed an integrated assessment framework for quantifying and forecasting water-related multi-hazard risk. It is first applied in the Greater London catchment to estimate the risk of building loss and road networks damage due to the collective impact of heavy rain, extreme river flow and storm surge. Combined with UKV numerical weather prediction model, the framework is also employed in the Eden catchment for flood and risk forecasting in consideration of two hazards: the entire-catchment rainfall and the estuary sea level. The results are presented as quantitative risk curves and maps that can be visualised in real-time on free digital maps, such as Google Earth. The framework provides an effective and efficient tool to understand the regional disaster risk due to multiple hazards and provide timely risk warnings to residents and decision makers.

The highlights of the thesis are as follow:

- Analysis of dependence and joint probability analysis for the three coincident mechanisms of flooding.
- Broad scale full 2D hydrodynamic simulation of multiple sources of flooding and their physical interactions.
- Developed a fully quantitative and probabilistic risk assessment framework for multi-hazard floods
- Developed a real-time hazard and risk forecast framework for multi-hazard floods

8.1 Review of objectives

- **Multi-hazard dependence and joint probability analysis**

For the three water-related hazards considered in this thesis, strong dependence can be found in the inter-station observations from the same hazard, and the weak but statistically significant correlations are observed from the daily records of different hazards. This can be explained by the potential effect of the same weather system moving across south and east England. Therefore, when estimating the multi-hazard joint probability distribution, the dependence must be considered in the probability function.

Copula theory is introduced to construct the joint probability function according to the marginal distributions of each hazard and their correlations. A family of the Archimedean copula, the trivariate Clayton copula, is found to be best fit and employed to generate the trivariate cumulative distribution function with the three margins. The joint return period distribution is then derived from the probability function to quantify the frequency of multi-hazard events in years.

With the joint distribution functions, numerous multi-hazard events are randomly generated through the Monte Carlo method with known recurrence intervals, which means the 3D space of the three hazards is fully defined by the joint frequency of triple-hazard with various magnitudes.

- **Hydrodynamic modelling for multi-hazard flood**

A 2D hydrodynamic model has been used to simulate physical interactions between the three different sources of flooding (rainfall, flow, and costal storm surge) to assess inundation depth and extent. The hydrodynamic model, HiPIMS, which is configured on a $20\ m \times 20\ m$ grid over the Greater London catchment and achieved the broad-scale and fully 2D modelling.

The model is validated with rainfall-runoff progress, flow and tide interaction, and historic flood events. The fluvial and coastal flood defence facilities in London are examined in the model and tested with different failure scenarios. The defence system is found to be able to protect London city centre from the concurrent of the recorded maximum flow and highest storm surge. However, some sections of the facilities are not in good condition, and the defence failure of these parts can result in serious flooding when facing extreme events.

The random multi-hazard events with given frequency generated from the joint distribution function are simulated in HiPIMS. The output of HiPIMS is the peak inundation depth for each grid. The results are connected with the frequency of the causing events to generate inundation-frequency curves and probabilistic inundation maps for the Greater London catchment and several local regions. According to the inundation maps, the impact of the three hazards varies in different areas of the catchment. The river flow has the smallest influencing extent that is limited to the upstream riverside of the Thames. The storm surge is dangerous to all the riverside and coastal area. The inland region is only subjected to heavy rainfall that has the largest impacting area in the catchment among the three hazards. As for every local area, the effective hazards are distinguished so that the inundation with the same frequency may be derived from the completely different combinations and magnitudes of

hazards. The integrated hazard curve for depth-frequency function is estimated separately at each cell of the $100\ m \times 100\ m$ grid over the whole catchment for risk assessment.

- **Multi-hazard risk assessment**

Exposure is analysed for residential buildings, non-residential buildings and road networks, which shows the spatial distribution of the three elements at risk. Vulnerability functions of the three types of exposure are selected from MCM to give functional relationships between inundation depth and the resultant damage to the exposure. Economic loss is the measurement of risk for the two types of buildings. Inundated distance is used to represent the loss of the road networks.

The multi-hazard risk assessment is achieved by combining the data and results from the three essential components of disaster risk, hazard, vulnerability, and exposure. The assessment framework for quantifying multi-hazard risk is constructed. The framework has managed to cover three water-related hazards, estimate the correlations of the occurrence of hazards in joint distribution function, and simulate the physical interaction of the hazards with the hydrodynamic model. The results are fully quantitative and shown as risk curves for loss-frequency function and risk maps for the expected average annual loss.

The risk curves give the full range probabilistic estimation of disaster loss due to the multiple hazards for every assessing unit (one-hectare square cell). The risk map illustrates the general pattern of the risk level in the whole research area. It is more likely to experience severe loss in the middle and west area of the Greater London catchment. The south riverside between Vauxhall Bridge and Greenwich is the region at most risk for building loss due to the multi-hazard flooding.

- **Multi-hazard flood and risk forecasting**

The UKV numerical weather prediction model is coupled with the multi-hazard risk assessment framework to provide real-time flood and risk forecasting. The forecasting framework is applied in the Eden catchment with the consideration of rainfall over the whole domain and the sea level at the Eden river mouth.

The flood forecasting system is built on the basis of UKV model and HiPIMS model and validated with a historical event that happened in the Eden catchment. The lead time and accuracy of the forecasting system are evaluated and compared over several grids with different spatial resolution, and the 20 m-grid is chosen as the most suitable assessing unit

with current data and device conditions. The propagation of the prediction error from rainfall to the inundation depth and the extent is proved to not be amplified between the two models via uncertainty analysis.

The risk forecasting combining the inundation forecasting and local vulnerability functions can provide fast disaster loss predictions. The flood inundation prediction together with loss estimation can give more comprehensive and detailed warning information to decision makers and residents and guide them to take instant actions on flood preparation and prevention. As the case study in the Eden Catchment for Storm Desmond shows (Figure 7-10), the proposed flood and risk forecasting system produced a forecast of 4.19 km^2 inundated land and 4917 inundated buildings. Compared with the current flood warning service in Carlisle, the forecasting system can give 12 hours earlier flood warning to the public with much more quantitative predictions.

8.2 Implications of assumptions and uncertainties

A lot of assumptions and simplifications have been made to reduce the complexity of the framework and make the large-scale hydrodynamic simulations computationally feasible.

The sub-daily temporal variation of all the three water sources and the spatial variation of the rainfall over the Greater London catchment are neglected. However, to consider these factors means much higher dimensions of joint probability analysis and also the exponential increase of the required number of multi-hazard flood simulations. Therefore, the trivariate joint probability analysis is used to represent each hazard with only one variable to constrain the dimensions of the input domain of the hydrodynamic model. Nevertheless, this simplification results in a great uncertainty of the inundation map produced by the hydrodynamic model. Any temporal or spatial concentration of the water input may lead to a more severe flood in some areas of the research domain. If more information on sub-daily hazard intensities is available, more outcomes can be produced to decrease the uncertainty via a number of simulations for various spatial and temporal combinations of hazards.

The drainage system can play an important role in urban flood mitigation if it is well designed and keeps functional during flooding. However, the hydrodynamic model applied in this thesis does not have a sub-surface module to reflect the drainage system. It is because the underground module of HiPIMS is still under development and the detailed data of the drainage system is not available for the research areas. Currently, a conceptualised drainage

network is implemented along all the main streets with certain infiltration rates to denote the capacity of the sewage pipes. The gap between the predicted and the real capacity of drainage system may lead to uncertainties of flood prediction. However, the gap can be reduced if more flooding events and observations are available to better estimate the drainage efficiency in different areas of the research region.

The circumstance of defence facilities can be varied along the river bank and the coast. There would be countless scenarios of defence failures in the research area with different engineered, hydraulic, and environmental conditions. The impact of the occurrence time is investigated with only several scenarios of defence failure to confine the number of simulations. The circumstance of the flood defence system during flooding involves a large number of human and natural factors, which means very uncertain outcomes of flooding in the riverine and coastal regions. To constrain these types of uncertainties requires a more comprehensive appraisal of the conditions of the defence facilities and failure scenarios that are implemented in the flood simulating models.

Apart from the aforementioned uncertainties due to assumptions, the data and model parameters can also result in more or fewer uncertainties that need to be identified as follows:

- Because of the limited sample size of the hazards, uncertainties can exist in the fitted joint probability and return period distributions. These types of uncertainties are measurable according to the number of extreme events in the case study and can be reduced if a longer time series of hazard record is available.
- The applied hydrodynamic model requires much fewer parameters than traditional hydrological models, which means the uncertainties from model parameters are significantly cut down. However, the two parameters employed in HiPIMS, Manning and infiltration coefficients, can contribute to the uncertainty of water depth and velocities in the outputs. The uncertainty from model parameters can be reduced by more specific model calibrations based on complete local observations.
- A lot of factors are involved in the vulnerability analysis that relies on reported disaster loss and damage survey. The uncertainty of vulnerability curves corresponds to upper and lower estimation of the possible loss, which is a typical contributor to the uncertainties in the risk curves. The comprehensive data collection and analysis can help to refine the probability-damage functions and then reduce the related uncertainties.

- The uncertainties from the rainfall predictions can affect the output of flood inundation and are usually increasing with longer lead time. Ensemble outputs are provided by some numerical weather prediction models to give a probabilistic forecast instead of the traditional deterministic weather reports. To run all the probabilistic predictions of rainfall in the hydrodynamic is an effective way to constrain the uncertainties from weather model.

8.3 Data and validation challenge

The basic data requirements in this thesis include historical daily records of hazard intensities, high-resolution terrain and landcover data, numerical weather prediction data, and observations of flooding. For the risk assessment module, long time series (over 40 years) of rainfall, river flow, and tide height are essential for statistical analysis. For the forecasting module, the numerical rainfall predictions with high quality is the basis to accurately forecast flooding. It is also important to collect observations like river stages, flooded extent, and surface rainfall, which are useful for parameter adjustment and model calibration.

The required datasets are not difficult to obtain in most catchments of the UK, Europe and some other developed countries with advanced disaster management and flood monitoring systems. Global flood forecasting models have become available in recent years thanks to advances in meteorological and hydrological modelling, increased data sources and quality, and improvements in computing efficiency and capacity (Bierkens, 2015). For example, the Global Flood Awareness System (GloFAS) has been operational at global scale covering world large river basins since 2011 (Alfieri et al., 2013). However, due to the lack of high-resolution hydrodynamic models, GloFAS is designed for early warning purposes, rather than for quantitative discharge forecasting, let along for producing inundation predictions. It is still challenging to apply a fully quantitative and physically-based forecasting system in developing regions where the high-resolution NWP products, DEM and landcover data, and river and precipitation observations, are usually not available.

In the proposed frameworks, the validation of hazard analysis is performed with observed data, which is a typical and straightforward way. However, the risk assessment aims to predict the probability of occurrence of future extremes. The validation of risk is always a big challenge as the extremes are typically rare and hard to be verified according to the current or near future data. A compromised way is to use historical loss data that was completely and consistently recorded in a long time, which is not very feasible in most cases.

8.4 Transferability of the framework

The framework of the multi-hazard risk assessment is especially valuable to areas affected by dependent multiple water-related hazards. For example, cyclones in coastal regions bring heavy rain and strong winds that may cause the coincidence of pluvial and coastal flooding. If the cyclone is large enough to influence the upper-catchments, it may also lead to fluvial flooding. Coastal regions are intensively distributed worldwide, main areas exposed to typhoons and hurricanes, such as south-eastern China, and the north coast of the Gulf of Mexico. The risk assessment framework can be applied in these regions to better understand the disaster risk in consideration of multi-hazard dependence and interactions, if the required data is available.

The transferability of the forecasting module is more flexible, which can be used to predict flooding due to either individual or multiple sources. The main limitations of transferability are weather prediction and computing capacity. The ideal form of rainfall prediction is grid-based rainfall rates with high spatial and temporal resolutions and enough lead time. However, even without high-resolution weather forecast, the framework can still work based on coarse rainfall predictions but may result in the production of less accurate flood forecasting. Another limitation is the computing capacity that may confine the model domain to smaller areas or lower resolutions. With the current devices at Newcastle University, real-time flood and risk forecasting is feasible for catchments with an area of thousands of square kilometres. For broader-scale simulations, like the entire Yangtze River catchment of 1.8 million km^2 much greater number of GPUs are required for real-time forecasting without sacrificing the spatial resolution. Fortunately, the computing requirement is increasing linearly rather than exponentially with the catchment area and the price of GPUs are much cheaper compared to the cost of supercomputers. Therefore, the proposed flood forecasting system is highly applicable in regions covered by rainfall forecast with enough computing resources.

8.5 Trade-offs in risk analysis

Countless multi-hazard events can be randomly generated based on the joint return period function. Greater number of simulations by the hydrodynamic model means more accurate results of the risk assessment, which also spend larger computational resources. In addition to the variation of defence failure scenarios, the computing time is even longer. So, the trade-off

between computing time and the number of simulated events and the considered scenarios is worth pondering. In the case study of this thesis, the performed simulations are confined to hundreds of times due to the limited computing capacity and time. However, if the framework is applied in a larger research project with more resources, the accuracy of risk assessment may be improved via more hydrodynamic simulations.

For the module of flood and risk forecasting, a similar trade-off between accuracy and time also needs to be considered. A different issue is that the computing time is of great concern because a long enough lead time is critical to a forecasting system. The accuracy of forecasting can be improved by a higher spatial resolution, more scenarios about the status of defence facilities, and using ensemble rainfall forecasts to simulate floods. However, all these improvements must make sure the simulations are finished and the forecast is released before the real flood arrives.

8.6 Future work

- **Multi-hazard assessment framework for other hazard groups**

The hazards considered in this thesis are the three water-related hazards. To date these have been analysed separately whereas, their physical interactions are simulated using a hydrodynamic model. In future work of the framework, the sequencing of multi-hazard events, cascading effect between hazards, frequency of hazard repetition (e.g. two events within one week which lead to higher river levels etc.) are interesting topics to explore. The framework could be extended to incorporate other hazard groups. This would require the simulation of relevant physical interactions, a further advancement for flood risk would be to incorporate groundwater flows. However, other substantively different hazards such as earthquakes, landslides, fire etc. would require incorporation of different physical simulation models, and considerations of the likelihood of events occurring coincidentally.

- **More efficient hydrodynamic model**

HiPIMS is very fast compared with most of the traditional 2D hydrodynamic models. However, the multi-hazard risk assessment requires numerous runs of the model to cover the 3D hazard space for all the possible combinations. Especially in the urban area, the spatial resolution must be high enough to reflect the complex urban ground surface and thus requires enormous computing capacity. One way to improve the model efficiency is to employ non-

uniform grid that can be denser in complex terrain and sparser in the flat ground. Thus, the number of cells in the research domain may be significantly reduced and therefore, so will the computing time.

- **More comprehensive vulnerability and exposure analysis**

The risk assessment in the research region is employed only for three types of exposures. There is still a lot of work to do to give a more detailed risk assessment to all the main regional elements at risk. For example, the more comprehensive vulnerability and exposure analysis that produce more detailed information of the internal and external attributes of the exposure and vulnerability functions under various scenarios. Furthermore, to consider the dynamic vulnerability characters in the multi-hazard environment is also a necessary way to improve the accuracy of vulnerability evaluation.

- **Ensemble flood and risk forecasting**

Ensemble weather forecasting has been developed in several platforms, which means the ensemble flood forecasting becomes feasible for hydrological models or small-scale hydrodynamic models. The ensemble flood forecasting provides probabilistic flood prediction that can be used to give probabilistic loss prediction. Currently, the main limitation for ensemble hydrodynamic forecasting is the computing speed as the forecast always requires a long lead time. But with the rapid development of computer hardware and the model efficiency, it will not be too long to provide ensemble flood and risk forecast according to the framework in this thesis.

8.7 Implications of this research

Multi-hazard disasters are a subsistent threat to human society. Flooding derived from multiple water sources is one of the most destructive and widespread of all natural disasters. The methodology and findings about risk assessment and forecast of multi-hazard flood are of interest to a broad range of sectors and stakeholders.

Risk analyst: this work provides a new framework of quantitative risk assessment for multiple hazards with dependence of occurrence and physical interactions. The application of multivariate copula function provides a novel approach to generate three-dimensional joint probability and return period distributions for dependent triple hazards. Using a 2D hydrodynamic model for numerous simulations of multi-source flooding becomes practicable

for both probabilistic evaluation of multiple hazards and physical modelling of the hazards integrating.

Flood modeller and forecaster: the flood and risk forecasting module has proposed a new structure for large-scale flood forecasting systems. A high-performance hydrodynamic model is the key module that provides high-accuracy and reduced time-consuming running flood simulations for the forecasting system. It can be a new norm to replace the traditional hydrological model-based systems used in catchment-scale forecasting in order to reduce the system complexity and improve its performance.

Catchment manager and regulator: the framework provides risk assessment and forecasts for multi-source flooding in broad catchments. It can help catchment managers and regulators to take effective actions before and during flooding events, such as, to manage sluice gates and to adjust water storage in reservoirs.

City planners and local authorities: the framework can assist local decision makers to assess multi-source flood risk in local regions. Planners can refer to the results of the risk assessment in city planning. The framework can also test the effectiveness of the facilities and strategies for flood mitigation, which is especially useful to local authorities of disaster prevention and risk management.

Bibliography

Adamowski, K., 1985. Nonparametric Kernel Estimation of Flood Frequencies. *Water Resour. Res.* 21, 1585–1590. https://doi.org/10.1029/WR021i011p01585

Adger, W.N., 2006. Vulnerability. *Glob. Environ. Chang.* 16, 268–281. https://doi.org/http://dx.doi.org/10.1016/j.gloenvcha.2006.02.006

Alfieri, L., Burek, P., Dutra, E., Krzeminski, B., Muraro, D., Thielen, J., Pappenberger, F., 2013. GloFAS - global ensemble streamflow forecasting and flood early warning. *Hydrol. Earth Syst. Sci.* 17, 1161–1175. https://doi.org/10.5194/hess-17-1161-2013

Anderson, M.J., Braak, C.J.F.T.E.R., 2003. Permutation tests for multi-factorial analysis of variance. *J. Stat. Comput. Simul.* 73, 85–113. https://doi.org/10.1080/00949650215733

Apel, H., Trepat, O.M., Hung, N.N., Chinh, D.T., Merz, B., Dung, N. V., 2015. Combined fluvial and pluvial urban flood hazard analysis: method development and application to Can Tho City, Mekong Delta, Vietnam. *Nat. Hazards Earth Syst. Sci.* https://doi.org/10.5194/nhessd-3-4967-2015

ARMONIA, 2006. Methodology for a harmonised integrated map and development of a guideline for an EU directive on harmonisation of multi-hazard risk mapping: Report on new methodology for multi-risk assessment and the harmonisation of different natural risk maps, Ecosystems.

Arnold, M., Chen, R.S., Deichmann, U., Dilley, M., Lerner-Lam, A.L., Pullen, R.E., Trohanis, Z., 2006. Natural Disaster Hotspots Case Studies, Risk Management. World Bank Publications, Washington,D.C.

Ashley, R.M., Balmforth, D.J., Saul, A.J., Blanskby, J.D., 2005. Flooding in the future – predicting climate change, risks and responses in urban areas. *Water Sci. Technol.* 52, 265–273. https://doi.org/10.2166/wst.2005.0142

Ballard, S.P., Li, Z., Simonin, D., Caron, J.F., 2016. Performance of 4D-Var NWP-based nowcasting of precipitation at the Met Office for summer 2012. *Q. J. R. Meteorol. Soc.* 142, 472–487. https://doi.org/10.1002/qj.2665

Bartholmes, J.C., Thielen, J., Ramos, M.H., Gentilini, S., 2009. The european flood alert system EFAS – Part 2: Statistical skill assessment of probabilistic and deterministic operational forecasts. *Hydrol. Earth Syst. Sci.* 13, 141–153. https://doi.org/10.5194/hess-13-141-2009

Bauer, P., Thorpe, A., Brunet, G., 2015. The quiet revolution of numerical weather prediction. *Nature* 525, 47–55. https://doi.org/10.1038/nature14956

Bell, R., Glade, T., 2004. Quantitative risk analysis for landslides – Examples from

Bíldudalur, NW-Iceland. *Nat. Hazards Earth Syst. Sci.* 4, 117–131. https://doi.org/10.5194/nhess-4-117-2004

Bell, V.A., Kay, A.L., Jones, R.G., Moore, R.J., 2007. Development of a high resolution grid-based river flow model for use with regional climate model output. *Hydrol. Earth Syst. Sci.* 11, 532–549. https://doi.org/10.5194/hess-11-532-2007

Bierkens, M.F.P., 2015. Global hydrology 2015: State, trends, and directions. *Water Resour. Res.* 51, 4923–4947. https://doi.org/10.1002/2015WR017173

Blöschl, G., Reszler, C., Komma, J., 2008. A spatially distributed flash flood forecasting model. *Environ. Model. Softw.* 23, 464–478. https://doi.org/10.1016/j.envsoft.2007.06.010

Breinl, K., Strasser, U., Bates, P., Kienberger, S., 2017. A joint modelling framework for daily extremes of river discharge and precipitation in urban areas. *J. Flood Risk Manag.* 10, 97–114. https://doi.org/10.1111/jfr3.12150

Buishand, T.A., 1984. Bivariate extreme-value data and the station-year method. *J. Hydrol.* 69, 77–95. https://doi.org/10.1016/0022-1694(84)90157-4

Campolo, M., Andreussi, P., Soldati, A., 1999. River flood forecasting with a neural network model. *Water Resour. Res.* 35, 1191–1197. https://doi.org/10.1029/1998WR900086

Capobianco, M., DeVriend, H.J., Nicholls, R.J., Stive, M.J.E., 1999. Coastal Area Impact and Vulnerability Assessment: The Point of View of a Morphodynamic Modeller. *J. Coast. Res.* 15, 701–716.

Carlsson-Hyslop, A., 2010. Storm surge science: the London connection 1928-1953, in: Galloway, J.A. (Ed.), Tides and Floods: New Research on London and the Tidal Thames from the Middle Ages to the Twentieth Century, Centre for Metropolitan History Working Papers Series, Vol. 4. Institute of Historical Research, London.

Carolina, S., Management, E., 2006. STATE OF SOUTH CAROLINA HAZARDS ASSESSMENT. *Assessment*.

Carpignano, a., Golia, E., Di Mauro, C., Bouchon, S., Nordvik, J.P., 2009. A methodological approach for the definition of multi-risk maps at regional level: first application. *J. Risk Res.* 12, 513–534. https://doi.org/10.1080/13669870903050269

Carrivick, J.L., 2006. Application of 2D hydrodynamic modelling to high-magnitude outburst floods: An example from Kverkfjöll, Iceland. *J. Hydrol.* 321, 187–199. https://doi.org/10.1016/J.JHYDROL.2005.07.042

Carsell, K.M., Pingel, N.D., Ford, D.T., 2004. Quantifying the Benefit of a Flood Warning System. *Nat. Hazards Rev.* 5, 131–140. https://doi.org/10.1061/(ASCE)1527-6988(2004)5:3(131)

Chau, K.W., Wu, C.L., Li, Y.S., 2005. Comparison of Several Flood Forecasting Models in Yangtze River. *J. Hydrol. Eng.* 10, 485–491. https://doi.org/10.1061/(ASCE)1084-0699(2005)10:6(485)

Chen, A.S., Djordjević, S., Leandro, J., Savić, D.A., 2010. An analysis of the combined consequences of pluvial and fluvial flooding. *Water Sci. Technol.* 62, 1491–1498.

https://doi.org/10.2166/wst.2010.486

Chen, L., Singh, V.P., Shenglian, G., Hao, Z., Li, T., 2012. Flood Coincidence Risk Analysis Using Multivariate Copula Functions. *J. Hydrol. Eng.* 17, 742–755. https://doi.org/10.1061/(ASCE)HE.1943-5584.0000504

Chen, W.-B., Liu, W.-C., Chen, W.-B., Liu, W.-C., 2014. Modeling Flood Inundation Induced by River Flow and Storm Surges over a River Basin. *Water* 6, 3182–3199. https://doi.org/10.3390/w6103182

Chiang, Y.M., Hsu, K.L., Chang, F.J., Hong, Y., Sorooshian, S., 2007. Merging multiple precipitation sources for flash flood forecasting. *J. Hydrol.* 340, 183–196. https://doi.org/10.1016/j.jhydrol.2007.04.007

Chow, V. Te, 1959. Open-channel hydraulics. McGraw-Hill New York, New York.

Cloke, H.L., Pappenberger, F., 2009. Ensemble flood forecasting: A review. *J. Hydrol.* 375, 613–626. https://doi.org/10.1016/j.jhydrol.2009.06.005

Coles, S., Heffernan, J., Tawn, J., 2000. Dependence Measures for Extreme Value Analyses. *Extremes* 2, 339–365. https://doi.org/10.1023/A:31009963131610

Corbella, S., Stretch, D.D., 2013. Simulating a multivariate sea storm using Archimedean copulas. *Coast. Eng.* 76, 68–78. https://doi.org/10.1016/j.coastaleng.2013.01.011

Crichton, D., 1999. The risk triangle, Natural Disaster Management. Tudor Rose, London.

Cutter, S., Boruff, B., 2003. Social Vulnerability to Environmental Hazards. *Soc. Sci. Q.* 84, 242–261.

Cutter, S.L., Barnes, L., Berry, M., Burton, C., Evans, E., Tate, E., Webb, J., 2008. A place-based model for understanding community resilience to natural disasters. *Glob. Environ. Chang.* 18, 598–606. https://doi.org/10.1016/J.GLOENVCHA.2008.07.013

Cutter, S.S.L., Mitchell, J.T.J., Scott, M.M.S., 2000. Revealing the Vulnerability of People and Places: A Case Study of Georgetown County, South Carolina. *Ann. Assoc. Am. Geogr.* 90, 713–737. https://doi.org/10.2307/1515440

Davies, T., Cullen, M.J.P., Malcolm, A.J., Mawson, M.H., Staniforth, A., White, A.A., Wood, N., 2005. A new dynamical core for the Met Office's global and regional modelling of the atmosphere. *Q. J. R. Meteorol. Soc.* 131, 1759–1782. https://doi.org/10.1256/qj.04.101

de Roo, A.P.J., Gouweleeuw, B., Thielen, J., Bartholmes, J., Bongioannini-Cerlini, P., Todini, E., Bates, P.D., Horritt, M., Hunter, N., Beven, K., Pappenberger, F., Heise, E., Rivin, G., Hils, M., Hollingsworth, A., Holst, B., Kwadijk, J., Reggiani, P., Van Dijk, M., Sattler, K., Sprokkereef, E., 2003. Development of a European flood forecasting system. *Int. J. River Basin Manag.* 1, 49–59. https://doi.org/10.1080/15715124.2003.9635192

Di Mauro, C., Bouchon, S., Carpignano, A., Golia, E., Peressin, S., 2006. Definition of Multi-Risk Maps at Regional Level as Management Tool: Experience Gained by Civil Protection Authorities of Piemonte Region, in: Proceedings of the 5th Conference on Risk Assessment and Management in the Civil and Industrial Settlements.

Dilley, M., Chen, R.S., Deichmann, U., Lerner-Lam, A.L., Arnold, M., 2005. Natural disaster hotspots: a global risk analysis, Earth Science. The World Bank, Washington.

Done, J., Davis, C.A., Weisman, M., 2004. The next generation of NWP: explicit forecasts of convection using the weather research and forecasting (WRF) model. *Atmos. Sci. Lett.* 5, 110–117. https://doi.org/10.1002/asl.72

Dottori, F., Szewczyk, W., Ciscar, J.-C., Zhao, F., Alfieri, L., Hirabayashi, Y., Bianchi, A., Mongelli, I., Frieler, K., Betts, R.A., Feyen, L., 2018. Increased human and economic losses from river flooding with anthropogenic warming. *Nat. Clim. Chang.* 8, 781–786. https://doi.org/10.1038/s41558-018-0257-z

Dutta, D., Alam, J., Umeda, K., Hayashi, M., Hironaka, S., 2007. A two-dimensional hydrodynamic model for flood inundation simulation: a case study in the lower Mekong river basin. *Hydrol. Process.* 21, 1223–1237. https://doi.org/10.1002/hyp.6682

Ehlen, M. a., Vargas, V.N., 2013. Multi-hazard, multi-infrastructure, economic scenario analysis. *Environ. Syst. Decis.* 33, 60–75. https://doi.org/10.1007/s10669-013-9432-y

El-Masri, S., Tipple, G., 2002. Natural Disaster, Mitigation and Sustainability: The Case of Developing Countries Souheil El-Masri & Graham Tipple. *Int. Plan. Stud.* 7, 157–175. https://doi.org/10.1080/13563470220132236org/10.1080/13563470220132236

Ellingwood, B.R., Rosowsky, D. V., Li, Y., Kim, J.H., 2004. Fragility Assessment of Light-Frame Wood Construction Subjected to Wind and Earthquake Hazards. *J. Struct. Eng.* 130, 1921–1930. https://doi.org/10.1061/(ASCE)0733-9445(2004)130:12(1921)

Environment Agency, 2017. Understanding the performance of flood forecasting models. Bristol.

Environment Agency, 2016. Carlisle Flood Investigation Report: Flood Event 5-6th December 2015.

Environment Agency, 2012. Thames Estuary 2100: Managing flood risk through Londong and the Thames estuary.

Environment Agency, 2009. Eden Catchment Flood Management Plan. Warrington, UK.

Escobar, G., Vargas, W., Bischoff, S., 2004. Wind tides in the Rio de la Plata estuary: Meteorological conditions. *Int. J. Climatol.* 24, 1159–1169. https://doi.org/10.1002/joc.1026

ESPON, 2006. The Spatial Effects and Management of Natural and Technological Hazards in Europe, ESPON.

Falconer, R.H., Cobby, D., Smyth, P., Astle, G., Dent, J., Golding, B., 2009. Pluvial flooding: new approaches in flood warning, mapping and risk management. *J. Flood Risk Manag.* 2, 198–208. https://doi.org/10.1111/J.1753-318X.2009.01034.X

Favre, A.-C., El Adlouni, S., Perreault, L., Thiémonge, N., Bobée, B., 2004. Multivariate hydrological frequency analysis using copulas. *Water Resour. Res.* 40, 1–12. https://doi.org/10.1029/2003WR002456

FEMA, 2011. Getting started with HAZUS-MH 2.1, Technical Manual. Department of

Homeland Security, Washington.

Fisher, N.I., Switzer, P., 2001. Graphical Assessment of Dependence: Is a Picture Worth 100 Tests? *Am. Stat.* 55, 233–239. https://doi.org/10.1198/000313001317098248

Fleming, K., Zschau, J., Gasparini, P., 2014. The New Multi-HAzard and MulTi-RIsK Assessment MethodS for Europe (MATRIX) Project-An overview of its major findings. *EGU Gen. Assem. …* 16, 6584.

Fread, D.L., Shedd, R.C., Smith, G.F., Farnsworth, R., Hoffeditz, C.N., Wenzel, L.A., Wiele, S.M., Smith, J.A., Day, G.N., 2002. Modernization in the National Weather Service River and Flood Program. *Weather Forecast.* 10, 477–484. https://doi.org/10.1175/1520-0434(1995)010<0477:mitnws>2.0.co;2

Freer, J., Beven, K.J., Neal, J., Schumann, G., Hall, J., Bates, P., 2013. Flood risk and uncertainty, in: Rougier, J., Sparks, S., Hill, L. (Eds.), Risk and Uncertainty Assessment for Natural Hazards. Cambridge University Press, pp. 190–233.

Fuchs, S., Heiss, K., Hübl, J., 2007. Towards an empirical vulnerability function for use in debris flow risk assessment. *Nat. Hazards Earth Syst. Sci.* 7, 495–506.

Gallina, V., Torresan, S., Critto, A., Sperotto, A., Glade, T., Marcomini, A., 2016. A review of multi-risk methodologies for natural hazards: Consequences and challenges for a climate change impact assessment. *J. Environ. Manage.* 168, 123–132. https://doi.org/10.1016/j.jenvman.2015.11.011

Garrote, L., Bras, R.L., 1995. A distributed model for real-time flood forecasting using digital elevation models. *J. Hydrol.* 167, 279–306. https://doi.org/10.1016/0022-1694(94)02592-Y

Gauthier, P., Tanguay, M., Laroche, S., Pellerin, S., Morneau, J., Gauthier, P., Tanguay, M., Laroche, S., Pellerin, S., Morneau, J., 2007. Extension of 3DVAR to 4DVAR: Implementation of 4DVAR at the Meteorological Service of Canada. *Mon. Weather Rev.* 135, 2339–2354. https://doi.org/10.1175/MWR3394.1

Ge, Y., Dou, W., Gu, Z., Qian, X., Wang, J., Xu, W., Shi, P., Ming, X., Zhou, X., Chen, Y., 2013. Assessment of social vulnerability to natural hazards in the Yangtze River Delta, China. *Stoch. Environ. Res. Risk Assess.* 27, 1899–1908. https://doi.org/10.1007/s00477-013-0725-y

Genest, C., Favre, A.-C., 2007. Everything You Always Wanted to Know about Copula Modeling but Were Afraid to Ask. *J. Hydrol. Eng.* 12, 347–368. https://doi.org/10.1061/(ASCE)1084-0699(2007)12:4(347)

Genest, C., Rémillard, B., 2004. Test of independence and randomness based on the empirical copula process. *Test* 13, 335–369. https://doi.org/10.1007/BF02595777

Genest, C., Rémillard, B., Beaudoin, D., 2009. Goodness-of-fit tests for copulas: A review and a power study. *Insur. Math. Econ.* 44, 199–213. https://doi.org/http://dx.doi.org/10.1016/j.insmatheco.2007.10.005

Gill, J.C., Malamud, B.D., 2016. Hazard interactions and interaction networks (cascades) within multi-hazard methodologies. *Earth Syst. Dyn.* 7, 659–679.

Gill, J.C., Malamud, B.D., 2014. Reviewing and visualizing the interactions of natural hazards. *Rev. Geophys.* 680–722. https://doi.org/10.1002/2013RG000445.Received

Goel, N.K., Seth, S.M., Chandra, S., 1998. Multivariate modeling of flood flows. *J. Hydraul. Eng.* 124, 146–155. https://doi.org/10.1061/(asce)0733-9429(1998)124:2(146)

Greiving, S., Fleischhauer, M., L U Ckenk O Tter, J., Lückenkötter, J., 2006. A Methodology for an integrated risk assessment of spatially relevant hazards. *J. Environ. Plan. Manag.* 49, 1–19. https://doi.org/10.1080/09640560500372800

Grünthal, G., Thieken, A.H., Schwarz, J., Radtke, K.S., Smolka, A., Merz, B., 2006. Comparative Risk Assessments for the City of Cologne – Storms, Floods, Earthquakes. *Nat. Hazards* 38, 21–44. https://doi.org/10.1007/s11069-005-8598-0

Guha-Sapir, D., Below, R., Hoyois, P., 2015. EM-DAT: International disaster database. *Cathol. Univ. Louvain Brussels, Belgium* 27, 57–58.

Gutierrez, B.T., Plant, N.G., Thieler, E.R., 2011. A Bayesian network to predict coastal vulnerability to sea level rise. *J. Geophys. Res.* 116, F02009. https://doi.org/10.1029/2010JF001891

Hainzl, S., Kraft, T., Wassermann, J., Igel, H., Schmedes, E., 2006. Evidence for rainfall-triggered earthquake activity. *Geophys. Res. Lett.* 33, L19303. https://doi.org/10.1029/2006GL027642

Hapuarachchi, H.A.P., Wang, Q.J., Pagano, T.C., 2011. A review of advances in flash flood forecasting. *Hydrol. Process.* 25, 2771–2784. https://doi.org/10.1002/hyp.8040

Hawkes, P.J., Gouldby, B.P., Tawn, J.A., Owen, M.W., 2002. The joint probability of waves and water levels in coastal engineering design. *J. Hydraul. Res.* 40, 241–251. https://doi.org/10.1080/00221680209499940

Horsburgh, K.J., Wilson, C., 2007. Tide-surge interaction and its role in the distribution of surge residuals in the North Sea. *J. Geophys. Res.* 112, C08003. https://doi.org/10.1029/2006JC004033

Housener, G.W., 1989. An International Decade of Natural Disaster Reduction: 1990-2000. *Nat. Hazards* 2, 45–75. https://doi.org/10.1007/BF00124757

Hsu, Y. chao, Yen, H., Tseng, W. hsiao, Jan, C. deng, 2014. Numerical simulation on a tremendous debris flow caused by Typhoon Morakot in the Jiaopu Stream, Taiwan. *J. Mt. Sci.* 11, 1–18. https://doi.org/10.1007/s11629-013-2754-x

Hult, H., Lindskog, F., 2002. Multivariate extremes, aggregation and dependence in elliptical distributions. *Adv. Appl. Probab.* 34, 587–608. https://doi.org/10.1017/S0001867800011770

IDNDR, 1994. Yokohama Strategy and Plan of Action for a Safer World, in: World Conference on Natural Disaster Reduction. Yokohama, Japan, pp. 23–27.

IPCC, 2014a. Climate Change 2014 Synthesis Report, Contribution of Working Groups I, II and III to the Fifth Assessment Report of the Intergovernmental Panel on Climate Change. Geneva, Switzerland.

IPCC, 2014b. Summary for Policymakers, Climate Change 2014: Synthesis Report. Contribution of Working Groups I, II and III to the Fifth Assessment Report of the Intergovernmental Panel on Climate Change. https://doi.org/10.1017/CBO9781107415324

Jeong, D.-I., Kim, Y.-O., 2005. Rainfall-runoff models using artificial neural networks for ensemble streamflow prediction. *Hydrol. Process.* 19, 3819–3835. https://doi.org/10.1002/hyp.5983

Jiang, X., Tatano, H., Hori, T., 2013. A Methodology for Spatial Flood Risk Assessment Taking Account of Spatial-Temporal Characteristics of Rainfall. *J. Integr. Disaster Risk Manag.* 3, 74–90. https://doi.org/10.5595/idrim.2013.0057

Jongman, B., Ward, P.J., Aerts, J.C.J.H., 2012. Global exposure to river and coastal flooding: Long term trends and changes. *Glob. Environ. Chang.* 22, 823–835. https://doi.org/10.1016/J.GLOENVCHA.2012.07.004

Kameshwar, S., Padgett, J.E., 2014. Multi-hazard risk assessment of highway bridges subjected to earthquake and hurricane hazards. *Eng. Struct.* 78, 154–166. https://doi.org/10.1016/j.engstruct.2014.05.016

Kao, S.-C., Govindaraju, R.S., 2008. Trivariate statistical analysis of extreme rainfall events via the Plackett family of copulas. *Water Resour. Res.* 44, n/a-n/a. https://doi.org/10.1029/2007WR006261

Kappes, M.S., Keiler, M., Elverfeldt, K., Glade, T., von Elverfeldt, K., Glade, T., 2012. Challenges of analyzing multi-hazard risk: a review. *Nat. Hazards* 64, 1925–1958. https://doi.org/10.1007/s11069-012-0294-2

Kappes, M.S., Keiler, M., Glade, T, 2010. From Single-to Multi-Hazard Risk Analyses: a concept addressing emerging challenges, in: Malet, J.-P., Glade, Thomas, Casagli, N. (Eds.), Mountain Risks: Bringing Science to Society. CERG, cerg.u-strasbg.fr, FIRENZE, pp. 24–26.

Kelman, I., 2002. Physical Flood Vulnerability of Residential Properties in Coastal Eastern England. University of Cambridge.

Kendon, E.J., Roberts, N.M., Senior, C.A., Roberts, M.J., Kendon, E.J., Roberts, N.M., Senior, C.A., Roberts, M.J., 2012. Realism of Rainfall in a Very High-Resolution Regional Climate Model. *J. Clim.* 25, 5791–5806. https://doi.org/10.1175/JCLI-D-11-00562.1

Kew, S.F., Selten, F.M., Lenderink, G., Hazeleger, W., 2013. The simultaneous occurrence of surge and discharge extremes for the Rhine delta. *Nat. Hazards Earth Syst. Sci.* 13, 2017–2029. https://doi.org/10.5194/nhess-13-2017-2013

Khanduri, A.C., Morrow, G.C., 2003. Vulnerability of buildings to windstorms and insurance loss estimation. *J. Wind Eng. Ind. Aerodyn.* 91, 455–467. https://doi.org/http://dx.doi.org/10.1016/S0167-6105(02)00408-7

Klein, R.J.T., Nicholls, R.J., 1999. Assessment of Coastal Vulnerability to Climate Change. *Ambio* 28, 182–187.

Klerk, W.J., Winsemius, H.C., van Verseveld, W.J., Bakker, A.M.R., Diermanse, F.L.M.,

2015. The co-incidence of storm surges and extreme discharges within the Rhine–Meuse Delta. *Environ. Res. Lett.* 10, 035005. https://doi.org/10.1088/1748-9326/10/3/035005

Kojadinovic, I., Yan, J., 2011. A goodness-of-fit test for multivariate multiparameter copulas based on multiplier central limit theorems. *Stat. Comput.* 21, 17–30. https://doi.org/10.1007/s11222-009-9142-y

Kojadinovic, I., Yan, J., 2010. Modeling Multivariate Distributions with Continuous Margins Using the copula R Package. *J. Stat. Softw.* 34, 1–20. https://doi.org/10.1007/978-3-540-74686-7

Koks, E.E., Thissen, M., 2016. A Multiregional Impact Assessment Model for disaster analysis. *Econ. Syst. Res.* 28, 429–449. https://doi.org/10.1080/09535314.2016.1232701

Kron, W., 2002. Keynote lecture: Flood risk = hazard × exposure × vulnerability. Science Press.

Krstanovic, P.F., Singh, V.P., 1987. A Multivariate Stochastic Flood Analysis Using Entropy, in: Hydrologic Frequency Modeling. Springer Netherlands, Dordrecht, pp. 515–539. https://doi.org/10.1007/978-94-009-3953-0_37

Kumbier, K., Carvalho, R.C., Vafeidis, A.T., Woodroffe, C.D., 2018. Investigating compound flooding in an estuary using hydrodynamic modelling: A case study from the Shoalhaven River, Australia. *Nat. Hazards Earth Syst. Sci.* 18, 463–477. https://doi.org/10.5194/nhess-18-463-2018

Lall, U., Devineni, N., Kaheil, Y., 2016. An Empirical, Nonparametric Simulator for Multivariate Random Variables with Differing Marginal Densities and Nonlinear Dependence with Hydroclimatic Applications. *Risk Anal.* 36, 57–73. https://doi.org/10.1111/risa.12432

Lamb, R., Keef, C., Tawn, J., Laeger, S., Meadowcroft, I., Surendran, S., Dunning, P., Batstone, C., 2010. A new method to assess the risk of local and widespread flooding on rivers and coasts. *J. Flood Risk Manag.* 3, 323–336. https://doi.org/10.1111/j.1753-318X.2010.01081.x

Lean, H.W., Clark, P.A., Dixon, M., Roberts, N.M., Fitch, A., Forbes, R., Halliwell, C., Lean, H.W., Clark, P.A., Dixon, M., Roberts, N.M., Fitch, A., Forbes, R., Halliwell, C., 2008. Characteristics of High-Resolution Versions of the Met Office Unified Model for Forecasting Convection over the United Kingdom. *Mon. Weather Rev.* 136, 3408–3424. https://doi.org/10.1175/2008MWR2332.1

Lee, K.H., Rosowsky, D. V., 2006. Fragility analysis of woodframe buildings considering combined snow and earthquake loading. *Struct. Saf.* 28, 289–303. https://doi.org/10.1016/j.strusafe.2005.08.002

Leonard, M., Westra, S., Phatak, A., Lambert, M., van den Hurk, B., McInnes, K., Risbey, J., Schuster, S., Jakob, D., Stafford-Smith, M., 2014. A compound event framework for understanding extreme impacts. *Wiley Interdiscip. Rev. Clim. Chang.* 5, 113–128. https://doi.org/10.1002/wcc.252

Lewis, M., Bates, P., Horsburgh, K., Neal, J., Schumann, G., 2013. A storm surge inundation model of the northern Bay of Bengal using publicly available data. *Q. J. R. Meteorol. Soc.* 139, 358–369. https://doi.org/10.1002/qj.2040

Li, H., Apostolakis, G.E., Gifun, J., VanSchalkwyk, W., Leite, S., Barber, D., 2009. Ranking the Risks from Multiple Hazards in a Small Community. *Risk Anal.* 29, 438–456. https://doi.org/10.1111/j.1539-6924.2008.01164.x

Li, Ji, Chen, Y., Wang, H., Qin, J., Li, Jie, Chiao, S., 2017. Extending flood forecasting lead time in a large watershed by coupling WRF QPF with a distributed hydrological model. *Hydrol. Earth Syst. Sci.* 21, 1279–1294. https://doi.org/10.5194/hess-21-1279-2017

Li, Y., van de Lindt, J.W., 2012. Loss-based formulation for multiple hazards with application to residential buildings. *Eng. Struct.* 38, 123–133. https://doi.org/10.1016/j.engstruct.2012.01.006

Lian, J.J., Xu, K., Ma, C., 2013. Joint impact of rainfall and tidal level on flood risk in a coastal city with a complex river network: A case study of Fuzhou City, China. *Hydrol. Earth Syst. Sci.* 17, 679–689. https://doi.org/10.5194/hess-17-679-2013

Liang, Q., 2010. Flood Simulation Using a Well-Balanced Shallow Flow Model. *J. Hydraul. Eng.* 136, 669–675. https://doi.org/10.1061/(ASCE)HY.1943-7900.0000219

Liang, Q., Smith, L.S., 2015. A high-performance integrated hydrodynamic modelling system for urban flood simulations. *J. Hydroinformatics* 17, 518. https://doi.org/10.2166/hydro.2015.029

Liu, B., Siu, Y.L., Mitchell, G., 2016. Hazard interaction analysis for multi-hazard risk assessment: a systematic classification based on hazard-forming environment. *Nat. Hazards Earth Syst. Sci.* 16, 629–642. https://doi.org/10.5194/nhess-16-629-2016

Liu, Z., Guo, S., Xiong, L., Xu, C.-Y., 2018. Hydrological uncertainty processor based on a copula function. *Hydrol. Sci. J.* 63, 74–86. https://doi.org/10.1080/02626667.2017.1410278

Liu, Z., Martina, M.L. V., Todini, E., 2005. Flood forecasting using a fully distributed model: application of the TOPKAPI model to the Upper Xixian Catchment. *Hydrol. Earth Syst. Sci.* 9, 347–364. https://doi.org/10.5194/hess-9-347-2005

Lozoya, J.P., Sardá, R., Jiménez, J. a., Sard A, R., Jim E Nez, J.A., 2011. A methodological framework for multi-hazard risk assessment in beaches. *Environ. Sci. Policy* 14, 685–696. https://doi.org/10.1016/j.envsci.2011.05.002

Lung, T., Lavalle, C., Hiederer, R., Dosio, A., Bouwer, L.M., 2013. A multi-hazard regional level impact assessment for Europe combining indicators of climatic and non-climatic change. *Glob. Environ. Chang.* 23, 522–536. https://doi.org/10.1016/j.gloenvcha.2012.11.009

Macdonald, N., 2012. Trends in flood seasonality of the River Ouse (Northern England) from archive and instrumental sources since AD 1600. *Clim. Change* 110, 901–923. https://doi.org/10.1007/s10584-011-0117-6

Mallakpour, I., Villarini, G., 2015. The changing nature of flooding across the central United States. *Nat. Clim. Chang.* 5, 250–254. https://doi.org/10.1038/nclimate2516

Mardfekri, M., Gardoni, P., 2015. Multi-hazard reliability assessment of offshore wind turbines. *Wind Energy* 18, 1433–1450. https://doi.org/10.1002/we.1768

Marzocchi, W., Garcia-Aristizabal, A., Gasparini, P., Mastellone, M.L., Di Ruocco, A., 2012. Basic principles of multi-risk assessment: a case study in Italy. *Nat. Hazards* 62, 551–573. https://doi.org/10.1007/s11069-012-0092-x

McCloskey, J., Nalbant, S.S., Steacy, S., 2005. Earthquake risk from co-seismic stress. *Nature* 434, 291–291. https://doi.org/10.1038/434291a

McCuen, R.H., Knight, Z., Cutter, A.G., 2006. Evaluation of the Nash–Sutcliffe Efficiency Index. *J. Hydrol. Eng.* 11, 597–602. https://doi.org/10.1061/(ASCE)1084-0699(2006)11:6(597)

Mcenery, J., Ingram, J., Duan, Q., Adams, T., Anderson, L., Mcenery, J., Ingram, J., Duan, Q., Adams, T., Anderson, L., 2005. NOAA'S Advanced Hydrologic Prediction Service: Building Pathways for Better Science in Water Forecasting. *Bull. Am. Meteorol. Soc.* 86, 375–385. https://doi.org/10.1175/BAMS-86-3-375

Met Office, 2003. Met Office Rain Radar Data from the NIMROD System.

Miles, S.B., Keefer, D.K., Region, W., Hazards, E., Survey, U.S.G., Park, M., 2007. A Comprehensive Areal Model of Earthquake-induced Landslides using Fuzzy Logic Systems. *Knowl. Creat. Diffus. Util.*

Ming, X., Xu, W., Li, Y., Du, J., Liu, B., Shi, P., 2015. Quantitative multi-hazard risk assessment with vulnerability surface and hazard joint return period. *Stoch. Environ. Res. Risk Assess.* 29, 35–44. https://doi.org/10.1007/s00477-014-0935-y

Mittermaier, M.P., Csima, G., 2017. Ensemble versus Deterministic Performance at the Kilometer Scale. *Weather Forecast.* 32, 1697–1709. https://doi.org/10.1175/WAF-D-16-0164.1

Moftakhari, H.R., Salvadori, G., AghaKouchak, A., Sanders, B.F., Matthew, R.A., 2017. Compounding effects of sea level rise and fluvial flooding. *Proc. Natl. Acad. Sci.* 114, 9785–9790. https://doi.org/10.1073/PNAS.1620325114

Mosquera-Machado, S., Dilley, M., 2009. A comparison of selected global disaster risk assessment results. *Nat. hazards* 48, 439–456. https://doi.org/10.1007/s11069-008-9272-0

Munich Re, 2003. Annual review: natural catastrophes 2002. *Europe*.

Munoz, S.E., Giosan, L., Therrell, M.D., Remo, J.W.F., Shen, Z., Sullivan, R.M., Wiman, C., O'Donnell, M., Donnelly, J.P., 2018. Climatic control of Mississippi River flood hazard amplified by river engineering. *Nature* 556, 95–98. https://doi.org/10.1038/nature26145

Nadal, N.C., Zapata, R.E., Pagán, I., López, R., Agudelo, J., 2010. Building Damage due to Riverine and Coastal Floods. *J. Water Resour. Plan. Manag.* 136, 327–336. https://doi.org/10.1061/(ASCE)WR.1943-5452.0000036

NAO, 2001. Inland Flood Defence. Report by the comptroller and auditor general of the National Audit Office. London.

Nasiri, H., Mohd Yusof, M.J., Mohammad Ali, T.A., 2016. An overview to flood vulnerability assessment methods. *Sustain. Water Resour. Manag.* https://doi.org/10.1007/s40899-016-0051-x

Nayak, P.C., Sudheer, K.P., Ramasastri, K.S., 2005. Fuzzy computing based rainfall-runoff model for real time flood forecasting. *Hydrol. Process.* 19, 955–968. https://doi.org/10.1002/hyp.5553

Neelin, J.D., Battisti, D.S., Hirst, A.C., Jin, F.-F., Wakata, Y., Yamagata, T., Zebiak, S.E., 1998. ENSO theory. *J. Geophys. Res. Ocean.* https://doi.org/10.1029/97JC03424

Nelson, R., 1999. An Introduction to Copulas. Springer, New York.

Novelo-Casanova, D. a., Suárez, G., 2012. Exposure of main critical facilities to natural and man-made hazards in Grand Cayman, Cayman Islands. *Nat. Hazards* 61, 1277–1292. https://doi.org/10.1007/s11069-011-9982-6

O'Brien, G., O'Keefe, P., Rose, J., Wisner, B., 2006. Climate change and disaster management. *Disasters* 30, 64–80. https://doi.org/10.1111/j.1467-9523.2006.00307.x

Olbert, A.I., Comer, J., Nash, S., Hartnett, M., 2017. High-resolution multi-scale modelling of coastal flooding due to tides, storm surges and rivers inflows. A Cork City example. *Coast. Eng.* 121, 278–296. https://doi.org/10.1016/J.COASTALENG.2016.12.006

Olfert, A., Greiving, S., 2006. Regional multi-risk review, hazard weighting and spatial planning response to risk-Results from European case studies, in: Schmidt-thomé, P. (Ed.), Natural and Technological Hazards and Risks Affecting the Spatial Development of European Regions. Geological Survey of Finland, pp. 125–151.

Pagano, T.C., Shrestha, D.L., Wang, Q.J., Robertson, D., Hapuarachchi, P., 2013. Ensemble dressing for hydrological applications. *Hydrol. Process.* 27, 106–116. https://doi.org/10.1002/hyp.9313

Paiva, R.C.D., Collischonn, W., Tucci, C.E.M., 2011. Large scale hydrologic and hydrodynamic modeling using limited data and a GIS based approach. *J. Hydrol.* 406, 170–181. https://doi.org/10.1016/J.JHYDROL.2011.06.007

Palmer, T.N., Brankovic, C., Molteni, F., Tibaldi, S., Ferranti, L., Hollingsworth, A., Cubasch, U., Klinker, E., Palmer, T.N., Brankovic, C., Molteni, F., Tibaldi, S., Ferranti, L., Hollingsworth, A., Cubasch, U., Klinker, E., 1990. The European Centre for Medium-Range Weather Forecasts (ECMWF) Program on Extended-Range Prediction. *Bull. Am. Meteorol. Soc.* 71, 1317–1330. https://doi.org/10.1175/1520-0477(1990)071<1317:TECFMR>2.0.CO;2

Paprotny, D., Vousdoukas, M.I., Morales-Nápoles, O., Jonkman, S.N., Feyen, L., 2018. Compound flood potential in Europe. *Hydrol. Earth Syst. Sci. Discuss.* 1–34. https://doi.org/10.5194/hess-2018-132

Penning-Rowsell, E., Priest, S., Parker, D., Morris, J., Tunstall, S., Viavattene, C., Chatterton, J., Owen, D., 2013. Flood and coastal erosion risk management: a manual for economic appraisal. Routledge.

Petroliagkis, T.I., 2018. Estimations of statistical dependence as joint return period modulator of compound events. Part I: storm surge and wave height. *Nat. Hazards Earth Syst. Sci.* 1–46. https://doi.org/10.5194/nhess-2017-177

Petroliagkis, T.I., Voukouvalas, E., Disperati, J., Bidlot, J., 2016. Joint Probabilities of Storm Surge, Significant Wave Height and River Discharge Components of Coastal Flooding

Events. EUR 27824 EN. https://doi.org/10.2788/677778

Pingel, N., Watkins, D., 2010. Multiple Flood Source Expected Annual Damage Computations. *J. Water Resour. Plan. Manag.* 136, 319. https://doi.org/10.1061/(ASCE)WR.1943-5452.0000031

Pregnolato, M., Ford, A., Wilkinson, S.M., Dawson, R.J., 2017. The impact of flooding on road transport: A depth-disruption function. *Transp. Res. Part D Transp. Environ.* 55, 67–81. https://doi.org/10.1016/j.trd.2017.06.020

Pugh, D.T., 1996. Tides, surges and mean sea-level (reprinted with corrections). John Wiley & Sons Ltd, Chichester.

Quan Luna, B., Blahut, J., van Westen, C.J., Sterlacchini, S., van Asch, T.W.J., Akbas, S.O., 2011. The application of numerical debris flow modelling for the generation of physical vulnerability curves. *Nat. Hazards Earth Syst. Sci.* 11, 2047–2060. https://doi.org/10.5194/nhess-11-2047-2011

Reiss, R.-D., Thomas, M., 2007. Statistical Analysis of Extreme values: With Applications to Insurance, Finance, Hydrology and Other Fields.

Robson, A., Reed, D., 1999. Flood Estimation Handbook Volume 3, in: Statistical Procedures for Flood Frequency Estimation. pp. 63–76.

Rød, J.K., Berthling, I., Lein, H., Lujala, P., Vatne, G., Bye, L.M., 2012. Integrated vulnerability mapping for wards in Mid-Norway. *Local Environ.* 17, 695–716. https://doi.org/10.1080/13549839.2012.685879

Rowland, C.S., Morton, R.D., Carrasco, L., McShane, G., O'Neil, A.W., Wood, C.M., 2017. Land Cover Map 2015 (vector, GB).

Sackl, B., Bergmann, H., 1987. A Bivariate Flood Model and Its Application, in: Hydrologic Frequency Modeling. Springer Netherlands, Dordrecht, pp. 571–582. https://doi.org/10.1007/978-94-009-3953-0_40

Sadegh, M., Moftakhari, H., Gupta, H. V., Ragno, E., Mazdiyasni, O., Sanders, B., Matthew, R., AghaKouchak, A., 2018. Multihazard Scenarios for Analysis of Compound Extreme Events. *Geophys. Res. Lett.* 45, 5470–5480. https://doi.org/10.1029/2018GL077317

Saleh, F., Ramaswamy, V., Wang, Y., Georgas, N., Blumberg, A., Pullen, J., 2017. A multi-scale ensemble-based framework for forecasting compound coastal-riverine flooding: The Hackensack-Passaic watershed and Newark Bay. *Adv. Water Resour.* 110, 371–386. https://doi.org/10.1016/j.advwatres.2017.10.026

Salvadori, G., De Michele, C., 2015. Multivariate real-time assessment of droughts via copula-based multi-site Hazard Trajectories and Fans. *J. Hydrol.* 526, 101–115. https://doi.org/10.1016/j.jhydrol.2014.11.056

Salvadori, G., De Michele, C., Durante, F., 2011. On the return period and design in a multivariate framework. *Hydrol. Earth Syst. Sci.* 15, 3293–3305. https://doi.org/10.5194/hess-15-3293-2011

Salvadori, G., Durante, F., De Michele, C., Bernardi, M., Petrella, L., 2016. A multivariate copula-based framework for dealing with hazard scenarios and failure probabilities.

Water Resour. Res. 52, 1333–1352. https://doi.org/10.1002/2014WR015716

Sanders, B.F., Schubert, J.E., Detwiler, R.L., 2010. ParBreZo: A parallel, unstructured grid, Godunov-type, shallow-water code for high-resolution flood inundation modeling at the regional scale. *Adv. Water Resour.* 33, 1456–1467. https://doi.org/10.1016/J.ADVWATRES.2010.07.007

Schmid, F., Schmidt, R., 2007. Multivariate conditional versions of Spearman's rho and related measures of tail dependence. *J. Multivar. Anal.* 98, 1123–1140. https://doi.org/10.1016/J.JMVA.2006.05.005

Schmidt-Thomé, P., 2006. Natural and Technological Hazards and Risks Affecting the Spatial Development of European Regions Edited by Philipp Schmidt-Thomé, Geological Survey of Finland, Special Paper 42.

Schmidt-thomé, P., Kallio, H., Greiving, S., Fleischhauer, M., 2003. Development of Natural Hazard maps for European Regions, in: EU-MEDIN Forum on Disaster Research "The Road to Harmonisation." Thessaloniki.

Schmidt, J., Matcham, I., Reese, S., King, A., Bell, R., Henderson, R., Smart, G., Cousins, J., Smith, W., Heron, D., 2011. Quantitative multi-risk analysis for natural hazards: a framework for multi-risk modelling. *Nat. Hazards* 58, 1169–1192. https://doi.org/10.1007/s11069-011-9721-z

Schreider, S.Y., Smith, D.I., Jakeman, A.J., 2000. Climate Change Impacts on Urban Flooding. *Clim. Change* 47, 91–115. https://doi.org/10.1023/A:1005621523177

Schulte, M., Schumann, a. H., 2015. Extensive spatio-temporal assessment of flood events by application of pair-copulas. *Proc. Int. Assoc. Hydrol. Sci.* 370, 177–181. https://doi.org/10.5194/piahs-370-177-2015

Schwarz, J., Maiwald, H., 2012. Empirical vulnerability assessment and damage for description natural hazards following the principles of modern macroseismic scales, in: 14th WCEE-World Conference of Earthquake ….

Selva, J., 2013. Long-term multi-risk assessment: statistical treatment of interaction among risks. *Nat. Hazards* 67, 701–722. https://doi.org/10.1007/s11069-013-0599-9

Seo, D.-J., Herr, H.D., Schaake, J.C., 2006. A statistical post-processor for accounting of hydrologic uncertainty in short-range ensemble streamflow prediction. *Hydrol. Earth Syst. Sci. Discuss.* 3, 1987–2035. https://doi.org/10.5194/hessd-3-1987-2006

Serinaldi, F., Kilsby, C.G., 2016. A Blueprint for Full Collective Flood Risk Estimation: Demonstration for European River Flooding. *Risk Anal.* https://doi.org/10.1111/risa.12747

Shi, P., 2011. Atlas of Natural Disaster Risk of China. Science Press, Beijing.

Shi, P., Kasperson, R., 2015. World Atlas of Natural Disaster Risk, World Atlas of Natural Disaster Risk, IHDP/Future Earth-Integrated Risk Governance Project Series. Springer Berlin Heidelberg, Berlin, Heidelberg. https://doi.org/10.1007/978-3-662-45430-5

Shi, P., Shuai, J., Chen, W., Lu, L., 2010. Study on large-scale disaster risk assessment and risk transfer models. *Int. J. Disaster Risk Sci.* 1, 1–8. https://doi.org/10.3974/j.issn.2095-

0055.2010.02.001

SHIEH, C.L., CHEN, Y.S., TSAI, Y.J., WU, J.H., 2009. Variability in rainfall threshold for debris flow after the Chi-Chi earthquake in central Taiwan, China. *Int. J. Sediment Res.* 24, 177–188. https://doi.org/10.1016/S1001-6279(09)60025-1

Shinozuka, M., Feng, M.Q., Lee, J., Naganuma, T., 2000. Statistical Anlysis of Fragility Curves. *J. Geotech. Geoenvironmental Eng.* 126, 1998–2001.

Shukla, J., Misra, B.M., Shukla, J., Misra, B.M., 1977. Relationships Between Sea Surface Temperature and Wind Speed Over the Central Arabian Sea, and Monsoon Rainfall Over India. *Mon. Weather Rev.* 105, 998–1002. https://doi.org/10.1175/1520-0493(1977)105<0998:RBSSTA>2.0.CO;2

Singhal, A., Kiremidjian, A.S., 1996. Method for Probabilistic Evaluation of Seismic Structural Damage. *J. Struct. Eng.* 122, 1459–1467. https://doi.org/10.1061/(ASCE)0733-9445(1996)122:12(1459)

Sklar, A., 1959. Fonctions de répartition à n dimensions et leurs marges. *Publ. Inst. Stat. Univ. Paris* 8, 229–231. https://doi.org/10.1007/978-3-642-33590-7

Smit, B., Wandel, J., 2006. Adaptation, adaptive capacity and vulnerability. *Glob. Environ. Chang.* 16, 282–292. https://doi.org/10.1016/j.gloenvcha.2006.03.008

Smith, D., 1994. Flood damage estimation-A review of urban stage-damage curves and loss function. *Water SA* 20, 231–238. https://doi.org/10.1007/978-981-287-365-1_13

Smith, L.S., Liang, Q., 2013. Towards a generalised GPU/CPU shallow-flow modelling tool. *Comput. Fluids* 88, 334–343. https://doi.org/10.1016/j.compfluid.2013.09.018

Spencer, T., Brooks, S.M., Evans, B.R., Tempest, J.A., Möller, I., 2015. Southern North Sea storm surge event of 5 December 2013: Water levels, waves and coastal impacts. *Earth-Science Rev.* 146, 120–145. https://doi.org/10.1016/J.EARSCIREV.2015.04.002

Steers, J.A., 1953. The East Coast Floods. *Geogr. J.* 119, 280–295.

Stott, P.A., Stone, D.A., Allen, M.R., 2004. Human contribution to the European heatwave of 2003. *Nature* 432, 610–614. https://doi.org/10.1038/nature03089

Svensson, C., Jones, D.A., 2004. Dependence between sea surge, river flow and precipitation in south and west Britain. *Hydrol. Earth Syst. Sci.* 8, 973–992. https://doi.org/10.1002/joc.794

Svensson, C., Jones, D.A., 2002. Dependence between extreme sea surge, river flow and precipitation in eastern Britain. *Int. J. Climatol.* 22, 1149–1168. https://doi.org/10.1002/joc.794

Tang, Y., Lean, H.W., Bornemann, J., 2013. The benefits of the Met Office variable resolution NWP model for forecasting convection. *Meteorol. Appl.* 20, 417–426. https://doi.org/10.1002/met.1300

Tawn, J.A., 1988. Biometrika Trust Bivariate Extreme Value Theory : Models and Estimation. *Biometrika* 75, 397–415.

Teng, J., Jakeman, A.J., Vaze, J., Croke, B.F.W., Dutta, D., Kim, S., 2017. Flood inundation modelling: A review of methods, recent advances and uncertainty analysis. *Environ. Model. Softw.* 90, 201–216. https://doi.org/10.1016/J.ENVSOFT.2017.01.006

Thieken, A.H., Müller, M., Kreibich, H., Merz, B., 2005. Flood damage and influencing factors: New insights from the August 2002 flood in Germany. *Water Resour. Res.* 41, 1–16. https://doi.org/10.1029/2005WR004177

Thielen, J., Bartholmes, J., Ramos, M.-H., de Roo, A., 2009. The European Flood Alert System - Part 1: Concept and development. *Hydrol. Earth Syst. Sci. Discuss.* 13, 125–140. https://doi.org/10.5194/hessd-5-257-2008

Thierry, P., Stieltjes, L., Kouokam, E., Nguéya, P., Salley, P.M., 2008. Multi-hazard risk mapping and assessment on an active volcano: the GRINP project at Mount Cameroon. *Nat. Hazards* 45, 429–456. https://doi.org/10.1007/s11069-007-9177-3

Thompson, C.M., Frazier, T.G., 2014. Deterministic and probabilistic flood modeling for contemporary and future coastal and inland precipitation inundation. *Appl. Geogr.* 50, 1–14. https://doi.org/10.1016/J.APGEOG.2014.01.013

Thywissen, K., 2006. Components of risk: a comparative glossary, UNU-EHS. UNU-EHS, Paffenholz, Bornheim, Germany.

UNISDR, 2009. UNISDR Terminology for Disaster Risk Redution, United Nations International Strategy for Disaster Reduction (UNISDR). Geneva, Switzerland.

United Nations, 1999. International Decade for Natural Disaster Reduction (IDNDR) Programme Forum 1999, in: International Decade for Natural Disaster Reduction (IDNDR). Geneva, Switzerland, pp. 1–138.

Uzielli, M., Nadim, F., Lacasse, S., Kaynia, A.M., 2008. A conceptual framework for quantitative estimation of physical vulnerability to landslides. *Eng. Geol.* 102, 251–256. https://doi.org/10.1016/J.ENGGEO.2008.03.011

Van Den Hurk, B., Van Meijgaard, E., de Valk, P., van Heeringen, K.-J.J., Gooijer, J., 2015. Analysis of a compounding surge and precipitation event in the Netherlands. *Environ. Res. Lett.* 10, 035001. https://doi.org/10.1088/1748-9326/10/3/035001

Wahl, T., Jain, S., Bender, J., Meyers, S.D., Luther, M.E., 2015. Increasing risk of compound flooding from storm surge and rainfall for major US cities. *Nat. Clim. Chang.* 5, 1–6. https://doi.org/10.1038/nclimate2736

Wahl, T., Ward, P.J., Winsemius, H.C., AghaKouchak, A., Bender, J., Haigh, I.D., Jain, S., Leonard, M., Veldkamp, T.I.E., Westra, S., 2018. When Environmental Forces Collide. *Eos (Washington. DC).* https://doi.org/10.1029/2018EO099745

Wang, C., Chang, N. Bin, Yeh, G.T., 2009. Copula-based flood frequency (COFF) analysis at the confluences of river systems. *Hydrol. Process.* 23, 1471–1486. https://doi.org/10.1002/hyp.7273

Wang, Z., He, F., Fang, W., Liao, Y., 2013. Assessment of physical vulnerability to agricultural drought in China. *Nat. Hazards* 67, 645–657. https://doi.org/10.1007/s11069-013-0594-1

Ward, P.J., Couasnon, A., Eilander, D., Haigh, I.D., Hendry, A., Muis, S., Veldkamp, T.I.E.E., Winsemius, H.C., Wahl, T., 2018. Dependence between high sea-level and high river discharge increases flood hazard in global deltas and estuaries. *Environ. Res. Lett.* 13, 084012. https://doi.org/10.1088/1748-9326/aad400

Ward, P.J., Jongman, B., Aerts, J.C.J.H., Bates, P.D., Botzen, W.J.W., DIaz Loaiza, A., Hallegatte, S., Kind, J.M., Kwadijk, J., Scussolini, P., Winsemius, H.C., 2017. A global framework for future costs and benefits of river-flood protection in urban areas. *Nat. Clim. Chang.* https://doi.org/10.1038/nclimate3350

Westen, C. Van, Kappes, M.S., Luna, B.Q., Frigerio, S., Glade, T., Malet, J., 2014. Mountain Risks: From Prediction to Management and Governance, in: Van Asch, T., Corominas, J., Greiving, S., Malet, J.-P., Sterlacchini, S. (Eds.), Mountain Risks: From Prediction to Management and Governance, Advances in Natural and Technological Hazards Research, Advances in Natural and Technological Hazards Research. Springer Netherlands, Dordrecht. https://doi.org/10.1007/978-94-007-6769-0

Westen, C. Van, Montoya, L., Boerboom, L., 2002. Multi-Hazard Risk Assessment using GIS in urban areas: A case study for the city of Turrialba, Costa-Rica, in: Proc. Regional Workshop. pp. 53–72.

White, C.J., 2007. The Use of Joint Probability Analysis to Predict Flood Frequency in Estuaries and Tidal Rivers. University of Southampton.

Winsemius, H.C., Aerts, J.C.J.H., Van Beek, L.P.H., Bierkens, M.F.P., Bouwman, A., Jongman, B., Kwadijk, J.C.J., Ligtvoet, W., Lucas, P.L., Van Vuuren, D.P., Ward, P.J., 2016. Global drivers of future river flood risk. *Nat. Clim. Chang.* https://doi.org/10.1038/nclimate2893

Wipulanusat, W., Nakrod, S., Prabnarong, P., 2009. Multi-hazard Risk Assessment Using GIS and RS Applications: A Case Study of Pak Phanang Basin. *Walailak J. Sci. Technol.* 6, 109–125.

Wolf, J., 2009. Coastal flooding: Impacts of coupled wave-surge-tide models. *Nat. Hazards*. https://doi.org/10.1007/s11069-008-9316-5

Woodruff, J.D., Irish, J.L., Camargo, S.J., 2013. Coastal flooding by tropical cyclones and sea-level rise. *Nature* 504, 44–52. https://doi.org/10.1038/nature12855

Wyncoll, D., Gouldby, B., 2013. Integrating a multivariate extreme value method within a system flood risk analysis. *J. Flood Risk Manag.* 8, 145–160. https://doi.org/10.111/jfr3.12069

Xia, X., Liang, Q., Ming, X., 2019. HiPIMS: A High-Performance Integrated hydrodynamic Modelling System for high-resolution simulation of flooding processes in large catchments. *under Rev.*

Xia, X., Liang, Q., Ming, X., Hou, J., 2017. An efficient and stable hydrodynamicmodel with novel source term discretization schemes for overland flow and flood simulations. *Water Resour. Res.* 53, 3730–3759. https://doi.org/10.1002/2016WR020055

Xu, L., Meng, X., Xu, X., 2014. Natural hazard chain research in China: A review. *Nat. Hazards*. https://doi.org/10.1007/s11069-013-0881-x

Xu, Y., Huang, G., Fan, Y., 2017. Multivariate flood risk analysis for Wei River. *Stoch. Environ. Res. Risk Assess.* 31, 225–242. https://doi.org/10.1007/s00477-015-1196-0

Yan, J., 2007. Enjoy the Joy of Copulas : With a Package copula. *J. Stat. Softw.* 21, 1–21.

Yin, Y.-J., Li, Y., 2011. Probabilistic loss assessment of light-frame wood construction subjected to combined seismic and snow loads. *Eng. Struct.* 33, 380–390. https://doi.org/10.1016/j.engstruct.2010.10.018

Yue, S., Ouarda, T.B.M.., Bobée, B., Legendre, P., Bruneau, P., 1999. The Gumbel mixed model for flood frequency analysis. *J. Hydrol.* 226, 88–100. https://doi.org/10.1016/S0022-1694(99)00168-7

Zhang, H., 2014. Urban Flood Simulation by Coupling a Hydrodynamic Model with a Hydrological Model. Newcastle Univerisity.

Zhang, L., Singh, V.P., 2007. Trivariate Flood Frequency Analysis Using the Gumbel–Hougaard Copula. *J. Hydrol. Eng.* 12, 431–439. https://doi.org/10.1061/(ASCE)1084-0699(2007)12:4(431)

Zhang, L., Singh, V.P., ASCE, F., 2006. Bivariate Flood Frequency Analysis Using the Copula Method. *J. Hydrol. Eng.* 11, 150–164. https://doi.org/10.1061/(ASCE)1084-0699(2006)11:2(150)

Zheng, F., Leonard, M., Westra, S., 2015. Efficient joint probability analysis of flood risk. *J. Hydroinformatics* 17, 584. https://doi.org/10.2166/hydro.2015.052

Zheng, F., Westra, S., Leonard, M., Sisson, S.A., 2014. Modeling dependence between extreme rainfall and storm surge to estimate coastal flooding risk. *Water Resour. Res.* 50, 2050–2071. https://doi.org/10.1002/2013WR014616.Received

Zheng, F., Westra, S., Sisson, S. a., 2013. Quantifying the dependence between extreme rainfall and storm surge in the coastal zone. *J. Hydrol.* 505, 172–187. https://doi.org/10.1016/j.jhydrol.2013.09.054

Zhou, Q., Leng, G., Su, J., Ren, Y., 2019. Comparison of urbanization and climate change impacts on urban flood volumes: Importance of urban planning and drainage adaptation. *Sci. Total Environ.* 658, 24–33. https://doi.org/10.1016/J.SCITOTENV.2018.12.184